Scattering Analysis of Supramolecular Nanoparticle Formation through Electrostatic Self-Assembly

Der Friederich-Alexander-Universität Erlangen-Nürnberg

Der Naturwissenschaftlichen Fakultät

Zur

Erlangung des Doktorgrades Dr. rer. nat.

vorgelegt von:

Giacomo MARIANI

aus Senigallia/Italien

Als Dissertation genehmigt von der Naturwissenschaftlichen Fakultät der Friedrich-Alexander-Universität Erlangen-Nürnberg.

Tag der mündlichen Prüfung:

Vorsitzender des Promotionsorgans: Gutachter/in:

Prof. Dr. Franziska Gröhn

Prof. Dr. Andreas Hirsch

Die vorliegende Arbeit entstand im Zeitraum von Dezember 2011 bis Juli 2017 im Departement für Chemie und Pharmazie (Interdisciplinary Center for Molecular Materials) der Friedrich-Alexander-Universität Erlangen-Nürnberg im Arbeitskreis von Frau Prof. Dr. Franziska Gröhn. Ein Teil der vorliegenden Arbeit entstand am Institut Laue-Langevin (Grenoble, Frankreich) unter Betreuung von Dr. Ralf Schweins.

Contents

Abstract

In the last years, nanomaterials have become more and more important in everyday life for a wide range of applications from medicine and information storage to sunscreens and cosmetics. Among the different strategies to form nanomaterials, self-assembly is scientifically and technologically interesting since it is the favourite process in nature to form functional materials and it yields to an incredible range of different structures. Despite its success, the nanoparticle formation process, the relationships of nanoparticle structure and functionality, nanoparticle stability and many other basic aspects remain not fully understood.
In the present work, the electrostatic self-assembly of positively charged polyelectrolytes and oppositely charged organic dyes into supramolecular assemblies is presented. The model system consists of cationic polyamidoamine dendrimers of different generations and anionic di- and trivalent dyes. Different interactions occur leading to the formation of the supramolecular nanoparticles: electrostatic interaction between the building blocks, mutual π-π interaction between the dye molecules and geometrical effects. Stable and well-defined nanoparticles form in solution. Under focus is the interplay of electrostatic and π-π interaction and its effects on the self-assembly and on the nanoparticle structure. The structural characterisation consists of scattering methods such as static and dynamic light scattering and small angle neutron scattering and of atomic force microscopy. The nanoparticle charge has been studied via ζ-potential measurements. The interaction thermodynamics has been investigated using isothermal titration calorimetry, while the dye stacking due to the π-π interaction has been studied via UV-Vis

spectroscopy.

Well-defined nanoparticles with dimensions from few tens of nanometers to microns and shapes ranging from simple spheres to more complex elongated structures are formed in solution by simple mixing of appropriate building blocks. The role of the electrostatic and the π-π interaction has been studied changing the solution pH and ionic strength while studying at the same time the thermodynamics of the self-assembly. The aggregation free energy exchange can be divided in two terms: one describing the electrostatic interaction and the other describing the π-π interaction. We have shown that the electrostatic one is responsible for nanoparticle stabilisation and size, while the π-π one determines their shape. Strong π-π interacting dyes result in elongated nanoparticles, while weak interacting ones result in spherical aggregates.

Nanoparticles that can be controlled by external stimuli, as for example light, have been realised by using a dye that trans-cis isomerize upon irradiation. Nanoparticles with light-tuneable shape have been obtained using acid yellow 38 as counterions and poly(diallyldimethyl-ammonium chloride) as polyelectrolyte. In this case, flexible cylinders with elliptical cross-section form before irradiation, while the system exhibits core-shell ellipsoids after irradiation.

To conclude, this study brings new insights into the factors controlling the nanoparticle stabilisation, shape and dimensions in electrostatic self-assembly. In particular, it proves that the thermodynamics of interaction occurring in the self-assembly has a fundamental role. From these results, it will be possible to predict nanoparticle shapes knowing only the thermodynamic parameters for the interaction of the chosen molecular building blocks. Thus, a precise molecular design of the dye molecule (i.e., choosing appropriate substituents) will allow tailoring the structure of the nanoparticles. Hence, fundamental steps in developing a box of molecular "building bricks" allowing for a targeted structural design are made. This may, for example, be of potential in the development of novel self-assembled photocatalysts or smart therapeutic carrier systems.

Kurzzusammenfassung

Während der letzten Jahre gewannen Nanomaterialien zunehmend an Bedeutung: Ihre Anwendungen reichen von der Medizin bis hin zur Datenspeicherung und zur Kosmetik. Unter den verschiedenen Strategien zur Herstellung von Nanomaterialien stellte sich das Konzept der Selbst-Assemblierung als wissenschaftlich und technologisch interessante Methode heraus, insbesondere da dieses Vorgehen von Vorgängen in der Natur inspiriert ist und eine Vielzahl verschiedener Strukturen erzielen kann. Trotz der weit-reichenden Anwendung sind die Bildungsprozesse von Nanopartikeln, deren Stabilität und der Zusammenhang von Struktur und Funktionalität noch nicht voll-ständig verstanden.
In der vorliegenden Arbeit wurde die elektrostatische Selbst-Assemblierung von positiv geladenen Polyelektrolyten und entgegengesetzt geladenen organischen Farbstoffen in supramolekulare Aggregate untersucht. Das untersuchte Modellsystem bestand aus kationischen Poly(amido amin)-Dendrimeren verschiedener Generationen und anionischen di- bzw. trivalenten Farbstoffen. Die Assoziation in stabile und definierte supramolekulare Aggregate erfolgte hier auf der Grundlage verschiedener Wechselwirkungen: elektrostatische Interaktion zwischen den Bausteinen, π-π Wechselwirkungen der Farbstoffe sowie durch den Einfluss geometri-scher Effekte. Im Fokus der Arbeit stand dabei das Zusammenspiel von elektrostatischen und π-π Wechselwirkungen und dessen Effekt auf den Selbst-Assemblie-rungsprozess und die Nanopartikel Struktur. Die strukturelle Charakterisierung erfolgte mittels verschiedener Streumethoden, darunter statische und dynamische Lichtstreuung, Neutronen-Kleinwinkelstreuung sowie Ras-

terkraftmikroskopie. Die Stabilisierung der Nanopartikel durch Ladungen wurde durch ζ-Potential Messungen untersucht, während die Thermodynamik der Bindungsprozesse mittels Isothermer Titrationskalorimetrie und die π-π Wechselwirkungen der Farbstoffe mittels UV/Vis Spektroskopie analysiert wurden.
Durch einfaches Mischen von geeigneten Bausteinen in wässriger Lösung bilden sich definierte Nanopartikel mit Dimensionen von wenigen Nanometern bis hin zu Mikrometern und vielfältigen Formen von einfachen kugelförmigen bis hin zu komplexen, elongierten Strukturen. Der Einfluss von elektrostatischen und π-π Wechselwirkungen auf Strukturbildung und thermodynamische Bindungsprozesse wurde durch Änderung von pH Wert und Ionenstärke der Lösung untersucht. Die freie Energie der Aggregation bestand dabei aus zwei Beiträgen: zum einen der elektrostatischen Wechselwirkung und zum anderen der π-π Wechselwirkung. Wir konnten zeigen, dass der elektrostatische Beitrag für die Stabilisierung und Größe der Nanopartikel verantwortlich ist, während die π-π Wechselwirkungen die Form der Nanopartikel bestimmen. Dabei resultieren aus starken π-π Wechselwirkungen elongierte Nanopartikel, während schwache Wechselwirkungen zur Bildung von kugelförmigen Aggregaten führen.
Nanopartikel, die durch äußere Einflüsse wie Licht kontrolliert werden können, konnten durch Farbstoffe mit der Fähigkeit zur trans-cis Isomerisierung hergestellt werden. Dabei ergaben sich Nanopartikel mit Licht-responsiver Form aus Acid Yellow 38 und Poly(diallydimethyl ammonium chlorid) als Polyelektrolyt. Vor der Bestrahlung der Aggregate konnten hier flexible Zylinder mit elliptischem Querschnitt beobachtet werden, während nach der Bestrahlung elliptische Core-Shell Strukturen entstanden.
Zusammenfassend ermöglicht diese Arbeit neue Einblicke in die Faktoren, welche für die Nanopartikel Stabilisierung, deren Form und Größe verantwortlich sind. Insbesondere konnte gezeigt werden, dass der thermodynamische Einfluss der Wechselwirkungen eine fundamentale Rolle zur Bildung der Aggregate durch elektrostatische Selbst-Assemblierung spielt. Ausgehend von diesen Ergebnissen

wird es in Zukunft möglich sein, die Form von Nanopartikeln vorauszusagen, wenn die thermodynamischen Parameter der Wechselwirkung der Bausteine bekannt sind. Die Struktur der Nanopartikel kann damit durch präzises Design der molekularen Strukturen der Farbstoffe gesteuert werden. Folglich erzielte diese Arbeit fundamentale Schritte in der Entwicklung einer Werkzeugkiste molekularer Bausteine, die das gezielte, strukturelle Design von Nanopartikeln ermöglicht. Damit können selbst-assemblierte Strukturen entstehen, welche großes Potential als Photokatalysatoren oder intelligente therapeutische Transportsysteme zeigen.

Chapter 1 Introduction

1.1 Self-Assembly

Self-assembly is the autonomous organization of building blocks into order aggregates without human intervention [1]. Since the first example in 1967 from Charles J. Pedersen [2], the concept of self-assembly has attracted many scientist because the ability of molecules to recognize each other and to form well-defined complexes lies at the basis of many biological processes. The remarkable importance of this concept has been recognized in 1987 when the Nobel prize was awarded to Pedersen, Jean-Marie Lehn and Donald J. Cram for their pioneering work. Supramolecular chemistry was defined by Lehn as *the chemistry of the intermolecular bound* [3], hence, supramolecular self-assembly is based on non-covalent interaction.

In the early stages, the formation of host-guest complexes, dimers or the binding of host molecules to bulk material were the central theme of the research in this field as it is clear from the work of the the three Nobel laureate scientist. Under focus was the synthesis of organic compound of low molecular weight mostly designed to specifically and selectively bind other molecules [4; 5]. The factors that determine the ability of the molecules to recognize each other and fit into one another like a key fits a lock were elucidated. Hence, host-guest complexes or enzyme-like complexes (one or more compounds of low molecular weight bind to a specific region in a bulk compound) were formed [6]. In the last decade, self-assembly has proven itself as a route to produce nanoparticles; therefore, the

interest has shifted from aggregates of few molecules towards the nanoscale. In his editorial in the 2014 special issue of *Angewandte Chemie* completely dedicated to nanotechnology, nanomaterials, nanotoxicology and nanomedicine, Younan Xia asks if we are entering the nano era stating that *nanotechnology has become ubiquitous in our everyday lives, from medicine and information storage to sunscreens and cosmetics* [7]. However despite the large success of the nanoscience, the nanoparticle formation process, the relationships of nanoparticle structure and functionality, the interplay of different interactions, nanoparticle stability and many other basic aspects remains not completely understood. Indeed, in the same editorial Xia stresses that *many nanomaterials have a long way to go to move from the lab to industrial application, because the production of precisely defined nanoparticles on an industrial scale is extremely difficult*.

Different strategies have been designed to form nanoparticles. Among them, self-assembly is scientifically and technologically interesting. First of all, it has a central importance in life: the cell contains an incredible amount of complex structure formed by self-assembly such as lipid membranes, folded proteins, structured nucleic acids, protein aggregates or molecular machines [8].

Secondly, self-assembly occurs in systems with great potential for use in materials and condensed matter science [9]; for instance, great potential lies in nature-inspired nanosystems that can be used in drug delivery [10; 11].

In addition, self-assembly is extremely versatile since simply choosing different building blocks and/or different interactions a wide range of different systems can be formed. It has crucial importance for the formation of molecular crystals [12], colloids [13], supramolecular polymers [14] or monolayers of different components [15].

All these properties make self-assembly one of the most general strategies available for forming nanoparticles that are of interest in a wide range of fields, from chemistry, biology to material science and nanoscience. Often, it shows all the requirement for practical application: it is economic, easy-controlled and fast. For

example, self-assembled colloids are often use as solvents, supramolecular polymers are used as adhesives, in printing, in cosmetics, in the field of personal care or as coatings.

Last but not least, philosophically the concept of order created from disorder has always fascinated the humans and self-assembly is one of the main route to achieve such an objective.

Sometimes, the self-assembly is divided into two similar and at the same time different main categories: dynamic and static self-assembly [16]. To the first belong all the systems, as many of biological origin, where the assembled structures require to dissipate energy in order to prevent degradation. For instance, this is the case of biological cells. Instead, the second groups all the systems that are at global or local equilibrium and do not require energy dissipation as for example globular proteins. Often, static self-assembly requires energy in order to form assembled structures, however after nanoparticle formation the system is thermodynamically at equilibrium. Hence, the free energy gain on structure formation must be significantly higher than the thermal energy in this cases. It must be noted that this definition does not separate spontaneous and induced self-assembly, it is only based on the stabilization of the self-assembled structures.

Herein, I will focus on equilibrium self-assembly analyzing the driving forces and the connections between building blocks and nanoparticle final structure. Unveiling these fundamental relationships is crucial to tailor the nanoparticle shape for specific application and to design new route for nanoparticle formation. This is particularly important since understanding the structure is often the key to understand the function. In addition, there is a lack in understanding how the thermodynamics of the interaction between the building blocks acts on self-assembly in more complex systems than the amphiphilic ones.

1.2 Strategies for Equilibrium Self-Assembly

Before describing in details the concept and the objective of the PhD project, an analysis of the different approaches and of the different interactions used to perform supramolecular self-assembly is needed. Only a multidisciplinary approach comparing the different self-assembly strategies to find similarities and differences can lead to the understanding of the fundamental principles behind self-assembly and provides the possibility for developing new self-assembly routes. In addition, unveiling the basic relationship of building block interactions with nanoparticle morphology and function from the molecular to the supramolecular scale is of fundamental technological importance. Scientifically, understanding how the thermodynamics of the system affect the self-assembly general principles is challenging.
Self-assembled structures can be formed using different interactions: hydrophobic interactions, hydrogen bonding, metal coordination, ionic interactions, π-π interaction and their combination. Nanoaggregates with size ranging from few nanometers as in the case of π-stacked dye dimers [17] to macro meters as in the case of the flat discs obtained in salt-free cationic surfactant solutions can be obtained selecting appropriate building blocks [18]. In the following the different interactions that can be used in self-assembly will be discussed.

1.2.1 Hydrogen Bonding

A hydrogen bond is a weak type of force that forms a special type of dipole-dipole attraction which occurs when a hydrogen atom bonded to a strongly electronegative atom exists in the vicinity of another electronegative atom with a lone pair of electrons. These bonds are generally stronger than ordinary dipole-dipole and dispersion forces, but weaker than true covalent and ionic bonds. Due to its selectivity and directionality, it is widely used in supramolecular self-assembly combining appropriate molecules. In addition, the formation of hydrogen bounds is

reversible and depends on the chemical environment such as the solvent, hence the nanoparticle physical properties determined by the hydrogen bounds can be directly controlled varying the external parameters [19; 20; 21].

The hydrogen bond is at the base of the formation of many systems in biology. Among the others, nucleoside such as guanine and its derivatives have been successfully used since 1962 when hydrogels made by 5'-guanosine monophosphate have been formed [22]. The self-complementary hydrogen bonding edges and aromatic surfaces of the guanosine derivatives make them perfect to self-associate; different structures can be formed controlling the conditions [23]. It is well known that nucleosides are part of the nucleotides and that the latter are the molecular building-blocks of DNA and RNA. Therefore, the specific bonding of DNA base pairs not only provides the chemical foundation for genetics, but it can be used in nanotechnology to direct the assembly of highly structured materials with specific nanoscale features. More than two decades ago, the first artificial DNA structure was realized: a stick-cube, whose edges were double helices [24]. Along the years, DNA has proved to be a versatile building block for programmable construction of complex structures as for example two-dimensional crystals [25], nanotubes [26; 27; 28], and three-dimensional wire-frame nanopolyhedra [29; 30; 31]. In the last years, Douglas et al. have realized custom three-dimensional shapes formed as pleated layers of helices constrained to a honeycomb lattice [32].

One limitation in this approach is the strength of the hydrogen bounding: the more polar the solvent is, the weaker the hydrogen bonds are because of the increasing competitive solvation of donor and acceptor sites by solvent molecules [33]; a single hydrogen bond possesses a considerable binding energy only in unpolar, aprotic solvents such as hexane or toluene. Stable supramolecular assemblies can be obtained in more polar solvents such as chloroform or acetonitrile by a combination of several such weak interactions in binding motifs with multiple hydrogen bonds. Triple hydrogen-bonding motifs have been studied ex-

tensively in the past by the research groups of Whitesides [34; 35], Zimmermann [36], and Meijer [37]. In the last years, quadruple hydrogen bonding motifs have been formed [38]. This concept is very powerful since, in addition to the heterodimerization reachable with the triple hydrogen bound motive, it gives rise to two arrays capable of homodimerization [39].

The attachment of more than one binding motif to oligomer or polymer chains enables new applications in the field of polymer chemistry and material science to emerge. These binding motifs not only results in dimerization but also in supramolecular polymerization: a sort of *supra-polymerization* [40]. In contrast to conventional polymers in which the macromolecular chains consist of covalently and hence irreversibly connected monomer units, supramolecular polymers only demonstrate their polymeric properties by the self-association of the corresponding binding motifs [41; 42]. This is a first step towards intelligent materials with tailor-made properties. The first reversible homopolymer based on this principle was realized by Meijer et al.: compounds with association number of more than 500 have been formed in chloroform [14]. Relying on this concept, polymers with a wide range of structures have been realized combining different building blocks. For example, in 2013 a complex polymeric architecture based on a block copolymer with a cylindrical brush block and a single-chain polymeric nanoparticle block folded due to strong intramolecular hydrogen bonds has been obtained [43]. As a H-bonding moiety, the ureido-pyrimidinone (UPy) group has been used due to its ability to form strong, reversible, quadruple hydrogen bonds [14]. This group is used in a wide range of self-assembly-based application [44; 45]. These results are of special relevance since cylindrical brushes are used as building blocks whose represent a new class of polymeric materials that feature self-assembly on mesoscales, ultra-soft elastomers, intramolecular mechanochemistry, lubrication of cartilage, and mucus clearance in lung airways.

Metal Coordination

A coordination complex or metal complex is composed of a central atom or ion, which is usually metallic and a surrounding array of bound molecules or ions. The term coordination refers to the *coordinate covalent bonds* (i.e. dipolar bonds) between the ligands and the central atom. In a typical complex, a metal ion is bonded to several donor atoms, which can be the same or different species.
Since 1990, this strategy has been largely applied in self-assembly. For example, Lehn [46], Raymond [47] and Albrecht developed and explored the self-organization of supramolecular helicates [48]. In particular, Lehn demonstrated that, in the presence of Cu^{1} ions, mixtures of oligobipyridine strands containing between 2 and 5 bipyridine units self-organize into double helicates exclusively composed of oligobipyridine strands of the same length.
Along the years, after proving the possibility of using metal coordination motifs as effective self-assembly strategy, the research has shifted towards the mimicking of biological material properties in order to realize new polymer materials with property-control design. For example, K. Y. C. Lee, inspired by the iron-binding catechol-rich proteins secreted during self-assembly of the self-healing mussel holdfast threads [49], has demonstrated how dilute low viscosity aqueous solutions of catechol-modifed polyethyleneglycol (PEG) polymers and $FeCl_3$ changes to strong viscoelastic fluids following a basic pH jump due to instant Fe^{3+} catechol coordination crosslinking [50]. The coordination-crosslinked polymer networks display elastic moduli approaching covalently crosslinked hydrogels under high strain rates with complete recovery after failure. Since several metals in addition to iron are utilized by marine and terrestrial invertebrates to control the mechanical properties of secreted catechol-rich polymeric materials via coordination based crosslinking [51], vanadium, iron and aluminum salts and simple catechol-modifed PEG polymers have been used showing that metal-ion identity provides remarkable control over hydrophilic metal-coordinating polymer mechanics by dictating crosslink dynamics [52]. Metal-coordination provides the

opportunity to tune viscoelastic properties of hydrophilic polymer materials over several orders of magnitude purely by the simple choice of coordinating metal ion identity (Figure 1.1). These results highlight the importance of bio-inspired metal-coordination system to gain control over material properties.

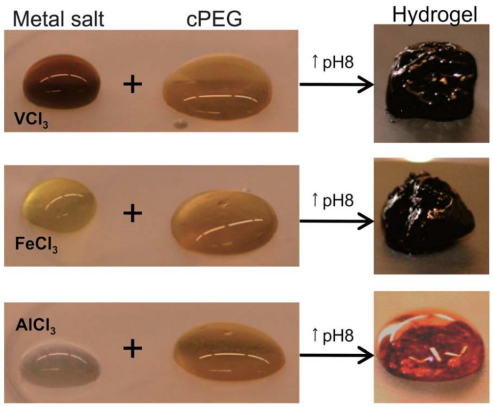

Figure 1.1: *Three different trivalent metal ion cross-linkers are used to establish three different polymer networks. The rheological properties of the networks are different. [52]*

1.2.2 Hydrophobic Effect

The hydrophobic effect arises when low water-soluble molecules called hydrophobes are put into water. This effect tends to clump up together the molecules instead of uniformly distribute them in water to minimize the contact with the solvent. This occurs because interactions between the hydrophobic molecules enable the displaced water molecules to make hydrogen bonds more freely with each other and increase the number of hydrogen bonds they are involved with. This results in the decrease of the overall free energy. More precisely, the hydrophobic effect is an extreme case of solution non-ideality. This is expressed by the very high values of the molar excess free energy of the solute (i.e., the difference between the chemical potential of the solute and its chemical potential had the solution been ideal).

A number of self-assembly processes are driven by the hydrophobic effect, including micelle, vesicles and bilayers formation [53; 54], or protein folding [55]. When amphiphiles are added in solution there is a favorable free energy associated with the coming together of the hydrophobic tails. Their aggregation is accompanied by a large anomalous positive entropy change peculiar to water [56].

The typical, but nevertheless important, example of self-assembly based on hydrophobic effect is the surfactant one. These molecules are amphiphilic and self-assemble once dispersed in solution achieving segregation of their hydrophobic parts from water [57]. The aggregates may be spherical, globular, or rodlike or have the structure of spherical bi-layers depending on the type of surfactant and on solution conditions. Vesicles are valuable both in biological science to reproduce the cell wall and to study the behaviour of the membrane proteins and in pharmaceutical science as perfect system for drug delivery. The self-assembly behaviour can be described using the concept of molecular packing parameter, introduced by Israelachvili, Mitchell and Ninham [58; 59; 60]. This is based on geometrical considerations taking into account the volume and the length of the surfactant tail and the equilibrium area per molecule at the aggregate surface. Unfortunately, this parameters is useful to explain the observed structures, but has a very limited predictive power since it is almost impossible to know the equilibrium area per molecule a priori. The calculation of the free energy required to form an equilibrated structure is required to gain a deep understanding of surfactant self-assembly.

Over the last few years, the interest has shifted towards more complex systems in order to mimicking biological structures, to form new and more stable structures and to generate biocompatible and bioactive drug delivery systems. Polymeric systems with enhanced biofunctionality such as amphiphilic block copolymers that can act as mimetic for biological membranes are one of these new systems. Polymer hybrid materials are promising for applications in biomedicine

and biotechnology since there are virtually no limits to combinations of monomers, biologic and synthetic building blocks. The design of (amphiphilic) block copolymers is one of the oldest and most researched themes in polymer chemistry and substantial progress has been made over the last 20 years. Historically, these systems where formed joining together two segments (one hydrophobic and one hydrophilic) through a carbon-carbon single bond and they can thus not be cleaved. More recently, new amphiphilic block copolymers have been obtained linking the two segments via a weaker linkage offering the opportunity for disassembly in response to an external trigger such as temperature or a change of pH [61]. These systems are of specific interest for nanoengineering and nanoscience. These linkage points include covalent ones (for example Diels-Alder or hydrolysable units, as well as photocleavable moieties) and supramolecular systems, for example those based on hydrogen bonding motifs, metal complexes, or host–guest systems [62; 60]. Replacing lipids with high molecular weight block copolymers results in thicker, less permeable, and mechanically more stable membranes and vesicles [63].

Recently, functional membrane proteins have been incorporated into polymer membranes, opening a wealth of new approaches to confer bioactivity to these containers. Polypeptide-based block or graft copolymers that can self-assemble to form various structures such as micelles or vesicles have been extensively studied due to their advantages, including biocompatibility, stimuli-responsiveness, and possessing the essential structures and functions of proteins [64; 65; 66; 67]. Polypeptides that adopted an ordered conformation such as α-helices or β-sheets would influence the amphiphilic nature and morphology of the assemblies [68; 69]. For polymer vesicles, the molecular assembly and amphiphilic nature of the polymer chains in the membranes would dictate their membrane permeability, which is essential for applications such as drug delivery and protein encapsulation [70; 71]. For instance, Chen and co-workers and Song and co-workers presented recently suitable system consisting of self-assembled vesicles made of am-

phiphilic copolymers [72; 73]. In particular, Chen reported the synthesis of alkyl chain-grafted poly(L- lysine) (PLL) that can self-assemble to form vesicles with different chain conformations and sizes, which were controlled by the degree of substitution and alkyl chain length. The interplay between the hydrophobic interaction and the conformational changes upon alkyl chain substitution determines their molecular assembly and amphiphilicity and, subsequently, their membrane permeability. In addition, they can be conjugated with functional ligands and stabilized by genipin- cross-linking, making them potentially useful for applications in drug delivery and biomimetic encapsulants. Using doxorubicin (DOX) as model drug for encapsulation, Chen showed that the drug release rate was accelerated due to the increase in membrane permeability as the pH decreases. In addition, the water solubility of DOX molecules increased at acidic condition. Despite the interest of this approach, at the moment self-assembled nanoparticles are prone to disintegration and structural change upon application in a different environment. Moreover, the synthesis via self-assembly is generally lacking in control over the size, porosity, and thickness of the shell. Hence, different synthesis route are often used to produce systems for drug-delivery application such as inverse miniemulsion periphery RAFT polymerization [74]. However, great potential lies in self-assembly based on hydrophobic effect.

1.2.3 π-π Interaction

The name π-π interaction indicates the interaction occurring between an electron-rich π system of a molecule and either a metal (cationic or neutral) either an anion or, most of the times, another π system [75]. This interaction has key importance in biological process such as protein-ligand recognition [76].

Due to its importance in biological systems, the π-π interaction has been widely used for self-assembly. For instance, dyestuff aggregation based on π-π interaction in aqueous solution shows striking analogies to protein aggregation and may serve as a simple synthetic model system for the reversible polymerization

in physiological systems like the growth of actin strands in the cytoskeleton [8] or like protein fiber formation in protein folding diseases, such as Alzheimer's disease [77]. In the case of two different cationic dye mixture, the self-assembly leads to the formation of micelle-like mixed entities that can be converted into well-defined worm-like nanoparticles upon addition of Mg^{2+} ions [78].
In addition, π-π stacking between π donors and π accepting ring systems can govern the self-assembly of a variety of complexes and interlocked molecular compounds such as catenanes and rotaxanes in both the solid and solution states [79].
Despite the wide use as self-assembly strategy, π-π interaction is still not fully understood on the theoretical level. The molecular parameters defining the interaction strength are still discussed, in particular when substituents are present at the aromatic rings. In the early 1990s, qualitative "ground rules" for understanding and anticipating aromatic-aromatic interactions have been established by Hunter and Sanders [80; 81; 82; 83]. Polarized aromatic π-systems and general electrostatic arguments, such as the interaction of two quadrupole moments, have been used. Indeed, the π electron density on most aromatic rings creates a quadrupole moment with partial negative charge above both aromatic faces and a partial positive charge around the periphery. Two such quadrupole moments in proximity should not stack in face-centred parallel geometry in favor of perpendicular edge-to-face interactions or off-centred parallel stacking. The Hunter and Sanders model predicts that the situation is entirely different when one member of an aromatic pair possesses a strongly electron-withdrawing group that polarize the π electron density away from the aromatic core relative to an underivatized aromatic molecules. A reversal in the direction of the overall quadrupole moment results in a central area of relative electron deficiency, thereby setting the stage for electrostatic attraction with a more electron-rich aromatic, leading to a preference for face-centred pairing [84]. Despite good success in describing the general π-π interaction, the Hunter and Sanders model fails to describe the situa-

tion when more than one substituent is present in the aromatic rings or when both the interacting systems have substituents. Indeed, when applied to more complex systems beyond monosubstituted benzene rings, expectations based on these π-polarization viewpoints cannot be reconciled with accurate computational data [85; 86; 87; 88]. Wheeler has introduced a new model capable of a better description of the π-π interaction in the presence of substituents [89]. In essence, local, direct interactions between the substituent and the closest vertex of the other ring have been considered. Three general rules have been suggested:

- Additivity of substituent effects in stacking interactions, regardless of the ring to which the substituents are attached, as long as local, direct interactions are conserved.

- Transferability of substituent effects between different stacking interactions in which the local, direct interactions are congruent; i.e. substituent effects are unaffected by the presence of heteroatoms in either the substituted or nonsubstituted ring, as long as the local, direct interactions are unaltered.

- In π-π stacking interactions in which both rings bear substituents, the substituent effects depend on the relative position of the substituents.

This model suggests that substituent effects in π-π interactions between complex aromatic systems can be understood in terms of individual, local interactions. Such an approach provides a simple view of tackling substituent effects in large aromatic systems with multiple heteroatoms and many substituents than traditional models based on π-polarization do. For example, studying the strengths of the stacking interaction in the case of *meta*- and *para*-substituted *N*-benzyl- 2-(2-fluorophenyl)pyridinium bromides, the electrostatic interaction of the polarized atoms associated with more polarized substituents was shown to dominate the geometries and energetics of stacked systems [90].
However, considering only the local, direct interaction of the substituent and the

closest vertex of the other ring is not always sufficient to understand and predict the π-π interaction strength. For example, substituents may introduce steric effects resulting in a change of the planarity of the π system and, hence, of the interaction strength and stacking [91]. This issue is of crucial importance for the application of π-π interaction for self-assembly since it does not permit a simple and univocal control on the process just controlling the π-π interacting molecules. Indeed, great potential lies in the understanding of the relation of the π-π interaction and the supramolecular assembly structural properties such as shape or dimensions. For example, π conjugated molecules have advantages due to optical properties and structural controllability, therefore, they are extremely potential for applications in organic light- emitting diodes (OLEDs), fluorescent sensors, or biological imaging [92; 93]. In the case of aggregation-induced emitters such as self-assembled *N,N'*-bis(salicylidene)-*p*- phenylenediamine derivatives, it has been shown that the π-π interaction strength and, more precisely, the different electron-donor substitutions controls the color emitted by the nanoparticles and their nanostructure [91]. Understanding the relations of the molecular structure, the molecular interactions, the nanostructure and the nanoparticle properties is crucial to develop new materials and to predict properties in new and different systems.

1.2.4 Electrostatic Interaction

Another route for nanoparticle self-assembly is based on electrostatic interaction. The process is based on Coulomb interaction between building blocks, and hence, the only requirement is their ionicity. Despite the simplicity of the concept, electrostatic self-assembly is far from being completely understood: control over nanoparticle properties, dimensions and shape is still missing in many cases. This is in difference to the well-understood self-assembly based on hydrophobic effect. However, the only requirement to form electrostatic self-assemblies is the building blocks to be charged and it can be easily performed in polar solvent in

difference to hydrogen bounding based self-assembly. Hence, it is a very versatile concept and many substantially different kind of molecules can be used. For example, polyelectrolytes, charged polypeptides, DNA, charged surfactants, lipids and charged dyes have been successfully combined. In addition, building blocks with distinct geometrical shape, functionality and that can interact with different secondary interactions can be used due to the non-selectivity and long range of the Coulombic force. Faul and Antonietti define it as a "real supramolecular chemistry" [94]. Different secondary interaction can be used:

- geometric constrains induced by the well-defined shape of building blocks such as oligopeptides, inorganic clusters or geometric multivalent counterions;
- $\pi - \pi$ interaction and anisotropic polarizability as in the case of charged dyes;
- hydrophobic effects for charged surfactants and lipids;

Historically, the combination of ionic interaction and amphiphilicity has been widely investigated for the formation of solid materials with different structures. Antonietti, Thünemann and others have studied polyelectrolyte-surfactant assemblies [95; 96; 97], while more recently, Faul et al. have focus on the self-assembly of dye-surfactant systems [94; 98; 99]. Mesoporous silicas with variable pore size and architecture were made by using aqueous solutions of block copolymers with one polyelectrolyte block (ionic block copolymers) as templates in a sol-gel process [100].
A fundamental case is the so-called layer-by-layer deposition of oppositely charged polyelectrolytes where a surface is alternately exposed to the polyelectrolytes. This leads to the formation of stable polyelectrolyte films or capsules [101; 102]. Recently, an high performance polymer solar cell has been reported based on a large-area cathode interlayer with controlled film composition, uniformity, and

thickness under a nanometer scale obtained using an electrostatic layer-by-layer self-assembly process [103]. On the opposite, kinetically controlled structures with only low degree of ordering forms when oppositely charged polyelectrolytes are combined in solution [104; 105].
As in the other self-assembly strategies, in the last years the interest has shifted towards the formation of nanoparticles in solution. When polyelectrolytes are combined with counterions without a particular geometry such as inorganic ions or small monovalent organic ions, *polyelectrolyte effects* arise such as the structuring of polyelectrolytes in salt free solution [106], changes in viscosity [107] or a special diffusion behavior [108; 109]. Structures domains presenting higher particle density are formed, however there are still large distances between the polyelectrolytes and this is different to the close association desired for the formation of supramolecular nanoparticles. The association of macroions and inorganic counterions has been successfully used to build organic-inorganic hybrid nanoparticles in aqueous solution [110; 111]. For example, a polyelectrolyte of a certain geometry can interact with oppositely charged metal ions; the latter accumulates inside and around it. These metal ions can, in a second stage, chemically transformed in an inorganic nanocluster with the polyelectrolyte as template. This principle was first demonstrated by Antonietti, Gröhn and at al. for the formation of gold and iron oxide colloids with "non-classical shape" [110].

1.3 Electrostatic Interaction in Colloidal Systems

When a colloidal particle is immersed in an electrolyte solution, it is usually charged due to adsorption of ions on the particle surface or to the ionization of dissociable groups on the surface. In solution, the counterions tend to approach the particle surface and to neutralize the particle surface charges to some extend. However, the thermal motion of these ions prevents their accumulation and hence a counterions cloud forms around the charged nanoparticles in so-

lution. In the ionic cloud, the concentration of counter ions becomes very high while the one of the coions is very low. Hence, an electrostatic layer is formed around the colloidal particles. The electric potential $\psi(r)$ at position r outside the particle can be calculated starting from the charge density $\rho_{el}(r)$ by the Poisson equation:

$$\Delta\psi(r) = -\frac{\rho_{el}(r)}{\epsilon_r \epsilon_0} \tag{1.1}$$

Where Δ is the Laplacian and ϵ_r the relative permittivity of the electrolyte solution and ϵ_0 the permittivity of vacuum. If the distribution of the electrolyte ions $n_i(r)$ obeys to the Boltzmann's low, the charge density $\rho_{el}(r)$ can be written as [13]

$$\rho_{el}(r) = \sum_{i=1}^{N} z_i e n_i e^{-\frac{z_i e\psi(r)}{kT}} \tag{1.2}$$

Hence, we can write

$$\Delta\psi(r) = -\frac{1}{\epsilon_r \epsilon_0} \sum_{i=1}^{N} z_i e n_i e^{-\frac{z_i e\psi(r)}{kT}} \tag{1.3}$$

For low potential, it becomes

$$\Delta\psi = \kappa^2\psi \tag{1.4}$$

with

$$\kappa = (\frac{1}{\epsilon_r \epsilon_0 kT} \sum_{i=1}^{N} z_i^2 e^2 n_i)^{\frac{1}{2}} \tag{1.5}$$

Equation 1.4 is the linearized Poisson-Boltzmann equation and κ in equation 1.5 is the inverse Debye-Hückel screening length. It corresponds to the extension of the counterions cloud.

The interaction and the stabilization of charged nanoparticles in a aqueous media can be described by the DLVO theory (Derjaguin Landau Verwey Overbeek) [112; 113]. For two identical particles, the interaction is composed of attractive Hamaker interaction and screened electrostatic repulsion described by the Yukawa potential. The Hamaker interaction is a non-directional, short-ranged interaction based on induced dipoles.

The interaction of atoms or small charged molecules in solution were firstly investigated by van-der-Waals who proposed the potential to be proportional to $\sim \frac{1}{r^6}$. However, when larger objects such as colloidal particles are considered the attraction is of longer range. The attractive term for large systems has been calculated by Hamaker [114]. In the case of two spherical particles with radius R_1 and R_2 separate by r, sufficiently close ($\frac{r}{R_1} << 1$), the potential energy becomes

$$U(r) = -\frac{AR_1R_2}{(R_1 + R_2)6r} \tag{1.6}$$

Where A is the Hamaker coefficient which depends on material properties such as the number of molecules per unit volume in the two materials and the London constant for the interaction of the two systems.

When two like-charged particles come close to each other, the electrostatic forces lead to repulsion contrasted by the attractive part of the potential. The screened Coulomb interaction for two spheres of radius R at a distance r can be written as [112]

$$u_{el}(r) = \frac{Q_{eff}^2}{\epsilon_r \epsilon_0} \frac{e^{-\kappa(r-2R)}}{r(1+\kappa R)^2} \tag{1.7}$$

The equilibrium of electrostatic and Hamaker forces leads to the stabilization of charged nanoparticles in solution. In addition, the DLVO theory predicts the existence of a critical salt concentration at which inter-particle repulsion is at its minimum and there is no more energy barrier against aggregation resulting in nanoparticle precipitation [54; 115].

DLVO theory has been successfully used to descrive nanoparticle formation and equilibrium, however it has some limitation. For instance, it fails in highly charged systems [116; 117] or at very low salt concentration [113; 108; 106].

One widely discussed example of DLVO failure is the case of highly charged polyelectrolytes. While DLVO theory predicts a purely repulsive far field contribution, long-range attractive interaction have been experimentally observed resulting in interparticle distances smaller than expected and in void structures[118; 119; 120; 121]. Different complex models have been proposed to model the pair-

wise interaction. The first was proposed by Sogami and Ise who broke the assumption of repulsion-only interaction [122]. On this line, different models have been proposed successively based for example on non equilibrium hydrodynamic effects. Manning developed a theory based on counterions condensation around rodlike polyelectrolytes valid only in presence of multivalent counterions and if the number of counterions condensed on the polyions exceeds. Lastly, many-body interactions of highly charged colloids and counterions was considered by Tokuyama [123; 124]. Nowadays, despite large efforts, the results from different groups still do not fit into a consistent picture.

Moreover, DLVO theory cannot describe the already cited *polyelectrolyte effects*, and in particular, the dynamics of flexible polyelectrolytes when salt is added [108; 109]. DLVO theory predicts than the presence of salt screens the electrostatic interaction and that, at high salt concentration, the polyelectrolytes behave as a flexible neutral macromolecules such as a neutral polymer. However, Schurr et al. observed an unexpected change of the diffusion coefficient of poly(L-lysine) hydrobromide as a function of salt concentration [125]. This phenomena is the so called ordinary-extraordinary phase separation and it corresponds to a decrease of the diffusion coefficient by over an order of magnitude over a narrow ionic strength range indicating to the existence of some sort of clustering . The same transition has been observed in different polyelectrolyte systems such as DNA or bovine serum albumin [126; 127; 128].

The existence of an additional long-range attraction mediated by the counterions, its source and theoretical description have been debated for years and are still debated nowadays.

1.4 Thermodynamics of Self-Assembly

Self-assembled nanoparticles require an increase in order of the system, hence the process as such is entropically unfavorable. For this reason, when there are

no strong attractive interactions or driving forces, molecules that interact favorable with solvent behave as one single phase of free molecules dispersed in a solvent. When a driving force that is strong enough to overcome the unfavorable entropy change is present, spontaneous self-assembly can take place. Due to the importance for biological systems the thermodynamics of the self-assembly of amphiphilic molecules has been widely investigated [129; 58; 130], while the thermodynamics of different systems for which other interactions play a role remains largely unsolved. In the last years, the strong development of Isothermal Titration Calorimetry (ITC) permitted to obtain the equilibrium constant and the enthalpy change of the reaction. Different groups have addressed different intriguing relationships between the thermodynamic parameters as the change in entropy or enthalpy, and the self-assembled nanoparticle properties. In the following, first, a short introduction on the thermodynamics of the amphiphilic molecules self-assembly will be given, after which few examples of thermodynamics in different self-assembly cases will be considered.

1.4.1 Thermodynamics in Amphiphilic Self-Assembly

Amphiphilic molecules in solution may spontaneously form a single dispersed phase of thermodynamically stable self-associated interfaces, in addition to the options available for ordinary (non-amphiphilic) molecules, i.e. either to completely mix as free solute molecules with the solvent or to separate into two or more liquid phases. There is a favorable free energy associated with the coming together of the hydrocarbon tails. The aggregation of hydrocarbons is accompanied by a large anomalous positive entropy change peculiar in water. An incorrect view linked this entropy change on aggregation to the release of structured water from around the isolated chains which is supposed to provide a unique driving force for self-assembly in aqueous solution. However, the analysis of the thermodynamics of aqueous micelle formation across an extensive temperature

range shows that the free energy of hydrocarbon transfer is almost independent of temperature, and, if the structural properties of water are evident at low temperature, the water structural properties vanishes completely at high temperature [131; 56; 132]. Hence, since free energy change is the unique criterion for spontaneous process at constant temperature and pressure, the hydrophobic effect must be insensitive to changes in water structure. To better understand the phenomenon, the enthalpy and entropy changes on micellization must be considered. At low temperature the entropy change upon aggregation is large and positive, while at high temperature is large and negative. The negative value reflects the ordering and orientation imposed on the hydrocarbon chains. Hence, at high temperature aggregation is driven by the energetics of transfer of nonpolar groups out of a polar solvent. While at low temperature the entropy change is made up of two parts: a contribution due to the same ordering of hydrocarbon chains in the micelle such as at high temperature and a large structural contribution due to water reordering. The same is for the enthalpy change. Since the free energy remains constant, the water structuring effects almost cancel out and play a small part in the aggregation free energy. This phenomenon is called entropy-enthalpy compensation and it is widely discussed.

The nature of the aggregates formed on association is a more delicate problem and depends on the surface free energy [58; 133]. For surfactant alone, different aggregates are formed as already discussed. For dilute solution, the structure formed by hydrophobic self-assembly depends on the ratio between the volume of the hydrocarbon chain, the optimal length close to the fully extended chain length and the head group area [133; 134]. When the ratio is lower than $\frac{1}{3}$ spherical aggregates are formed, while if it is higher than $\frac{1}{3}$, but lower than $\frac{1}{2}$ vesicles, polydisperse cylindrical micelles are formed. At even higher values, vesicles, oblate micelles or bilayers occur.

In the case of micellar aggregation, different models have been build to describe quantitatively the phenomenon [135; 136]. Considering that the surfactant molecules

exchange continuously between the self-assemblies and as free molecules in the surrounding solution, the entropic dissociation driving force is too large at low surfactant concentrations for self-assembled interfaces with comparatively large free amphiphilic molecules in solution. As a result, self-assembled interfaces will only form above a certain concentration of surfactant, and above this concentration limit both free surfactants and self-assembled interfaces must coexist simultaneously in a dispersed surfactant solution. This threshold value is the so called critical micelle concentration (*CMC*) and is of fundamental importance to calculate the free energy of micellization

$$\Delta\mu_{mic} = RT \ln CMC \tag{1.8}$$

This equation is often called "pseudo phase separation-model". The free energy of micellization is an important parameter in micelle formation thermodynamics since the total equilibrium can be written as

$$\Delta\mu_{mic} = \Delta G_H P + \Delta G_{surface} \tag{1.9}$$

Where $\Delta G_H P$ is the transfer free energy for the hydrocarbon tail from water to the internal of the micelle and $\Delta G_{surface}$ the surface free energy. The *CMC* strongly depends on the molecular architecture of the amphiphilic molecules and in particular on the dimensions of the hydrophobic tail. In addition, it is sensitive to the concentration of the added salt in solution. For example, at at moderate and high salt concentration, the *CMC* approximately follows a linear relation [137; 54; 138]

$$\ln CMC = constant - B \ln c_{salt} \tag{1.10}$$

Direct determination of the enthalpy of micellization is not trivial. A common procedure consist of exploiting the temperature dependence of the *CMC* using the relation called van't Hoff equation

$$\left(\frac{\partial \ln CMC}{\partial T}\right)_P = \frac{\Delta H_m^0}{RT^2} \tag{1.11}$$

Or the modified one that consider also the changes in the aggregation number induced by the different temperatures [139]

$$RT^2(\frac{\partial \ln CMC}{\partial T})_P = -\Delta H_m^0(N) + T[\frac{\partial(G_{N+1} - G_N)}{\partial N}]_{T,P}(\frac{\partial N}{\partial T})_P \quad (1.12)$$

Where $G_{N=1}$ and G_N are the free energies of the surfactant molecules into the micelles with aggregation number of $N + 1$ and N. Hence, using techniques as differential scanning calorimetry (DSC) it is possible to evaluate the enthalpy of micellization [140].

1.4.2 Thermodynamics in Other Types of Self-Assembly

While the thermodynamics of amphiphilic system has been widely investigated experimentally and theoretically, there is a lack of insight for other self-assembly strategies. In particular, different research groups have different approach and a unique and elegant theory is missing. Some of the most interesting studies are reported here.

In the 1995, Chi et al. have applied arguments similar to the ones used in the case of amphiphilic systems to describe the thermodynamics of the self-assembly of cyclic structures based on zinc porphyrin-pyridine coordination interactions [141]. These systems self-assemble when the concentration of the monomers is high enough. This concentration strongly depends on the monomer used. Firstly, the authors focus on the effective molarity, a parameter that measures the concentration at which open polymeric structures start to compete with closed cyclic structures. Hence, it is the upper limit at which the self-assembled structures are stable. In absence of entropic solvent effects, the upper limit of effective molarity can be written

$$EM_{max} = e^{-\frac{\Delta S_{ref}}{R}} \quad (1.13)$$

Where ΔS_{ref} corresponds to the reference porphyrin-reference ligand entropy exchange. Secondly, the author used a two state equilibrium to calculate the critical

self-assembly concentration ($csac$) using the size of the oligomer (n) as a parameter

$$csac = \frac{1}{n^{\frac{1}{n-1}} EM^{\frac{1}{n-1}} K_{ref}^{\frac{1}{n-1}}} \tag{1.14}$$

Hence, large multicomponent systems will self-assemble to give stable structures at concentration between $\frac{1}{K_{ref}}$ and EM. There is no limit on the size of the aggregates. Using the maximum value for the effective molarity, the critical concentration can be rewritten

$$csac_{min} = \frac{1}{n^{\frac{1}{n-1}}} e^{\Delta H_{ref}/((n-1)RTK_{ref})} \tag{1.15}$$

$$csac_{min} = \frac{1}{n^{1/(n-1)}} e^{(n\Delta H_{ref})/((n-1)RT) - \Delta S_{ref}/R} \tag{1.16}$$

From this equation the efficiency of the self-assembly process (ϵ) can be calculated

$$\epsilon = \frac{n}{n-1} \log(EMK_{ref}) + \frac{\log(n)}{n-1} \tag{1.17}$$

The maximum efficiency is reached for

$$\epsilon = \frac{n}{n-1} \frac{\Delta H}{2.303RT} + \frac{\log(n)}{n-1} \tag{1.18}$$

Thus, while the entropy of the component interaction is important in determining the upper limit of the assembly stability, the enthalpy is important in determining the maximum concentration range over which assembly can take place. Knowing the interaction of the components of the system is therefore possible to estimate the efficiency of the self-assembly process.

The thermodynamics of the interaction of the molecular building blocks has been studied with different approaches. For example, Würthner has investigated the self-stacking of perylene bisimide derivative dyes focussing on the effect induced by different substituents on the assembly formation and on the thermodynamics of the interaction [142]. These molecules are interesting because they present exceptionally high photostability and their emission color can be tuned ranging from green to red selecting proper substituents. Studying the twist angle of the

perylene core for different substituents, the author has found a linear relationship between the logarithm of the aggregation constant K (proportional to the Gibbs interaction energy) and the twist angle. The highest driving force for π-π stacking has been found for the flat molecules, while more twisted systems have less strong π-π interaction. Despite the elegant results, an analysis on how these properties act on the self-assembled structure is still missing, even though it would give the possibility to design new fluorophore structures.

Our group has studied a system where more than one kind of interaction acts together forming well-defined nanostructures investigating the association of positively charged dendrimer and oppositely charged multivalent dyes. Using ITC, it has been shown that the dendrimer-dye association enthalpy is always negative and that π-π interaction of the dye molecules is the main enthalpic driving force for divalent dyes [143]. For the first time, a clear correlation between the assembly size (through the aggregation number) and the dye-dye π-π interaction free energy has been found [144]. Thus, knowing the thermodynamics of the interaction is possible to control the size of the aggregates and selecting appropriate building blocks to form nanoparticles of desired dimensions. This aspect is of extremely high relevance for the engineering of self-assembly and, especially for electrostatic self-assembly, it is still far to be completely understood and established.

On the side of experimental results and relationship, theoretical studies have been performed. Recently, the prediction of the crystal structures formed by the self-assembly of nanoparticles has been discussed. In particular, statistical thermodynamics has been used to describe two different cases: the self-assembly of spherical colloids into crystals and the self-assembly of anisotropic building blocks into complex structures. Statistical thermodynamics has successfully predicted the formation of colloidal crystal arrays for spheres interacting with central forces with spherical symmetry [145]. On the other hand, the self-assembly of anisotropic building block is of special importance since it has been proven to

results in crystalline arrays with complex unit cells that can be used to generate photonic band gap materials, negative index materials and metamaterials, however is far less understood [146; 147]. The aim of this research is to characterize the pair potential interaction in anisotropic systems, establish the phase diagram using statistical thermodynamics and develop field-assisted methods applicable to anisotropic colloids. On interesting example is reported by Pfleiderer et al. who were able to first predict a novel crystalline phase for hard ellipsoids with a unit cell of two rods with different orientations being more stable than the stretched fcc phase and to second calculate the phase diagram for the system (Figure 1.2) [148; 149]. Non crystalline clusters have been widely investigated by molecular dynamics in the case of patchy nanoparticles. These are systems with short-range interactions compared to their size. The final objective of these studies is to rationally control the dispersion and the properties of the nanocomposite materials.

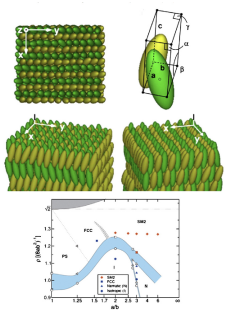

Figure 1.2: *Novel crystalline phases of hard ellipsoids. Monte Carlo simulations and thermodynamic integration have established volume fraction and aspect ratio conditions under which a monoclinic crystal, called SM2, with a unit cell of two rods each with different orientations is more stable than the stretched fcc phase. The top panels [148] show renderings of the structure and its unit cell. The bottom panel [149] shows the phase diagram of hard ellipsoids.*

In 2003, Glotzer et al. showed that, in a system of polyhedral nanoparticles in a dense bead-pring polymer melt under quiescent and steady shear, the clustering process is consisting with the model of equilibrium particle association

and that the viscosity of the dispersed configuration is larger compared to the one in cluster state in contrast to expectations based on macroscopic colloidal dispersions [150]. The authors suggest that an alteration of the polymer matrix properties in the vicinity of the nanoparticles must be considered. Sciortino et al. have calculated the equilibrium thermodynamic properties, percolation threshold, and cluster distribution functions for a model of associating colloids, which consists of hard spherical particles having on their surfaces three short-ranged attractive sites and sticky spots of two different types, *A* and *B* [151]. It is clear that such an approach is fundamental to generalize the experimental results and to deeply understand the relation of nanoaggregate structure and its properties. However, there are still limitations due to the calculation power needed to model more complex system. In addition, theories capable of describing complicate self-assembly processes are still missing. For example, only recently a systematic Flory-Huggins type theory has been introduced to describe the basic thermodynamic properties of the self-assembly by mutual interaction [152].

1.5 Concept and Objectives

In this framework, it is evident how investigating the self-assembly from a fundamental point of view is crucial to develop new and more efficient strategies to form nanoparticles, but also to understand how the existing strategies can be improved to gain full control on the resulting nanoparticles, for example on their dimensions or morphology. In particular, this is important for the relatively new concept of electrostatic self-assembly where more than one interaction occurs at the same time making the control over nanoparticle properties more challenging. Our research focused on the combination of electrostatic interaction and directional short-ranged π-π interaction. As model system for this study, the supramolecular self-assembly of positively charged polyelectrolytes such as polyamidoamine (PAMAM) dendrimers or poly(diallyldimethylammonium chlo-

ride) (PDADMAC) and oppositely charged azo dyes has been investigated (Figure 1.3). This leads to the formation of well-defined nanostructures in solution via the combination of isotropic electrostatic interaction (attractive between the polyelectrolyte and the dye and repulsive between the like charged molecules) and π-π interaction between the dyes.
The goal of this project is to elucidate the nanoparticle formation process to achieve control over their structural properties. In particular, we wanted to understand the role of the building blocks properties, such as geometry, dimensions, charge or flexibility on the final nanoaggregates. This is of crucial importance since it often is a secondary topic, while it has an important role on self-assembly. For what concerns the energetic arena of self-assembly, the objective was the extension of previous results on the thermodynamics of the process to develop a comprensive theory capable of predicting the nanoaggregate properties (mostly structural) on the basis of the interaction strength of the building blocks trying to understand how the two different interactions cooperate in the nanoparticle formation and stabilization. More in general, it is highly desirable to gain new knowledge of electrostatic self-assembly that might be extended to different self-assembly concepts.

1.6 State of Knowledge

Here, a general overview on the previous studies of self-assembly where organic dyes and polyelectrolytes are used singularly and combined together is given.
Few important polyelectrolyte self-assembly examples have been reported earlier, what it appears clearly from the large picture is that it is an extremely interesting and promising field. However, it is not easy to form stable and well-defined nanoparticles especially in solution. For instance when polyelectrolytes are combined with monovalent counterions, no nanoparticles are formed. Only the so-called *counterions condensation* occurs, due to the release of a fraction of the

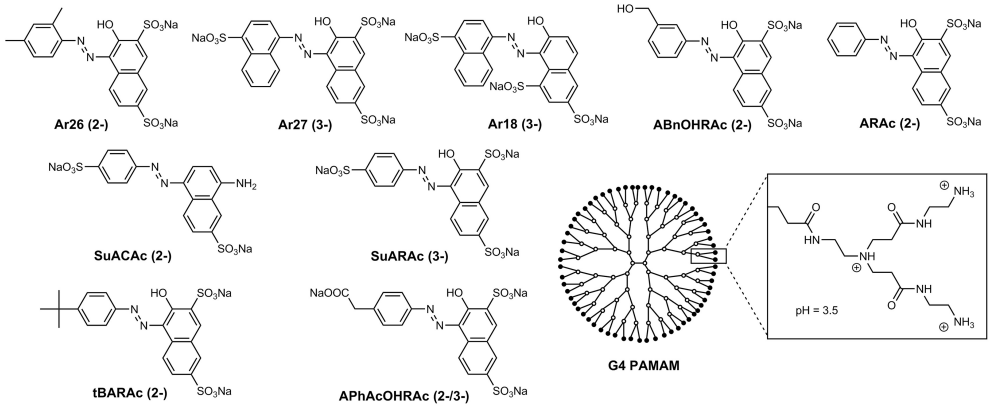

Figure 1.3: *Some of the building blocks used in the electrostatic self-assembly investigated in this study.*

counterions of the polyelectrolytes, while a part of the counterions is permanently located within the polyelectrolyte molecules [153; 154; 155]. Aggregation occurs when multivalent counterions are used as in the case of charged polyacrylamide in combination with calcium ions [156; 157; 158]. However, the size distribution of the resulting aggregates is very broad. Stable aggregates can be formed by layer-by-layer self-assembly deposing two oppositely charged polyelectrolytes on a solid surface alternatively. This results in materials with well-defined morphologies and ordered structures [159; 160]. Highly structured solid materials have been formed combining polyelectrolytes and surfactant [95; 96; 161; 162; 163]. The same combination leads to the formation of supramolecular complexes with high structural variety in solution mostly in organic solvents [164; 165; 166]. Another issue with this process is that it may be the case that the structures are formed under non-equilibrium conditions and therefore the nanoparticles depend on the preparation path. For the interesting system of oppositely charged polyelectrolytes/ surfactants, the driving force for the assembly is the entropic gain due to release of the small counterions and water molecules. Based on these considerations, our group introduced a new concept based on the combination

of polyelectrolytes with multivalent organic counterions of a certain geometry such as azo dyes. As compared to polyelectrolyte-polyelectrolyte complexes the lower charge of the counterion gives the possibility to form thermodynamically driven rather than kinetically trapped structures, as compared to flexible polyelectrolytes with simple multivalent counterions. The use of *structural units* as building blocks can lead to more defined structures, and in addition, potentially introduce functionalities. For the latter reason charged dye molecules have been used: on the one hand, they have a defined shape and the possibility for mutual overlap interactions, while on the other hand, they carry optical functionality.
The optical properties of the dyes and their electrical properties arising from the π electron system have attracted large interest for self-assembly [167; 168; 169; 170]. The self-interaction of this kind of molecules may lead to the formation of assembly that can, for example, enhance the properties of the single molecule. This is the case for perylene bisimide dyes where the aggregate presents enhanced emission properties [171]. Moreover, azo dyes are soluble in water and commercially available in a great variety of structures. The latter has key importance since it is easily possible by selecting the appropriate dye to modify a key parameter in self-assembly as the dye geometry. The valency of the dye is one of the parameters that can be controlled, and this has clearly special importance in the case of electrostatic self-assembly. The dye itself can self-aggregate in solution: from dimers at low concentration to assemblies with size about 100 nm [172; 173; 174]. However, it has been shown that only a small fraction of the total amount of dyes partecipates in the assembly formation. In addition, the formed assemblies are not stable in aqueous solution [175]. This shows that π-π interaction is capable of forming small aggregates, but fails to form large, stable nanosystems. A strategy that leads to the formation of stable aggregates is the combination of π-π interacting dyes with building blocks capable of different interactions. For instance, the group of K. Huber reports on the aggregation of anionic azo dyes into dyestuffs when Mg^{2+} ions are present in solution [78]. This process is of

interest since dyestuff aggregation in aqueous solution shows striking analogies to protein aggregation and may serve as a simple synthetic model system for the reversible polymerization in physiological systems and dyestuff aggregation is a process highly responsive toward changes of ambient conditions like salt concentration or temperature. Highly organized supramolecular architectures, which are crystalline/liquid crystalline in nature can be formed combining azo dyes and cationic surfactants [176; 94]. It is clear that the combination of azo dyes and building blocks capable of different interactions result in well-defined structures, however only few studies exist on the formation of nanoparticles. Along this direction, our group has combined azo dyes with polyelectrolytes taking the best from the two worlds resulting in promising well-defined and stable nanoparticles.

Firstly, the association of the anionic azo dye Acid Red 26 (Ar26) with cationic polyamidoamine (PAMAM) dendrimer has been investigated [177]. Stable and well-defined anisotropic supramolecular nanoparticles have been obtained. The size is about one order of magnitude larger than the original building blocks and it shows a narrow monomodal distribution. The use of PAMAM as building block provides the possibility of turning on and off the aggregation by simply changing the pH of the solution. PAMAM is a weak polyelectrolyte and its protonation state can be controlled changing the pH of the solution: at $pH > 10$, the molecule is neutral and no electrostatic interaction occurs, for $7 < pH < 10$ the primary amines are protonated, at $pH < 7$ primary and tertiary amines are protonated and finally at $pH < 4$ the molecule is completely charged. Hence, not only the interaction can be turned on and off, but its strength can be modulated as well tuning the pH. An important property of this system is that the assembly/disassembly process is reversible as long as the salt concentration is not too high since it can reduce the electrostatic stabilization of the nanoassemblies. Lastly, the role of the ratio between the building blocks l has been proven to be crucial for the assembly formation: an high excess of dendrimer leads to the formation of only host-guest

complexes. The concept has been then extended to other azo dyes such as Acid Red 18 (Ar18), Acid Red 27 (Ar27) and Acid Red 44 (Ar44), changing the dye molecular structure and the valency in order to observe their effects on the self-assembly [143]. Different shapes have been observed ranging from cylinders and spheres to core-shell particles. The self-assembly is shown in Figure 1.4.

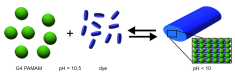

Figure 1.4: *Sketch of the self-assembly of PAMAM dendrimer and oppositely charged dyes: at pH 10.5 the dendrimers are uncharged and no interaction between the building blocks occurs, at pH ¡ 10 the dendrimers start to be protonated and the building blocks form well-defined nanoparticles. From [178].*

Beside a first structural characterization, the thermodynamics of the assembly formation has been investigated. For instance, the process has been shown to be cooperative. Driving force for the dye-dendrimer association is the enthalpy, which is always negative. In addition, the strength of the interaction of the building blocks strongly affects the size of the nanoparticle [179].
The concept has been extended to a wide range of building blocks: firstly, different dendrimer generations have been used resulting in a change of dimensions, charges and flexibility, secondly, linear polyelectrolytes such has polylysine (PolyLys) and polyallylaminehydrochloride (PAH) have been used [180]. For generation 0, no well-defined and stable aggregates have been found. A minimum size of the template is required in order to formate stable supramolecular nanoparticles. For the other dendritic molecules, the assembly size is very similar. The linear polyelectrolytes also result in stable nanoparticles, however the precipitation limit is already at slight excess of polyelectrolyte as compared to the dendritic molecules for whom it is at charge stoichiometry. The binding strength is similar for all the PAMAM generations, while assemblies from PolyLys and

PAH are more kinetically trapped.
Great interest lyes in system that can respond to external triggers since they can be used as nanosensors, for storing energy or as tunable nanocarries. As already discussed, the usage of PAMAM dendrimers results in pH controlled nanoparticles. On a second stage, light sensitive nanosystems have been formed using a dye that can trans-cis isomerize upon light irradiation as Acid Yellow 38 (Ay38) [177]. Upon irradiation, the size of the of the aggregates shift from hydrodynamic radius $R_H = 30nm$ to $R_H = 160nm$. The process is not reversible, but combining it with the pH responsiveness permits to go back to the initial state. More recently, the same light sensitive dye has been combined with linear polyelectrolytes resulting in nanoparticles with tunable size and density [181]. However, a full structural characterization of this system is still missing.
After investigating the role of the polyelectrolyte in the self-assembly, the focus has been putted on the role of the dye. Eight divalent azo dyes with similar backbones have been investigated [144]. A clear correlation between the assembly size thought the aggregation number and the dye-dye interaction free energy exchange has been established. The aggregation number has been further modelled according to equilibrium thermodynamics taking into account two different contributions: the electrostatic repulsion between like-charged dendrimers and the free energy of dendrimer-dye association. The results are given in Figure 1.5.

The concept of combining building blocks capable of different interaction with azo dyes has been further carried on. Ternary structures that consist of either gold or cadmium sulfide nano-clusters, cationic dendrimers and anionic dye molecules have been formed in a two-step procedure of electrostatic nanotemplating and electrostatic self-assembly [182]. For this system, the interplay of ionic, π-π and Hamaker interactions leads to well-defined hundred-nanometer-scale assemblies with narrow size distribution in aqueous solution (Figure 1.6). More recently, we have reported on nanoassemblies formed by cationic alkyltrimethylammonium bromide surfactants and the divalent anionic Ar26 in aqueous solution via

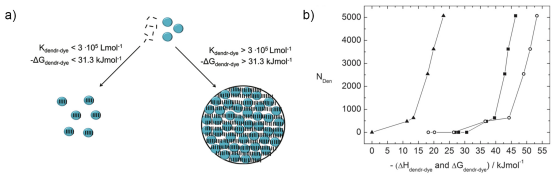

Figure 1.5: *a) Free energy threshold for host-guest complexation as compared to dendrimer interctonnection, and b) dendrimer aggregation number* N_{Den} *in dependence on dye-dendrimer interaction free energy* $\Delta G_{dye-den}$ *(squares) and enthalpy* $\Delta H_{dye-den}$ *(open circles) and dye-dye interaction free energy* $\Delta G_{dye-dye}$ *(triangles) for divalent dyes [144].*

the combination of electrostatic interactions of the oppositely charged building blocks, hydrophobic effect and π-π interaction [183].

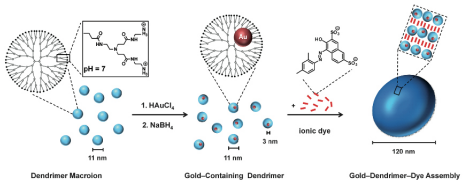

Figure 1.6: *Self-assembly of ternary structures of gold, cationic dendrimers and anionic dyes, the two set process is shown. From [182].*

Chapter 2 Nanoparticle Characterization

The nanoparticle structure has been investigated through dynamic and static light scattering and small angle neutron scattering SANS. Light scattering permits to gain first informations on the dimensions and size distribution of the nanoparticles in solution without affecting the equilibrium of the system. Static light scattering gives the radius of gyration of the nanoparticles R_g and the scattering intensity $I(q)$. The radius of gyration is the effective size of the scattering "particle" whether it is a polymer chain, part of a protein, a micelle, or a domain in a multiphase system. Dynamic light scattering gives the hydrodynamic radius R_H, which is the radius of a hard sphere that diffuses at the same rate as that solute. Gyration and hydrodynamic radius can be combined to get information on the nanoparticle shape. The ratio $\frac{R_g}{R_H}$ is equal to 0.78 for a spherical nanoassembly, while is higher than one for elongated one. Light scattering is particularly suitable for measuring nanoparticle size in solution since it is a non-invasive method and the result is averaged over the entire sample.
Another non invasive technique is SANS. This low resolution technique has been used to access the shape of the assemblies and their dimensions. The measured intensity in SANS experiment is

$$I(Q) = \frac{N_P}{V} {V_P}^2 \Delta\rho^2 P(Q) \tag{2.1}$$

Where N_P is the nanoparticle number, V_P the volume of the nanoparticles, $\Delta\rho$ the difference in scattering length between the nanoparticles and the solvent, $P(Q)$ is the form factor. Hence, the measured quantity is directly dependent on the form

or in other words the shape of the scattering objects. Moreover, this quantity can be modelled according to theoretical models and fitted to get not only the shape but also the dimensions of the nanoparticles. In difference with the light scattering, the resulting parameters are not obtained thought an approximation, but the real ones. For example, for a sphere of radius r the form factor is [184; 185]

$$P(Q) = \sqrt{3\frac{\sin(qr) - qr\cos(qr)}{(qr)^3}} \tag{2.2}$$

In addition, the nanoparticle structure has been investigated via atomic force microscopy. This technique is extremely useful because it permits to directly observe the nanoparticles and it has a very high resolution in comparison to light scattering and SANS. However, it requires the drying of the sample, and therefore, the observed structure may not correspond to the one in solution.

The stacking of the dye molecules induced by the π-π interaction has been investigated by UV-Vis spectroscopy. The absorption spectra changes when the geometry of the aggregates changes [186]. Classical exciton theory has been used to understand the spectra [187; 188; 189; 190]. The theory considers the interaction of the dye transition dipoles that come into spatial proximity when dimers or higher order aggregates are formed. In particular, when an aggregate is formed the splitting of the excited state takes place [174]. This happens when the dipole moments of the dye molecules are not exactly parallel to each other and they are tilted of a certain angle $\beta < 90°$. Exciton theory can be used to fit the spectra according to

$$\epsilon_D = \epsilon_J e^{-4\ln 2\frac{(\nu-\nu_J)^2}{\Delta\nu^2_{1/2,J}}} + \sum_{i=0}^{1} \epsilon_i e^{-4\ln 2\frac{(\nu-\nu_i)^2}{\Delta\nu^2_{1/2,i}}} \tag{2.3}$$

Where ϵ_D is the extinction coefficient of the dimer. This separation can be done because the spectral separation between the H- and J- band is greater than the vibronic progression. Therefore, the first term of the equation refers to the J-band with ϵ_J as extinction coefficient, ν_J as wavenumber and $\Delta\nu_{1/2,J}$ as half-width of the Gaussian. The second term represents the H-band extended to two vibronic

transitions. The results can be used to calculate the twist angle between the dye molecules β and the inter-dye distance R [172]

$$\beta = 2 \arctan \sqrt{\frac{f_J}{f_H}} \tag{2.4}$$

$$R = \left(\frac{2.14 \cdot 10^7 \cos \beta}{\nu_M \Delta \nu_{H,J}}\right)^{\frac{1}{3}} \tag{2.5}$$

Where f_i is the oscillator strength for the i-th band calculated by integration of the respective peak area.

Stabilization of the nanoparticles is of great interest and it can arise from either electrostatic repulsion either from steric shielding. In electrostatic self-assembly the former is the more common stabilization process. Around charged particles in solution an electrical double layer is formed: an excess of ions with charge opposite to the nanoparticle one is formed directly around the particles [191]. This layer is known as the Stern layer and moves with the particles. Hence, from the electrophoretic mobility of the particle the potential at this share plane can be calculated. This is the ζ-potential. For particles in solution with sufficiently high salt concentration and for sufficiently large nanoparticles (i.e. nanoparticle dimensions larger than the electrostatic double layer) the ζ-potential can be calculated via the Smoluchowski equation, a special case of the general Henry equation

$$\mu_{el} = \frac{\nu_{el}}{E} = \frac{2\zeta \epsilon_r \epsilon_0}{3\nu} f(\kappa a) \tag{2.6}$$

With $f(\kappa a) = 1.5$. κ is the inverse of the Debye screening length and a the nanoparticle radius. Measuring ζ permits to understand the electrostatic behaviour of the nanoassembly and, for electrostatically stabilized systems, it permits to estimate nanoparticle stability: more stable particles will present higher ζ-potential values.

Lastly, the thermodynamics of the interactions has been investigated via ITC. This technique is based on the online detection of the reaction heat when one reactant is titrated into the other reactant. It permits to directly measure the enthalpy and

the stoichiometry of the reaction. It also permits to access simultaneously all the thermodynamic parameter of the reaction: the integrated heat normalized per mole of injectant can be fitted according to theoretical model that relates the heat release or uptake with the thermodynamic parameters. For example in the case of the binding of a ligand molecule L to independent binding site on a molecule M, the so called one-site model can be described as

$$K_{ML} = \frac{[ML]}{[M][L]} = \frac{x[M]_0}{(1-x)[M]_0[L]} \tag{2.7}$$

Where $[M]_0$ is the total concentration, $[M]$ the current concentration of the macromolecule, $[L]$ the current concentration of the ligand, $[ML]$ the concentration of macromolecules with bound ligand and x is the degree of conversion. The total heat release or uptake after each injection Q_i can be written as

$$Q_i = xN[M]_0 \Delta H_{ML} V_0 \tag{2.8}$$

Solving this two equation permits to determine the equilibrium constant K_{ML}, the reaction enthalpy ΔH_{ML} and the stoichiometry N. This can be done by nonlinear curve fitting if the cell volume V_0 is known. From these parameters, the free energy ΔG_{ML} can be calculated

$$\Delta G_{ML} = -RT \ln K_{ML} \tag{2.9}$$

And then the entropy change ΔS_{ML} can be calculated. Titrating the polyelectrolyte into the dye and diluting a dye, it is possible to measure the different contribution separately and this permits to deeply understand the self-assembly from a thermodynamic point of view.

All these technique alone only access a piece of the puzzle that is the self-assembly, but together they permits to investigate the process on its integrity.

To conclude, goal of the project is to put together the puzzle pieces in order to fundamentally understand the electrostatic self-assembly, unveiling its driving forces and how the different interaction interplay to form the nanoparticles.

In addition, establishing a relationship between the interaction of the building blocks and the supramolecular structure is crucial. This permits the definition of a molecular toolbox to tailor nanoparticles of desired dimensions and shape by simple mixing of the building blocks.

Chapter 3 General Discussion

In the following chapters the combination of electrostatic and structural π-π interaction in self-assembly will be investigated from different perspective with special regards on how they work together defining the structure of the self-assembled nanoparticles. Under focus are the basic principles regulating the self-assembly.

3.1 Results

In chapter 4.1, the full structural characterisation of the self-assembled structures formed by multivalent organic dyes and different generation dendrimers is given. These systems result in different structures ranging from simple spherical aggregates to more complex elongated assemblies as worm-like chains. At the same time, the dimensions of the nanoparticles vary enormously with the building blocks: aggregates from 20 nm to microns are formed. This is more than one order of magnitude larger than the building blocks. Different parameters that controls the self-assembly have been investigated. Firstly, the dye generation has been changed: increasing the generation (i.e. decreasing the dendrimer flexibility) results in more anisotropic particles. Another important parameter regulating is the dye valency: divalent dyes form anisotropic nanoparticles, while trivalent dyes form spherical ones. Hence, we have demonstrated that choosing the appropriate dye it is possible to tune the shape of the self-assembled nanostructures. In addition, the ratio between the building blocks has been varied and

it has been shown that it controls the number of dendrimers per aggregate (aggregation number) and the nanoparticle dimensions. The stoichiometric ratio is 2.0, it has been shown that when it is lower than 1.5, a certain amount of dendrimers remains either free in solution or assembles forming dimers. When the nanoassemblies have an anisotropic shape, the building block ratio also regulates structural properties as the dimensions and the aspect ratio.
To better understand the role of the dye valency, the dye stacking has been investigated on the molecular level studying the stacking angle and relating it to the nanoparticle shape. For the trivalent dyes (forming isotropic nanoparticles) with different number of aromatic rings and different substituents the twist angle is always constant to 38 °. Instead, divalent dyes stack with larger angles different from one dye to another. To gain further insights on this effect the interaction of the building blocks has to be considered. Using isothermal titration calorimetry, it has been shown that the building block interaction is the crucial key defining the nanoparticle structure. For example considering the mutual interaction of the dyes, a threshold value of the enthalpy exchange $\Delta H_{dye-dye}$ separating isotropic and anisotropic nanoaggregates has been found. This indicates that a strong π-π interaction leads to anisotropic structures. For the dye-polyelectrolyte interaction, a threshold value was detected as well. This is a really important point since, so far, the π-π interaction was considered fundamental only to form nanoparticles with narrow size distribution, while we now know that it is also controlling the nanoparticle shape and that (if the dendrimer generation is fixed) it is the only parameter involved in the shape control. We have further examined which molecular parameters encode thermodynamics and thereby particle shape. The nanoparticle properties have been modelled by density function theory (DFT) showing that the electrostatic properties control the thermodynamics of the dye-dye interaction. In particular, the electrostatic potential at the molecular surface and the polar surface area (PSA) determine the strength of the dye-dye interaction, which again controls the nanostructure of the polyelectrolyte-dye particles.

The aspect ratio of the assemblies varies as a function of the polar surface area: more elongated nanoparticles are formed when the PSA is low and hence the π-π interaction is stronger, while spherical particles are formed for higher PSA values (i.e. low π-π interaction strength). From these results, it will be possible to predict nanoparticle shapes knowing only the thermodynamic parameters of the interaction of the chosen molecular building blocks. Thus, a precise molecular design of the dye molecule will allow tailoring the structure of the nanoparticles.
After understanding the importance of the π-π interaction in the self-assembly in chapter 4.1, the role of the electrostatic interaction of dendrimers and multivalent dyes has been investigated in chapter 4.2. Herein, the structure of the supramolecular assemblies formed by Ar26, APhAcOHRAc and generation 4 PAMAM dendrimer has been studied as a function of the solution pH. The PAMAM dendrimer is composed by amine groups and its protonation state can be tuned changing the pH. At pH $>$ 10, the dendrimer is neutral and no interaction occurs with the oppositely charged dyes; at 7 $<$ pH $<$ 10, the primary amines (on the surface of the dendrimer) start to be protonated and nanoparticles are formed; at 4 $<$ pH $<$ 7, the tertiary amines are protonated, and finally at pH $=$ 3.5, all the amines are protonated and the molecules is fully charged. Hence, the pH controls the charge of the dendrimer (and thus the electrostatic interaction strength). As a results, it has been proven that electrostatic interaction has a fundamental role in the stabilization and dimensions of the nanoparticles: more stable and smaller assemblies form at low pH when the electrostatic interaction is stronger (i.e. when the dendrimer is fully charged). For example, in the case of the dendrimer-APhAcOHRAc assemblies, spheres with radii from R $=$ 46 nm (pH $=$ 3.5) to R $=$ 165 nm (pH $=$ 6.7) can be created. The ζ-potential has been measured to have information on the nanoparticle charge: it is higher at low pH and decreases linearly with pH. Hence, the stabilisation mechanism is the same at all the pH and in particular is the same for pH $>$ 7.0 where only the primary amines are protonated and for pH $<$ 7.0 where also the inner tertiary amine groups are

protonated. This is a clear demonstration that the nanoparticles are electrostatically stabilised. While at pH = 3.5 the nanoparticles are stable for months, different pHs have different effects on the nanoparticle stability on long time. It has been shown that a stability range of pH exists for each system. This only depends on the molecular structure of the specific dye. These ageing studies have shown the importance of pH = 7 since tertiary amine groups start to be protonated, and it always represents one of the limits of the stability region.
In addition, pH is also a key to a tunable particle shape. For instance, we have shown that the pH can be used as a trigger to switch between nanoscale cylinders with elliptical cross sections and spherical nanoparticles and for ABnOHRAc between up to 2 μm long flexible cylinders and shorter (100-500 nm) stiff cylinders. In all cases, the pH can switch between a nanoassembly and dissociated building blocks.
Lastly, dynamic light scattering results have been combined with ζ-potential measurements to obtain the surface charge density. This parameter is the key to describe nanoparticle stability and size control: more stable and smaller nanoaggregates present a higher surface charge density, while the less stable ones have a low value.
The role of pH on the self-assembly process has ben further investigated in chapter 4.3. Despite the results reported in 4.2, some questions remain unanswered in particular on the existence of the instability region. To investigate the point from a different point of view, the pH has been changed keeping constant the charge ratio between the dyes and the dendrimers in difference to chapter 4.2 where the loading ratio was kept constant. In this case, stable nanoparticles are formed at all the pH while before we had some instability regions. In contrast, a change in the nanoparticle shape has been observed around pH = 7 where inner tertiary amines start to be protonated: cylindrical particles are formed at pH $<$ 6.5 while spherical particles are formed at pH $\geq$ 6.5. This means that the charge position is crucial to define the nanoparticle shape. The higher stability is explained consid-

ering that the nanoassemblies are stabilized by excess of dendrimer charge and that keeping constant the charge ratio results in a constant excess of dendrimer charge. Hence, here the results are really sensible to the charge position (in- or outside the dendrimer). This might be because the position and the number of the amine groups available for binding affect how the dye and dendrimer and hence the dye-dye can interact. Probably the dyes can stack better when the internal charges are available for binding than when only the external charge are available.

Another important result is that in this case nanoparticles become smaller as the pH increases in contrast to the results obtained at constant loading ratio. Again, This might be due to the different number and position of the charges available for binding. This has been observed investigating the dye-dye interaction: the environmental pH controls the dye-dye stacking modifying the twist angle between the dye molecules. When spherical nanoparticles are formed the angle remains constant, while when elongated ones are formed it increases continuously with pH. With this chapter and chapter 4.2, we have connected the pH effects on different levels, from the molecular to the supramolecular level, showing that the pH can be used as trigger to obtain stable nanoparticles with different shapes.

One of the most important results obtained in the studies presented in chapter 4.1 is that a threshold value exist in the dye-dye interaction separating elongated and isotropic nanoparticles. In chapter 4.4, we tried to understand this phenomenon better. To vary the dye-dye interaction and to try to cross the threshold between elongated and spherical nanoparticles, dyes with different valency have been combined. In principle, this should results in a π-π interaction strength between the stronger one of the divalent dye and the weaker one of the trivalent. Mixture of Ar26 (divalent) and Ar27 (trivalent) combined with generation 4 PAMAM dendrimer and of ABnOHRAc (divalent) and Ar27 (divalent) combined with generation 4 PAMAM dendrimer have been studied. Firstly, the nanoparticle formation has been investigated by SANS and light scattering. Well-defined

and stable nanoparticle are formed when dye mixtures are used. As expected, different dye mixing ratios results in different nanoaggregate structures. For example, Ar27 and generation 4 dendrimer form a spherical nanoparticle, and ABnOHRAc and generation 4 dendrimer result in long flexible cylinders with elliptical cross-section, while the mixture of the two dyes with dendrimers results in a different structure: ellipsoidal nanoparticles. Moreover, the aspect ratio depends on the mixing ratio: the nanoparticle is less elongated when Ar27 is the dominant dye and more elongated when ABnOHRAc is the dominant one. As in the other studies, we have investigated the dye-dye stacking on the molecular level showing that the different dyes can stack together forming heterostacks in addition the well-known homostacks. A simple model has been developed to understand the dye stacking: stacking can occur between homostacks of the different dyes or between single dye molecules and we have been able to identify the different cases from the UV-Vis spectra. This results are promising and may open a road to form nanoparticle with desired structure by appropriate mixing of existing dyes.
The role of electrostatic and π-π interactions is further investigated in chapter 4.5. In this study, we have investigated the nanoparticle properties as a function of the solution ionic strength. Changing this parameter permits to screen the electrostatic charge acting directly on its strength without acting on the dendrimer protonation as in the case of pH effect studies. First of all, the aggregates have been investigated using light scattering and, similarly to the case of varying pH, the nanoparticle size changes with changing ionic strength. In the case presented in chapter 4.5, the nanoparticle size increases as the ionic strength increases. This is a peculiar result since a ionic strength increase should lead to a reduction of the electrostatic interaction between the building blocks, and hence, to a lowering of the nanoaggregate size. To describe the phenomenon, the DLVO theory has been used. In our case, this theory has been able to describe both the nanoparticle stabilisation and the size trend as the ionic strength increases. On the one hand, the ionic strength screens the charges resulting in a decrease of the electrostatic

interaction, but on the other hand, the screened potential causes in the decrease of the nanoparticle repulsion resulting in larger assemblies. Obviously, this leads to the formation of larger nanoassemblies. Hence, the two interconnected phenomena regulate the nanoparticle size and can be used to tune nanoassembly size. In difference from the pH case, the shape of the nanoparticles (obtained by SANS) and the dye stacking (measured via UV-Vis spectroscopy) do not depend on the ionic strength. This is explainable considering the thermodynamics of the self-assembly. In a previous study it has been shown that the free energy gain of the process can be divided into two terms: one electrostatic arising from the dye-dendrimer interaction and one describing the π-π interaction of the dye molecules [144]. Obviously, the second term is independent of the ionic strength and therefore, as already seen in the other contributions, the π-π interaction encodes the nanoparticle shape and how the dye stacks, while the electrostatic interaction affects the nanoparticle dimensions though the control of the stabilisation process. This confirms the results reported in chapter 4.1 where the dye-dye interaction was considered the primary parameter controlling nanoparticle shape.
In chapter 4.6, we have investigated the self-assembly of multivalent organic dyes in combination with linear polyelectrolytes. These are completely different than the previously used dendrimers whose are highly branched spherical molecules. As polyelectrolytes, poly (diallyldimethyl-ammonium chloride) (PDADMAC) and Poly (N-methyl-4-vinylpyridinium nitrate) (QPVP) have been used, while Ar26 and Ar27 have been used as dyes. In addition, a different dye has been used: Acid Yellow 38 (Ay38). This dye trans-cis isomerizes upon irradiation with UV light, and thus, has been used to form light-sensitive nanoparticles. Firstly, it has been demonstrated that stable and well-defined nanoparticles form. This is important since the polyelectrolytes used are simple, common and easily available molecules. As in the other studies, the molecular dye structure is the key parameter regulating nanoaggregate shapes ranging from core-shell ellipsoids over highly anisotropic cylinders to flexible fiber-like nanostructures with nano-

diameter and micrometer length. Hence, the key role of the dye-dye interaction in defining the nanoaggregate shape is confirmed for different kind of polyelectrolytes. UV-Vis spectroscopy has revealed that the polyelectrolytes controls the dye stacking, while the nanoparticle are stabilised by the excess of charges. This again confirms that despite the evident difference in the polyelectrolytes the self-assembly is substantially identical. The results of the systems containing the light-sensitive dye Ay38 are worth noting. When Ay38 is used in combination with PDADMAC, the nanoparticles exhibit a shape change from a μm-long flexible cylinder to compact core-shell ellipsoids upon UV-light-irradiation. Basically, the nanoaggregate bends upon irradiation forming a much more spatially compact object. This is the first time that such phenomenon is observed for this kind of systems and permits to store energy transforming it into structural changes. On the opposite when Ay38 is used in combination with QPVP, no transition in shape is observed upon irradiation with UV-light. It is not easy to understand why the two systems behave differently. Possibly, the different behaviour arise from the different molecular structure of the two polyelectrolytes: QPVP has an aromatic ring in the lateral chain that might add an additional interaction preventing the transition, while PDADMAC has no additional aromatic rings. Despite its origin, the phenomenon is highly promising for applications as in the case of nanosensors.

Overall, This study has brought new insights on the factor controlling the nanoparticle stabilisation, shape and dimensions. In particular, it has proven that the thermodynamics of interaction occurring in the self-assembly has a fundamental role. Moreover, electrostatic interaction is the key factor for the stabilisation of the aggregates and their dimensions, while the π-π interaction controls the isotropicity of the aggregates.

3.2 Conclusions and Outlook

In conclusion, these studies yield new insights into the electrostatic self-assembly of charged polyelectrolytes and oppositely charged multivalent dyes. In particular, under focus are the different interactions and their interplay in the nanoparticle formation and stabilisation. Stable and well-defined nanoparticles with dimensions from 100 nm to the micrometers are formed by electrostatic self-assembly. The investigated self-assembly is based on the electrostatic interaction between the oppositely charged building blocks and the π-π interaction of the dye molecules.

Choosing different building blocks results in the formation of nanoparticles with different shape and dimensions. Different parameters are responsible of this phenomenon. The study of the interactions between the nanometric building blocks permitted to understand that each interaction has his specific role. For example, the electrostatic interaction controls the nanoparticle stability, and hence, their dimensions. Changing its intensity through the screening of the building block charge results in a change in dimensions: lowering the electrostatic interaction results in larger aggregates. This has been described using the DLVO theory and it results from the lowering of the repulsion between the building blocks. On the other hand, the secondary interaction (i.e. π-π interaction) controls the nanoparticle shape. This is striking since the electrostatic interaction (fundamental to form the nanoparticle) has no influence at all on the shape of the formed assembly. The existence of a threshold value in the π-π interaction separating the building blocks forming elongated nanoparticles and the ones forming spherical ones has been proven. In this case, ITC has been of fundamental importance since it allowed to access the thermodynamics of the systems. From these studies it has been confirmed that the entropy exchange generated by the nanoparticle formation can be divided into two terms one describing the electrostatic interaction and one the π-π interaction; and it has been proven that each term has his own role

on the nanoparticle formation. Changing the solution pH and the ionic strength of the solution has been crucial to investigate the two terms separately. The π-π stacking of the dyes is totally independent on the electrostatic interaction, while it depends on the dendrimer generation used. This because the dendrimer generation means different molecular flexibility and volume, and hence, different geometrical constrains. The important role of the thermodynamics of the interactions has to be further investigated. For instance, it would have extreme importance the study of the self-assembled nanoparticles and of the building blocks interaction as a function of the temperature. This would give the possibility to establish even more general conclusions on the role of the different interactions. In addition, it would be crucial to extend these findings to other self-assembled systems since understanding the general principles behind nanoparticle formation is the key to optimize the self-assembly process for example for industrial application.
Moreover, additional interaction could be added to the systems as for example metal coordination or hydrogen bounding. This may results in more stable assemblies or even in new morphologies. For example, the addition of hydrophobic moieties might lead to the formation of hollow structures. Once the stability in temperature is defined, it would be interesting to incorporate drug molecules and study the stability of the assemblies and the release rate at different pH.
In addition to the effects of the building blocks interactions, another parameter controls the self-assembly: the ratio between the building blocks. At low ratio smaller nanoparticles are formed and free dendrimers are present in solution, while at higher values all the dendrimers are aggregated and larger nanoparticles are formed.
The existence of the threshold value in the dye interaction separating the dyes forming elongated structures and the one forming spherical assemblies has lead to the studies of different dye mixtures in combination with generation 4 dendrimer. In principle mixing different dyes should simulate a dye with a π-π interaction strength in between the values of the single dyes. First of all, we have

shown that the different dyes can stack on each other forming heterostacks. This results in a change of the nanoparticle shape. For example in the case of ABnOHRAc and Ar27, elliptical nanoparticles are formed who are different than the spheres formed by Ar27 and the long cylinders formed by ABnOHRAc. This proves that it is possible to use mixture of dyes to simulate a dye with different π-π interaction strength. However, further studies are needed in the future in order to understand more precisely how the different dye stacks. For example, theoretical simulation of the dye stacking are needed. In addition, circular dichroism measurements could help to get more detailed information on the changes induced by the dye complexation.
Lastly, long linear polyelectrolytes have been used in combination with the same set of azo dyes. Stable and well-defined nanoparticles are obtained also in this case proving the generality of our self-assembly process. The elongated nature of the polyelectrolytes molecules results in the formation of elongated nanoparticles for all the dyes. Using a light controlled trans-cis isomerizable dye, it has been possible to form light sensitive nanoparticles. Their shape can be changed from ellipsoids to long fiber-like cylinders. In future studies, it will be possible to use different polyelectrolytes to see if the shape transition can be observed for other systems. In addition, polyelectrolytes with specific lateral chain can be used to form nanoparticle with specific functionality.

This study is one of the few able to relate the structural properties on the supramolecular scale to the interaction forces of the building blocks on the molecular arena and to their molecular properties. The finding of general relationships between these properties will become more and more important in the future leading to the understanding of general principles behind supramolecular self-assembly. From these results, it will be possible to predict nanoparticle shapes knowing only the thermodynamic parameters for the interaction of the chosen molecular building blocks. Thus, a precise molecular design of the dye molecule

(e.g. choosing appropriate substituents) will allow tailoring the structure of the nanoparticles. Hence, with this thesis fundamental steps in developing a box of molecular "building bricks" allowing for a targeted structural design have been made. This may, for example, be of potential in the development of novel self-assembled photocatalysts or smart therapeutic carrier systems.

Chapter 4 First-Author Contributions

4.1 Elucidating Electrostatic Self-Assembly: Molecular Parameters as Key to Thermodynamics and Nanoparticle Shape

JACS
JOURNAL OF THE AMERICAN CHEMICAL SOCIETY

Article

pubs.acs.org/JACS

Elucidating Electrostatic Self-Assembly: Molecular Parameters as Key to Thermodynamics and Nanoparticle Shape

Giacomo Mariani,[†,‡] Daniel Moldenhauer,[†] Ralf Schweins,[‡] and Franziska Gröhn*[,†]

[†]Department of Chemistry and Pharmacy and Interdisciplinary Center for Molecular Materials (ICMM), Friedrich-Alexander-Universität Erlangen-Nürnberg, Egerlandstrasse 3, D-91058 Erlangen, Germany

[‡]Institut Laue-Langevin, DS/LSS, 71 Avenue des Martyrs, 38000 Grenoble, France

ABSTRACT: The rational design of supramolecular nanoparticles by self-assembly is a crucial field of research due to the wide applications and the possibility of control through external triggers. Understanding the shape-determining factors is the key for tailoring nanoparticles with desired properties. Here, we show how the thermodynamics of the interaction control the shape of the nanoparticle. We highlight the connection between the molecular structure of building blocks, the interaction strength, and the nanoassembly shape. Nanoparticles are prepared by electrostatic self-assembly of cationic polyelectrolyte dendrimers of different generations and oppositely charged multivalent organic dyes relying on the combination of electrostatic and $\pi-\pi$ interactions. Different building blocks have been used to vary interaction strength, geometric constraints, and charge ratio, providing insights into the assembly process. The nanoassembly structure has been characterized using atomic force microscopy, static light scattering, small angle neutron scattering, and UV−vis spectroscopy. We show that the isotropy/anisotropy of the nanoassemblies is related to the dye valency. Isothermal titration calorimetry has been used to investigate both dye−dye and dye−dendrimer interaction. The existence of a threshold value in entropy and enthalpy change separating isotropic and anisotropic shapes for both interactions has been demonstrated. The effects of the dye molecular structure on the interaction thermodynamics and therefore on the nanoparticle structure have been revealed using molecular modeling. The polar surface area of the dye molecule takes a key role in the dye self-interaction. This study opens the possibility for a priori shape determination knowing the building blocks structure and their interactions.

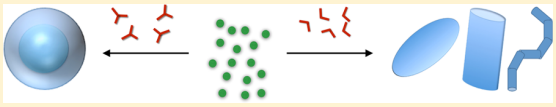

INTRODUCTION

Self-assembly is an important route to organizing soft matter.[1−9] A variety of structures and functions in natural systems is realized by supramolecular assemblies, ranging from cell membranes to protein complexes for photosynthesis. Synthetic self-assembled structures with high potential are, for example, supramolecular polymers,[10−14] composite materials,[15−18] or carrier systems.[19−23] Great potential lies in the synthetic design for solar cells or drug delivery. In this framework, understanding the shape-determining factors is the key to a rational creation of target nanostructures. However, fundamental understanding of self-assembly often is limited. The architecture of the molecular building blocks has been demonstrated to be one of the key factors controlling the structure of the final nanoscale assemblies.[24−29] In the last years, the driving forces and the basic principles of the self-assembly process have been the topic of theoretical developments.[30−32] While the structure control in the self-assembly of amphiphilic systems is quite well known, different noncovalent interactions and their combinations have come into focus for nanostructure design more recently.[16,18,19,33] For example, we developed a new concept of electrostatic self-assembly for the formation of supramolecular nanoscale assemblies that show a well-defined size and exhibit a variety of shapes such as spheres, cylinders, and hollow spheres with narrow size distribution.[35−38] The process is based on the interconnection of macroions through "structural" multivalent organic counterions under secondary interaction effects such as $\pi-\pi$ stacking or geometric factors. Hence, the key point is a general combination of interactions, rather than relying on specific binding motifs. For instance, multivalent azo dye building blocks interconnect dendrimeric macroions into nanoparticles with sizes up to more than 100 nm.[35,39−42] Switchable nanoparticles that can respond to external triggers, such as pH or light, have been built,[7,35,41,42] and of particular potential are organic−inorganic hybrid assemblies where the polyelectrolyte enables the "communication" of an inorganic nanoparticle and the dye molecules.[43] Porphyrin−polyelectrolyte assemblies form a novel functional photocatalytic nanosystem for light energy conversion.[44]

Recently, the influence of the dendrimer size and the molecular structure of the dye building blocks on the resulting nanoparticle structures has been demonstrated.[45,46] A threshold in free energy below which no dendrimer interconnection takes place and a quantitative relation of the self-assembled nanoparticle size and the free energy of dye−dye and dye−dendrimer association became evident. The free energy of the assembly formation was shown to consist of an electrostatic contribution between dyes and dendrimers and a $\pi-\pi$ contribution between the dyes. Ultimately, a simple model has been developed to connect the free energy with the aggregation number.[47]

Received: November 3, 2015
Published: December 7, 2015

DOI: 10.1021/jacs.5b11497
J. Am. Chem. Soc. 2016, 138, 1280−1293

Scheme 1. Azo Dyes and Dendrimer Building Blocks

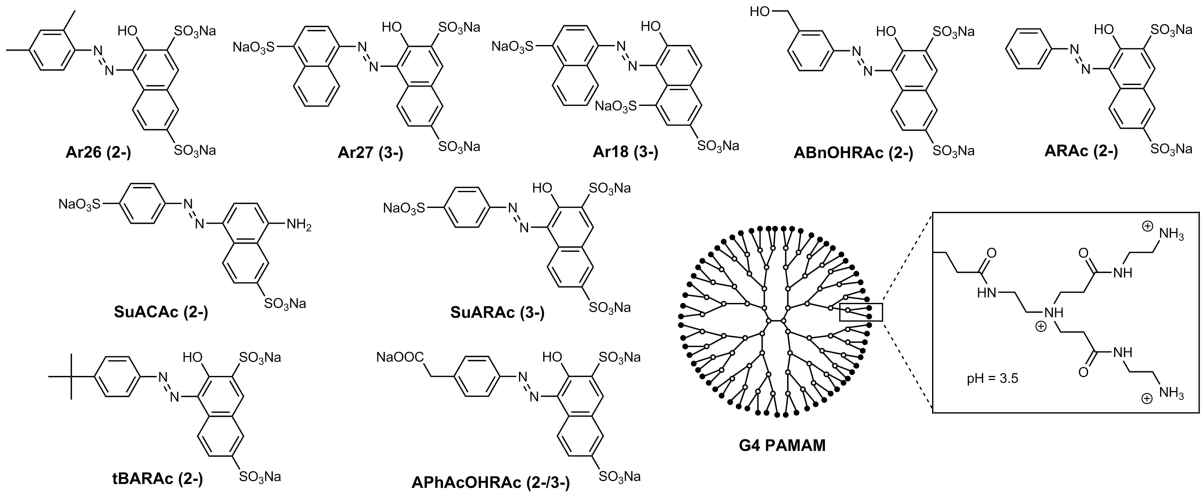

In contrast to the size tuning, the encoding of particle shape so far has not been understood, while this would open the possibility for shape control through building block selection.

At this point, for a thorough fundamental understanding on how electrostatic interaction, $\pi-\pi$ stacking, and geometric factors act together in the self-assembly on shape, a detailed structural characterization of the self-assembled nanoparticles is required focusing on the interplay of interactions with special attention to the role of the molecular building blocks. As a model system, we investigated electrostatically self-assembled nanoparticles from polyamidoamine (PAMAM) dendrimers and oppositely charged azo dyes (Scheme 1). The structure of the aggregates will be investigated as a function of the azo dye molecular structure, of the dendrimer generation (from 2 to 8), and of the component ratio. These parameters permit the modification of interaction strength, flexibility of the particles, geometric constraints, and charge compensation providing insights into the assembly process. An extended set of azo dyes, partially synthesized within this study, allows a systematic variation of the valency, the π-backbone, and the position of the charged groups. The nanoparticle structure has been characterized using atomic force microscopy (AFM), small angle neutron scattering (SANS), static light scattering (SLS), and UV−vis spectroscopy. Isothermal titration calorimetry (ITC) has been performed to study thermodynamics. Molecular modeling of the dye then permits one to connect the nanoscale structure and thermodynamics with the molecular dye properties. We present insight into the delicate balance of factors governing structure formation: it will be shown how the thermodynamics of the interaction between the building blocks controls not only the nanoassembly size but also their shape. Moreover, a relationship between the dye molecular properties and the interaction strength is established. This is a crucial step in creating a molecular toolbox allowing for directed self-assembly into tailor-made nanoparticles with desired shape and size by selecting appropriate building block combinations. To the best of our knowledge, this is the first time that a relationship of building block molecular properties, thermodynamics, and nanoscale shape is observed in electrostatic self-assembly.

RESULTS AND DISCUSSION

This study comprises the structural characterization of the dye−dendrimer nanoparticles and the thermodynamic analysis of their formation including both the electrostatic interaction between dyes and dendrimers and the mutual $\pi-\pi$ interaction that occurs between the dyes, analyzing the changes in free energy, entropy, and enthalpy. The focus lies on understanding the structures formed, in particular, the assembly shape. Some of the dyes were already investigated in a previous study[50] (Ar26, tBARAc, ARAc, Ar27, Ar18, and SuARAc), while others have been synthesized within this study (APhAcOHRAc, ABnOHRAc, and SuACAc). To explore the role of electrostatic interaction, both di- (Ar26, ABnOHRAc, ARAc, tBARAc) and trivalent (APhAcOHRAc, Ar18, Ar27, SuARAc) dyes have been studied. In section 1 the structural characterization will be presented. It consists of AFM, SANS, and SLS to investigate the shape and size of the nanoparticles and UV−vis spectroscopy to study the $\pi-\pi$ stacking of the dye molecules. The loading ratio is defined as the molar ratio of dye sulfonate to dendrimer primary amino groups

$$l = \frac{c(-SO_3^-)}{c(-NH_2)} \quad (1)$$

In section 2 a detailed analysis of the dye−dye and dye−dendrimer interaction thermodynamics is presented where a key point is to draw a connection of the structural features on the nanoscale with the molecular level. In section 3, it is shown how the molecular electrostatic properties of the dye molecules control the dye−dye interaction and thereby the nanoparticle structure.

1. Structural Characterization. *AFM.* To obtain first structural information on the nanoaggregates, AFM measurements have been carried out. We investigated Ar26 with generation 4 and 8 dendrimers (G4 and G8). Results are displayed in Figure 1. The images show individual particles with different shapes for the two different samples. Ar26 and G4 dendrimers (Figure 1a) form ellipsoidal particles, while the shape is completely different when G8 is used (Figure 1b). In the latter case the nanoparticles are again elongated, but the aspect ratio is larger. These nanoaggregates are rod-like with a length of roughly 1 μm and a cross-section of 100 nm. In addition, these nanoparticles appear to be rather flexible in

DOI: 10.1021/jacs.5b11497
J. Am. Chem. Soc. 2016, 138, 1280−1293

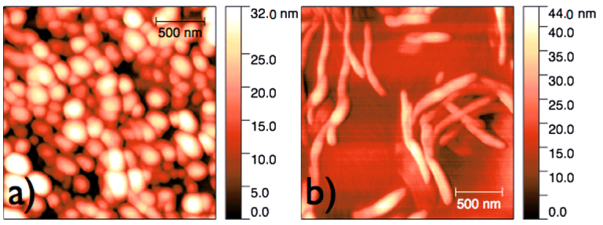

Figure 1. AFM images for (a) Ar26 + G4 at l = 1.8 and (b) Ar26 + G8 at l = 1.8.

comparison to the ones for Ar26 and G4. Therefore, we can conclude that different dendrimer generations result in different assembly shapes.

SANS and SLS Measurements. To gain insights into the nanoparticle shape and dimensions in solution we performed SANS experiments. Samples were prepared at pH 3.5 to provide complete protonation of the polyelectrolyte. Considering that a loading ratio of 2 corresponds to charge stoichiometry, we investigated loading ratios between 1 and 1.8, i.e., with excess of polyelectrolyte leading to well-defined and stable dye–dendrimer nanoparticles.[39] To better understand the shape of the nanoparticles, static light scattering measurements have been carried out. These measurements permit extending the q range to lower q values, covering the dimensions of the large nanoparticles.

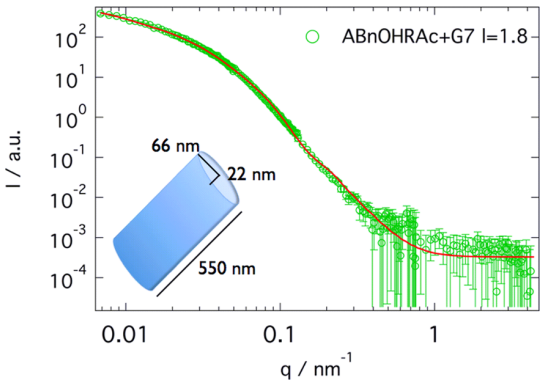

Figure 2. SANS results for ABnOHRAc + G7 at l = 1.8.

The results for ABnOHRAc and G7 dendrimer are depicted in Figure 2. The SANS curve, at low q, clearly indicates the presence of nanoparticles in solution. From the $I(q_{min})$, one can conclude that the size is larger than 600 nm, which is 100 times larger than the building block size. To obtain the shape and the dimensions of the nanoaggregates, the curve has been fitted using structural models. In the case of ABnOHRAc and G7, the resulting nanoparticles are cylinders with elliptical cross-section with a length of 550 nm; the minor axis of the cross-section is 22 nm; the major one is 66 nm. Scattering curves for the most important samples including a series of varying loading ratios are shown in Figure 3. The corresponding shapes and dimensions are summarized in Tables 1 and 2: for different dyes and dendrimer generations, nanoparticles different in shape and dimension can be found. In the case of Ar26 and G4 dendrimer (Figure 3a) the nanoparticles are cylinders with elliptical cross-section; the length of the nanoparticles increases with the loading ratio, while the cross-section remains constant. From loading ratio 1.0 to 1.8 the length almost doubles, from 170 nm to 300 nm. This may be due to the incorporation of more dendrimer molecules; they are free at low loading ratios, while they connect to the nanoparticles at higher loading ratios. The polyelectrolyte molecules attach to the cylinders at the two ends, increasing their length and not changing the cross-section, thus modifying the particle aspect ratio. A different behavior can be found choosing APhAcOHRAc and G4 as building blocks (Figure 3c). Aggregates have a core–shell spherical shape and become smaller with loading ratio (from a total radius R_{tot} = 87 nm to R_{tot} = 46 nm). The fitting model describes a particle with a denser core and a less dense shell. Probably less dyes and dendrimers are incorporated in the shell, and hence, a less dense structure results. The behavior of ABnOHRAc and G7 (Figure 3d) is again different: at loading ratio 1.0 just single dendrimer molecules loaded with dye can be found. At loading ratios between 1.2 and 1.6, the molecular building blocks self-assemble into ellipsoids. At loading ratio 1.8 some of these ellipsoids aggregate together forming a larger elliptical cylinder. The same dye in combination with G8, as seen in Figure 3e, forms elliptical cylinders already at low loading ratio, and the cross-section remains unchanged while the length increases from 120 nm to 400 nm with the loading ratio. An interesting dependency results for Ar27 and G8 dendrimer (Figure 3f): at loading ratio 1.0 dendrimer dimers are observed, while at higher loading ratios two different structures coexist in solution: a small cylinder with the cross section of a single dendrimer molecule and a larger elliptical cylinder. The peculiarity of this system is that the cross-section of the elliptical cylinder increases with loading ratio, whereas in all other systems it remains constant.

In addition to the differences in the particle shape another behavior of the SANS curves results for all samples. At low loading ratio (below l = 1.5), the curves clearly show two contributions: one at low q and another around 0.7 nm^{-1}. The signal at low q arises from the large nanoparticles formed by the interaction of dendrimers and dye molecules as discussed above, while the other can be attributed to small particles, which can be either individual dye-loaded dendrimers or small aggregates (size between 8 nm and 20 nm). The signal of the smaller particles is higher at loading ratio 1.0, where the excess of polyelectrolyte charges is maximal, and decreases continuously until loading ratio 1.5. At even higher loading ratio only the larger nanoassemblies are present in solution. Here the free polyelectrolyte molecules are loaded with sufficient dye to be all interconnected.

To summarize, the loading ratio is a crucial parameter in nanoparticle formation: it controls the dimensions of the nanoassemblies and the ratio between unassembled molecular building blocks and nanoparticles. In some cases it also has an effect on the shape of the self-assembled nanoparticles. With one exception, it plays no role on the cross-section of the aggregate. The shape and cross-section crucially depend on the building blocks, as will be discussed in the following.

To investigate the role of the dye structure and valency in the self-assembly, measurements have been made keeping the loading ratio and the dendrimer generation constant. Shape results are depicted in Scheme 2. Reading horizontally the line regarding G4, both spherical and elongated particles can be found, while in the case of G8 only elongated structures occur. For generation G4, three different structures can be observed: core–shell spheres, ellipsoids, and cylinders. Therefore, the dyes can be divided into two groups: the first forming isotropic aggregates (Ar18, Ar27, SuARAc, and APhAcOHRAc) and the second forming anisotropic particles (Ar26, ABnOHRAc,

DOI: 10.1021/jacs.5b11497
J. Am. Chem. Soc. 2016, 138, 1280–1293

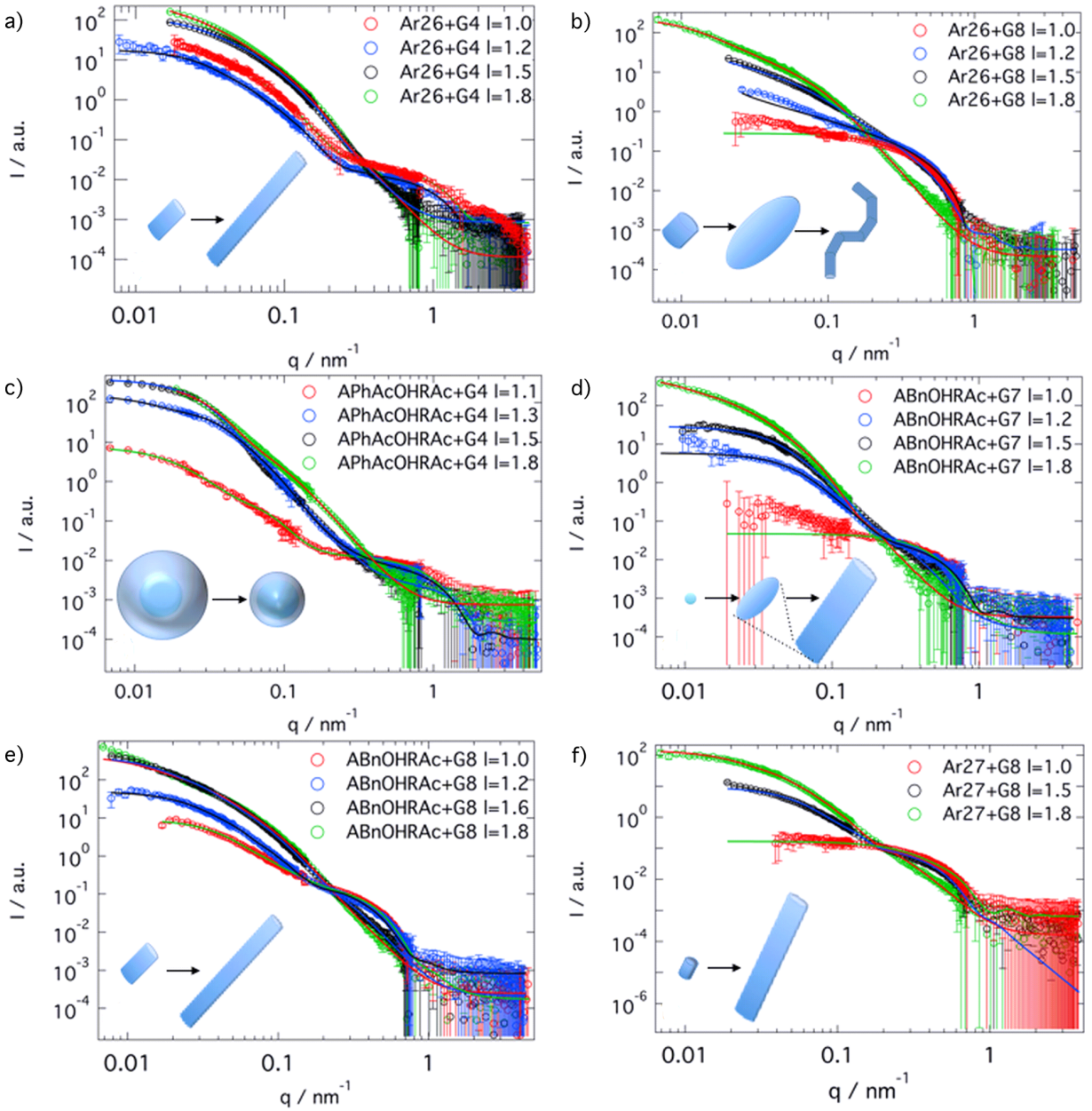

Figure 3. SANS results at different loading ratios for (a) Ar26 + G4, (b) Ar26 + G8, (c) APhAcOHRAc + G4, (d) ABnOHRAc + G7, (e) ABnOHRAc + G8, and (f) SuACAc + G8. Continuous lines represent the best fit. Results of the fits are summarized in Table 1.

SuACAc, ARAc, and tBARAc). For G4, among the dyes that form the same shape, the dimensions differ. In the case of spherical nanoparticles, the total radius R_{tot} varies between 44 nm and 143 nm. tBARAc and SuACAc form ellipsoids. The axes of the nanoparticles made of tBARAc are 13 nm and 60 nm, while the ones of SuACAc are 47 nm and 120 nm. Ar26, ABnOHRAc, and ARAc form cylinders with elliptical cross-section. Despite a difference in length, Ar26 and ARAc show similar cross-section dimensions, which may be understood considering that more dendrimers attach to the end of the structure than to the side of the cylinder determining a preferred direction during the self-assembly process. ABnOHRAc instead forms longer cylinders, which become flexible. The choice of dye is crucial in targeting the dimensions of the nanoparticles.

To further investigate the influence of polyelectrolyte dimension and flexibility on the assembly structure, different dendrimer generations have been used. The shape results are again depicted in Scheme 2: this time the table should be read vertically. The SANS curves are reported in Figure 4. It is evident that the nanoparticle shape is strongly dependent on the dendrimer generation. In most cases (except of ABnOHRAc), a higher anisotropy is found for dendrimers of higher generation.

No isotropic nanoparticles can be found with G8 dendrimer. It can be concluded that the larger the polyelectrolyte building block is, i.e., the less flexible, the higher the anisotropy of the nanoassemblies. Even dyes that tend to form isotropic particles as a cause of their structural constraints are “forced” to build elongated structures by the G8 dendrimer. Looking in more detail at Ar26, the nanoparticles become more anisotropic as the

DOI: 10.1021/jacs.5b11497
J. Am. Chem. Soc. 2016, 138, 1280−1293

Table 1. Geometric Parameters Resulting from the SANS Fits for Elongated Nanoparticles

			cross-section				
system	l	shape	R_{min} (nm)	R_{maj} (nm)	L (nm)	P (nm)	small particle
Ar26 + G2	1.8	ellipsoid	30 ± 1		160		none
Ar26 + G4	1.0	ellipt. cylinder	12 ± 1	44 ± 4	170 ± 10		G4
	1.2	ellipt. cylinder	12 ± 1	46 ± 4	180 ± 10		G4
	1.5	ellipt. cylinder	11 ± 1	30 ± 3	185 ± 5		G4
	1.8	ellipt. cylinder	11 ± 1	44 ± 4	300 ± 10		none
Ar26 + G5	1.8	cylinder	35 ± 2		220 ± 10		none
Ar26 + G7	1.0	ellipt. cylinder	35 ± 2	77 ± 5	175 ± 10		G7
	1.8	flex. ellipt. cylinder	22 ± 1	57 ± 3	870 ± 40	320 ± 20	none
Ar26 + G8	1.0	cylinder (= dimer)	4		19 ± 1		none
	1.2	cylinder	4		40 ± 2		none
	1.4	ellipsoid	11 ± 1		105 ± 5		cylinder as l = 1.2
	1.5	ellipsoid	9 ± 1		92 ± 5		cylinder as l = 1.2
	1.7	flex. ellipt. cylinder	9 ± 1	31 ± 4	1400 ± 80	500 ± 20	dimers
	1.8	flex. ellipt. cylinder	10 ± 1	26 + 3	1400 ± 80	420 ± 20	dimers
APhAcOHRAc + G8	1.0	cylinder (= dimer)	4		20 ± 2		none
	1.2	ellipsoid	19 ± 1		130 ± 10		dimers
ABnOHRAc + G4	1.5	flex. ellipt. cylinder	7 ± 1	35 ± 5	710 ± 30	300 ± 20	none
	1.8	flex. ellipt. cylinder	7 ± 1	42 ± 6	2100 ± 100	140 ± 10	none
ABnOHRAc + G5	1.0	ellipsoid	17 ± 1		180 ± 10		G5
ABnOHRAc + G7	1.0	none					G7
	1.2	ellipsoid	14 ± 1		86 ± 5		G7
	1.5	ellipsoid	18 ± 1		120 ± 10		G7
	1.65	ellipsoid	19 ± 1		130 ± 10		G7
	1.8	ellipt. cylinder	22 ± 1	66 ± 3	550 ± 20		none
APhAcOHRAc + G8	1.0	cylinder (= dimer)	4		20 ± 2		none
	1.2	ellipsoid	19 ± 1		130 ± 10		dimers
ABnOHRAc + G8	1.0	ellipt. cylinder	12 ± 1	46 ± 4	120 ± 10		G8
	1.1	ellipt. cylinder	12 ± 1	41 ± 4	170 ± 10		G8
	1.2	ellipt. cylinder	17 ± 1	56 ± 3	200 ± 10		G8
	1.5	ellipt. cylinder	10 ± 1	37 ± 4	200 ± 10		G8
	1.6	ellipt. cylinder	14 ± 1	55 ± 4	340 ± 20		G8
	1.8	ellipt. cylinder	12 ± 1	48 ± 4	400 ± 20		none
Ar27 + G8	1.0	cylinder (= dimer)	4		18 ± 1		none
	1.5	ellipt. cylinder	13 ± 1	33 ± 3	200 ± 10		cylinder
	1.8	ellipt. cylinder	28 ± 1	73 ± 3	260 ± 20		cylinder
SuARAc + G8	1.5	flex. ellipt. cylinder	11 ± 1	65 ± 7	210 ± 10	40 ± 3	G8
	1.8	flex. ellipt. cylinder	8 ± 1	55 ± 7	2100 ± 90	40 ± 3	none
SuACAc + G4	1.0	ellipsoid	11 ± 1		120 ± 10		dimers
	1.8	ellipsoid	47 ± 2		240 ± 20		none
SuACAc + G8	1.0	ellipsoid	15 ± 1		130 ± 10		dimers
	1.5	ellipsoid	32 ± 2		300 ± 20		none
	1.8	ellipsoid	21 ± 1		220 ± 20		none
tBARAc + G4	1.8	ellipsoid	13 ± 1		120 ± 10		none
ARAc + G4	1.8	ellipt. cylinder	19 ± 1	57 ± 3	470 ± 20		none
ARAc + G8	1.8	ellipsoid	28 ± 2		250 ± 10		none

dendrimer generation increases. Ar26 and G2 form ellipsoids with one axis of 80 nm and the other of 30 nm. With G4 and G5, cylindrical particles are found, e.g., for G4 the length is 300 nm and the cross-section is elliptical with a minor axis of 11 nm and a major one of 44 nm. With G7 and G8, Ar26 forms flexible cylinders. For G7 the length is 870 nm, the persistence length is 320 nm, and minor and major axis are 22 nm and 57 nm. For Ar26 and G8 the length is 1.3 μm, the persistence length is 420 nm, the minor axis is 10 nm, and the major one is 26 nm. Interestingly, the cross-section aspect ratio is constant, while the overall aspect ratio doubles. Thus, by increasing the dendrimer size the self-assembled nanoparticles become larger and more elongated. A similar behavior can be found for APhAcOHRAc, changing the structure from spherical particles for G4 to ellipsoids for G8.

Hence, structural characterization reveals that the loading ratio controls the number of dendrimers forming the nanoparticles. Single dendrimers or dimers can coexist with larger nanoassemblies at low loading ratio, while at loading ratios above 1.5 all dendrimers are aggregated. For elongated nanoparticles, as the loading ratio increases, the length grows while the cross-section remains constant. The aspect ratio is therefore strongly related to the loading ratio. On the other hand, the shape of the assemblies is not related to the loading ratio in most cases. The assembly shape is caused by building block choice: different shapes originate from different dyes and

DOI: 10.1021/jacs.5b11497
J. Am. Chem. Soc. 2016, 138, 1280−1293

Table 2. Geometric Parameters Resulting from the SANS Fits for Spherical Core−Shell Nanoparticles

system	l	R_{core} (nm)	R_{tot} (nm)	small particle
APhAcOHRAc + G4	1.1	19 ± 1	87 ± 4	G4
	1.3	29 ± 1	64 ± 3	G4
	1.5	37 ± 2	52 ± 3	G4
	1.8	28 ± 1	46 ± 2	none
APhAcOHRAc + G5	1.0	2.9		none
	1.8	61 ± 2	81 ± 3	none
APhAcOHRAc + G7	1.0	59 ± 3	86 ± 4	G4
	1.8	198 ± 10	273 ± 20	none
Ar27 + G4	1.8	13 ± 1	44 ± 3	none
Ar18 + G4	1.8	90 ± 3	143 ± 5	none
SuARAc + G4	1.8	45 ± 2	64 ± 3	none

Scheme 2. Nanoparticle Shapes Resulting from SANS as a Function of Dye Type and Dendrimer Generation

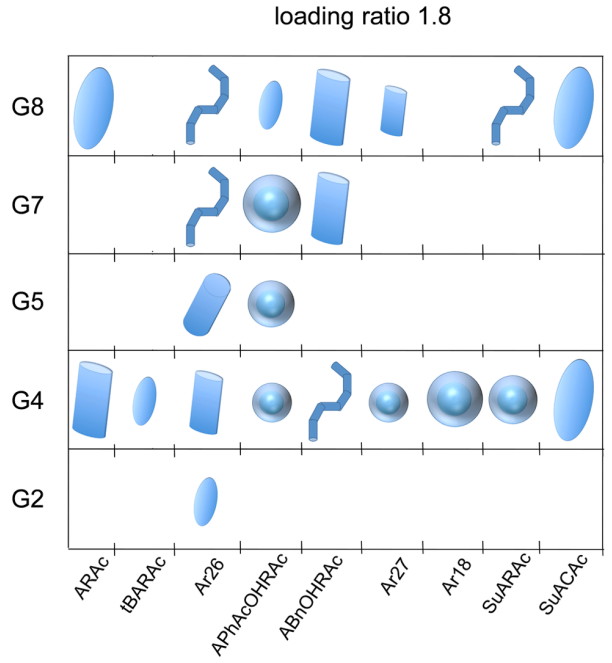

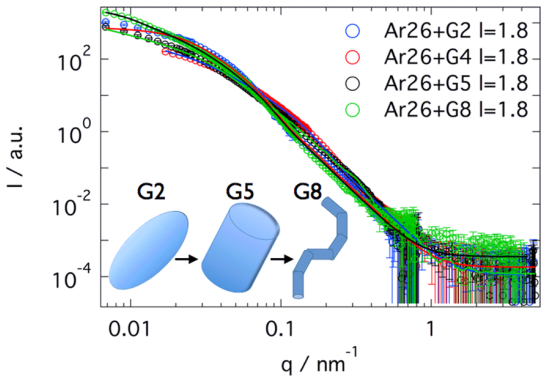

Figure 4. SANS curves of Ar26 and different dendrimer generations. Different shapes correspond to different generations.

different dendrimer generations. These two parameters together define the strength of dye−dendrimer and dye−dye interaction, stemming from differences in dye valency, geometry, dimensions, number of interacting points, and dendrimer flexibility. Higher dendrimer generations promote the formation of anisotropic nanoparticles as well as larger particle sizes.

UV−vis Spectroscopy. UV−vis results for different dyes and two dendrimer generations (G4 and G8) are depicted in Figure 5. The binding of dyes to dendrimers due to ionic interaction induces the spatial proximity of the dye molecules, and thereby dyes can mutually interact and form π-stacks.[38,39,47,48] This causes the splitting of the first excited state of the monomer and can be described applying exciton theory.[49−53] From this, two geometric parameters can be extracted: the intermolecular dye−dye distance R and the twist angle β between two dyes molecules.[54] The fitting results are given in Figure 5 and, for loading ratio l = 1.8 in Table 3. It is worth noting how the twist angle is related to the nanoparticle shape. For G4 dendrimer, for all systems forming isotropic structures the angle is around 37−38°, while for anisotropic structures it is higher than 40°. Moreover, with G8 (i.e., where all systems form elongated structures) only angles larger than 40° are observed. The twist angle versus the loading ratio is depicted in Figure 6. Taking into account the angular behavior in the case of G4, assemblies with different shape show a different variation of the twist angle. For spherical particles the angle remains constant (variation of less than 3°), while for elongated particles it changes by 15°. For G8, instead, the changes are larger than 25°. ABnOHRAc differs: it forms elongated structures with both G4 and G8, but the angle is independent of loading ratio and dendrimer generation. As shown from SANS measurements, it must be kept in mind that single dendrimers loaded with dyes can be found at loading ratios lower than 1.5. The presence of this second species can influence the UV−vis measurements and consequently the angle. The intermolecular dye distance R appears not to be connected to the shape of the nanoparticle but only depends on the dye itself. There appears to be a fixed range of dye−dye distances from 0.65 to 0.80 nm for all dyes.[55] Further discussions of the structural parameters obtained from the UV−vis measurements will be presented in the next section in context with the thermodynamics results. In conclusion, all dyes with twist angles larger than 40° form anisotropic nanoparticles, whereas the dyes that form isotropic aggregates have a constant angle of about 38°.

2. Thermodynamics. Previously, isothermal titration calorimetry has led to an attraction−repulsion model allowing the understanding of the finite assembly size. It has been demonstrated that the assembly process is governed by the mutual dye−dye interaction. No relation of thermodynamics and nanoscale shape of the self-assembled particles exists so far.

Herein, we extend the ITC measurements to a larger set of dyes and dendrimer generations while simultaneously elucidating how the thermodynamics of the interaction encodes the shape of the nanoparticles. For this purpose, both dye dilution experiments and dendrimer into dye titrations were performed to investigate the dye self-aggregation and the dye−dendrimer interaction, respectively. In the following, first, the results on dye−dye interaction and, second, those on dye−dendrimer interaction will be presented, relating all of them to the shape of the nanoparticles.

ITC raw data and their analysis are shown in Figure 7. The raw heat traces of the titration experiments are depicted in the upper plot. For the dilution experiments (Figure 7a and 7b), the lower plot shows the integrated heat for each injection versus the dye concentration in the titration cell. For the dye−dendrimer experiments (Figure 7c and 7d), again the lower plot

DOI: 10.1021/jacs.5b11497
J. Am. Chem. Soc. 2016, 138, 1280−1293

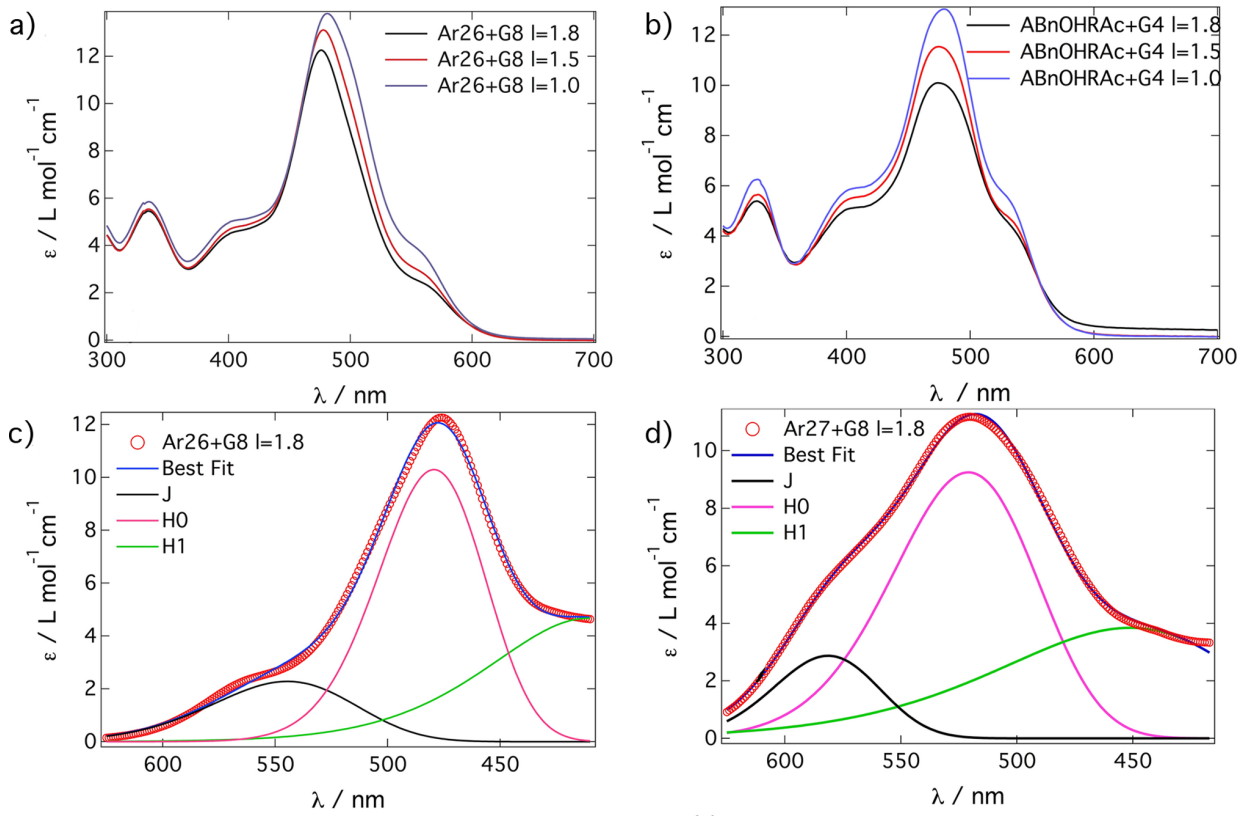

Figure 5. UV−vis spectroscopy. (a) Spectra for Ar26 + G8 at three loading ratios. (b) Spectra for ABnOHRAc + G4 at three loading ratios. (c and d) Exction theory applied to Ar26 + G8 and Ar27 + G8.

Table 3. Analysis of Mutual Dye Geometry According to Exciton Theory at Loading Ratio l = 1.8

system	R (nm)	β (deg)
Ar26 + G4	0.75 ± 0.03	55 ± 1
tBARAc + G4	0.65 ± 0.03	43 ± 1
ABnOHRAc+ G4	0.71 ± 0.03	38 ± 1
APhAcOHRAc + G4	0.74 ± 0.03	38 ± 1
SuARAc + G4	0.75 ± 0.03	38 ± 1
Ar27 + G4	0.65 ± 0.04	37 ± 1
Ar26 + G8	0.68 ± 0.04	51 ± 1
tBARAc + G8	0.68 ± 0.03	67 ± 1
ABnOHRAc + G8	0.73 ± 0.03	39 ± 1
APhAcOHRAc + G8	0.75 ± 0.03	41 ± 1
SuARAc + G8	0.75 ± 0.03	45 ± 1
Ar27 + G8	0.78 ± 0.02	46 ± 1

shows the integrated heat normalized per mole of injectant versus molar ratio of dendrimer to dye in the titration cell. The ITC curves can then be extrapolated to zero molar ratio to obtain the enthalpy of association, or they can be fitted with a one-site model. The two approaches yield the same results, and the one-site model will be applied in the following. It yields the equilibrium aggregation constant K and consequently the Gibbs free energy change of the association ΔG,[56,57] and together with the enthalpy change ΔH it leads to the entropy change ΔS:

$$\Delta G = -RT \ln K \quad (2)$$

$$\Delta G = \Delta H - T\Delta S \quad (3)$$

Results for the dye dilution are reported in Table 4. Values between $\Delta H_{\text{dye–dye}} = -30$ kJ mol^{-1} and $\Delta H_{\text{dye–dye}} = -8$ kJ mol^{-1} have been found, while the entropy change is between $T\Delta S_{\text{dye–dye}} = -21$ kJ mol^{-1} and $T\Delta S_{\text{dye–dye}} = -4$ kJ mol^{-1}. The trivalent dyes (Ar18, Ar27, and SuARAc) show a higher $\Delta H_{\text{dye–dye}}$ than the divalent ones. Their values vary between $\Delta H_{\text{dye–dye}} = -8$ kJ mol^{-1} and $\Delta H_{\text{dye–dye}} = -20$ kJ mol^{-1}, while the divalent ones have enthalpies lower than $\Delta H_{\text{dye–dye}} = -20$ kJ mol^{-1}. APhAcOHRAc with $\Delta H_{\text{dye–dye}} = -20.2$ kJ mol^{-1} lies between the trivalent dyes and the divalent ones. This is due to its carboxylic acid group with a pK_a of 4.1. At pH 3.5 the dye is to 20% in the trivalent and to 80% in the divalent state. This may be used to tune its valency by regulating the pH, opening new possibilities in the control of the nanoparticle shape.

Considering the $\Delta H_{\text{dye–dye}}$ in conjunction with the shape of the nanoparticles as measured by SANS (Figure 8), a threshold value clearly appears around $\Delta H_{\text{dye–dye}} = -21$ kJ mol^{-1}: below that self-assembly into spherical nanoparticles occurs, above it self-assembly into elongated structures occurs. Moreover, this value separates tri- and divalent dyes, because trivalent dyes form isotropic assemblies while divalent ones form anisotropic assemblies. Therefore, the valency of the organic dye ions is a crucial parameter in controlling the shape of the self-assembled nanoparticles. Due to the additional charge, trivalent dyes bind to a greater extent to protonated amino groups, and this may restrict the geometric conformations available. In the case of APhAcOHRAc, 20% of trivalent state is sufficient to prevent the formation of elongated particles and forces the nanoparticles to be spherical. Furthermore, the trivalent dye molecules likely require more expressed configuration changes of the dendrimer

DOI: 10.1021/jacs.5b11497
J. Am. Chem. Soc. 2016, 138, 1280−1293

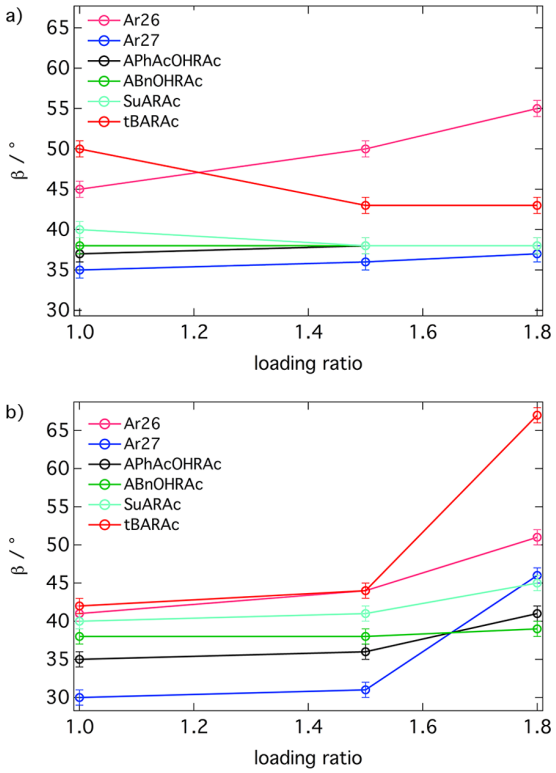

Figure 6. Geometric results from the exciton analysis: twist angle in dependence on different loading ratios (a) for G4 dendrimer and (b) for G8 dendrimer.

to realize a high number of ion pairs of dye sulfonate and dendrimer ammonium groups, and steric hindrance plays a role. This is confirmed when the ratio of the number of dyes bound to one dendrimer molecule to the maximum number of dye molecules that can bind to the dendrimer is considered: for divalent dyes this varies between 0.94 and 0.98, while for trivalent dyes it is between 0.90 and 0.93 only. Moreover, the divalent dyes have a lower value for the enthalpy than the trivalent dyes. This means that elongated particles can be formed only when the dye−dye interaction is strong enough and, in more detail, that only the dyes with a strong $\pi-\pi$ interaction can form anisotropic nanoparticles. This can be understood considering that the dye−dye interaction is mainly anisotropic and thus may induce a preferred growth direction to the assemblies.

Next, it is of interest to consider the free energy change $\Delta G_{\text{dye-dye}}$. Trivalent dyes show values between $\Delta G_{\text{dye-dye}} = -15$ kJ mol^{-1} and $\Delta G_{\text{dye-dye}} = 13$ kJ mol^{-1}, while the divalent ones have values lower than $\Delta G_{\text{dye-dye}} = -15$ kJ mol^{-1}. Again, APhAcOHRAc with $\Delta G_{\text{dye-dye}} = -16$ kJ mol^{-1} has a value that lies between the two kinds of counterions. The threshold also can be observed in dye−dye entropy $T\Delta S_{\text{dye-dye}}$. The fact that the threshold is evident in all thermodynamic dye−dye parameters but most expressed in $\Delta H_{\text{dye-dye}}$ reflects the fact that the dye−dye interaction is enthalpy dominated. It is predominantly caused by $\pi-\pi$ overlap energy rather than by a hydrophobic effect entropic in nature. Hence, it is clearly evident that the dye−dye interaction is crucial, not only for extended dendrimer interconnection but also for encoding the aggregate shape. For the first time it is possible to predict the structure of the nanoparticles formed by dendrimers and dyes by knowing the strength of the dye−dye interaction. This is a key step in the definition of a molecular toolbox that allows for a targeted structure design in terms of assembly size and shape.

Furthermore, the dye−dendrimer interaction has been investigated. For these studies G4 dendrimer has been used as polyelectrolyte, as reported in Table 5. In particular, trivalent dyes yielding spherical aggregates have lower values for both enthalpy and entropy change. Figure 9 displays the interplay of enthalpy and entropy. Here, the three trivalent dyes lie in the left corner of the graph. The difference in enthalpy and entropy change is approximately 10 kJ mol^{-1}. Spherical and elongated structures are again separated in $\Delta H_{\text{dye-den}}$ and $T\Delta S_{\text{dye-den}}$ as was found for the dye−dye interaction. For APhAcOHRAc, which is a mixture of di- and trivalent dyes at pH 3.5, $\Delta H_{\text{dye-den}}$ and $T\Delta S_{\text{dye-den}}$ lie between the two regions but closer to the values of the divalent dyes. This might be expected because the divalent configuration is predominant. In particular, $\Delta H_{\text{dye-den}}$ for APhAcOHRAc is almost identical to that of the divalent dye tBARAc, resulting in a less defined threshold between elongated and spherical aggregates. Despite the differences in enthalpy and entropy, the so-called entropy−enthalpy compensation can be

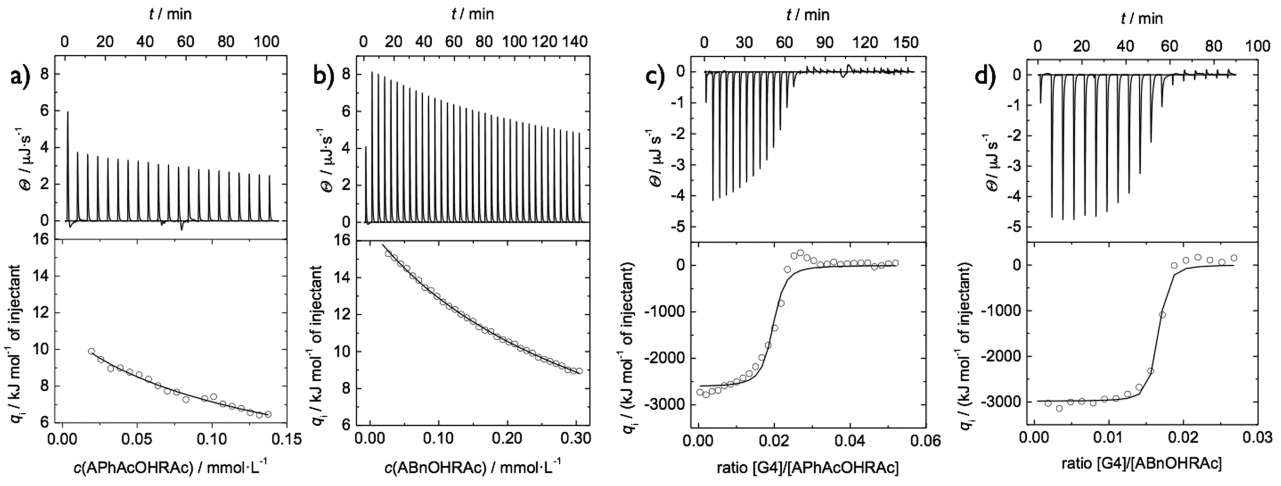

Figure 7. Isothermal titration calorimetry for (a) dilution of APhAcOHRAc, (b) dilution of ABnOHRAc, (c) titration of G4 dendrimer into APhAcOHRAc, and (d) titration of G4 dendrimer into ABnOHRAc, all in formic acid buffer (pH = 4).

DOI: 10.1021/jacs.5b11497
J. Am. Chem. Soc. 2016, 138, 1280−1293

Table 4. Thermodynamic Data for the Dye−Dye Interaction Resulting from ITC

dye	charge	$\Delta H_{dye-dye}$ (kJ mol^{-1})	$K_{dye-dye}$ (L mol^{-1})	$\Delta G_{dye-dye}$ (kJ mol^{-1})	$T\Delta S_{dye-dye}$ (kJ mol^{-1})
SuACAc	2−	−29.1	1.1×10^3	−17.4	−11.6
Ar26	2−	−29.0	2.9×10^3	−19.8	−9.2
tBARAc	2−	−25.4	6.3×10^2	−16.0	−9.4
ABnOHRAc	2−	−24.3	5.0×10^2	−15.4	−8.9
APhAcOHRAc	2−	−20.2	5.8×10^2	−15.8	−4.4
Ar27	3−	−20.0	1.3×10^2	−12.0	−8.0
SuARAc	3−	−8.2	5.6×10^{-3}	12.9	−21.1

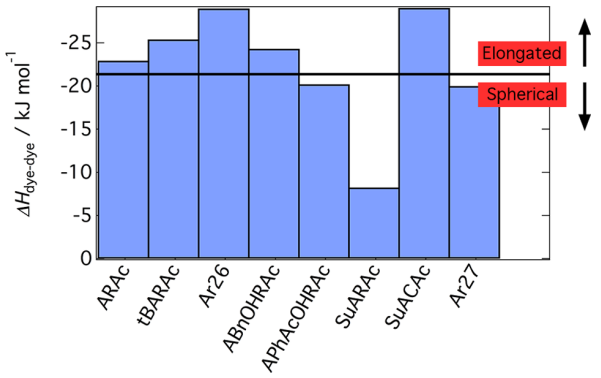

Figure 8. Enthalpy variation measured for dye−dye interaction. A threshold value at $\Delta H_{dye-dye} = -21$ kJ mol^{-1} separates elongated and spherical structures.

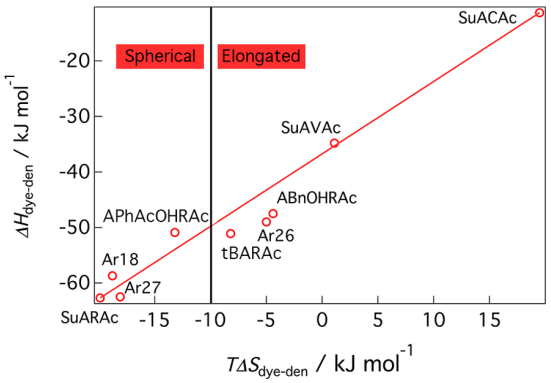

Figure 9. Enthalpy−entropy relation for dye−dendrimer interaction.

seen in Figure 9.[46] In the present study more dyes have been investigated and a more precise fit can be presented, which yields a slope of 1.3. This means that the interplay of enthalpy and entropy changes the free energy to some extent. A clear separation is found if the dye−dendrimer entropy exchange is taken into account: the trivalent dyes and APhAcOHRAc are the ones with the lowest entropy. A threshold value between anisotropic and isotropic structures can be identified for the interaction around $T\Delta S_{dye-dendrimer} = -10$ kJ mol^{-1}.

It is now of great interest to connect the results from UV−vis to the thermodynamic interaction parameters. First, the twist angle as a function of the dye−dye interaction enthalpy $\Delta H_{dye-dye}$ can be analyzed. As reported in Figure 10 for G4 dendrimer, the angle is constant for the isotropic structures, while it changes for elongated particles. Thus, it is evident that the twist angle is related to the nanoscale structure and, therefore, to the strength of the dye−dye interaction. For the dyes forming spherical particles the angle varies less than 1°, while for the others it changes by approximately 16°. Interestingly, the angle for the divalent dyes appears to vary linearly with $\Delta H_{dye-dye}$. Therefore, it can be concluded that a certain interaction strength is required to obtain elongated

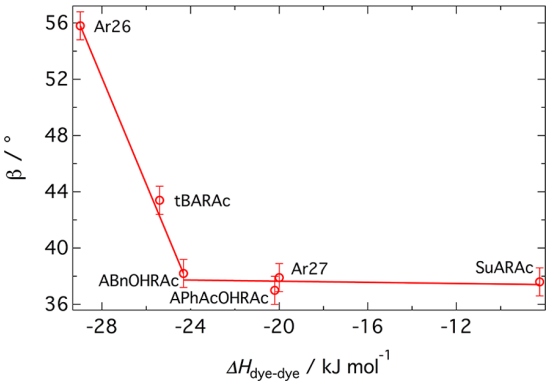

Figure 10. Twist angle in dependence on $\Delta H_{dye-dye}$. For trivalent dyes it is constant, while for divalent ones it changes linearly with $\Delta H_{dye-dye}$.

structures; this increased strength acts on the angle between the dye molecules, yielding a more tilted configuration. Remarkably, the angle of ABnOHRAc, a dye forming elongated structures, is equal to the value measured for the trivalent dyes. It is therefore equal to the twist angle of the dyes in the spherical structure.

Table 5. Thermodynamic Data for the Dye−Dendrimer G4 Interaction Resulting from ITC

dye	charge	$\Delta H_{dye-den}$ (kJ (mol dye)$^{-1}$)	$N_{dye\ per\ G4}$	$K_{dye-den}$ (L mol^{-1})	$\Delta G_{dye-den}$ (kJ (mol dye)$^{-1}$)	$T\Delta S_{dye-den}$ (kJ (mol dye)$^{-1}$)
SuACAc	1−	−11.3	206	2.6×10^5	−30.9	19.5
Ar26	2−	−49.0	62	5.0×10^7	−44.0	−5.0
ABnOHRAc	2−	−47.5	63	3.6×10^7	−43.1	−4.4
tBARAc	2−	−51.1	59	3.0×10^7	−42.9	−8.2
APhAcOHRAc	2−	−50.9	52	3.9×10^6	−37.6	−13.2
Ar18	3−	−58.7	38	1.0×10^7	−39.9	−18.8
Ar27	3−	−62.5	39	6.0×10^7	−44.4	−18.1
SuARAc	3−	−62.7	38	3.2×10^7	−42.8	−19.9

DOI: 10.1021/jacs.5b11497
J. Am. Chem. Soc. 2016, 138, 1280−1293

Scheme 3. Electrostatic Potential at the Molecular Surface for the Dye Molecules: Each Top View (left) and Front View (right)

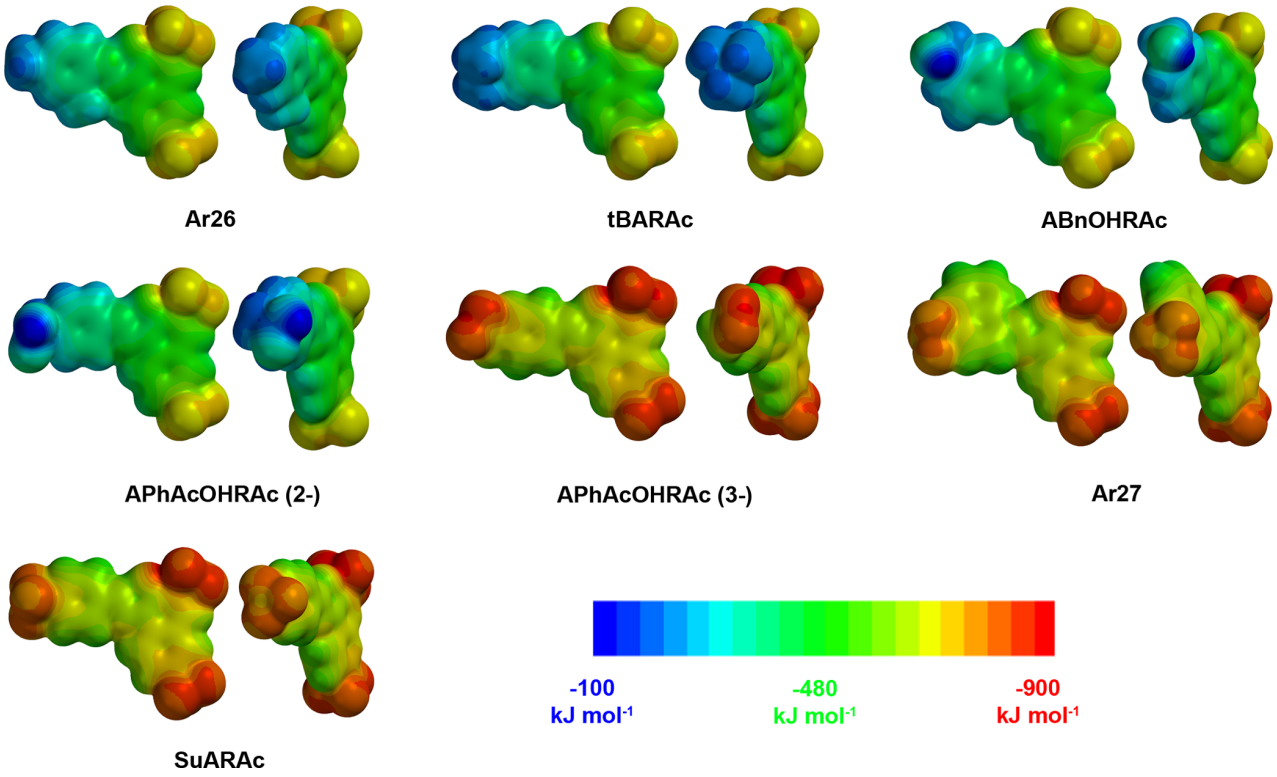

This means that the structural transition between isotropic and anisotropic nanoparticles is continuous and no steps occur.

If then the interaction with G8 is taken into account, no structural transition is observed and only anisotropic structures are formed. This may be understood considering that G8 dendrimer is larger, more dense, and less flexible than G4; therefore, the possibility for the dye to direct the stacking and exhibit varying twist angles is more limited as compared to the interaction with G4 dendrimer.

3. Molecular Building Block Parameters. The strong relationship of dye−dye interaction strength, dye twist angle, and nanoscale structure represents new insight into the concept of electrostatic self-assembly. It is highly desirable, yet challenging, to understand it more deeply. Evidently, thermodynamics encodes the nanoscale supramolecular structure, while the molecular structure of the building blocks encodes thermodynamics. The challenging question remaining at this point is which molecular parameter, property, or combination thereof is the basis.

From a theoretical point of view, the $\pi-\pi$ interaction of aromatic systems has been mainly investigated considering polarized π-systems and electrostatic arguments, for example, the interaction of two quadrupole moments.[58] Only in the last years, the role of the substituents in $\pi-\pi$-interaction has been in focus, for example, in the case of fluorine-substituted benzene derivatives.[59−63] Studying the strengths of the stacking interaction in the case of meta- and para-substituted *N*-benzyl-2-(2-fluorophenyl)pyridinium bromides, the electrostatic interaction of the polarized atoms associated with more polarized substituents was shown to dominate the geometries and energetics of stacked systems.[64]

To elucidate the role of the dye molecular structure on the dye−dye interaction and consequently on the self-assembly, we here consider the dipole moment μ, the polarizability α, and the polar surface area *PSA* of the molecule. The *PSA* is the sum of the areas of the van der Waals surfaces of the polar atoms in a molecule, which has been demonstrated to be crucial to predict drug transport properties.[65,66] The dipole moment has been related to the free energy of the dimerization for merocyanine dyes.[67]

First, the electrostatic potential at the molecular surface needs to be considered. This is the three-dimensional charge distribution of the molecule and can be used to understand its interaction with other molecules. A visual representation of the electrostatic potential is given in Scheme 3. The dye molecules can be divided in two parts: the R-Acid part with a naphthalene core and two sulfonate charges, chemically identical for all of them, and the "left part" with a benzene ring and a substituent (except Ar27 that possesses a naphthalene ring). The differences in electrostatic potential between the dye molecules originate from this "left part": depending on the substituent the aromatic system ($R_{left\text{-}part}-N{=}N-R_{R\text{-}Acid}$) changes the electrostatic potential. In a first approximation the electrostatic potential can be related to the dye−dye interaction strength: the $\Delta H_{dye-dye}$ decreases as the electrostatic potential in the "left part" becomes more negative. In particular, this molecular property can be the reason why the ABnOHRAc twist angle is remarkably lower than the one of the other divalent dyes. The differences in the electrostatic potential are due to the different substituents. If a charged substituent is present, i.e., for the trivalent dyes, the entire aromatic system shows a more negative electrostatic potential being equivalent to an electron-richer system. With a noncharged substituent, both the left and the R-acid part are less negative, i.e., a bit electron poorer. Further, the electrostatic potential of the noncharged substituent is less negative than the rest of the molecule. Fundamentally, the

DOI: 10.1021/jacs.5b11497
J. Am. Chem. Soc. 2016, 138, 1280−1293

potential is defined by the atoms and their electronegativity, thus also describing the bond character. For example, the methyl and *tert*-butyl groups in Ar26 and tBARAC, respectively, incorporate a high amount of hydrogen and therefore show a less negative potential (absence of electron density). In the carboxymethyl group of APhAcOHRAc the oxygen with its high electronegativity withdraws electron density and thus shows a more negative potential. At the same time this induces a less negative potential at the carboxylic acid hydrogen, revealing its protic character.

Further, it is of interest to establish connections between the dipole moment, the polarizability, and the *PSA* with the assembly behavior, all molecular properties based on the electrostatic potential. The parameters for the dyes used herein are reported in Table 6. The trivalent dyes' dipole moment is

Table 6. Electrostatic Parameters for the Different Dyes

dye (charge)	μ (D)	α (Å^3)	PSA (Å^2)	$\Delta H_{dye-dye}$ (kJ mol^{-1})	β (deg)
Ar26 (2−)	24.6	71.0	144.1	−29.0	55
tBARAc (2−)	30.9	73.9	145.6	−25.4	43
ABnOHRAc (2−)	23.3	70.1	165.3	−24.3	38
APhAcOHRAc (2−)	29.2	71.8	180.4	−20.2	38
APhAcOHRAc (3−)	3.8	71.6	175.1	−20.2	38
Ar27 (3−)	10.2	75.4	201.2	−20.0	37
SuARAc (3−)	2.5	71.0	204.9	−8.2	38

lower than that of the divalent ones: the dipole moment of the divalent APhAcOHRAc is μ = 29.2 D, while the trivalent configuration has a μ = 3.8 D. On the other hand, polarizability is very similar for all molecules: the highest polarizabilities are observed for one divalent (tBARAc) and one trivalent dye (Ar27) with α = 73.9 and 75.4 Å^3, respectively. Instead, the *PSA* is different for each dye, and trivalent dyes have higher values compared to the divalent ones.

It is then of interest to observe how the dipole moment and the *PSA*, i.e., the polar surface area of the molecule, vary as a function of the dye−dye interaction strength (i.e., $\Delta H_{dye-dye}$) and if they can be connected to the nanoparticle shape and the dye twist angle. It is evident that the dyes that interact strongly (divalent ones) have the highest dipole moment. The *PSA*, as described in Figure 11a, increases as the $\Delta H_{dye-dye}$ increases, and the dyes with the weaker interaction have larger *PSAs*. Since the PSA results from the area of the polar groups in the molecule and, in particular, takes the subsituents into account more explicitly than the polarizability that refers to the molecule as a whole, the PSA can be well related to the dye self-interaction. Hence, the PSA encodes the mutual dye interaction and, in particular, the dye−dye electrostatic repulsion. The lower the *PSA* the better the dye molecules can interact with each other. This explains the relationship of *PSA* and $\Delta H_{dye-dye}$: $\Delta H_{dye-dye}$ is higher (i.e., strong dye−dye interaction) for particles with low *PSA*. In detail, Ar26 is the dye with the lowest *PSA* and the highest $\Delta H_{dye-dye}$. The trivalent dyes instead show higher *PSA* values, resulting in a less strong interaction. This effect is opposite to electron-withdrawing and -donating substituents influencing the $\pi-\pi$ overlap interaction as such[63,68,69] and electron-rich substituents enhancing $\pi-\pi$ interaction likely through subsituent−π interaction[63,69,70] and in difference to steric subsituent effects influencing $\pi-\pi$ intercation strength, for example, by modifying the planarity of the π-system.[68] For sets

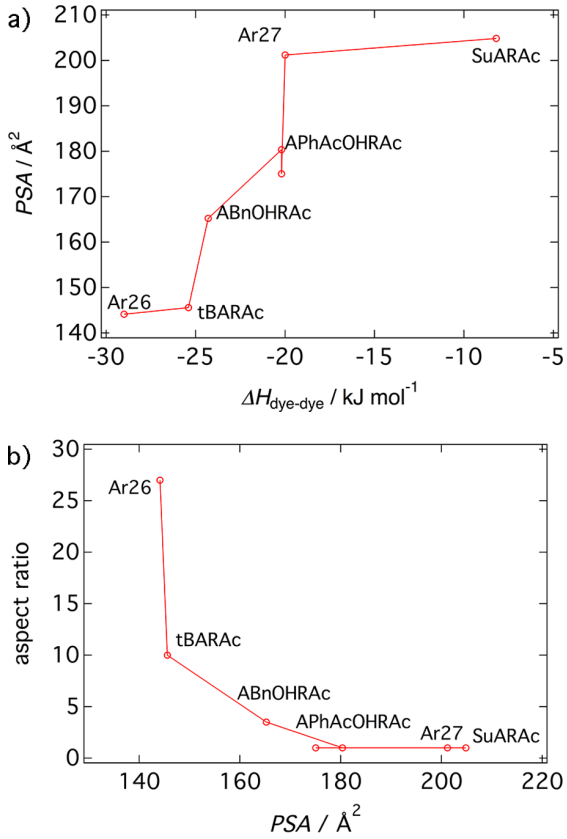

Figure 11. (a) Polar surface area as a function of $\Delta H_{dye-dye}$. (b) Nanoparticle aspect ratio as a function of *PSA*.

of building blocks with (almost) unchanged π-systems and strongly polar (e.g., negatively charged) subsituents, evidently, the substituent−substituent repulsion regulates the dye−dye intercation. Thus, *PSA* and, more in general, the electrostatic repulsion in between the dye molecules can be used to describe the dye−dye interaction and thereby the self-assembly scenario here: anisotropic nanoparticles are formed when the dye−dye electrostatic repulsion is lower and the interaction is strong, while weaker interaction yields isotropic nanoassemblies.

Lastly, the aspect ratio of the nanoparticles has been studied comparing it to the *PSA*. Results are reported in Figure 11b. It is evident that *PSA* controls the nanoparticle aspect ratio.[71] In particular, it decreases as the *PSA* increases. Again, if *PSA* is related to dye−dye interaction strength, it can be concluded that more anisotropic nanoparticles are formed when the dyes self-interact strongly, while weaker dye−dye interaction results in spherical assemblies. This relation of dye−dye interaction strength with supramolecular nanoparticle shape may be applied for other promising self-assembled systems such as in the case of aggregation-induced emission where subsituents control nanostructure and color.[68]

Strikingly, in the complex interplay of forces regulating electrostatic self-assembly, the *PSA* has a key role defining the shape of the nanoparticles. It summarizes the electrostatic repulsion of the interacting molecules and can be directly connected to the strength of the dye−dye interaction. Uncovering the role of the *PSA* as a molecular parameter controlling self-assembly is extremely promising and may be

DOI: 10.1021/jacs.5b11497
J. Am. Chem. Soc. 2016, 138, 1280−1293

used to predict the electrostatic self-assembly of a variety of kinds.

CONCLUSIONS

In conclusion, we elucidated the nanoscale shape control in electrostatic self-assembly based on the role of molecular building blocks. The aspect ratio of the nanoparticles is related to the polyelectrolyte dendrimer generation and to the dye counterion structure. For instance, higher dendrimer generations produce more anisotropic nanoparticles. The dye valency is the key to the basic shape of the assemblies: divalent dyes form anisotropic nanoparticles, while trivalent dyes form spherical ones. Complementary, the loading ratio controls the number of dendrimers per aggregate and the dimensions of the nanoparticles. When the nanoassemblies have an anisotropic shape, it also regulates structural properties as the dimensions and the aspect ratio. On a molecular association level, a relation between the valency of the dye, the stacking angle, and the assembly shape has been established for the interaction with G4 dendrimer. For the trivalent dyes with different number of aromatic rings and different substituents the twist angle is constant. Divalent dyes, instead, stack with larger and varying angles.

Thermodynamic measurements have shown that the interaction of the building blocks is the crucial key to the definition of the nanoparticle shape. Considering the mutual interaction of the dyes, a threshold value of $\Delta H_{dye-dye}$ separating isotropic and anisotropic nanoaggregates has been found. This indicates that a certain value of enthalpy exchange is needed to obtain elongated nanoparticles. In more detail, a strong $\pi-\pi$ interaction leads to anisotropic structures. For the dye−polyelectrolyte interaction, a threshold value was detected as well.

We further examined which molecular parameters encode thermodynamics and thereby particle shape. Modeling molecular properties of the dye molecules has shown that electrostatic properties control the thermodynamics of the dye−dye interaction. In particular, the electrostatic potential at the molecular surface and the polar surface area determine the strength of the dye−dye interaction, which again controls the nanostructure of the polyelectrolyte−dye particles.

From these results, it will be possible to predict nanoparticle shapes knowing only the thermodynamic parameters for the interaction of the chosen molecular building blocks. Thus, a precise molecular design of the dye molecule (i.e., choosing appropriate substituents) will allow tailoring the structure of the nanoparticles. Hence, fundamental steps in developing a box of molecular "building bricks" allowing for a targeted structural design have been made. This may, for example, be of potential in the development of novel self-assembled photocatalysts or smart therapeutic carrier systems.

EXPERIMENTAL SECTION

Chemicals and Synthesis. Poly(amidoamine) (PAMAM) dendrimer of different generations were obtained from Dendritech, Midland, MI, USA, and Sigma-Aldrich, Schnelldorf, Germany. The azo dyes Acid Red 26 (Ar26, C.I. 16150), Acid Red 27 (Ar27, C.I. 16185), and Acid Red 18 (Ar18, C.I. 16255) were obtained from Acros, Geel, Belgium. The azo dyes disodium 4-((4-*tert*-butylphenyl)-diazenyl)-3-hydroxynaphthalene-2,7-disulfonate (tBARAc), disodium 4-(phenyldiazenyl)-3-hydroxynaphthalene-2,7-disulfonate (ARAc), and trisodium 4-((4-sulfophenyl)diazenyl)-3-hydroxynaphthalene-2,7-disulfonate (SuARAc) were already synthesized and characterized in a previous study.[50] Disodium 4-((3-(hydroxymethyl)phenyl)diazenyl)-3-hydroxynaphthalene-2,7-disulfonate (ABnOHRAc), trisodium 4-((4-(carboxymethyl)phenyl)diazenyl)-3-hydroxynaphthalene-2,7-disulfonate (APhAcOHRAc), and disodium 5-((4-sulfophenyl)diazenyl)-8-aminonaphthalene-2-sulfonate (SuACAc) were newly synthesized by azo coupling according to the previously described procedure.[50] The precursors for synthesis were 4-aminophenylacetic acid (APhAcOH, Merck KGaA, Darmstadt, Germany), 3-aminobenzyl alcohol (ABnOH, Merck KGaA, Darmstadt, Germany), sulfanilic acid (SuA, Sigma-Aldrich, Schnelldorf, Germany), disodium 3-hydroxynaphthalene-2,7-disulfonate (R-Acid, RAc, Sigma-Aldrich, Schnelldorf, Germany), and 8-aminonaphthalene-2-sulfonic acid (1,7-Cleve's Acid, CAc, abcr, Karlsruhe, Germany). All azo dyes were purified as described previously[46] according to the literature.[72]

Characterization of Azo Dyes. Yields were calculated on the basis of carbon content from elemental analysis. NMR spectra showed that the product is salt free except for <1 wt % sodium acetate and a small amount of ethanol <1 wt % which could not be removed despite extended drying under high vacuum. The purities given below are corrected for residual amounts of sodium acetate and ethanol, which were determined by NMR. Azo dyes are known to possess multiple molecules of crystal water.[73] Thus, the pure dye contents are below 99%, which does not indicate impurities.

Ar26. ^{1}H NMR (D_2O, 300 MHz, 25 °C), δ [ppm]: 7.62 (s, 1H); 7.52−7.40 (m, 2H); 7.38 (s, 1H); 6.53 (d, J = 8.0 Hz, 1H); 5.95 (d, J = 8.1 Hz, 1H); 5.35 (s, 1H); 1.44 (d, J = 7.5 Hz, 6H). Anal. Calcd for $C_{18}H_{14}N_2Na_2O_7S_2$: C, 45.00. Found: C, 43.16. Dye content: 96%.

Ar27. ^{1}H NMR (D_2O, 300 MHz, 25 °C), δ [ppm]: 8.05 (d, J = 7.8 Hz, 1H); 8.01−7.93 (m, 2H); 7.87 (d, J = 8.4 Hz, 1H); 7.75 (d, J = 8.4 Hz, 1H); 7.68−7.50 (m, 2H); 7.16 (d, J = 7.5 Hz, 1H); 7.11−6.91 (m, 2H). Anal. Calcd for $C_{20}H_{11}N_2Na_3O_{10}S_3$: C, 39.74. Found: C, 37.54. Dye content: 94%.

Ar18. ^{1}H NMR (D_2O, 300 MHz, 25 °C), δ [ppm]: 8.96 (d, J = 8.3 Hz, 1H); 8.76 (s, 1H); 8.55 (d, J = 8.7 Hz, 1H); 8.30 (d, J = 8.3 Hz, 1H); 7.91 (s, 1H); 7.70 (d, J = 8.5 Hz, 1H); 7.50 (t, J = 7.8 Hz, 1H); 7.40−7.24 (m, 2H); 6.33 (d, J = 9.5 Hz, 1H). Anal. Calcd for $C_{20}H_{11}N_2Na_3O_{10}S_3$: C, 39.74. Found: C, 36.59. Dye content: 92%.

ABnOHRAc. ^{1}H NMR (D_2O, 400 MHz, 20 °C), δ [ppm]: 7.95 (d, J = 8.8 Hz, 1H); 7.71 (dd, J = 8.6, 1.8 Hz, 1H); 7.64 (s, 1H); 7.40 (d, J = 1.2 Hz, 1H); 7.00 (t, J = 8.0 Hz, 1H); 6.92 (d, J = 7.6 Hz, 1H); 6.87−6.85 (m, 2H); 4.35 (s, 2H). Anal. Calcd for $C_{17}H_{12}N_2Na_2O_8S_2$: C, 42.33. Found: C, 40.02. Dye content: 94%.

APhAcOHRAc. ^{1}H NMR (D_2O, 400 MHz, 20 °C), δ [ppm]: 8.09 (d, J = 8.8 Hz, 1H); 7.89 (s, 1H); 7.76 (dd, J = 8.6, 1.8 Hz, 1H); 7.64 (d, J = 1.2 Hz, 1H); 7.10 (d, J = 8.4 Hz, 2H); 6.93 (d, J = 8.4 Hz, 2H); 3.32 (s, 2H). Anal. Calcd for $C_{18}H_{11}N_2Na_3O_9S_2$: C, 40.61. Found: C, 37.16. Dye content: 91%.

SuACAc. ^{1}H NMR (D_2O, 300 MHz, 25 °C), δ [ppm]: 8.11 (d, J = 8.9 Hz, 1H); 7.92 (s, 1H); 7.67−7.54 (m, 3H); 7.13 (d, J = 8.2 Hz, 2H); 7.04 (d, J = 8.6 Hz, 1H); 6.24 (d, J = 8.6 Hz, 1H). Anal. Calcd for $C_{16}H_{11}N_3Na_2O_6S_2$: C, 42.58. Found: C, 42.51. Dye content: 99%.

Sample Preparation. Stock solutions were prepared in Milli-Q water (>18.2 MΩ/cm) at pH = 10.5, where the PAMAM dendrimer is fully deprotonated. pH values were adjusted by adding NaOH or HCl standard solutions. All pH values were counter-checked by a freshly calibrated pH electrode. An aqueous solution of the dye at pH = 10.5 was diluted with Milli-Q water adjusted to pH = 10.5. Dendrimer stock solution at the same pH was added. After mixing, HCl was added at once under turbulent mixing to adjust the sample pH to 3.5, inducing assembly formation.

Atomic Force Microscopy. For AFM sample preparation, solutions with the same concentration as for light scattering were spin coated on freshly cleaved mica at 3000 rpm for 40 s (including 10 s acceleration time). AFM images were recorded in noncontact mode on a NanoSurf Easy Scan instrument (Boston, MA). For data processing the open access software Gwyddion was used.

Light Scattering. Measurements were carried out using an ALV 5000 correlator with 320 channels, a CGS 3 goniometer (ALV Langen, Germany), and a HeNe laser with a wavelength of λ = 632.8 nm with 22 mW output power. A range of scattering angles of $30° < \theta < 150°$ was covered. The instrument performs simultaneously static and dynamic

DOI: 10.1021/jacs.5b11497
J. Am. Chem. Soc. 2016, 138, 1280−1293

light scattering measurements. In this study, to extend the SANS spectrum at lower q, the static results have been used. This approach extends the curves in the q range between 6.8×10^{-4} and 2.5×10^{-3} nm^{-1}. The data have been normalized to obtain the absolute intensity and then have been merged with the experimental data obtained by SANS. The standard concentration of PAMAM dendrimers was $c = 0.5$ g L^{-1}.

Small Angle Neutron Scattering. Samples for SANS were prepared in D_2O with a dendrimer concentration of 0.5 and 0.2 g L^{-1} for the samples not stable at the first concentration and transferred into quartz cells with 2 mm path length. Previous results on G4 nanoassemblies have shown no influence of the concentration on nanoparticle shape and a limited one on the dimensions. SANS studies were performed on D11 at the Institut Laue–Langevin, Grenoble, France, and on KWS2 at the Jülich Center for Neutron Scattering at the *Heinz Maier-Leibnitz Zentrum (MLZ)*, Munich, Germany. On D11 two different λ were used: 6 and 13 Å. The first was used for 3 different sample–detector distances: 1.2, 8, and 39 m. The second was used only in the case of big nanoparticles at 39 m. The wavelength spread $(\Delta\lambda/\lambda)$ was 0.09. A total scattering vector range of $0.007\ nm^{-1} < q < 5\ nm^{-1}$ was investigated. At KWS2, a wavelength of 4.55 Å was used with 3 sample–detector distances: 2, 8, and 20 m. For some samples a different combination was used: 2, 4, and 20 m: the 8 m distance was replaced with 4 m to obtain a very similar scattering vector with a higher neutron flux. In this case a total scattering vector of $0.035\ nm^{-1} < q < 5\ nm^{-1}$ was covered. Data were corrected for empty cell scattering, electronic background, and detector uniformity and then converted to absolute scale using secondary standards. Then the scattering of the solvent and the incoherent background was subtracted from the data. The scattering curve $I(q)$ was, where possible, analyzed by Guinier analysis followed by inverse Fourier transformation to obtain the pair distribution function $P(r)$ through the relationship

$$I(q) = 4\pi \int P(r)\frac{\sin(qr)}{qr}\mathrm{d}r \tag{5}$$

On the basis of the first results, structural modeling by standard fitting packages such as SASview was used to obtain the particle shape and dimensions.

For some samples the instrument resolution was taken into account in the fitting process to check its influence on the obtained results.

UV–vis Spectroscopy. Absorption spectra were recorded on a JASCO V-630 spectrometer using plastic cuvettes with 1 cm path length at dye concentrations of $c \approx 2 \times 10^{-5}$ mol L^{-1}. Once obtained, the experimental extinction coefficient has been fitted according to the relation

$$\varepsilon_D = \varepsilon_J \exp\left[-4 \ln 2\frac{(\nu - \nu_J)^2}{\Delta\nu_{1/2,J}^2}\right] + \sum_{i=0}^{1} \varepsilon_i \exp\left[-4 \ln 2\frac{(\nu - \nu_i)^2}{\Delta\nu_{1/2,i}^2}\right] \tag{6}$$

where ε_D is the extinction coefficient of the dimer. This separation can be done because the spectral separation between the H and the J band is greater than the vibronic progression. The first term of the equation refers to the J band with ε_J as extinction coefficient, ν_J as wavenumber, and $\Delta\nu_{1/2,J}$ as half-width of the Gaussian. The second term represents the H band extended to two vibronic transitions. From the fits, two different geometric parameters can be obtained according to the equation

$$\beta = 2 \arctan\sqrt{\frac{f_J}{f_H}} \tag{7}$$

$$R = \sqrt[3]{\frac{2.1410^7 \cos\beta}{\nu_M \Delta\nu_{H,J}}} \tag{8}$$

where f_i is the oscillator strength for the ith band.

Isothermal Titration Calorimetry. ITC measurements were carried out with a MicroCal VP-ITC from Malavern Instrument Ltd., U.K. For the dye dilution experiments, one initial injection of 10 μL to saturate the titration cell wall was followed by 20 injections of 5 μL each. Dilution heats of PAMAM dendrimer were negligible in comparison to dye–dendrimer interaction energies. The time span between subsequent injections was 300 s. All experiments were conducted at 25 °C. For dye–dendrimer experiments 15–50 injections of 5–15 μL each were used. The time span between subsequent injections was 300 s. All experiments were conducted at 25 °C. Formic acid/formiate at pH = 4 was used as buffer system with c(buffer) = 15 mmol. Data analysis for dye–dendrimer experiments was performed using a one-site model as implemented in the MicroCal ITC data analysis software for Origin 7.0. The fit of the integrated heat per injection is performed according to a stepwise disaggregation model as described in ref 50. Errors on the free energy change ΔG are of the order of 2%, on the enthalpy change ΔH are of the order of 5%, while on entropy change ΔS are 15%.

Molecular Modeling. Calculations were carried out using the Spartan'14 software (Wave function Inc., Irvine, CA, USA, 2014). Molecular properties and electrostatic potential surfaces were generated with the density functional B3LYP level of theory using 6-31G* basis set in vacuum. All molecules were optimized for the equilibrium geometry with the maxima and minima in the electrostatic potential surface (0.002 electrons au^{-3} isosurface) determined using a positive point charge in the vacuum as a probe. Here we might add that PSA has been calculated taking into account all the polar atoms in the molecule. This to highlight that we included also S into calculation that was not considered by the default program.

AUTHOR INFORMATION

Corresponding Author

*franziska.groehn@fau.de

Notes

The authors declare no competing financial interest.

ACKNOWLEDGMENTS

Major financial support of the projects involved by the German Science Foundation (DFG), the Interdisciplinary Center for Molecular Materials (ICMM, University Erlangen-Nürnberg) and the Institut Laue Langevin (ILL), Grenoble, France, is gratefully acknowledged. This work benefitted from SasView software, originally developed by the DANSE project under NSF award DMR-0520547. The study is based upon experiments performed at D11 at ILL, Grenoble, France, and at the KWS 2 instrument operated by JCNS at the Heinz Maier-Leibnitz Zentrum (MLZ), Garching, Germany. The authors also gratefully acknowledge the financial support provided by ILL, and by JCS to perform the neutron scattering measurements at ILL and at MLZ.

REFERENCES

(1) Lehn, J. M. *Angew. Chem., Int. Ed. Engl.* **1988**, *27*, 89–112.
(2) Faul, C. F. J.; Antonietti, M. *Adv. Mater.* **2003**, *15*, 673–683.
(3) Pochan, D. J.; Chen, Z. Y.; Cui, H. G.; Hales, K.; Qi, K.; Wooley, K. L. *Science* **2004**, *306*, 94–97.
(4) Kaiser, T. E.; Wang, H.; Stepanenko, V.; Würthner, F. *Angew. Chem., Int. Ed.* **2007**, *46*, 5541–5544.
(5) Elmahdy, M. M.; Dou, X.; Mondeshki, M.; Floudas, G.; Butt, H. J.; Spiess, H. W.; Müllen, K. J. *J. Am. Chem. Soc.* **2008**, *130*, 5311–5319.
(6) Smulders, M. M. J.; Schenning, A. P. H. J.; Meijer, E. W. *J. Am. Chem. Soc.* **2008**, *130*, 606–611.
(7) Willerich, I.; Gröhn, F. *Angew. Chem., Int. Ed.* **2010**, *49*, 8104–8108.
(8) Mauro, M.; Aliprandi, A.; Cebrián Ávila, C.; Wang, D.; Kübel, C.; De Cola, L. *Chem. Commun.* **2014**, *50*, 7269–7272.

DOI: 10.1021/jacs.5b11497
J. Am. Chem. Soc. 2016, 138, 1280–1293

(9) Park, J. I.; Nguyen, T. D.; de Queirós Silveira, G.; Bahng, J. H.; Srivastava, S.; Zhao, G.; Sun, K.; Zhang, P.; Glotzer, S. C.; Kotov, N. A. *Nat. Commun.* **2014**, *5*, 3593−3598.
(10) Sijbesma, R. P.; Beijer, F. H.; Brunsveld, L.; Folmer, B. J. B.; Ky Hirschberg, J. H. K.; Lange, R. F. M.; Lowe, J. K. L.; Meijer, E. W. *Science* **1997**, *278*, 1601−1604.
(11) Beck, J. B.; Rowan, S. J. *J. Am. Chem. Soc.* **2003**, *125*, 13922−13923.
(12) Northrop, B. H.; Zheng, Y.-R.; Chi, K.-W.; Stang, P. *Acc. Chem. Res.* **2009**, *42*, 1554−1563.
(13) Gröger, G.; Meyer-Zaika, W.; Böttcher, C.; Gröhn, F.; Ruthard, C.; Schmuck, C. *J. Am. Chem. Soc.* **2011**, *133*, 8961−8971.
(14) Grimm, F.; Ulm, N.; Gröhn, F.; Düring, J.; Hirsch. *Chem. - Eur. J.* **2011**, *17*, 9478−9488.
(15) Faul, C. F. J.; Antonietti, M. *Chem. - Eur. J.* **2002**, *8*, 2764−2768.
(16) Zhang, Y.; Guan, Y.; Yang, S.; Xu, J.; Han, C. C. *Adv. Mater.* **2003**, *15*, 832−834.
(17) Xu, Y.; Bolisetty, S.; Ballauff, M.; Müller, A. H. E. *J. Am. Chem. Soc.* **2009**, *131*, 1640−1641.
(18) Yan, M.; Fresnais, J.; Berret, J.-F. *Soft Matter* **2010**, *6*, 1997−2005.
(19) Zhou, S.; Burger, C.; Chu, B.; Sawamura, M.; Nagahama, N.; Toganoh, M.; Hackler, U. E.; Isobe, H.; Nakamura, E. *Science* **2001**, *291*, 1944−1947.
(20) Discher, D. E.; Eisenberg, A. *Science* **2002**, *297*, 967−973.
(21) Nikolic, M. S.; Olsson, C.; Salcher, A.; Kornowski, A.; Rank, A.; Schubert, R.; Frömsdorf, A.; Weller, H.; Förster, S. *Angew. Chem., Int. Ed.* **2009**, *48*, 2752−2754.
(22) DeMuth, P. C.; Su, X.; Samuel, R. E.; Hammond, P. T.; Irvine, D. *Adv. Mater.* **2010**, *22*, 4851−4856.
(23) Gröhn, F.; Klein, K.; Koynov, K. *Macromol. Rapid Commun.* **2010**, *31*, 75−80.
(24) Guan, Y.; Antonietti, M.; Faul, C. F. J. *Langmuir* **2002**, *18*, 5939−5945.
(25) Glotzer, S. C. *Science* **2004**, *306*, 419−420.
(26) Glotzer, S. C.; Solomon, M. *Nat. Mater.* **2007**, *6*, 557−562.
(27) Palmer, L. C.; Velichko, Y. S.; Olvera de la Cruz, M.; Stupp, S. *Philos. Trans. R. Soc., A* **2007**, *365*, 1417−1433.
(28) Peterca, M.; Imam, M. R.; Leowanawat, P.; Rosen, B. M.; Wilson, D. A.; Wilson, C. J.; Zeng, X.; Ungar, G.; Heiney, P. A.; Percec, V. *J. Am. Chem. Soc.* **2010**, *132*, 11288−11305.
(29) Percec, V.; Sun, H.-J.; Leowanawat, P.; Peterca, M.; Graf, R.; Spiess, H. W.; Zeng, Z.; Ungar, G.; Heiney, P. A. *J. Am. Chem. Soc.* **2013**, *135*, 4129−4148.
(30) Douglas, J. F.; Dudowicz, J.; Freed, K. F. *Phys. Rev. Lett.* **2009**, *103*, 135701.
(31) Zhang, H.; Wang, D. *Angew. Chem.* **2008**, *120*, 4048−4051.
(32) Mahalik, J. P.; Muthukumar, M. *J. Chem. Phys.* **2012**, *136*, 135101.
(33) Camerel, F.; Faul, C. F. J. *Chem. Commun.* **2003**, 1958−1959.
(34) Gröhn, F.; Klein, K.; Brand, S. *Chem. - Eur. J.* **2008**, *14*, 6866−6869.
(35) Willerich, I.; Gröhn, F. *Chem. - Eur. J.* **2008**, *14*, 9112−9116.
(36) Li, Y.; Yildiz, U. H.; Müllen, K.; Gröhn, F. *Biomacromolecules* **2009**, *10*, 530−540.
(37) Ruthard, C.; Maskos, M.; Kolb, U.; Gröhn, F. *Macromolecules* **2009**, *42*, 830−840.
(38) Gröhn, F. *Soft Matter* **2010**, *6*, 4296−4302.
(39) Willerich, I.; Ritter, H.; Gröhn, F. *J. Phys. Chem. B* **2009**, *113*, 3339−3354.
(40) Willerich, I.; Li, Y.; Gröhn, F. *J. Phys. Chem. B* **2010**, *114*, 15466−15476.
(41) Willerich, I.; Gröhn, F. *Macromolecules* **2011**, *44*, 4452.
(42) Ruthard, C.; Schmidt, M.; Gröhn, F. *Macromol. Rapid Commun.* **2011**, *32*, 706−711.
(43) Düring, J.; Hölzer, A.; Kolb, U.; Branscheid, R.; Gröhn, F. *Angew. Chem., Int. Ed.* **2013**, *52*, 8742−8745.
(44) Frühbeißer, S.; Gröhn, F. *J. Am. Chem. Soc.* **2012**, *134*, 14267−14270.
(45) Willerich, I.; Schindler, T.; Ritter, H.; Gröhn, F. *J. Phys. Chem. B* **2011**, *115*, 9710−9719.
(46) Willerich, I.; Gröhn, F. *J. Am. Chem. Soc.* **2011**, *133*, 20341−20356.
(47) Jansen, J. F. G. A.; de Brabander-van den Berg, E. M. M.; Meijer, E. *Science* **1994**, *266*, 1226−1229.
(48) Richter-Egger, D. L.; Landry, J. C.; Tesfai, A.; Tucker, S. A. *J. Phys. Chem. A* **2001**, *105*, 6826−6833.
(49) Neumann, B.; Huber, K.; Pollmann, P. *Phys. Chem. Chem. Phys.* **2000**, *2*, 3687−3695.
(50) McRae, E. G. *Aust. J. Chem.* **1961**, *14*, 329.
(51) McRae, E. G. *Aust. J. Chem.* **1961**, *14*, 344.
(52) McRae, E. G. *Aust. J. Chem.* **1961**, *14*, 354.
(53) Kasha, M.; Rawls, H. R.; Ashraf El-Bayoumi. *Pure Appl. Chem.* **1965**, *11*, 371.
(54) Monahan, A. R.; Blossey, D. F. *J. Phys. Chem.* **1970**, *74*, 4014.
(55) The resulting interdye distances, as compared to X-ray data from the literature,[58] seems to be too large as values between 0.3 and 0.4 nm were found in the literature. This difference is due to the approximation done using the exciton theory where the interacting dye molecules are described as point dipole.
(56) It must be said that this approach is formally incorrect: describing a cooperative binding with a one-site model is simplifying the process. However this approach is reasonable to obtain reliable results.[61]
(57) Bhadra, K.; Maiti, M.; Kumar, G. S. *Biochim. Biophys. Acta, Gen. Subj.* **2008**, *1780*, 1054−1061.
(58) Hunter, C. A.; Sanders, J. K. M. *J. Am. Chem. Soc.* **1990**, *112*, 5525−5534.
(59) Sinnokrot, M. O.; Sherrill, C. D. *J. Phys. Chem. A* **2003**, *107*, 8377−8379.
(60) Wheeler, S.; Houk, K. *J. Am. Chem. Soc.* **2008**, *130*, 10854−10855.
(61) Martinez, C. R.; Iverson, B. L. *Chem. Sci.* **2012**, *3*, 2191−2201.
(62) Wheeler, S. *J. Am. Chem. Soc.* **2011**, *133*, 10262.
(63) Cockroft, S. L.; Perkins, J.; Zonta, C.; Adams, H.; Spey, S. E.; Low, C. M. R.; Vinter, J. G.; Lawson, K. R.; Urch, C. J.; Hunter, C. A. *Org. Biomol. Chem.* **2007**, *5*, 1062−1080.
(64) Rashkin, M. J.; Waters, M. L. *J. Am. Chem. Soc.* **2002**, *124*, 1860−1861.
(65) Kelder, J.; Grootenhuis, P. D.; Bayada, D. M.; Delbressine, L. P.; Ploemen, J. P. *Pharm. Res.* **1999**, *16*, 1514−9.
(66) Ertl, P.; Rohde, B.; Selzer, P. *J. Med. Chem.* **2000**, *43*, 3714−3717.
(67) Wüthner, F.; Yao, S.; Debraedemaecker, T.; Wortmann, R. *J. Am. Chem. Soc.* **2002**, *124*, 9431−9447.
(68) Niu, C.; Zhao, L.; Fang, T.; Deng, X.; Ma, H.; Zhang, J.; Na, N.; Han, J.; Ouyang, J. *Langmuir* **2014**, *30*, 2351−2359.
(69) Chen, Z.; Lohr, A.; Saha-Möller, C. R.; Würthner, F. *Chem. Soc. Rev.* **2009**, *38*, 564−584.
(70) Su, W.; Zhang, Z.; Zhao, C.; Li, X.; Jiang, J. *ChemPhysChem* **2007**, *8*, 1857−1862.
(71) To calculate the aspect ratio of the nanoassemblies formed by ABnOHRAc and G4 dendrimer, the Kuhn length has been used instead of the total length. If the total length is used the aspect ratio is large and cannot be related to the *PSA* while the aspect ratio of the subunits does.
(72) Robinson, C.; Mills, H. A. T. *Proc. R. Soc. London, Ser. A* **1931**, *131*, 576−595.
(73) Kratky, O.; Pilz, I.; Ledwinka, H. *Monatsh. Chem.* **1967**, *98*, 227−230.

DOI: 10.1021/jacs.5b11497
J. Am. Chem. Soc. 2016, 138, 1280−1293

4.2 Structure Tuning of Electrostatically Self-Assembled Nanoparticles through pH

THE JOURNAL OF PHYSICAL CHEMISTRY B

Article

pubs.acs.org/JPCB

Structure Tuning of Electrostatically Self-Assembled Nanoparticles through pH

Giacomo Mariani,[†,‡] Ralf Schweins,[‡] and Franziska Gröhn*[,†]

[†]Department of Chemistry and Pharmacy and Interdisciplinary Center for Molecular Materials (ICMM), Friedrich-Alexander-Universität Erlangen-Nürnberg, Egerlandstraße 3, D-91058 Erlangen, Germany

[‡]Institut Laue-Langevin, DS/LSS, 71 Avenue des Martyrs, F-38000 Grenoble, France

ABSTRACT: pH can be used to tune the self-assembly of cationic polyelectrolyte dendrimers and oppositely charged dyes and to produce particles with a desired shape and size in aqueous solution. We present fundamental insight into the effect of pH on electrostatic self-assembly of poly(amidoamine) dendrimers of generation 4 and di- and trivalent anionic organic dyes. The solution pH is used as a key to turn on the interaction and to control the association by regulating the macroion charge. Stable and well-defined nanoparticles are formed in solution, being more stable at low pH where the dendrimer protonation is complete. Nanoparticle stability was correlated with ζ-potential measurements. We prove that the assemblies are electrostatically stabilized and elucidate the importance of the surface charge density. pH was also used as a key to nanoparticle dimension and shape. For example, smaller particles form at a lower pH. The nanostructures have been characterized using dynamic light scattering and small-angle neutron scattering. A "phase diagram" has been developed for each dye, showing the assembly size, shape, and instability regions dependent on the pH. Overall, a pH-responsive nanoparticle shape is a key step toward the design of novel smart therapeutic carrier systems.

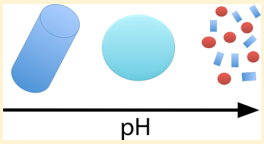

INTRODUCTION

Self-assembly is an efficient strategy to produce complex supramolecular structures that can respond to external triggers and are of interest in nanotechnology or as carrier systems.[1−15] Great potential lies in systems with tunable shape and dimension as this may allow a rational nanostructure design. In addition, particles with triggerable size and shape are of special interest for drug delivery. For example, the circulation lifetime of intravenously administered nanoparticles has been demonstrated to depend on their dimension and shape.[16−18] Among others, pH variation is commonly used as a trigger for size and shape.[19−28] In this context, we have recently introduced the concept of electrostatic self-assembly for the formation of responsive supramolecular nanoscale assemblies.[29−33] The process is based on the interconnection of dendrimeric macroions and oppositely charged multivalent azo dyes under secondary interaction effects such as $\pi-\pi$ stacking or geometric factors and leads to the formation of nanoparticles with sizes up to more than 100 nm.[34,35] The process relies on a general combination of interactions rather than on specific binding motifs. Choosing appropriate building blocks, switchable nanoparticles that respond to light and pH have been built.[33,36,37] An assembly with on−off switchability through pH is realized via protonation and deprotonation of the polyelectrolyte, that is, charging and uncharging the dendrimer macroions. Recently, we have investigated the role of the interactions of the molecular building blocks in these systems.[38] Thermodynamics revealed a quantitative relationship of the size of the self-assembled nanoparticles with the free energy of the dye−dendrimer association. In more detail, the free energy of the assembly formation was shown to be composed of an electrostatic dendrimer−dye interaction contribution and a secondary mutual $\pi-\pi$ interaction contribution of the dye molecules. A simple model has been developed to connect the free energy with the aggregation number.[38]

To gain further insight into the interplay of the different interaction effects in the self-assembly—electrostatics, $\pi-\pi$ stacking and geometric factors—we herein investigate nanoparticle stability and structure as a function of solution pH. We explore electrostatically self-assembled nanoparticles formed by poly(amidoamine) (PAMAM) dendrimers and various oppositely charged azo dyes (Scheme 1). As a polyelectrolyte, a fourth-generation dendrimer is chosen because it has been extensively studied, and the protonation state at different pH levels is well-known. Due to the molecular dendrimer structure, changing the pH of the solution permits modification of the number of protonated amine groups affecting the number of available binding sites, that is, the electrostatic interaction strength, and their position.

At pH 10.5, all amine groups are deprotonated and the molecule is neutral, at pH 7.0, all primary amines (on the surface of the molecule) are protonated, while at pH 3.5, both primary and tertiary amines (in the inner region) are protonated and the molecule is fully charged. This behavior permits investigation of the role of electrostatic interaction in self-assembly by controlling a parameter as simple as the pH of the solution. The self-assembly process is schematically depicted in Scheme 2. The effect of pH on the stability and structure will be analyzed for different dyes and different dye/dendrimer ratios. This allows for changing the valency of the dye and the molecular structure, two parameters important for

Received: November 9, 2015
Published: December 3, 2015

DOI: 10.1021/acs.jpcb.5b10966
J. Phys. Chem. B 2016, 120, 1380−1389

Scheme 1. Azo Dyes and PAMAM Molecule Used in the Present Study

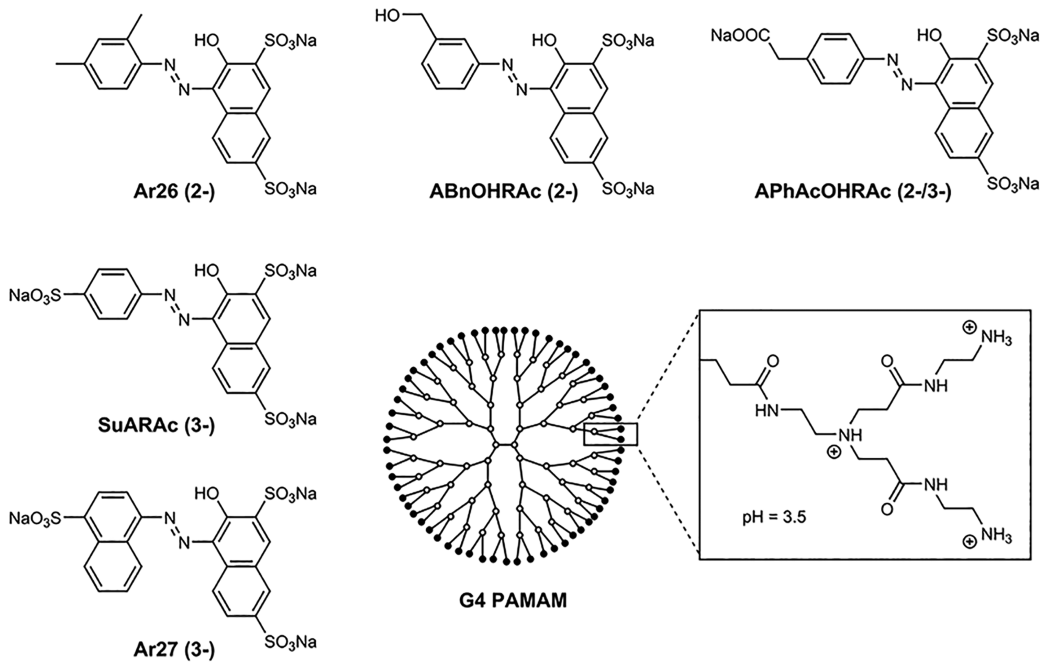

Scheme 2. Switching the Electrostatic Self-Assembly by pH[a]

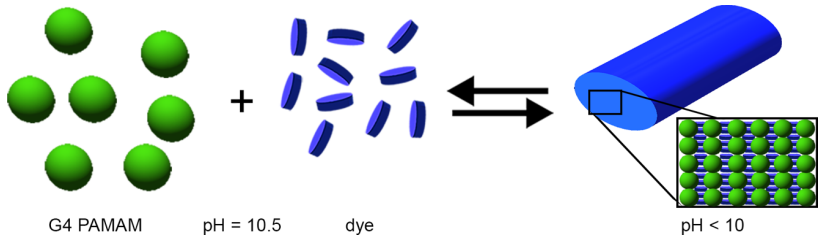

[a]At pH 10.5, the dendrimers are uncharged, and no interaction between the building blocks occurs; at pH < 10, the dendrimers start to be protonated, and the building blocks form well-defined nanoparticles.

controlling the self-assembly. The stability will be related to ζ-potential measurements; dynamic light scattering (DLS) and small-angle neutron scattering (SANS) will be used to characterize the dimension and shape of the nanoparticles. The presence of instability regions in pH will be highlighted, resulting in the definition of a "phase diagram" for every dye. By combining stability and structural results, a first important understanding of the role of electrostatic interaction in the self-assembly is achieved. At the same time, knowing both the shape and dimension as a function of pH may in the future allow for the tailoring of particles with a desired shape and size, representing a key step toward applications like drug delivery.

EXPERIMENTAL SECTION

Chemicals. The PAMAM dendrimer of fourth generation was obtained from Dendritech, Midland, MI, U.S.A. and Sigma-Aldrich, Germany. The azo dyes Acid Red 26 (Ar26, C.I. 16150) and Acid Red 27 (Ar27, C.I. 16185) were obtained from Acros, Belgium. Disodium 4-((3-(hydroxymethyl)-phenyl)diazenyl)-3-hydroxynaphthalene-2,7-disulfonate (ABnOHRAc) and trisodium 4-((4-(carboxymethyl)phenyl)-diazenyl)-3-hydroxynaphthalene-2,7-disulfonate (APhAcOHRAc) were synthesized by azo-coupling according to the previously described procedure.[33] The precursors for synthesis were 4-aminophenylacetic acid (APhAcOH, Merck KGaA, Germany), 3-aminobenzyl alcohol (ABnOH, Merck KGaA, Germany), sulfanilic acid (SuA, Sigma-Aldrich, Germany), disodium 3-hydroxynaphthalene-2,7-disulfonate (R-acid, RAc, Sigma-Aldrich, Germany), and 8-aminonaphthalene-2-sulfonic acid (1,7-Cleve's acid, CAc, abcr, Germany). All azo dyes were purified according to the literature.[39]

Characterization of the Azo Dyes. Yields were calculated on the basis of carbon content from elemental analysis. NMR spectra showed that the product is salt-free except for <1 wt % sodium acetate and a small amount of ethanol, <1 wt %, which could not be removed despite extended drying under high vacuum. The purities given below are corrected for residual amounts of sodium acetate and ethanol, which were determined by NMR. Azo dyes are known to possess multiple molecules of crystal water. Thus, the pure dye contents are below 99%, which does not indicate impurities.

Ar26. ^{1}H NMR (D_2O, 300 MHz, 25 °C), δ [ppm]: 7.62 (s, 1H); 7.52–7.40 (m, 2H); 7.38 (s, 1H); 6.53 (d, J = 8.0 Hz, 1H); 5.95 (d, J = 8.1 Hz, 1H); 5.35 (s, 1H); 1.44 (d, J = 7.5 Hz, 6H). Anal. Calcd for $C_{18}H_{14}N_2Na_2O_7S_2$: C, 45.00; Found: C, 43.16; dye content: 96%.

DOI: 10.1021/acs.jpcb.5b10966
J. Phys. Chem. B 2016, 120, 1380–1389

Ar27. (D_2O, 300 MHz, 25 °C), δ [ppm]: 8.05 (d, J = 7.8 Hz, 1H); 8.01−7.93 (m, 2H); 7.87 (d, J = 8.4 Hz, 1H); 7.75 (d, J = 8.4 Hz, 1H); 7.68−7.50 (m, 2H); 7.16 (d, J = 7.5 Hz, 1H); 7.11−6.91 (m, 2H). Anal. Calcd for $C_{20}H_{11}N_2Na_3O_{10}S_3$: C, 39.74; Found: C, 37.54; dye content: 94%.

ABnOHRAc. ^{1}H NMR (D_2O, 400 MHz, 20 °C), δ [ppm]: 7.95 (d, J = 8.8 Hz, 1H); 7.71 (dd, J = 8.6, 1.8 Hz, 1H); 7.64 (s, 1H); 7.40 (d, J = 1.2 Hz, 1H); 7.00 (t, J = 8.0 Hz, 1H); 6.92 (d, J = 7.6 Hz, 1H); 6.87−6.85 (m, 2H); 4.35 (s, 2H). Anal. Calcd for $C_{17}H_{12}N_2Na_2O_8S_2$: C, 42.33; Found: C, 40.02; dye content: 94%.

APhAcOHRAc. ^{1}H NMR (D_2O, 400 MHz, 20 °C), δ [ppm]: 8.09 (d, J = 8.8 Hz, 1H); 7.89 (s, 1H); 7.76 (dd, J = 8.6, 1.8 Hz, 1H); 7.64 (d, J = 1.2 Hz, 1H); 7.10 (d, J = 8.4 Hz, 2H); 6.93 (d, J = 8.4 Hz, 2H); 3.32 (s, 2H). Anal. Calcd for $C_{18}H_{11}N_2Na_3O_9S_2$: C, 40.61; Found: C, 37.16; dye content: 91%.

Sample Preparation. Stock solutions were prepared in D_2O at the desired pH where the PAMAM dendrimer is fully deprotonated (pH = 10.5). pH values were adjusted by adding NaOH or HCl standard solutions. All pH values were counterchecked by a freshly calibrated pH electrode. An aqueous solution of the dye at pH = 10.5 was diluted with D_2O adjusted to pH = 10.5. A dendrimer stock solution at the same pH was added. After mixing, the appropriate amount of HCl was added at once under turbulent mixing to adjust the pH, inducing assembly formation.

ζ-Potential. ζ-Potential measurements were carried out on a Zetasizer Nano ZS analyzer with an integrated 4 mW HeNe laser, k 1/4 633 nm (Malvern Instruments Ltd., U.K.). Samples with concentrations between 9.5×10^{-7} and 1.6×10^{-7} mol/kg were prepared. The electrophoretic mobility was measured using the laser Doppler anemometry technique after applying an electric field across the sample solution. The ζ-potential was calculated from the electrophoretic mobility using the Smoluchowski equation.[40] All measurements were carried out at room temperature using folded capillary cells (DTS 1060) in five replicate measurements.

Light Scattering. Measurements were carried out on an ALV CGS 3 goniometer with an ALV 5000 correlator (ALV Germany) equipped with a HeNe laser with a wavelength of λ = 632.8 nm and 20 mW output power. Measurements covered an angular range of $30 \le \theta \le 150°$. Data analysis was carried out by converting the measured intensity autocorrelation function into the electric field autocorrelation function using the Siegert relation. The electric field autocorrelation functions were further analyzed by regularized inverse LaPlace transformation using the program CONTIN by S. Provencher to obtain the distribution of relaxation times. From this, the apparent diffusion coefficient was calculated using the relation $D_{app} = q^{-2} \cdot \tau^{-1}$. To determine the hydrodynamic radius R_H, the apparent diffusion coefficient D_{app} was extrapolated to zero scattering angle and then converted into R_H through the Stokes−Einstein relationship. Static light scattering (SLS) measurements were performed with the same instrument to combine the results with the SANS curves to extend the q-range for the larger nanoparticles. Measured intensities were corrected for scattering volume with a toluene standard, and the solvent intensity was subtracted from the sample intensity prior to further analysis.

Small-Angle Neutron Scattering. Samples for SANS were prepared in D_2O with a dendrimer concentration of 3.5×10^{-5} mol/kg and transferred into quartz cells with a 2 mm path length. SANS studies were performed on D11 at the Institut Laue-Langevin, Grenoble, France and on NGB-30m at the NIST center for neutron scattering, MD, U.S.A. On D11, a wavelength of 6 Å was used for three different sample−detector distances, 1.2, 8, and 39 m. The wavelength spread ($\Delta\lambda/\lambda$) was 0.09. A total scattering vector range of $0.02 < q < 5$ nm^{-1} was investigated. For large nanoparticles, a second wavelength (13 Å) was used at 39 m. This permits investigation of a total scattering vector of $0.007 < q < 5$ nm^{-1}. At the NIST center for neutron scattering, a wavelength of 6 Å was used with three sample−detector distances, 1, 4, and 13 m, covering a total scattering vector range of $0.04 < q < 5$ nm^{-1}. For a selected number of samples, a wavelength of 8.4 Å at 13 m using a lens configuration was used to measure lower q; in this case, a total scattering vector of $0.02 < q < 5$ nm^{-1} was covered. Data were corrected for empty cell scattering and electronic background and detector uniformity and then converted to absolute scale using secondary standards. Then, the scattering of the solvent and the incoherent background were subtracted from the data. The scattering curve $I(q)$ was first analyzed by Guinier analysis, where possible, and by inverse Fourier transformation to obtain the pair distribution function $P(r)$ through the relationship $I(q) = 4\pi\int P(r)[\sin(qr)/qr]\,dr$. On the basis of the first results, structural modeling by standard fitting packages such as SASview was used to obtain the particles' shape and dimensions. The SANS intensity can be described as $I(q) = \phi V_{NP}(\Delta\rho_{SLD})^2 P(q)$, where ϕ is the volume fraction, V_{NP} the nanoparticle volume, $\Delta\rho_{SLD}$ the difference in scattering length density between the nanoparticle and the solvent and $P(q)$ the nanoparticle form factor describing the nanoparticle shape. The form factor is the square of the normalized total scattering amplitude $F(q)$ caused by intramolecular interfernces $P(q) = F(q)^2$. For example, for a sphere with radius r, the scattering amplitude $F(q)$ is[41,42]

$$F(q) = 3\frac{\sin qr - qr\cos qr}{(qr)^3} \tag{1}$$

In the case of a core−shell sphere, the intensity becomes[41,42]

$$I(q) = \frac{\phi}{V_{NP}}\left[3V_c(\rho_c - \rho_s)\frac{\sin qr_c - qr_c\cos qr_c}{(qr_c)^3} + 3V_s(\rho_s - \rho_{solv})\frac{\sin qr_s - qr_s\cos qr_s}{(qr_s)^3}\right]^2 \tag{2}$$

where V_s is the volume of the outer shell, V_c the volume of the core, r_s the radius of the shell, r_c the radius of the core, ρ_s the scattering length density of the shell, ρ_c the scattering length density of the core, and ρ_{solv} the scattering length density of the solvent. For a cylinder with length L and radius r, $F(q)$ is[43]

$$F(q) = \int_0^1 \frac{4J_1(qr\sqrt{1-x^2})\sin\frac{qLx}{2}}{q^2 r\sqrt{1-x^2}Lx}\,dx \tag{3}$$

where J_1 is the first-order Bessel function. In the case of cylinders with an elliptical cross section, the scattering intensity can be described as[47]

$$I(q) = \frac{\phi}{V_{NP}}\int d\psi\int d\phi\int p(\theta,\phi,\psi)F^2(\mathbf{q},\alpha,\psi)\sin\theta\,d\theta \tag{4}$$

with the functions $F(q,\alpha,\psi) = 2[J_1(a)/a][\sin b/b]$, $a = q\sin\alpha(r_{major}^2\sin^2\psi + r_{minor}^2\cos^2\psi)^{1/2}$, and $b = q(L/2)\cos\alpha$.

DOI: 10.1021/acs.jpcb.5b10966
J. Phys. Chem. B 2016, 120, 1380−1389

For flexible cylinders with an elliptical cross section, the model used is a corrected version of the one described by Pedersen et al.[44,45] For all of the systems, the polydispersity has been used as a fixed parameter in the fit. Good agreement with the experimental results has been obtained using 0.3 for all of the models. For some samples, the instrument resolution has been taken in account in the fitting process to check its influence on the obtained results.

RESULTS AND DISCUSSION

We present the investigation of self-assembled nanoparticles composed of PAMAM dendrimers of generation 4 and oppositely charged di- or trivalent azo dyes. The complete set of dyes used for this study is presented in Scheme 1. Due to the molecular structure of the dendrimers, changing the pH of the solution causes a change of the degree of protonation of the amine groups. Hence, the samples have been prepared at different pHs, varying from pH 10.0 to pH 3.5 to investigate the full range of protonation states. Different dyes have been analyzed: three divalent (Ar26, ABnOHRAc, and APhAcOHRAc) and two trivalent (Ar27 and SuARAc) dyes. The loading ratio is defined as the molar ratio of dye sulfonate groups to dendrimer primary amines $l = c(SO_3^-)/c(NH_2)$; together with the pH-dependent dendrimer protonation, it gives the charge ratio $c_r = c(SO_3^-)/[c(NH_2)\cdot\alpha]$, where α is the degree of protonation of the dendrimer. Thus, changing the pH of the solution does not affect the loading ratio, while it significantly affects the charge ratio.

In the present study, we show the effect of the dendrimer protonation state on the nanoassembly stability and structure. The focus is the definition of a phase diagram for dendrimer assemblies with every dye reporting the behavior of the system as a function of pH and charge ratio. The stability will be discussed in connection with a systematic ζ-potential analysis. The structural characterization is based on DLS and SANS measurements to investigate the size and the shape of the aggregates, respectively. Uncovering the relationship of nanoparticle stabilization and structure is of major importance to fundamentally understand the electrostatic self-assembly process. This can lead to nanoassembly structure control through an external trigger such as pH.

ζ-Potential and Stability Investigation. To elucidate the type of nanoparticle stabilization, ζ-potential measurements have been performed. This technique measures the difference of electrostatic potential between the solvent and the layer of fluid attached to the dispersed nanoparticles. For these experiments, samples with dendrimer concentrations of 9.5×10^{-7} and 1.6×10^{-7} mol/kg have been prepared. Results for the different dyes are displayed in Figure 1. Despite some differences in ζ-potential, there is a common behavior of all of the dyes; the ζ-potential increases as the pH becomes more acidic. This means that in all cases, the charge of the nanoparticles is higher when the dendrimers are completely protonated. This shows that the nanoparticles are electrostatically stabilized and suggests that at low pH, the nanoparticles may be more stable due to a higher charge.

An interesting aspect of the results is that the data show a linear dependence and that there is no discontinuity at around pH 7.0 when the internal amine groups (tertiary amines) start to be protonated and become available for binding. This means that the effective charge and thereby the stability of the nanoaggregates only depend on the number of charged amine groups available for binding and not on their type.

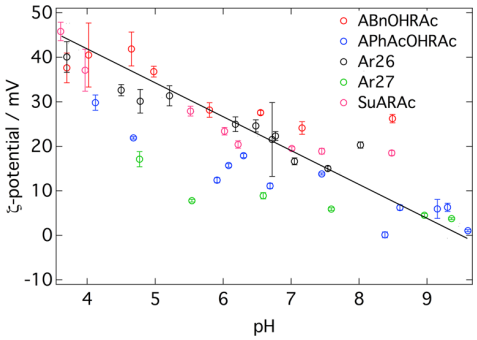

Figure 1. ζ-Potential for different dye–dendrimer systems. The line is to guide the eyes.

No discontinuity is observed for APhAcOHRAc, which is of great interest because this dye possesses a –COOH group with a pK_a of 4.3; thus, it is divalent until pH 4.3, and it starts to exist in trivalent configuration below this value (20% at pH 3.5). Therefore, a discontinuity may be expected around this pH. The absence proves that the stabilization process does not depend on the dye valency but, again, on the total assembly charge only.

Furthermore, the SuARAc–dendrimer sample shows the highest ζ-potential at low pH, while the system with the lowest ζ-potential value is the Ar27–G4 dendrimer. These two dyes have the same valency, showing again that valency has no major effect on the stabilization as such. The difference in ζ-potential may be related to differences in molecular structures; Ar27 is the only dye of the set with four aromatic rings. This additional ring likely crucially affects the mutual dye–dye interaction controlling at the same time the dye–dendrimer interaction and the stabilization. The ζ-potential for the other dyes lies between the ones of Ar27 and SuARAc.

For a better understanding, the ζ-potential has been measured not only changing the charge ratio but also varying the loading ratio while keeping pH = 3.5 constant for the model system of Ar26 and the G4 dendrimer. Results are reported in Table 1. It is evident that the behavior in the two cases is completely different. As already shown in Figure 1, the ζ-potential increases with decreasing charge ratio, while it is constant when the loading ratio is varied. This means that the stabilization of the nanoparticles depends on the amount of dendrimer charges available, that is, the protonation degree, for binding and not on the molecular ratio of the building blocks.

Table 1. ζ-Potential Results at Different Loading and Charge Ratios for Ar26 and the G4 Dendrimer

Ar26–G4 l	charge ratio c_r	pH	ζ-potential (mV)
1.0	1.0	3.5	42 ± 2
1.2	1.2	3.5	39 ± 2
1.5	1.5	3.5	39 ± 2
1.6	1.6	3.5	42 ± 2
1.8	1.8	3.5	42 ± 2

At this point, stability over time must be taken into account in addition. Despite the linear dependence of the ζ-potential, aging affects samples at different pHs differently. This has been followed by observation of turbidity and precipitation of the sample solutions by eye. The case of the Ar26–G4 sample at loading ratio l = 1.8 after 4 days is depicted in Figure 2. At a pH between 3.5 and 4, the solution is clear, and the nanoparticles

DOI: 10.1021/acs.jpcb.5b10966
J. Phys. Chem. B 2016, 120, 1380–1389

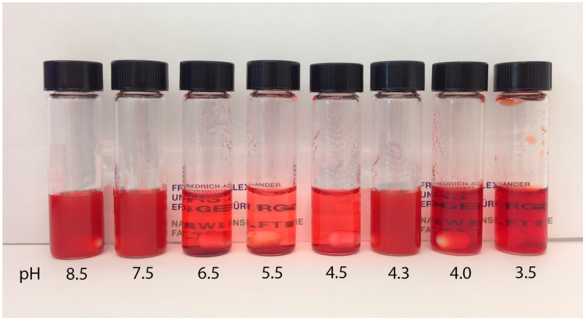

Figure 2. Ar26-G4 samples prepared at different pHs; between 3.5 and 4.0, clear and stable samples were obtained; between 4.3 and 7, samples were not stable; at pHs higher than 7, stable and turbid samples were obtained.

are stable; at pH 4.9, the solution is turbid, and the particles are still stable. At 4.5 ≤ pH ≤ 7.0, the solution appears clear because all of the particles precipitated due to the aging. At pH > 7.0, the solution is opalescent again, and the nanoparticles are stable. Instead, the opposite behavior is observed if loading ratio l = 1.0 is chosen for the preparation; the nanoparticles are not stable at a pH higher than 7.0, while they are stable between 3.0 and 7.0. Therefore, certain pH values lead to stable particles, and others lead to nanoassembly precipitation. The location of these pH ranges depends on the loading ratio and, as will be discussed later, on the counterion.

Thus, we can conclude that the nanoparticles are electrostatically stabilized and that the stabilization depends on the dendrimer charge only. In addition, the nanoassemblies are more stable at low pH. In all of the systems, the most stable assemblies can be found at pH 3.5 where both the primary and the tertiary amine groups are protonated. At the same time, aging is important. It shows the existence of different stability ranges where nanoparticles are stable for months or precipitate after a few days.

Structural Characterization. *Dynamic Light Scattering.* DLS has been performed on Ar26−G4 dendrimer samples at loading ratio l = 1.8 to investigate the nanoassembly dimensions at different pHs. This technique permits determination of the hydrodynamic radius R_H of the nanoparticles as the first major information on the overall dimensions. The samples have been prepared at a concentration of 9.3 × 10^{-6} mol/kg. Figure 3 depicts the electric field autocorreletion function $g^1(\tau)$ and the relaxation time distribution $A(\Gamma)$ for a

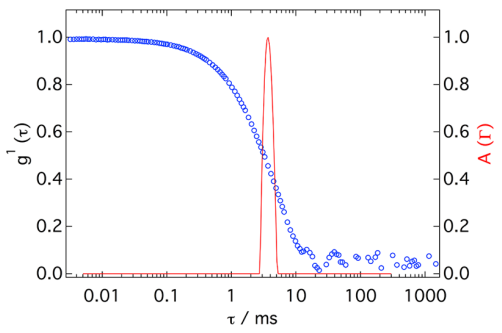

Figure 3. DLS: electric field autocorrelation function $g^1(\tau)$ (blue) and relaxation time distribution $A(\Gamma)$ (red) for an Ar26−dendrimer sample at pH = 8.5 and l = 1.8 (c_r = 6.6).

Ar26−G4 sample at pH = 8.5 and l = 1.8 (c_r = 6.6). It can be immediately concluded that well-defined nanoparticles with a size of R_H = 300 nm are formed at high pH.

R_H as a function of pH is given in Figure 4a; it is evident that the dimension of the nanoassemblies changes with pH. In more detail, R_H is constant at 3.5 ≤ pH ≤ 4 where the dendrimer molecule is completely protonated, while for higher pH, the radius increases continuously from R_H = 50 nm at pH = 4 to R_H = 300 nm at pH = 8. Between pH = 8 and 9, R_H is constant again.

To further understand the stabilization, it is elucidating to use R_H to estimate the effective surface charge density (σ_{eff}) at the shear plane as a possible parameter regulating the nanoparticle stability. This can be done by combining R_H and the ζ-potential according to[47]

$$\sigma_{eff} = \frac{\varepsilon\zeta}{R_{eff}} \approx \frac{\varepsilon\zeta}{R_H} \quad (1)$$

Results are given in Figure 4b. It is evident that the effective surface charge density changes with pH; it decreases as the pH increases, and at pH > 7.0, it remains almost constant. As shown in Figure 4a, a smaller R_H is observed at low pH. Hence, a higher surface charge density corresponds to smaller particles. The same correlation has been observed for light-responsive nanoparticles,[46,48] and it can be understood considering the energetically less-favorable larger surface area for smaller nanoparticles needing a higher charge density for stabilization. This demonstrates once more that the nanoparticles are electrostatically stabilized and, moreover, that the surface charge density is the parameter controlling the stability.

We can conclude that stable and well-defined nanoparticles can be formed at pH higher than pH = 3.5. In addition, the dimensions of the nanoparticles depend on the solution pH; larger assemblies are formed at higher pH. Also, the fact that R_H is constant between pH = 4 and 3.5 where the dendrimer protonation state does not change shows that the hydrodynamic radius is strongly related to the dendrimer charges. Lastly, the importance of the surface charge density in the stabilization has been demonstrated. Smaller particles are more stable and show a higher surface charge density.

Small-Angle Neutron Scattering. To elucidate whether and how pH affects the nanoparticle shape, we performed SANS measurements. The samples were prepared at a concentration of 3.5 × 10^{-5} mol/kg (i.e., higher than the concentration used for the ζ-potential study). To study the effect of the molecular building block ratio, for Ar26 and G4 dendrimer, two different loading ratios (l = 1.8 and 1.0) were investigated. The first one is close to the stoichiometric point (l = 2.0) and corresponds to a slight excess of 10% dendrimer charges, while the second one corresponds to a great excess of polyelectrolyte. Different dyes have been used to vary the strength of dye−dendrimer and dye−dye interaction, stemming from differences in valency, geometry, molecular volume, and molecular dimensions. Due to the differences in stability of the self-assembled nanoparticles upon aging, the complete pH range was not available for SANS measurements. For certain pH ranges, no stable particles have been found. These pH limits differ in dependence on dye and loading ratio.

Results for Ar26 and the G4 dendrimer at l = 1.8 at pH = 7.2 and a corresponding charge ratio c_r = 3.5 are depicted in Figure 5. From the low q signal of the SANS scattering curves, one can identify the nanoassemblies present in solution. Considering

DOI: 10.1021/acs.jpcb.5b10966
J. Phys. Chem. B 2016, 120, 1380−1389

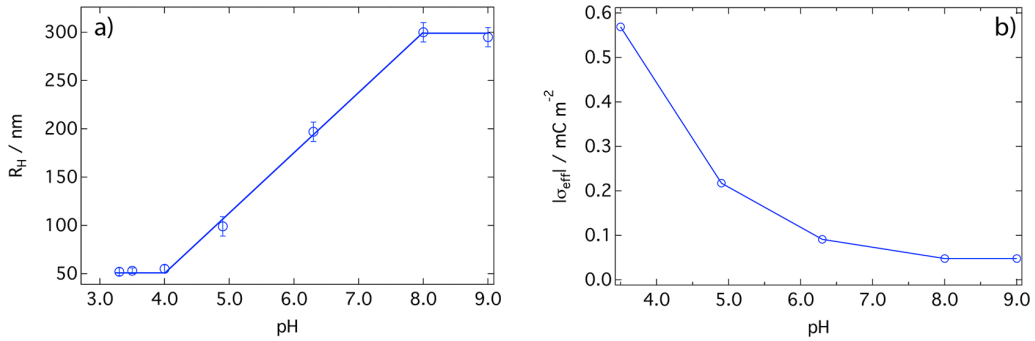

Figure 4. (a) Hydrodynamic radius R_H as a function of pH for an Ar26−G4 sample with l = 1.8. The line is a guide to the eye. (b) Surface charge density as a function of pH; it decreases as the pH increases for an Ar26−G4 sample.

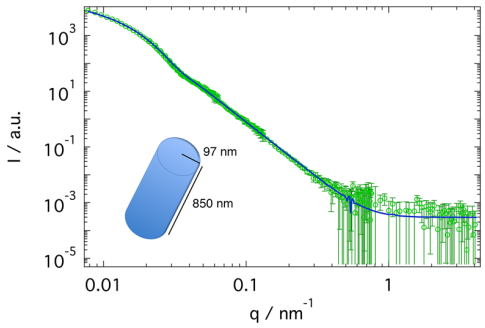

Figure 5. SANS results for an Ar26−G4 dendrimer sample at l = 1.8, pH = 7.2, and c_r = 3.5. The continuous line is the fit according to the sketched cylinder.

the $I(q_{min})$, it can be immediately concluded that their size is at least around 800 nm. To obtain the shape and the dimensions of the nanoparticles in detail, the curve has been fitted with structural models (more info is given in the Experimental Section). The fit of the curve in Figure 5 corresponds to cylindrical nanoparticles with a length of L = (850 ± 30) nm and a cross section radius of r_c = (97 ± 5) nm, as indicated in the sketch.

For some samples, SLS has been carried out to permit extension of the q range of the spectra in the region of the low q down to 6.8 × 10^{-4} nm^{-1}. This is crucial for the samples where it was possible to obtain only limited information from SANS due to the limited q range. An example is given in Figure 6.

Scattering curves for all samples are displayed in Figure 7, and the structural parameters obtained by fitting the SANS

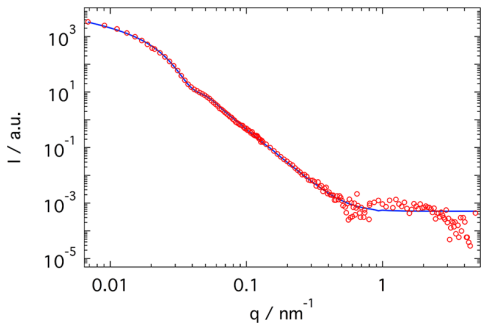

Figure 6. Ar26−G4 dendrimer at l = 1.8, pH = 8.5, and c_r = 6.7; the experimental curve results from the merge of SLS (low q) and SANS data.

curves are reported in Table 2. From Figure 7a, c, and e, it is evident that for all of the dyes, the curves obtained at pH 3.5 are different than the ones at higher pH. In particular, for Ar26 and APhAcOHRAc, the curves at high pH show a shoulder at around q = 0.05 nm^{-1} that is missing at pH = 3.5. The difference can be understood by a change in the structure; this means that by changing the pH, it is possible to obtain different nanostructures. In addition, the position of the shoulder varies with pH. For the Ar26−G4 dendrimer samples (Figure 7b), it shifts from q = 0.025 nm^{-1} for pH = 9.5 (c_r = 18.0) to q = 0.042 nm^{-1} for pH = 7.2 (c_r = 3.5), which can be related to a change in dimensions leading to a strong relationship between nanoassembly dimensions and pH/charge ratio. The same behavior can be observed for APhAcOHRAc; here, the shoulder shifts from q = 0.023 to 0.047 nm^{-1}.

For Ar26 and G4 dendrimer (Figure 7a), at loading ratio l = 1.8 and pH = 3.5 (c_r = 1.8), the nanoparticles are cylinders with an elliptical cross section. The length is L = 300 nm, the radius of the long axis of the cross section is 44 nm, and the radius of the short axis is 11 nm. The anisotropic cross section is probably due to the $\pi-\pi$ interaction between the dye molecules that is anisotropic. Therefore, also on the cross section, one direction is favored during the growth process, as indicated in Scheme 2. When the pH changes to pH = 7.0 (c_r = 3.5), the nanoassemblies become cylinders with an isotropic cross section. Hence, the cross section changes with pH. The change can be understood considering that at pH = 7.0, only the dendrimer primary amines are protonated, and therefore, the dye−dendrimer interaction changes. This change may also affect the dye−dye interaction, resulting in an isotropic cross section. The length of the cylinder is L = 850 nm, and the cross section radius is 97 nm. From pH 7.0 to 9.5, the shape remains constant, the cylinder length decreases from 850 to 720 nm, while the radius decreases to 62 nm at pH 7.8 (c_r = 4.0) and increases again to 130 nm at pH 9.5. When the pH is close to 10 where only very few amine groups are protonated, the shape changes again, and spherical assemblies can be found in solution. All results are depicted in Scheme 3.

A similar behavior in pH is found when considering a loading ratio of 1.0. From pH = 3.5 (c_r = 1.0) to pH = 5 (c_r = 1.2), cylinders with an elliptical cross section are observed, while at pH > 5, the nanoparticles are spherical. For the cylinders, the length becomes smaller as the pH increases (from 600 to 370 nm), while the cross section remains almost constant. Instead, the spheres become larger as the pH increases, with the radius changing from 22 nm at pH 5.1 (c_r = 1.2) to 70 nm at pH 6.9 (c_r = 1.9). The nanoassemblies are unstable at higher pH.

DOI: 10.1021/acs.jpcb.5b10966
J. Phys. Chem. B 2016, 120, 1380−1389

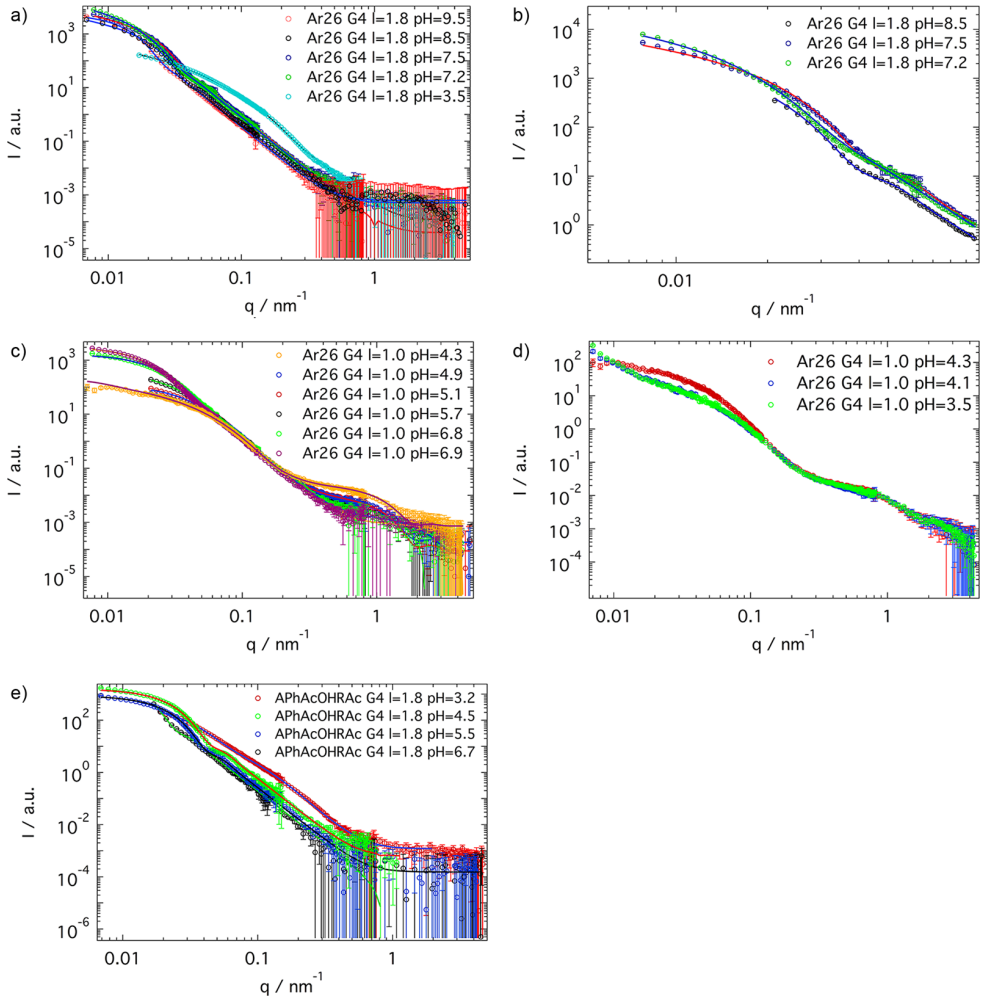

Figure 7. SANS scattering curves: (a) Ar26−dendrimer, loading ratio l = 1.8 at different pH; (b) low q enlargement of (a) at pH > 7; The shoulder shifts with pH. (c) Ar26−dendrimer with loading ratio l = 1.0 at different pHs. (d) Comparison of the spectra obtained for pH < 4.5. At pH 4.1 and 3.5, a signal at low q arises. (e) APhAcOHRAc−dendrimer with a loading ratio l = 1.8 at different pHs.

Considering the charge ratio, the stability range boundaries are the same as those for loading ratio 1.8 (range at c_r < 1.8 and > 3.4), while they are different if the pH is taken into account.

At pH < 6, an additional second signal arises in the SANS spectra at q = 0.8 nm^{-1}. This signal can be understood by taking into account the presence of unaggregated dendrimer molecules when the charge ratio is lower than 1.5. As the pH approaches the level of 4 (Figure 7d), another signal arises at q = 0.015 nm^{-1}, which is due to the formation of larger assemblies with an overall dimension larger than 900 nm. Because the signal remains the same as the pH changes from pH = 4.1 to 3.5, it may be caused by the stacking of the elliptical cylinders observed at pH 4.3. In the SANS curve, the presence of larger assembies results in the appearance of a signal at lower q and in the decrease of the elliptical cylinder signal. We can identify these larger assemblies as the elliptical cylinders stacking on each other because by lowering the pH, the signal at low q remains constant, while the formation of new particles would result in a signal increase. Hence, we can conclude that different loading ratios lead to different shape changes as the pH varies. In contrast, the component ratio does not affect the stability region limits if the charge ratio is considered.

The results for APhAcOHRAc are reported in Figure 7e. In this case, no shape changes are observed as the pH changes. The nanoparticles are spherical at all pHs, while at pH < 4, that is, when all primary and tertiary dendrimer amine groups are protonated, a structural change may be identified. Here, the spherical assemblies show a core−shell structure. In this case, the fit model describes a particle with a denser core and a less dense shell, which can be due to a different dye content and hence a different degree of interconnection in the shell and in the core of the supramolecular sphere. As in the case of Ar26 at loading ratio 1.0, the nanoparticles become larger as the pH increases, from 82 nm at pH = 4.0 (c_r = 1.8) to 165 nm at pH = 6.7 (c_r = 3.1).

We showed above how the ζ-potential changes continuously around the pK_a of the −COOH group (pH = 4.3). The SANS data prove that also the shape is not affected by the protonation. Therefore, the valency of the dye has no effect on both stabilization and pH shape dependence. While for Ar26 at a loading ratio of l = 1.0 and 1.8, the same stability range was found, it is different for APhAcOHRAc; stable nanoassemblies can be found between charge ratio c_r = 1.8 and 3.1.

For ABnOHRAc−dendrimer samples, elongated particles have been observed at all pHs. The nanoparticles have a

DOI: 10.1021/acs.jpcb.5b10966
J. Phys. Chem. B 2016, 120, 1380−1389

Table 2. Structural Parameters Obtained from Fitting the SANS Curves

pH	charge ratio	shape	radius (nm)	length (nm)	minor axis (nm)	major axis (nm)	volume (10^6 nm^3)
Ar26−G4 l = 1.8							
9.8	35.9	sphere	190 ± 10				28.7
9.5	18.0	cylinder	130 ± 10	720 ± 40			38.2
9.3	12.9	cylinder	95 ± 5	720 ± 40			38.2
8.6	6.7	cylinder	72 ± 5	820 ± 50			13.4
8.2	4.8	cylinder	65 ± 5	800 ± 40			10.6
8.0	4.3	cylinder	66 ± 5	710 ± 40			9.7
7.8	4.0	cylinder	62 ± 5	720 ± 40			8.7
7.5	3.9	cylinder	82 ± 10	930 ± 40			19.6
7.4	3.8	cylinder	81 ± 10	850 ± 40			17.5
7.2	3.5	cylinder	97 ± 5	850 ± 40			25.1
6.8	3.4	cylinder	97 ± 5	850 ± 30			25.1
3.5	1.8	elliptical cylinder		300 ± 10	11 ± 1	44 ± 4	0.5
Ar26−G4 l = 1.0							
6.9	1.9	sphere	70 ± 5				1.4
6.8	1.9	sphere	57 ± 3				0.8
6.5	1.8	sphere	46 ± 3				0.4
5.7	1.4	sphere	25 ± 2				0.07
5.1	1.2	sphere	22 ± 2				0.05
4.9	1.2	elliptical cylinder		370 ± 10	17 ± 1	36 ± 2	0.7
4.3	1.1	elliptical cylinder		500 ± 20	16 ± 1	34 ± 2	0.9
4.1	1.1	elliptical cylinder		600 ± 50	13 ± 1	27 ± 2	0.7
3.5	1.0	elliptical cylinder		600 ± 50	13 ± 1	27 ± 2	0.7
APhAcOHRAc−G4 l = 1.8							
6.7	3.1	sphere	165 ± 30				18.8
5.5	2.5	sphere	98 ± 1				3.9
4.5	1.9	sphere	93 ± 1				3.3
4.0	1.8	sphere	82 ± 1				2.3
3.5	1.8	core−shell sphere	core: 28 ± 1 total: 46 ± 3				0.4
ABnOHRAc−G4 l = 1.8							
5.7	2.5	cylinder	86 ± 2	500 ± 10			11.6
4.5	1.9	cylinder	86 ± 2	120 ± 10			2.8
1.8	1.8	flex. ellipt. cyl.	min: 7 ± 1 max: 42 ± 6	total: 2100 ± 100 Kuhn: 140 ± 10		1.9	
Ar27−G4 l = 1.8							
5.0	2.1	sphere	77 ± 1				1.9
3.5	1.8	core−shell sphere	core: 13 + 1 total: 44 ± 3				0.4

cylindrical shape at a pH higher than 4, while at lower pH, the nanoparticles are long flexible cylinders with an elliptical cross section. Interestingly, the radius of the cylinder does not change with pH, while the length increases as the pH increases. The stability range regarding the charge ratio is the same as that for APhAcOHRAc. Results on the stability range and the shape for these two systems are given in Scheme 3. Further, for Ar27, the case is almost identical to the one of APhAcOHRAc; pH variation does not affect the nanoparticle shape, but it changes their structure, that is, it causes the formation of a less-dense shell at pH < 4.0. Again, the nanoparticles become larger as the pH increases. Stable particles have been found between charge ratio 1.8 and 2.5 for this system.

Therefore, we can conclude that the stability range for ionic dendrimer−dye assemblies in aqueous solution only depends on the dye used. If the nanoassemblies are spherical, the shape remains unchanged over the complete pH range, while at pH 3.5 (loading ratio and charge ratio $l = c_r = 1.8$), the nanoparticles show a core−shell structure with regions of different density. The dyes forming anisotropic nanoparticles at loading ratio 1.8 and pH 3.5 form isotropic assemblies in certain pH ranges, that is, they show a shape transition. Also, nanoparticle dimensions are strongly related to pH; at higher pH, larger structures are formed. Therefore, pH is a crucial parameter in the nanoparticle design through electrostatic self-assembly. It allows for a targeted structure design and for tuning and triggering the dimension and shape of the supramolecular assemblies in solution. These findings can, for example, be of importance in drug delivery or carrier systems in nanotechnology. While this study focuses on general principles, it also includes several structures that are stable over a physiologic pH range and undergo shape changes in this region. Because a facile building block concept is used, structures may then easily be target-designed for a specific application in the future.

CONCLUSIONS

In conclusion, we elucidated pH as a key to tunable particle stability, shape, and size in the electrostatic self-assembly of ionic dendrimers and oppositely charged dyes in aqueous solution. Supramolecular dendrimer−dye nanoparticles are more stable at low pH when both primary and tertiary dendrimer amine groups are protonated. The ζ-potential is higher at low pH and varies linearly with pH. This indicates

DOI: 10.1021/acs.jpcb.5b10966
J. Phys. Chem. B 2016, 120, 1380−1389

Scheme 3. Stability Plots for Ar26 and Dendrimer G4 at I = 1.8 and 1.0 and for APhAcOHRAc and ABnOHRAc at I = 1.8

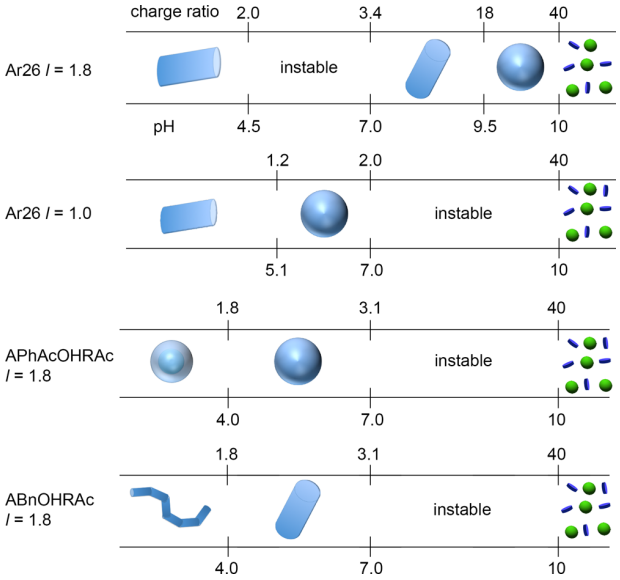

that the stabilization mechanism is the same at pH > 7.0 where the dye molecules can bind only to the "outside" of the dendrimer molecules and at pH < 7.0 where the dye can bind also to the inner tertiary amine groups. Therefore, it is demonstrated that the nanoparticle stability arises from electrostatic stabilization. Furthermore, the aging of the samples determines the existence of instability regions at certain values of pH and charge. For each system, we were able to identity a peculiar stability range that is determined by the molecular structure of the specific dye. Changes in the loading ratio result in the shift of the upper or lower stability limit in pH, while the limits in charge ratio remain unchanged. This again confirms the ionic nature of the stabilization and, in particular, shows the primary importance of the charge ratio over the other parameters. pH = 7.0 is a crucial value because tertiary amine groups start to be protonated, and it always represents one of the limits of the stability region.

Stable and well-defined nanoparticles can be formed at pH ≥ 3.5. Here, nanoparticle dimensions strongly depend on the solution pH. Combining results of DLS and ζ-potential measurements, the surface charge density has been shown to be the crucial parameter in nanoparticle stability and size control. Dimensions of the supramolecular nanoparticles, as revealed by SANS, can be tuned over a wide range by regulating the pH, with a higher pH yielding larger nanoparticles. For example, in the case of the dendrimer−APhAcOHRAc assemblies, spheres with radii from R = 46 nm (pH 3.5) to R = 165 nm (pH 6.7) can be created. Moreover, pH is also a key to a tunable particle shape. For example, for Ar26, the pH can be used as a trigger to switch between nanoscale cylinders with elliptical cross sections and spherical nanoparticles and for ABnOHRAc between up to 2 μm long flexible cylinders and shorter (100−500 nm) stiff cylinders. In all cases, the pH can switch between a nanoassembly and dissociated building blocks.

Well-defined nanoparticles, the size and shape of which can be triggered by controlling the pH of the solution, are of fundamental importance for tailoring self-assembly to yield target structures and properties. In particular, a pH-responsive shape can be of great potential for novel smart therapeutic carrier systems.

AUTHOR INFORMATION

Corresponding Author

*E-mail: franziska.groehn@fau.de.

Notes

The authors declare no competing financial interest.

ACKNOWLEDGMENTS

This work benefitted from SasView software, originally developed by the DANSE project under NSF Award DMR-0520547. We acknowledge the support of Institut Laue-Langevin, Grenoble, France and of the National Institute of Standards and Technology (NIST), Gaithersburg, MD, U.S.A. for providing the neutron research facilities used in this work. We thank Paul Butler, National Institute of Standards and Technology (NIST), U.S. Department of Commerce, MD, USA, for support with SANS measurements. Financial support of Deutsche Forschungsgemeinschaft (DFG), of the Interdisciplinary Centre for Molecular Materials (ICMM), and of the Institut Laue-Langevin is gratefully acknowledged.

REFERENCES

(1) Ringsdorf, H.; Schlarb, B.; Venzmer, J. Molecular Architecture and Function of Polymeric Oriented Systems: Models for the Study of Organization, Surface Recognition, and Dynamics of Biomembranes. *Angew. Chem., Int. Ed. Engl.* **1988**, *27*, 113−158.

(2) Zhou, S.; Burger, C.; Chu, B.; Sawamura, M.; Nagahama, N.; Toganoh, M.; Hackler, U. E.; Isobe, H.; Nakamura, E. Spherical Bilayer Vesicles of Fullerene-based Surfactants in Water: A Laser Light Scattering Study. *Science* **2001**, *291*, 1944−1947.

(3) Discher, D. E.; Eisenberg, A. Polymer Vesicles. *Science* **2002**, *297*, 967−973.

(4) Zhang, Y.; Guan, Y.; Xu, S.; Yang, S.; Xu, J.; Han, C. C. Fabrication of Hollow Capsules Based on Hydrogen Bonding. *Adv. Mater.* **2003**, *15*, 832−835.

(5) Pergushov, D. V.; Remizova, E. V.; Feldthusen, J.; Zezin, A. B.; Müller, A. H. E.; Kabanov, V. A. Novel Water-Soluble Micellar Interpolyelectrolyte Complexes. *J. Phys. Chem. B* **2003**, *107*, 8093−8096.

(6) Schmuck, C.; Schwegmann, M. A Molecular Flytrap for the Selective Binding of Citrate and Other Tricarboxylates in Water. *J. Am. Chem. Soc.* **2005**, *127*, 3373−3379.

(7) Jonkheijm, P.; van der Schoot, P.; Schenning, A. P. H. J.; Meijer, E. W. Probing the Solvent-assisted Nucleation Pathway in Chemical Self-Assembly. *Science* **2006**, *313*, 80−83.

(8) Nikolic, M. S.; Olsson, C.; Salcher, A.; Kornowski, A.; Rank, A.; Schubert, R.; Frömsdorf, A.; Weller, H.; Förster, S. Micelle and Vesicle Formation of Amphiphilic Nanoparticles. *Angew. Chem., Int. Ed.* **2009**, *48*, 2752−2754.

(9) Srivastava, S.; Santos, A.; Critchley, K.; Kim, K.-S.; Podsiadlo, P.; Sun, K.; Lee, J.; Xu, C.; Lilly, G. D.; Glotzer, S. C.; et al. Light-controlled Self-Assembly of Semiconductor Nanoparticles into Twisted Ribbons. *Science* **2010**, *327*, 1355−1359.

(10) Murphy, R. J.; Pristinski, D.; Migler, K.; Douglas, J. F.; Prabhu, V. M. Dynamic Light Scattering Investigations of Nanoparticle Aggregation Following a Light-induced pH Jump. *J. Chem. Phys.* **2010**, *132*, 194903.

(11) Sumino, A.; Dewa, T.; Noji, T.; Nakano, Y.; Watanabe, N.; Hildner, R.; Bosch, N.; Kohler, J.; Nango, M. Influence of Phospholipid Composition on Self-Assembly and Energy-Transfer Efficiency in Networks of Light-Harvesting 2 Complexes. *J. Phys. Chem. B* **2013**, *117*, 10395−10404.

DOI: 10.1021/acs.jpcb.5b10966
J. Phys. Chem. B 2016, 120, 1380−1389

(12) Longo, G. S.; Olvera de la Cruz, M.; Szleifer, I. Equilibrium Adsorption of Hexahistidine on pH-Responsive Hydrogel Nanofilms. *Langmuir* **2014**, *30*, 15335−15334.
(13) Eakins, G. L.; Gallaher, J. K.; Keyzers, R. A.; Falber, A.; Webb, J. E. A.; Laos, A.; Tidhar, Y.; Weissman, H.; Rybtchinski, B.; Thordarson, P.; Hodgkiss, J. M. Thermodynamic Factors Impacting the Peptide-Driven Self-Assembly of Perylene Diimide Nanofiber. *J. Phys. Chem. B* **2014**, *118*, 8442−8651.
(14) Chiappisi, L.; Simon, M.; Gradzielski, M. Toward Bioderived Intelligent Nanocarriers for Controlled Pollutant Recovery and pH-Sensitive Binding. *ACS Appl. Mater. Interfaces* **2015**, *7*, 6139−6145.
(15) Kumar, V. A.; Shi, S.; Wang, B. K.; Li, I.-C.; Jalan, A. A.; Sarkar, B.; Wickremasinghe, N. C.; Hartgerink, J. D. Drug-Triggered and Cross-Linked Self-Assembling Nanofibrous Hydrogels. *J. Am. Chem. Soc.* **2015**, *137*, 4823−4830.
(16) Geng, Y.; Dalhaimer, P.; Cai, S.; Tsai, R.; Tewari, M.; Minko, T.; Discher, D. E. Shape Effects of Filaments Versus Spherical Particles in Flow and Drug Delivery. *Nat. Nanotechnol.* **2007**, *2*, 249−255.
(17) Petros, R. A.; DeSimone, J. M. Strategies in the Design of Nanoparticles for Therapeutic Applications. *Nat. Rev. Drug Discovery* **2010**, *9*, 615−627.
(18) Popovic, Z.; Liu, W.; Chauhan, V. P.; Lee, J.; Wong, C.; Greytak, A. B.; Insin, N.; Nocera, D. G.; Fukumura, D.; Jain, R. K.; Bawendi, M. G. A Nanoparticle Size Series for In Vivo Fluorescence Imaging. *Angew. Chem.* **2010**, *122*, 8831−8834.
(19) Xu, Y.; Bolisetty, S.; Drechsler, M.; Fang, B.; Yuan, J.; Ballauff, M.; Müller, A. H. E. pH and Salt Responsive poly (N, N-dimethylaminoethyl methacrylate) Cylindrical Brushes and Their Quaternized Derivatives. *Polymer* **2008**, *49*, 3957−3964.
(20) Nam, J.; Won, N.; Jin, H.; Chung, H.; Kim, S. pH-induced Aggregation of Gold Nanoparticles for Photothermal Cancer Therapy. *J. Am. Chem. Soc.* **2009**, *131*, 13639−13645.
(21) Tauk, L.; Schröder, A. P.; Decher, G.; Giuseppone, N. Hierarchical Functional Gradients of pH-responsive Self-Assembled Monolayers Using Dynamic Covalent Chemistry On Surfaces. *Nat. Chem.* **2009**, *1*, 649−656.
(22) Kuciauskas, D.; Caputo, G. A. Self-Assembly of Peptide−Porphyrin Complexes Leads to pH-dependent Excitonic Coupling. *J. Phys. Chem. B* **2009**, *113*, 14439−1447.
(23) Yoo, J.-W.; Irvine, D. J.; Discher, D. E.; Mitragotri, S. Bio-inspired, Bioengineered and Biomimetic Drug Delivery Carriers. *Nat. Rev. Drug Discovery* **2011**, *10*, 521−535.
(24) Ghosh, A.; Haverick, M.; Stump, K.; Yang, X.; Tweedle, M. F.; Goldberger, J. E. Fine-tuning the pH Trigger of Self-Assembly. *J. Am. Chem. Soc.* **2012**, *134*, 3647−3650.
(25) Nie, S. Y.; Sun, Y.; Lin, W. J.; Wu, W. S.; Guo, X. D.; Qian, Y.; Zhang, L. J. Dissipative Particle Dynamics Studies of Doxorubicin-Loaded Micelles Assembled from Four-Arm Star Triblock Polymers 4AS-PCL-*b*-PDEAEMA-*b*-PPEGMA and Their pH-Release Mechanism. *J. Phys. Chem. B* **2013**, *117*, 13688−13697.
(26) Bogomolova, A.; Keller, S.; Klingler, J.; Sedlak, M.; Rak, D.; Sturcova, A.; Hruby, M.; Stepanek, P.; Filippov, S. K. Self-Assembly Thermodynamics of pH-Responsive Amino-Acid-Based Polymers with a Nonionic Surfactant. *Langmuir* **2014**, *30*, 11307−11318.
(27) Mandal, T.; Kumar, M. V. S.; Maiti, P. K. DNA Assisted Self-Assembly of PAMAM Dendrimers. *J. Phys. Chem. B* **2014**, *118*, 11805−11815.
(28) Sarangapani, P. S.; Hudson, S. D.; Jones, R. L.; Douglas, J. F.; Pathak, J. A. Critical Examination of The Colloidal Particle Model of Globular Proteins. *Biophys. J.* **2015**, *108*, 724−737.
(29) Gröhn, F.; Klein, K.; Brand, S. Facile Route to Supramolecular Structures: Self-Assembly of Dendrimers and Naphthalene Dicarboxylic Acids. *Chem. - Eur. J.* **2008**, *14*, 6866−6869.
(30) Willerich, I.; Gröhn, F. Switchable Nanoassemblies from Macroions and Multivalent Dye Counterions. *Chem. - Eur. J.* **2008**, *14*, 9112−9116.
(31) Li, Y.; Yildiz, U. H.; Müllen, K.; Gröhn, F. Association of DNA with Multivalent Organic Counterions: From Flowers to Rods and Toroids. *Biomacromolecules* **2009**, *10*, 530−540.
(32) Ruthard, C.; Maskos, M.; Kolb, U.; Gröhn, F. Finite-size Networks from Cylindrical Polyelectrolyte Brushes and Porphyrins. *Macromolecules* **2009**, *42*, 830−840.
(33) Gröhn, F. Soft Matter Nanoparticles with Various Shapes and Functionalities Can Form through Electrostatic Self-Assembly. *Soft Matter* **2010**, *6*, 4296−4302.
(34) Willerich, I.; Ritter, H.; Gröhn, F. Structure and Thermodynamics of Ionic Dendrimer− Dye Assemblies. *J. Phys. Chem. B* **2009**, *113*, 3339−3354.
(35) Willerich, I.; Li, Y.; Gröhn, F. Influencing Particle Size and Stability of Ionic Dendrimer− Dye Assemblies. *J. Phys. Chem. B* **2010**, *114*, 15466−15476.
(36) Willerich, I.; Gröhn, F. Thermodynamics of Photoresponsive Polyelectrolyte−Dye Assemblies with Irradiation Wavelength Triggered Particle Size. *Macromolecules* **2011**, *44*, 4452−4461.
(37) Ruthard, C.; Schmidt, M.; Gröhn, F. Porphyrin−Polymer Networks, Worms, and Nanorods: pH-triggerable Hierarchical Self-assembly. *Macromol. Rapid Commun.* **2011**, *32*, 706−711.
(38) Willerich, I.; Gröhn, F. Molecular structure encodes nanoscale assemblies: understanding driving forces in electrostatic self-assembly. *J. Am. Chem. Soc.* **2011**, *133*, 20341−20356.
(39) Robinson, C.; Mills, H. A. T. The Colloid Chemistry of Dyes: The Aqueous Solutions of Benzopurpurine 4B and Its Isomer Prepared from m-Tolidine. Part I. *Proc. R. Soc. London, Ser. A* **1931**, *131*, 576−595.
(40) Hunter, R. J. *Zeta Potential in Colloid Science*; Academic Press: New York, 1981.
(41) Guinier, A.; Fournet, G. *Small-Angle Scattering of X-Rays*; John Wiley and Sons: New York, 1955.
(42) Porod, G. In *Small Angle X-ray Scattering*; Glatter, O., Kratky, O., Eds.; Academic Press, Inc;: New York, 1982; Chapter 2, pp 17−52.
(43) Feigin, L. A.; Svergun, D. I. *Structure Analysis by Small-Angle X-ray and Neutron Scattering*; Plenum: New York, 1987.
(44) Pedersen, J. S.; Schurtenberger, P. Scattering functions of semiflexible polymers with and without excluded volume effects. *Macromolecules* **1996**, *29*, 7602−7612.
(45) Chen, W.-R.; Butler, P. D.; Magid, L. J. Incorporating Intermicellar Interactions in the Fitting of SANS Data from Cationic Wormlike Micelles. *Langmuir* **2006**, *22*, 6539−6548.
(46) Willerich, I.; Gröhn, F. Photoswitchable Nanoassemblies by Electrostatic Self-Assembly. *Angew. Chem., Int. Ed.* **2010**, *49*, 8104−8108.
(47) Willerich, I.; Schindler, T.; Ritter, H.; Gröhn, F. Controlling the size of electrostatically self-assembled nanoparticles with cyclodextrin as external trigger. *Soft Matter* **2011**, *7*, 5444−5450.
(48) Moldenhauer, D.; Gröhn, F. Nanoassemblies with light-responsive size and density from linear flexible polyelectrolytes. *J. Polym. Sci., Part B: Polym. Phys.* **2013**, *51*, 802−816.

DOI: 10.1021/acs.jpcb.5b10966
J. Phys. Chem. B 2016, 120, 1380−1389

4.3 Structure Tuning of Electrostatically Self-assembled Nanoparticles through pH: the Role of Charge Ratio

Submitted to Physical Chemistry Chemical Physics

Journal Name

Structure Tuning of Electrostatically Self-Assembled Nanoparticles through pH: the Role of Charge Ratio

Received 00th January 20xx,
Accepted 00th January 20xx

DOI: 10.1039/x0xx00000x

www.rsc.org/

G. Mariani,[a,b] R. Schweins[b] and F. Gröhn[a]

Systems that can be controlled through external triggers are of interest for a variety of applications. Here, we discuss the effects of pH on the electrostatic self-assembly of poly(amidoamine) dendrimers of generation 4 and a divalent azo dye keeping constant the charge ratio of the building blocks. Stable nanoparticles stabilized by an excess of dendrimer charge can be formed at 3.5 ≤ pH ≤ 8.5. The nanoparticle structure strongly depends on the solution pH. For example, at 7 ≤ pH ≤ 8.5, where only the primary amines of the dendrimer are protonated, spherical particles are formed, while at 3.5 ≤ pH < 7 where also the tertiary amines are protonated, cylinders are formed. Moreover, the change in dendrimer protonation affects the self-assembly not only on the nano-scale level, but also the molecular-scale resulting in a change of the dye stacking: the twist angle of the dye molecules increases as the pH decreases. The results have been related to changes in the dye-dendrimer and dye-dye interaction, in particular spherical nanoparticles are formed when the interaction is small. Lastly, the structures at different pH and constant charge ratio are compared to results at constant loading ratio to understand the overall role of the pH on electrostatic self-assembly with particular attention to pH responsive shape, who is of great interest, for example, for nanosensors.

1. Introduction

Self-assembly has been proven to be a powerful strategy for the synthesis of supramolecular nanostructures,[1-8] in particular, nanoparticles that can respond to external triggers. Goal is a rational design of target nanostructures, for example controlling the particle morphology. This is of crucial importance for applications such as drug delivery, where it has been demonstrated that the circulation lifetime in veins depends on nanoparticle size and shape.[9-11]

A versatile way of structural control is the use of building blocks with pH-dependent molecular structure.[12-16] For example, we have recently introduced a concept of electrostatic self-assembly relying on a general combination of interactions leading to the synthesis of well-defined supramolecular nanoscale assemblies.[17] The process is based on the self-assembly of polyelectrolytes and organic counterions and results in electrostatically stabilized nanoparticles with sizes up to more than hundred nanometers.[18] As counterions, multivalent organic dyes have been used to interconnect the polyelectrolyte molecules. Additionally, secondary interactions such as π-π stacking of the dye molecules or geometric effects occur during the process. The choice of the building blocks allows to form nanoparticles switchable by external triggers: for example, nanoparticles responsive to light and pH have been built.[19-20] To achieve control over the process via pH, polyamidoamine (PAMAM) dendrimers have been applied as macroions, the charge of which can be adjusted by regulating the solution. Thereby assembly on-off switchability was achieved via protonation and deprotonation of the dendrimer molecules.

Scheme 1 Molecular Structures of the Building Blocks Used in the Present Study.

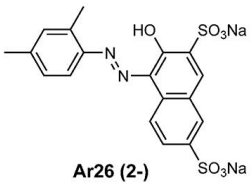

Ar26 (2-)

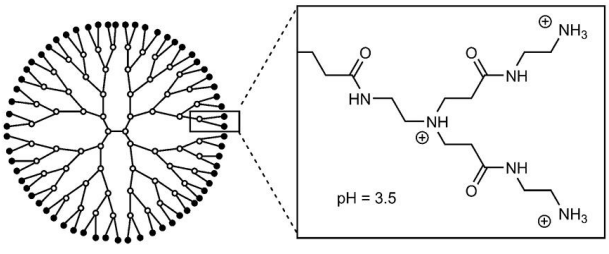

G4 PAMAM

[a] Department of Chemistry and Pharmacy and Interdisciplinary Centre for Molecular Material (ICMM), Friedrich-Alexander-Universität Erlangen-Nürnberg Egerlandstraße 3, D-91058 Erlangen, Germany
[b] DS/LSS Institut Laue-Langevin, 71 avenue des Martyrs, F-38000 Grenoble, France.

To understand the delicate balance of electrostatics, π-π interaction and geometric effects, we have investigated the nanoassembly structures and the thermodynamics of dye-dye and dye-dendrimer interaction.[21] More recently, we focused on the effect of the pH, i.e. dendrimer protonation degree, on the self-assembly showing that nanoparticles are electrostatically stabilized and more stable at full protonation of the dendrimer (pH = 3.5). In addition, the pH has been shown to control the nanoassembly shape and dimensions.[22]

Herein, we study the influence of pH from a different perspective. Nanoparticle stability and structure are investigated keeping constant the ratio of the charges of the dyes and of the dendrimers when varying the pH. This is in difference to the earlier study where the molar ratio of dye sulfonate groups to dendrimer primary amines was kept constant.[22] The new approach is extremely promising to fundamentally understand pH effects in ionic supramolecular structures. Lastly, the results at constant charge ratio are combined with the previous results obtained varying the pH keeping constant the loading ratio to understand the overall role of pH in electrostatic self-assembly.[22] The two studies combined together yield insight on how the electrostatic interaction and the secondary interactions work together in the self-assembly

Specifically, we have investigated the self-assembly of polyamidoamine (PAMAM) dendrimers of generation 4 and the negatively charged divalent azo dye Ar26 (Scheme 1) as a model system. Nanoassembly stability is related to ζ-potential measurements, while the structural characterization consists of small angle neutron scattering (SANS) to investigate shape and dimensions and UV-Vis spectroscopy to study the dye stacking induced by ionic association. A phase diagram of nanoparticles shape and dimensions in dependence on pH is established and compared with previous results.

Elucidating the stability and the structures of supramolecular nanoparticles is of crucial importance to better understand how the interactions interplay in the self-assembly and to be able to exploit the effect of pH as a trigger. A targeted triggering of the nanoparticle structure and properties is the key for applications as smart drug carrier systems or sensors.

1. Experimental Section

1.1 Chemicals

Poly(amidoamine) (PAMAM) dendrimer of generation 4 was obtained from Dendritech, Midland, MI, USA and Sigma-Aldrich, Schnelldorf, Germany. The azo dyes Acid Red 26 (Ar26, C.I. 16150) was obtained from Acros, Geel, Belgium.

1.2 Sample preparation

Ar26 and G4 dendrimer stock solution were mixed at pH = 10.5, their volume fraction was adjusted to obtain the desired charge ratio (1.8) at the selected pH. The appropriate amount of *HCl* was then added at once under turbulent mixing to adjust the pH inducing assembly formation. Samples were prepared at six different pH values: 3.5, 4.5, 5.5, 6.5, 7.5 and 8.5.

1.3 ζ-potential measurements

ζ-potential measurements of samples with concentrations between 9.5 10^{-7} mol/kg and 1.6 10^{-7} mol/kg were carried out on a Zetasizer Nano ZS analyzer with integrated 20 mW HeNe laser with λ = 633 nm (Malvern Instruments Ltd, U.K.). Measurements were carried out at room temperature using folded capillary cells (DTS 1060) in three replicate measurements. The ζ-potential has been calculated from the electrophoretic mobility using the Von-Smoluchowski equation.

1.4 SANS measurements

For SANS, samples with a dendrimer concentration of 3.5 10^{-5} mol/kg were transferred into quartz cells with 2 mm path length. SANS studies were performed on D11 at the Institut Laue-Langevin, Grenoble, France using a wavelength of 6 Å. The samples were measured at 3 different sample-detector distances, 1.2 m, 8 m and 39 m. The wavelength spread ($\delta\lambda/\lambda$) was 0.09. Thereby a total scattering vector range of: 0.009 $nm^{-1} < q < 5\ nm^{-1}$ was covered. Data were corrected for empty cell scattering, electronic background and detector uniformity and then converted to absolute scale using secondary standards. Then, the scattering of the solvent and the incoherent background were subtracted. Structural modeling has been used to obtain the particles shape and dimensions. For some samples the instrument resolution has been taken in account in the fitting process to check its influence on the obtained results. The SANS intensity can be written as: $\boldsymbol{I(q) = \phi V_{NP} (\Delta\rho_{SLD})^2 F^2(q)}$, where Φ is the volume fraction, V_{NP} the nanoparticle volume, $\Delta\rho_{SLD}$ the difference in scattering length density between the nanoparticle and the solvent and $F(q)$ the scattering amplitude. The latter parameter describes the nanoparticle shape. For a sphere of radius r, the scattering amplitude is:[23,24]

$$F(q) = 3\frac{\sin qr - qr\cos qr}{(qr)^3} \qquad (1)$$

In the case of cylinders with elliptical cross-section, the scattering intensity can be written as:[25]

$$I(q) = \frac{\phi}{V_{NP}} \int d\psi \int d\phi \int p(\theta,\phi,\psi) P^2(\boldsymbol{q},\alpha,\psi) \sin\theta\, d\theta \quad (2)$$

With the functions: $P(q,\alpha,\psi) = 2\frac{J_1(a)}{a}\frac{\sin b}{b}$, $a = q\sin\alpha\sqrt{r_{major}^2\sin^2\psi + r_{minor}^2\cos^2\psi}$ and $b = q\frac{L}{2}\cos\alpha$. J_1 is the first order Bessel function.

1.5 UV-Vis spectroscopy

Absorption spectra were recorded on a JASCO V-630 spectrometer using quartz cuvettes with 10 cm path length at dye concentrations of c = 2 10^{-5} mol/kg. The experimental extinction coefficient has been fitted according to:

$$\varepsilon_D = \varepsilon_J \exp\left[-4ln2\frac{(\nu-\nu_J)^2}{\Delta\nu_{1/2,J}^2}\right] + \sum_{i=0}^{1}\varepsilon_i \exp[-4\ ln2\ \frac{(\nu-\nu_i)^2}{\Delta\nu_{1/2,i}^2}] \quad (3)$$

where ε_D is the extinction coefficient of the dimer. This separation can be done because the spectral separation between the H- and J- band is greater than the vibronic progression. Therefore, the first term of the equation refers to the J band with ε_J as extinction coefficient, ν_J as wavenumber and $\Delta\nu_{1/2,J}$ as half-width of the Gaussian. The second term represents the H band extended to two vibronic transitions.

2. Results and discussion

In the following, a structural characterization and a stability analysis of the self-assembled nanoparticles formed by G4 dendrimers and the azo dye Ar26 at different pH will be presented. The pH controls the degree of protonation of the dendrimer.[26] Thus, changing the pH modifies the number of dendrimer protonated amine groups resulting in a change of available binding sites, i.e. electrostatic association capability, and of their position, i.e. geometric factors.

Herein, the loading ratio is defined as molar ratio of dye sulfonate groups to dendrimer protonated amino groups at pH = 7.0: $l = c(SO_3^-)/(c(NH_2) * 0.5)$, where 0.5 is the dendrimer protonation at pH 7, together with the pH dependent dendrimer protonation α it gives the charge ratio $c_r = c(SO_3^-)/(c(NH_2) * \alpha)$. Hence, changing the pH of a certain solution does not affect the loading ratio, while it significantly changes the charge ratio.

We have investigated samples prepared at different pH varying the ratio of the building blocks such that the charge ratio c_r is kept constant. Therefore, at each pH the number of dendrimers and their charge position (primary or tertiary amines) differs, while the ratio of dye to dendrimer charges remains constant. This approach has been chosen since it permits to investigate the effects of protonated amine group position on nanoparticle stability and structure. Focus is the definition of a phase diagram reporting nanoassembly structures as a function of pH.

The dendrimer is uncharged at pH = 10.5, where all the amine groups are deprotonated. As the pH decreases, the primary amines start to be protonated and the dendrimer becomes positively charged. At pH = 7.0 all primary amines are protonated. Between pH = 7.0 and pH = 4.0, the tertiary amine groups, mostly in the inside of the molecule, become protonated, and at pH = 3.5 both, primary and tertiary amines, are protonated and the molecule is fully charged. [26]

2.1 Particle stabilization: ζ-potential

For the understanding of nanoparticle stabilization, ζ-potential measurements have been performed. This measures the differences of electrostatic potential between the solvent and the layer of fluid attached to the dispersed nanoassemblies. Therefore, when the nanoparticles are electrostatically stabilized, it is related with the stability of the aggregates: more stable nanoassemblies usually show a higher ζ-potential value in comparison to less stable ones.

Measurements have been performed at different pH adjusting the ratio of dendrimer and dye molecules to keep the charge ratio constant at c_r = 1.8. This charge ratio has been chosen since here all the dendrimers aggregate into the nanoparticles, while at lower values the nanoparticle shape remains constant but free dendrimers are present in solution.[27] Results are shown in Figure 1. When the solution pH changes, the ζ-potential remains almost constant between 37 ± 4 mV and 48 ± 4 mV. Hence, when the charge ratio is kept constant, the nanoparticle charge does not depend on the solution pH. The protonation state of the dendrimer, i.e. the number of charged amine groups and their position, does not play any role in the stabilization process as long as the dye to dendrimer charge ratio remains constant. Moreover, keeping constant the charge ratio c_r, it is possible to obtain stable particles at high pH, even when the corresponding loading ratio is rather small as in the case of pH = 8.5 where the corresponding loading ratio is *l* = 0.5, two times less than the stoichiometric ratio.

This behavior is completely different from what has been observed when the loading ratio is kept constant to *l* = 1.8 (Figure 1) changing the pH.[22] In this case, the ζ-potential is not constant: it decreases continuously from 42 mV at pH = 3.5 (c_r = 1.8) to 20 mV at pH = 8.0 (c_r = 4.3). Hence, it is evident that in the two cases the nanoparticles show different stability and that the choice of the parameter, which is kept constant while changing the pH, has a substantially different impact in the particle stabilization. Further, the case of constant loading ratio results in the definition of pH ranges where the nanoparticles are stable and ranges where precipitation occurs, while when the charge ratio is kept constant the nanoparticles are stable and do not precipitate at any pH. This is another sign of the importance of the charge ratio in the stabilization process. Constant charge ratio means constant excess of dendrimer charges at each pH, i.e. less dye molecules per dendrimer for decreasing dendrimer charge, while constant loading ratio means decrease of the dendrimer charge excess. The results confirm that the nanoparticles are stabilized by the excess of dendrimer charges.

Figure 1 ζ-potential results for: Ar26 and G4 at constant charge ratio c_r = 1.8 and Ar26 and G4 at constant loading ratio *l* = 1.8.[22]

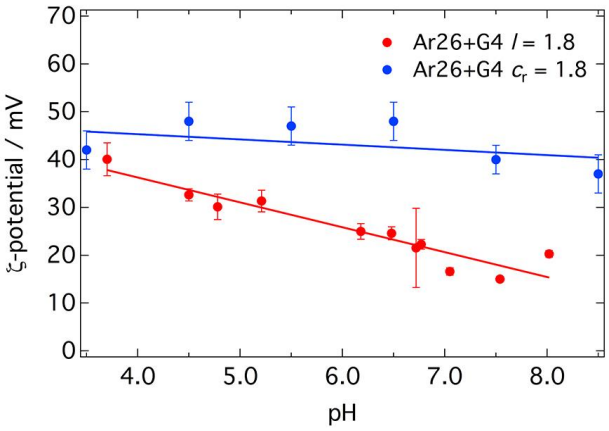

In conclusion we have demonstrated that, when the charge ratio is kept constant, stable nanoparticle can be formed at each pH, even when the loading ratio is low (I = 0.5). We have shown that the dendrimer protonation has no effect on the stabilization. This is in difference to the results measured keeping constant the loading ratio. These results clearly indicate the importance of the charge ratio on the self-assembly and the role of electrostatic interaction on nanoparticle stabilization. The delicate balance of dye and dendrimer charges is the key to control nanoparticle stability.

2.2 Nanostructure Characterization: Small Angle Neutron Scattering

The nanoparticle shapes and dimensions have been investigated by SANS. This technique permits the investigation of the nanoassembly structure as a function of the pH giving insight into the role of the dendrimer protonation on the self-assembly process.

Figure 2 a) SANS curves measured at different pH keeping the c_r constant. Different shapes are observed. b) Comparison of Ar26+G4 at pH = 4.5 forming cylinders with elliptical cross-section and Ar26+G4 at pH = 7.5 forming spheres.

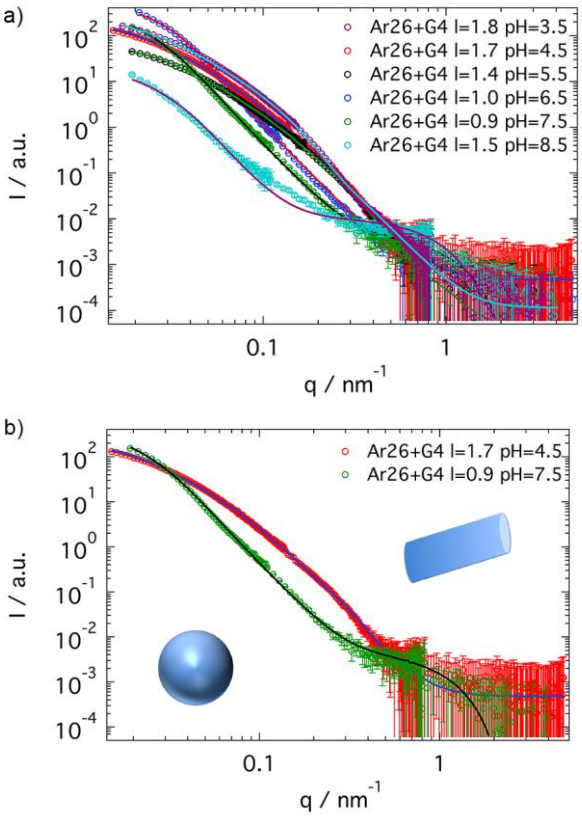

pH	I	Shape	Cross–section		L / nm	R / nm
			r_{min} / nm	r_{maj} / nm		
3.5	1.8	Ellipt. Cylinder	11 ± 1	44 ± 4	300	
4.5	1.7	Ellipt. Cylinder	10 ± 1	40 ± 4	220 ± 10	
5.5	1.4	Ellipt. Cylinder	9 ± 1	36 ± 4	170 ± 10	
6.5	1.0	Sphere				46 ± 2
7.5	0.9	Sphere				36 ± 2
8.5	0.5	Sphere				32 ± 2

Table 1 Geometric Parameters as resulting from the SANS fit for Ar26 + G4 at C_r = 1.8

The SANS results for Ar26 and G4 dendrimer at different pH are depicted in Figure 2a. First, it is evident that the curves rise at low q indicating the presence of nanoparticles in solution. From the smallest measured wave vector $q_{min,}$ it is possible to obtain information on the dimension that the nanoparticle at least has, which in this case it is in the order of hundreds nanometers. To obtain the shapes and the dimensions of these nanoassemblies precisely, the curves have been fitted using structural models. Two fits and resulting particle shapes are given in Figure 2b: One of the SANS curves corresponds to elongated nanoparticles with elliptical cross section and the other one to spherical particles. As evident in Figure 2a, changing the pH and keeping constant the charge ratio, two different nanoparticle structures can be identified: between pH = 3.5 and pH = 5.5, Ar26 and G4 dendrimer form cylinders with elliptical cross section, while at pH higher than pH = 6.5 spherical nanoassemblies are formed. The parameters resulting from the fits are given in Table 1. Between pH = 3.5 (I = 1.8) and pH = 5.5 (I = 1.4), Ar26 and G4 dendrimer form cylinders with elliptical cross section. The length decreases as the pH increases from L = 300 nm to L = 170 nm, while the cross-section remains almost constant (minor axis r_{min} = 10 nm and major axis r_{maj} = 40 nm). At pH = 6.5 the shape changes and the nanoparticles become spherical. At higher pH the nanoparticle shape remains spherical and the dimensions decrease from R = 46 nm (pH = 6.5) to R = 32 nm (pH = 8.5). Evidently, while the pH has no effect on the nanoparticle stability in general, it controls the nanoparticle shape: from cylindrical nanoparticles at pH < 6.5 to spheres at pH ≥ 6.5. The transition takes place around pH = 6.5, where all the external primary amines and only few internal amine groups are protonated. Therefore, there is a strong connection of shape with dendrimer protonation: when only the primary amine groups are protonated, isotropic nanoparticles are observed, while when there are sufficient protonated internal tertiary amines, anisotropic nanoparticles are observed. Hence, pH can be used as external trigger to obtain stable particles with different shapes. In addition, at pH > 6.5 a second signal around q = 0.7 nm^{-1} arises in the SANS curves. This effect is due to the loading ratio. At pH = 6.5, the loading ratio is lower than 1.5 and some free dendrimer molecules can be found in

solution. The signal grows as the pH increases, because the amount of free dendrimer molecules increases as the loading ratio decreases.

The decrease in size with increasing pH is interesting because it is opposite to what has been observed when keeping constant the loading ratio for the spherical nanoparticles. In addition for the elongated nanoparticles, here the size decrease is followed by a decrease of the loading ratio, while in the previous case it was followed by an increase of the charge ratio.[25] A first explanation may lie in the nanoparticle stability: when the loading ratio is kept constant, less stable nanoparticles are formed at high pH and these particles incorporate more building blocks resulting in larger aggregates, while when the charge ratio is kept constant, stability does not change. This finding points out the crucial importance of the electrostatic interaction in the self-assembly process. Electrostatic interactions do not only interconnect the molecular building blocks, but also control the dimensions of the nanoassemblies.

Due to the impact of the dendrimer protonation degree on the nanoparticle structure, it is worth to compare the structural results obtained at fixed pH and different charge ratio c_r to our previous results obtained at different loading ratio *l*.[22] This might be a first step in the understanding of the role of the ratio between the building blocs on nanoparticle formation and stabilization. The comparison is depicted in Figure 3: it is evident that different nanoparticle structures can be observed at the same pH. For example, at pH = 4.5 at loading ratios *l* = 1.0 and *l* = 1.7 (Figure 3a), the same shape is observed: the nanoassemblies are cylinders with elliptical cross-section. When the pH rises to pH = 5.5 (Figure 3b), different shapes can be found at *l* = 1.4 (cylinders with elliptical cross-section) and at *l* = 1.0 (spheres). The same happens at pH = 7.5 and pH = 8.5 (Figure 3c and d). This means that the nanoparticle shape is not only controlled by the pH, but also by the ratio of the building blocks. The effects are summarized in Scheme 2. From the lowest loading ratio to the highest, it can be seen that when the loading ratio is smaller than 1.0, i.e. for a great excess of dendrimer charges, the building blocks form spherical aggregates, while when the loading ratio increases anisotropic nanoparticles are formed.

Figure 3 Comparison of SANS curves measured at the same pH for Ar26+G4: a) at pH 4.5 at l = 1.0 (c_r = 1.1) and l = 1.7 (c_r = 1.8) b) curves measured at pH 5.5 at l = 1.0 (c_r = 1.3) and l = 1.4 (c_r = 1.8) c) curves measured at pH 7.5 at l = 1.8 (c_r = 3.9) and l = 0.9 (c_r = 1.8) d) curves measured at pH 8.5 at l = 1.8 (c_r = 6.7) and l = 0.5 (c_r = 1.8)

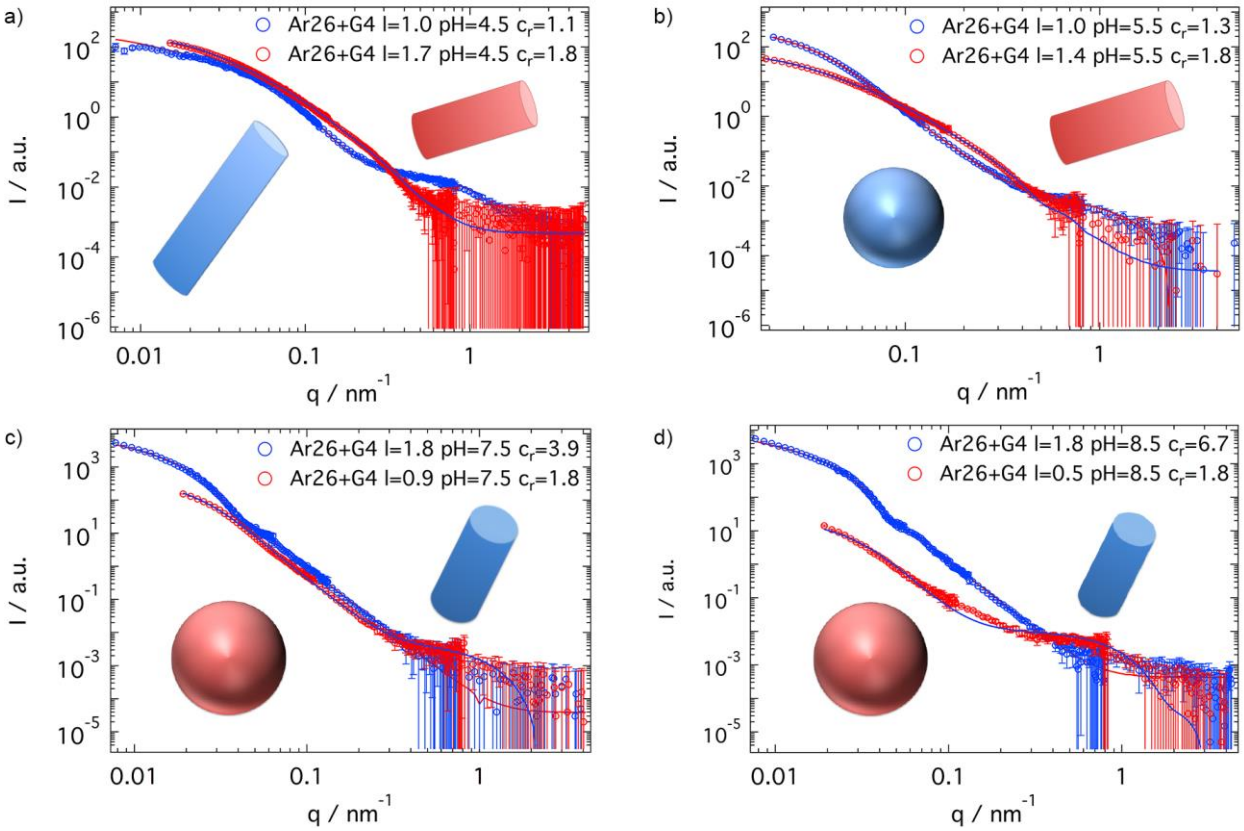

c_r	1.8	1.8	1.8	1.8	1.8	1.8	3.6	6.7
I	0.5	0.9	1.0	1.4	1.7	1.8	1.8	1.8
pH	8.5	7.5	6.5	5.5	4.5	3.5	7.5	8.5

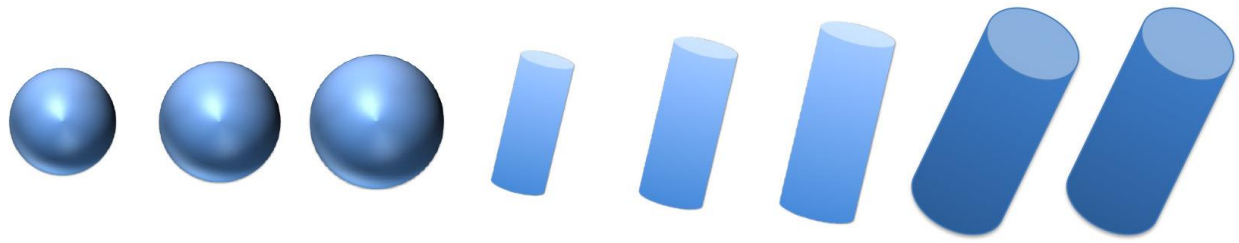

Scheme 2 Nanoparticle shape as a function of charge ratio and loading ratio. pH value is reported for clarity

This might be related to the π-π interaction strength: since only few dye molecules bind to the dendrimers, the π-π interaction is not sufficient to form anisotropic nanoparticles at these loading ratios. When the loading ratio *I* is higher than 1.0, dyes and dendrimers form cylinders with elliptical cross-section. The nanoparticles become larger as the loading ratio *I* increases. When the loading ratio *I* is 1.8, the charge ratio c_r increases. This has been realized by changing the number of protonated amine groups and keeping constant the amount of dye molecules. The resulting particle again is a cylindrical assembly, but in this case the cross-section is circular. The length of the nanoparticle continues to increase. The transition again can be explained considering the mutual inter-dye π-π interaction. Changing the charge ratio decreases the number of available binding sites and shifts the interaction to the primary amine groups of the dendrimer. In this configuration the π-π interaction is sufficiently strong to form elongated nanoparticles, but the formation of an anisotropic cross-section is prohibited.

Concluding the structural analysis, we showed how pH controls the nanoparticle structure regulating the shape and the dimension. When only the external primary amine groups of the dendrimer are protonated (pH > 6.5) spherical particles result, whereas when both primary and tertiary (internal) amine groups are protonated, elongated structures are formed. In addition, we have shown that nanoparticle dimensions decrease as the pH increases when the charge ratio c_r is constant. This finding has great potential for example for drug delivery since pH can trigger the dimensions of the nanoparticles or their shape. In addition, we demonstrated how the building block ratio is crucial in structure determination when the pH is constant. A phase diagram has been built describing the structural behavior as a function of the building block ratio and the π-π interaction.

2.3 π-π Stacking: UV-Vis Spectroscopy

To understand the pH effects on the nanoparticle structure more deeply we investigated the dye-dendrimer association on the molecular scale via UV-Vis spectroscopy. Nanoparticle formation through electrostatic interaction between dyes and dendrimers induces spatial proximity of the dye molecules that then can mutually interact.[19,28,29]

Figure 4 a) UV-Vis spectra for Ar26 and G4 at different pH. The peak position and intensity change with pH. b) Fit of the UV-Vis spectra of Ar 26 and G4 at pH = 6.5 according to exciton theory. Three Gaussian curves have been used to obtain good agreement with the experimental data.

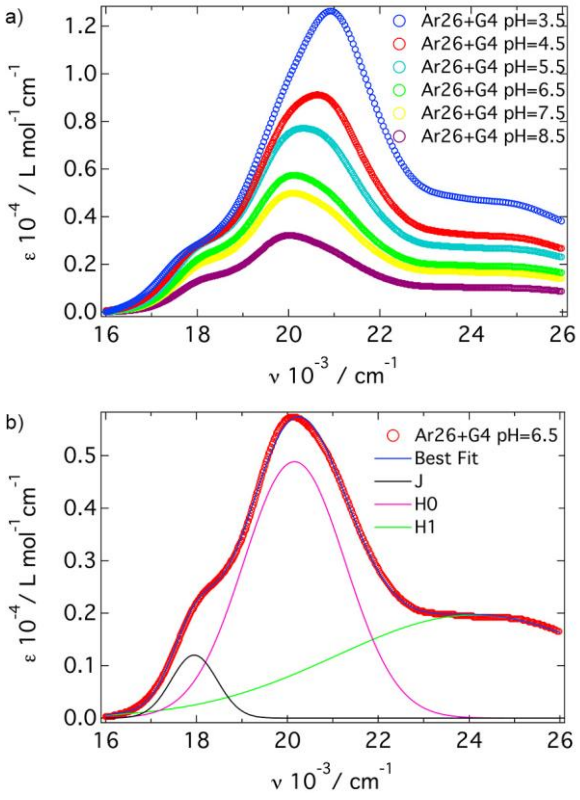

This interaction corresponds to a mutual arrangement of the two interacting π-systems and results in a modification of the UV-Vis spectrum. In more detail, the dye-dye interaction causes the splitting of the first excited state of the monomer.[30] Therefore, the π-π stacking can be studied with UV-Vis spectroscopy and the results can be described by the exciton theory.[31-34] For this system, good agreement with the experimental data has been obtained fitting the spectra with three Gaussian curves resulting in three transitions: J, H_0 and H_1. The measured UV-Vis spectra and a fit example are given in Figure 4a and b.

The first parameter obtained from the fit is the peak position, and, as is evident from Figure 4a, it changes with the pH. The trend is shown in Figure 5a where the peak position for the H_0 band is given as a function of pH. Two different regimes can be identified: for 3.5 ≤ pH ≤ 6.5 the peak shifts continuously, decreasing form 20751 cm^{-1} at pH = 3.5 to 20150 cm^{-1} at pH = 6.5, while at pH > 6.5 the position remains steady around 20100 cm^{-1}. From the SANS results, this effect is clearly connected to the nanoparticle shape. The peak position changes when the nanoparticles are elongated and remains constant at pH higher than 6.5 where spheres are formed.

Now it is possible to obtain a geometric parameter describing the dye-dye molecular interaction: the twist angle β between two dyes molecules: [35]

$$\beta = 2\, arctan\sqrt{\frac{f_J}{f_H}} \qquad (4)$$

Where f_i is the oscillator strength for the *i*-th band calculated by integration of the respective peak area.

The twist angle as a function of pH is reported in Figure 5b. Two different regimes can be identified: pH < 6.5 and pH > 6.5. In the first, the twist angle β decreases continuously from 55° (pH = 3.5) to 37° (pH = 6.5), while in the second it remains constant around 38°. As in the case of the peak position, this behavior can be understood if the nanoparticle structure is taken into account: the angle is constant for spherical nanoassemblies, whereas it changes for elongated ones.

Thus, by UV-Vis spectroscopy, we showed that pH acts not only on the nanocale structure, but also on the dye-dye molecular stacking. It results in a twist angle change and a relationship of twist angle and nanoparticle structure has been obtained.

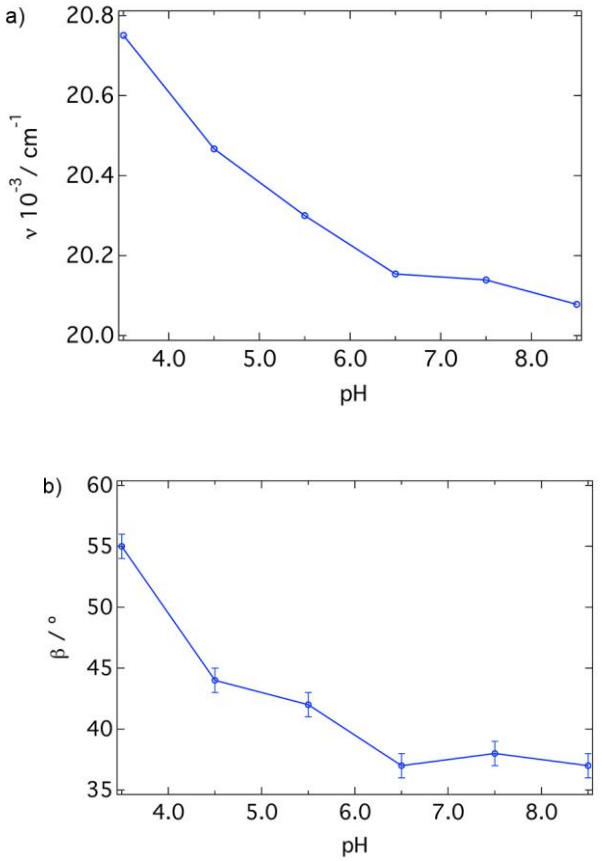

Figure 5 a) Peak position as obtained from the fit according to exciton theory for H0 band. The peak position changes with pH and b) .Twist angle as obtained from equation (1) as a function of solution pH. From pH = 6.5 the angle is constant around 38°, for pH < 6.5 it decreases continuously and it is always higher than 40°.

Conclusions

Key understanding of pH effects in electrostatic self-assembly in solution has been gained. We have shown that keeping constant the charge ratio, i.e. the excess of dendrimer charges, results in stable nanoparticles over a wide range of pH (3.5 ≤ pH < 8.5). Hence, the position of the charged groups does not affect the nanoparticle stability if the charge ratio is kept constant. In contrast, a change in nanoparticle shape has been observed around pH = 6.5. Cylindrical particles are formed at pH < 6.5 while spherical particles are formed at pH ≥ 6.5. The nanoparticles become smaller as the pH increases. Hence, pH can be used to tailor the nanoparticle structure. Spherical nanoparticles are formed when only primary amines are protonated, the cylinders are formed when also the tertiary amines are protonated, thus the position of the charge is crucial in defining the nanoparticle shape. This might be because the position and the number of the amine groups available for binding affect the interaction between dye and dendrimer and the dye-dye interaction. Furthermore, the environmental pH controls the dye-dye stacking: it modifies the twist angle between the dye molecules. When spherical nanoparticles are formed the angle remains constant around, while when elongated ones

are formed it increases continuously with pH. Overall, we have connected the pH effect on different levels, from the molecular to the supramolecular level, showing that the pH can be used as trigger to obtain stable nanoparticles with different shapes if the charge ratio is kept constant. We have shown how the control of the dendrimer protonation modifies the dye-dye stacking resulting in structural changes. This is key in understanding the nanoparticle formation in electrostatic self-assembly and is of great interest for application such as drug delivery where smart carrying systems are used.

Acknowledgements

This work benefitted from SasView software, originally developed by the DANSE project under NSF award DMR-0520547. We acknowledge the support of Institut Laue-Langevin, Grenoble, France. Financial support of Deutsche Forschungsgemeinschaft (DFG), of the Interdisciplinary Centre for Molecular Materials (ICMM), and of the Institut Laue-Langevin is gratefully acknowledged. The support of the Partnership for Soft Condensed Matter (PSCM) is acknowledged.

Notes and references

1 H. Ringsdorf, B. Schlarb and J. Venzmer, *Angew. Chem., Int. Ed. Engl.*, 1988, **27**, 113–158;
2 S. Zhou, C. Burger, B. Chu, M. Sawamura, N. Nagahama, M. Toganoh, U. E. Hackler, H. Isobe and E. Nakamura, *Science*. 2001, **291**, 1944–1947;
3 D. E. Discher and A. Eisenberg, *Science*, 2002, **297**, 967–973;
4 C. Schmuck and M. A. Schwegmann, *J. Am. Chem. Soc.*, 2005, **127**, 3373–3379;
5 P. Jonkheijm, P. van der Schoot, A. P. H. J. Schenning and E. W. Meijer, *Science*, 2006, **313**, 80–83;
6 M. S. Nikolic, C. Olsson, A. Salcher, A. Kornowski, A. Rank, R. Schubert, A. Frömsdorf, H. Weller and S. Förster, *Angew. Chem., Int. Ed.*, 2009, **48**, 2752–2754;
7 R. J. Murphy, D. Pristinski, K. Migler, J. F. Douglas and V. M. Prabhu, *J. Chem. Phys.*, 2010, **132**, 194903;
8 H. Meng, M. Xue, T. Xia, Y.-L. Zhao, F. Tamanoi, J. F. Stoddart, J. I. Zink and A. E. Nel, *J. Am. Chem. Soc.*, 2010, **132**, 12690–12697;
9 Y. Geng, P. Dalhaimer, S. Cai, R. Tsai, M. Tewari, T. Minko and D. E. Discher, *Nat. Nanotech.*, 2007, **2**, 249–255;
10 R. A. Petros and J. M. DeSimone, *Nat. Rev. Drug Discov.,* 2010, **9**, 615–627;
11 Z. Popovic, W. Liu, V. P. Chauhan, J. Lee, C. Wong, A. B. Greytak, N. Insin, D. G. Nocera, D. Fukumura, R. K. Jain and M. G. Bawendi, *Angew. Chem., Int. Ed.*, 2010, **49**, 8649–8652;
12 J.-W. Yoo, D. J. Irvine, D. E. Discher and S. Mitragotri, *Nat. Rev. Drug Discov*., 2011, **10**, 521–535;
13 J. Nam, N. Won, H. Jin, H. Chung and S. Kim, *J. Am. Chem. Soc.*, 2009, **131**, 13639–13645;
14 A. Bogomolova, S. Keller, J. Klingler, M. Sedlak, D. Rak, A. Sturcova, M. Hruby, P. Stepanek and S. K. Filippov, *Langmuir*, 2014, **30**, 11307−11318;
15 A. Ghosh, M. Haverick, K. Stump, X. Yang, M. F. Tweedle and J. E. Goldberger, *J. Am. Chem. Soc.,* 2012, **134**, 3647−3650;
16 L. Tauk, A. P. Schröder, G. Decher and N. Giuseppone, *Nat. Chem.*, 2009, **1**, 649–656;
17 F. Gröhn, *Soft Matter* 2010, **6**, 4296–4302;
18 I. Willerich, Y. Li and F. Gröhn, *J. Phys. Chem. B*, 2010, **114**, 15466–15476;
19 I. Willerich and F. Gröhn, *Macromolecules*, 2011, **44**, 4452–4461;
20 C. Ruthard, M. Schmidt and F. Gröhn, *Macromol. Rapid Commun.*, 2011, **32**, 706–711;
21 I. Willerich and F. Gröhn, *J. Am. Chem. Soc.*, 2011, **133**, 20341–20356;
22 G. Mariani, R. Schweins and F. Gröhn, *J. Phys. Chem. B.*, 2016, **120**, 1380–1389;
23 A. Guinier and G. Fournet, Small-Angle Scattering of X-Rays, John Wiley and Sons, New York, 1955.
24 G. Porod, Small Angle X-ray Scattering; O. Glatter, O. Kratky, Eds.; Academic Press, Inc; New York, 1982; Chapter 2, pp 17-52.
25 L. A. Feigin, D. Svergun, Structure Analysis by Small-Angle X-Ray and Neutron Scattering, Plenum, New York, 1987.
26 D. A. Tomalia, H. Baker, J. Dewald, M. Hall, G. Kallos, S. Martin, J. Roeck, J. Ryder and P. Smith, *Polymer J.,* 1985, **17**, 117–132;
27 G. Mariani, D. Moldenhauer, R. Schweins, and F. Gröhn, *J. Am. Chem. Soc.*, 2016, **138**, 1280-1293;
28 J. F. G. A. Jansen, E. M. M. de Brabander-van den Berg and E. Meijer, *Science*, 1994, **266**, 1226–1229;
29 D. L. Richter-Egger, J. C. Landry, A. Tesfai and S. A. Tucker, *J. Phys. Chem. B*, 2001, **105**, 6826–6833;
30 B. Neumann, K. Huber and P. Pollmann, *Phys. Chem. Chem. Phys.*, 2000, **2**, 3687–3695;
31 E. G. McRae, *Aust. J. Chem.*, 1961, **14**, 329–343;
32 E. G. McRae, *Aust. J. Chem.*, 1961, **14**, 344–353;
33 E. G. McRae, *Aust. J. Chem.*, 1961, **14**, 354–371;
34 M. Kasha, H. R. Rawls and A. El-Bayoumi, *Pure Appl. Chem.*, 1965, **11**, 371-392;
35 A. R. Monahan and D. F. Blossey, *J. Phys Chem.*, 1970, **74**, 4014-4021.

4.4 Inducing Hetero-Aggregation of Different Azo Dyes through Electrostatic Self-Assembly

Submitted to Chemistry - A European Journal

Inducing hetero-aggregation of different azo dyes through electrostatic self-assembly.

Giacomo Mariani,[a,b] Anne Kutz,[a] Zhenyu Di,[c] Ralf Schweins[b] and Franziska Gröhn*[a]

Abstract: Combining chemically different building blocks in supramolecular nanoparticles is a promising key to tailored structures and functionalities. π–π –heterostacks of dye molecules form upon electrostatic self-assembly with a polyelectrolyte, resulting in stable ternary nanoassemblies in aqueous solution. Core-shell spheres, cylinders and flexible cylinders result, which exhibit new shapes different from the binary systems. Particle shapes can be tuned via the dye composition.

The association of building blocks into supramolecular particles is of great importance as it allows for an elegant synthesis of a variety of functional structures.[1] In nature, self-assembly is the origin of complex architectures. Synthetic assemblies of high potential are supramolecular polymers,[2] or carrier systems.[3] Of particular interest is the association of building blocks with different properties to create nanoassemblies with enhanced or with novel functionalities. For example, the coadsorbance of two dyes in SiO_2 optical thin films causes enhanced fluorescent emission in the near-IR where the characteristics of the energy transfer can be controlled through the dye ratio.[4]

Recently, we have introduced a concept to create well-defined nano-objects in solution by electrostatic self-assembly of macroions and multivalent aromatic counterions.[5] Different assembly shapes ranging from spheres over cylinders and vesicles to networks have been created and an external control of the nanoparticle size through pH and light has been demonstrated.[5e,6] The assembly is based on the ionic interconnection of macroions through multivalent organic counterions, with thereby induced secondary interaction effects such as π-π stacking. Hence, the association does not rely on a specific binding motif. Specifically, we have shown that multivalent ionic azo dyes interconnect dendrimeric macroions to form nanoparticles with sizes up to more than hundred nanometers.[7] Recently, we have revealed a relationship of the size of the self-assembled nanoparticles with the free energy of dye-dye association.[8] Thus, dye stacking plays a key role in the self-assembly process. However, up to now only the aggregation of dendrimeric macroions with one dye species has been studied. By combining dyes with different properties ways towards the synthesis of novel systems with tailored properties may be openend, for example in the fields of nonlinear optical properties[9] or solar energy conversion.[10] In addition, systems in which multiple dyes are jointly used to interconnect the polyelectrolytes are of fundamental interest with regard to the role of dye π-stacking. It is well known that H- and J-aggregation of identical dye molecules (homoaggregates) can be described by exciton theory,[11] but only a few investigations on heteroaggregation exist. For example, stacking of different dyes has been achieved using specifically synthesized DNA derivatives as support[12] or by addition of ions such as Mg^{2+}.[13]

Herein, we present an extension of the concept of dendrimer-induced aggregation of dye molecules into stable supramolecular nanoparticles, to binary dye mixtures. Again, stable nanoassemblies form. The interaction of the different dyes results in the formation of heterostacks. The structure of the assemblies is discussed and compared to the one formed in the single dye-dendrimer case.

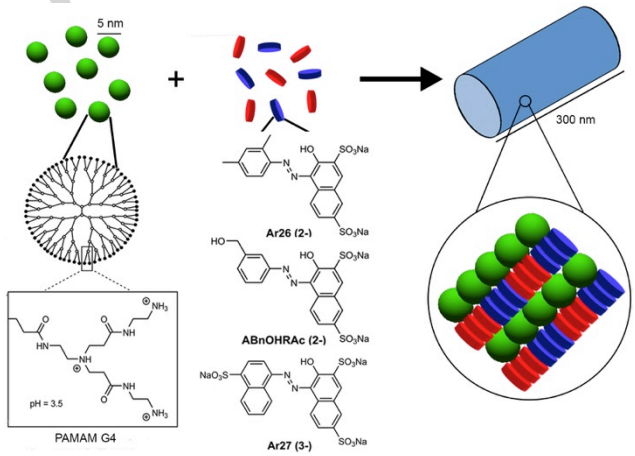

Scheme 1. Molecular structure of the building blocks used in this study and schematic representation of the self-assembly process.

We have formed electrostatically assembled nanoparticles of polyamidoamine (PAMAM) generation 4 dendrimers and a mixture of two different azo dyes (Scheme 1): a trivalent (Ar27) in combination with a divalent dye (Ar26 or ABnOHRAc). The three dyes chosen are known to stack with different twist angles: Ar27 and Ar26 exhibit different angles of 38° and 55°, while Ar27 and ABnOHARAc stack with the same angle (38°).[7b,14] All samples have been prepared at a loading ratio (molar ratio of the sum of the sulfonate groups of the two dyes to dendrimer primary amine groups) of I = 1.8, since at this well-defined stable dye-dendrimer nanoparticles result for the binary cases.

Dynamic light scattering (DLS) was used to analyze the nanoparticle formation. Electric field autocorrelation functions $g^1(\tau)$ and relaxation time distributions $A(\tau)$ for dendrimer-dye

[a] G. Mariani, A. Kutz, Prof. Dr. F. Gröhn
Department of Chemistry and Pharmacy and Interdisciplinary Centre for Molecular Material (ICMM)
Friedrich-Alexander-Universität Erlangen-Nürnberg
Egerlandstraße 3, D-91058 Erlangen, Germany
E-mail: franziska.groehn@fau.de
[b] Dr. R. Schweins
DS/LSS
Institut Laue-Langevin
71 avenue des Martyrs, F-38000 Grenoble, France
[c] Zhenyu Li
Jülich Centre for Neutron Science, Outstation at MLZ,
Lichtenbergstr. 1, 85747 Garching, Germany

Supporting information for this article is given via a link at the end of the document.

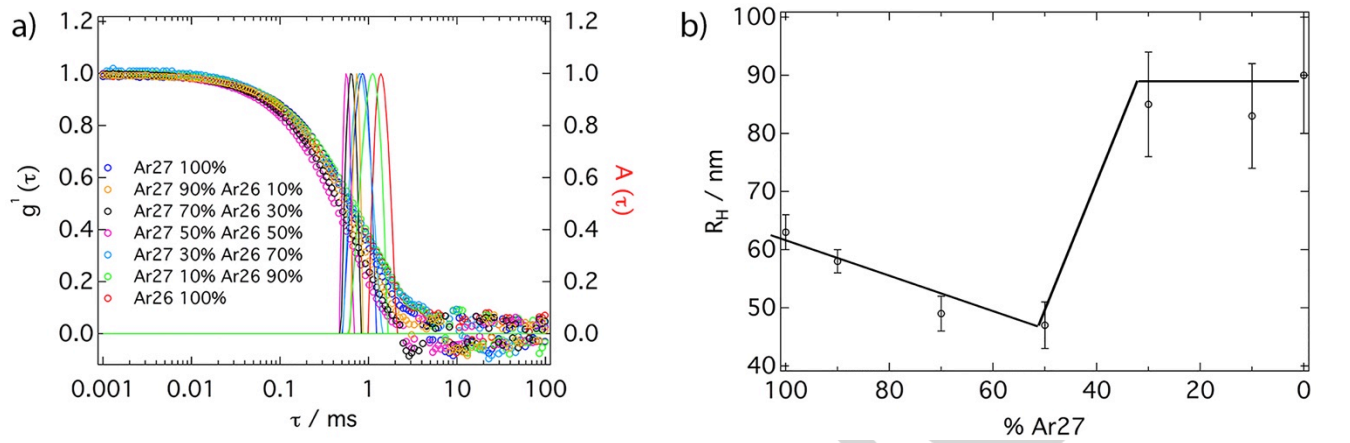

Figure 1. a) Dynamic light scattering analysis of ternary mixed-dye-dendrimer samples: electric field autocorrelation function $g^1(\tau)$ and distribution of relaxation time $A(\tau)$ for Ar27-Ar26-dendrimer G4 samples at I = 1.8 and b) Hydrodynamic radius R_H as a function of the Ar27 percentage in the sample

assemblies with Ar27 and A26 at different dye mixing ratios are depicted in Figure 1a. Formation of well-defined nanoparticles of a certain size occurs. Only one kind of assembly is present showing that the two dyes jointly form a new type of assembly. DLS data change with the mixing ratio: starting from Ar27 and increasing the percentage of Ar26, the characteristic decay time shifts to smaller values indicating a size decrease, reaching a minimum when equal amounts of Ar27 and Ar26 are present. When Ar26 becomes the major dye, the peak shifts back to longer relaxation times. Results in terms of the hydrodynamic radius R_H are given in Figure 1b showing the two different regimes: for 100 ≥ % Ar27 ≥ 50, R_H decreases from 63 nm to 47 nm and for % Ar27 < 50, R_H is constant around 85 nm. Hence, the combination of two dyes with different molecular structure and charge results in the formation of a single type of stable and well-defined nanoparticle in solution. Both dyes must be combined in one assembly and dimensions depend on the dye mixing-ratio.

Further, assembly formation and dye stacking have been investigated by UV-Vis spectroscopy, as depicted in Figure 2a-b. As the sample composition changes, the signal continuously shifts from the signal of one dye to the other. For Ar27 and ABnOHRAc (Figure 2b), the H-peak shifts from approximately 19000 cm^{-1} for Ar27 to 20500 cm^{-1} for ABnOHRAc. As reference, the spectra of the dye mixtures in absence of dendrimer have been measured (Figure 2c-d). Also here, a spectral shift is observed. Despite this similarity, the intensity and the form of the spectra significantly differ. The decrease in intensity when dendrimers are in solution is due to the formation of the nanoparticles, while the variation in the spectral form indicates that the dye stacking is different. Moreover, this difference reveals that no dye-only stacks are present in solution once the nanoparticles have formed. In both the cases, on first sight, the absorbance appears to possibly result from the sum of the signals of the single dye-dendrimer assemblies or of the pure dyes. Hence, the sum weighted according to the sample composition has been used to describe the experimental signal. A selection of the results for the dye-dendrimer system is given in Figures 2e-f, while the results without dendrimer are reported in the SI. For 70 % Ar26 and for 10 % ABnOHRAc in combination with Ar27, the calculated absorbance describes the experimental one perfectly. In contrast, for 10 % Ar26 and for 70 % ABnOHRAc in combination with Ar27, calculated and experimental spectra differ: here, the dye stacking changes, resulting in a change in the UV-Vis absorbance. To check if this effect is due to a different composition, a simple fit has been performed describing the experimental curve with the sum of the two single dye-dendrimer spectra with the dye percentage as fitting parameter (Figure 2e): the curve does not reproduce the experimental curve either; hence, the absorbance cannot be described on the basis of the single dye-dendrimer spectra. This behavior must be related to dye heterointeraction and heterostacking. The effect is observed for certain dye mixing ratios only, which differ for both systems. Evidently, the effect strongly depends on the molecular dye structure and on the sample composition. The same analysis has been performed for the dye-only mixtures: here, most of the experimental spectra can be described as the sum of the pure dye spectra. Only for one sample composition the fit does not reproduce the experimental spectrum: 70 % Ar27 and 30 % divalent dye, for both of the divalent dyes. This is in contrast to the dye-dendrimer case where the behavior depends on the dye used.

In terms of dye stacking, in general, different phenomena may occur: hetero- and homo-stacks, dye-only stacks and dye-dendrimer complexes without any dye-dye alignment. The existence of dye-only stacks can be excluded since at loading ratio I = 1.8, all the dye is bound to the dendrimers.[7b] No evidence of dye-dendrimer assemblies without dye-dye alignment has been found since the molecular dye structures are compatible such that even in absence of dendrimer the dyes can easily interact. In particular, un-aligned dyes would result in the presence of individual non-interconnected dye-loaded dendrimers, as without π–π stacking the dyes are unable to interconnect the dendrimers,[8b] a scenario which is not observed.

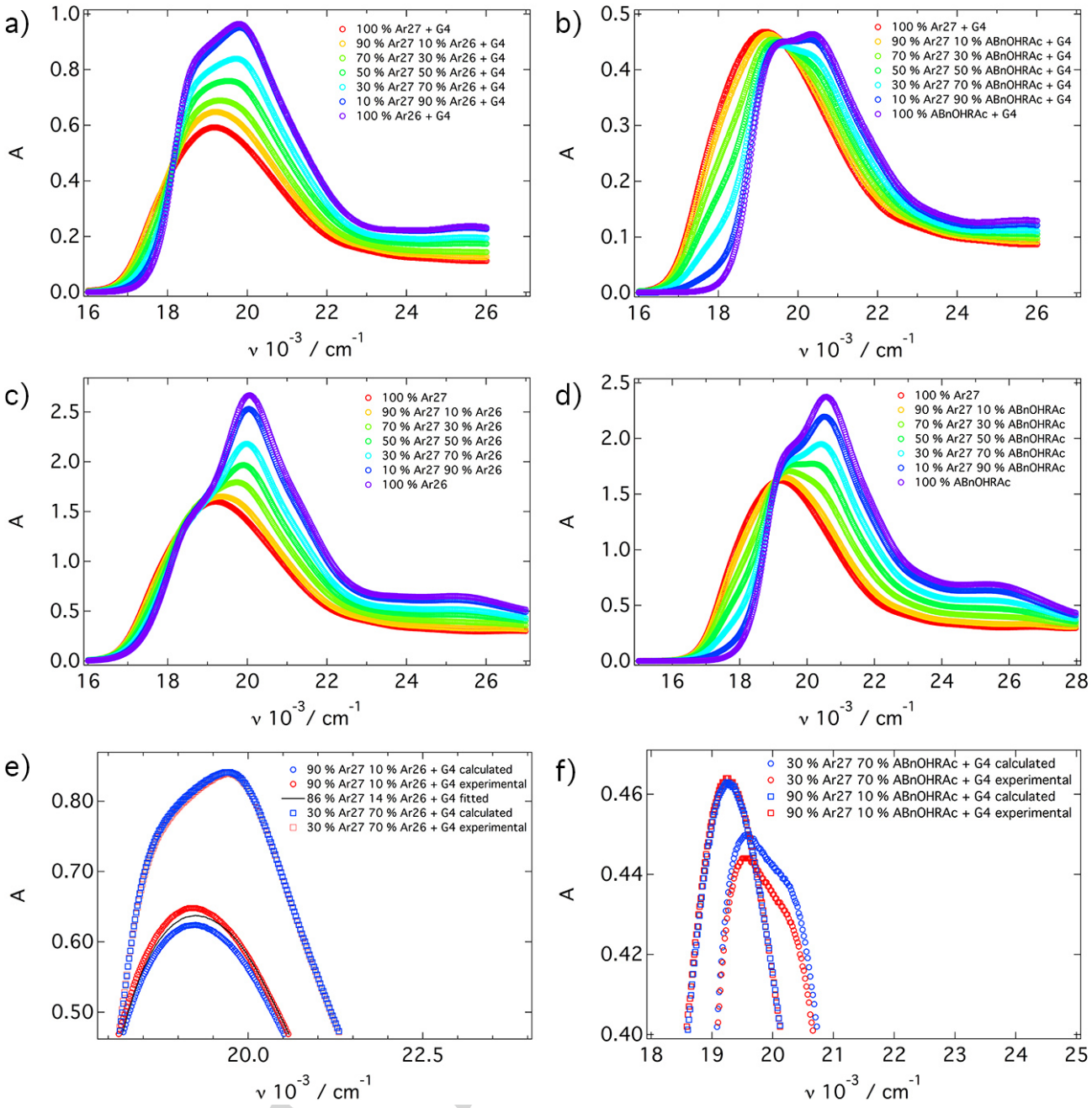

Figure 2. UV-Vis analysis of ternary mixed-dye-dendrimer samples: a) Ar27-Ar26-dendrimer samples at different dye mixing ratios; b) Ar27-ABnOHRAc-dendrimer samples at different dye mixing ratios; c) Ar27-Ar26 without dendrimer at different dye mixing ratios; d) Ar27-ABnOHRAc without dendrimer at different dye mixing ratios; e) Details for 30 % Ar27 and 70 % Ar26: good agreement of experimental and calculated absorbance, and 90 % Ar27 and 10 % Ar26: no agreement of experimental, calculated and fitted absorbance; f) Details for 90 % Ar27 and 10 % ABnOHRAc: good agreement of experimental and calculated absorbance, and for 30 % Ar27 and 70 % ABnOHRAc: no agreement of experimental and calculated absorbance.

When the experimental spectrum overlaps with the calculated one, the interaction of the dyes does not destroy the homostacks and homostacks coexist in one aggregate, heterointeraction may occur between the homostacks (case A in Scheme 2). At mixing ratios where the experimental spectra differ from the calculated ones, the homostacks are partially destroyed because the heterointeraction is stronger and more heterointeractions result (case B in Scheme 2). The proposed model is in good agreement with our recent results on the thermodynamics of the dye-dye interaction and with our calculation of the dye molecule spatial configuration.[15] The enthalpy change for the dye-dye interaction is $\Delta H_{\text{dye-dye}}$ $\Delta H_{\text{dye-dye}}$ = -29.0 kJ mol^{-1} for Ar26, $\Delta H_{\text{dye-dye}}$ = -24.3 kJ mol^{-1} for ABnOHRAc and $\Delta H_{\text{dye-dye}}$ = -20.0 kJ mol^{-1} for Ar27. In

addition, in the single dye-dendrimer case, Ar27 and ABnOHRAc have the same stacking angle, while Ar26 stacks with a larger angle. Hence, differences between the measured and calculated spectra can be due to the different compatibility of the dyes mixed. Ar27 and ABnOHRAc, with the same tilt angle and similar π-π interaction strength, behave accordingly to case A when the amount of the less strongly interacting dye (Ar27) is low (≤ 30 %). When the two dyes are present in more equal quantity, the system behaves accordingly to case B: the affinity between the different dye molecules breaks the homostacks and heterostacks form. In contrast, Ar27 and Ar26, with different tilt angle and more differing π-π interaction strength, behave accordingly to case B when the amount of the second dye species is low (≤ 10 %) because of their limited compatibility. The homostacks cannot easily stack on one another and the dye-dye interaction strength of the predominant dye disassembles the homostacks. In contrast, they behave accordingly to case A when the two species are present in more equal amounts, likely because the homo-interaction is strong and preserves the homostacks and only few homostacks are broken. In contrast, when the dye stacks form in the absence of dendrimer, the homostacks are not broken except when Ar27, the less strongly interacting dye, is present in low quantity (≤ 30 %). In this case the more strongly interacting dyes cause the disassembly of the less strong homostacks resulting in the formation of heterostacks.

Hence, we have demonstrated that heterointeraction occurs between the different dye species when spatial proximity is induced by electrostatic self-assembly. Heterointeraction can be exhibited between the homostacks or the homostacks break and multiple heterointeractions takes place between the different dye molecules.

To elucidate how dye mixing and heterostacking affect the assembly structure, small angle neutron scattering (SANS) has been performed. The SANS curves are shown in Figure 3.[16] It can be noted directly from the scattering curves that the two mixtures behave differently. In the case of Ar26 and Ar27 (Fig. 3a), the curves obtained for Ar27 90 % and 70 % and dendrimers are identical to the one obtained for

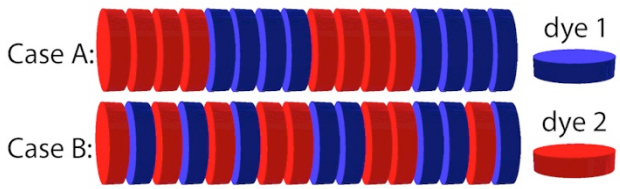

Scheme 2. Sketch of the model introduced showing the formation of hetero and homostacks describing UV-Vis absorption spectra.

Ar27- and different from the one of Ar26-dendrimer assemblies. Hence, these dye mixing ratios do not change the nanoparticle shape compared to Ar27. In contrast, for Ar26 and ABnOHRAc (Fig. 3b), the scattering curves are all different from the ones of the single dye-dendrimer assemblies. Thus, the two dyes assembling with the dendrimer form a new, different structure. To reveal the shape and dimensions, the curves have been fitted with structural models, results of which are depicted in Figure 3 as well. For the Ar26-Ar27 mixture, the assemblies with Ar27 90 % and 70 % Ar27 are core-shell spheres similar to Ar27-dendrimer. The total radius R_{tot} decreases from (44 ± 3) nm for 100 % Ar27 to (34 ± 3) nm for 70 % Ar27. Instead, for Ar26 forms an elliptical cylinder with a length L = (300 ± 10) nm and a cross-section with major axis R_{maj} = (44 ± 4) nm and minor axis R_{min} = (11 ± 1). Therefore, when Ar27 is the preponderant dye the shape remains the same as the Ar27 only. Larger amounts of Ar26 are needed to build different structures. In contrast, when Ar27 is mixed with ABnOHRAc, a new nanoparticle shape is found upon electrostatic self-assembly with the dendrimer. When the amount of Ar27 lies between 90 % and 70 %, the system forms ellipsoids. This structure is different from both, the one formed in the Ar27-dendrimer system (core-shell sphere) and the one formed by ABnOHRAc and dendrimer (flexible elliptical cylinder). Hence, dye mixtures with dendrimer macroions can be used to form new structure types. The ellipsoids become smaller as the Ar27 amount decreases: for 90 % Ar27 the minor axis is R_{min} = (9 ± 1) nm and the major axis R_{maj} = (60 ± 1) nm, whereas for 70 % Ar27 the minor axis is the same and the major axis decreases to R_{maj} = (50 ± 1) nm. At 50 % Ar27, the system forms flexible elliptical cylinders as found for ABnOHRAc and dendrimer. Here, the dimensions increase with increasing amount of ABnOHRAc from a total length L = (1500 ± 200) nm for 50 % ABnOHRAc to L = (2100 ± 100) for ABnOHRAc only. The cross-section remains almost unchanged with the minor axis R_{min} = (6 ± 1) nm and major axis R_{maj} = (30 ± 5) nm (ABnOHRAc 50 %) and R_{min} = (7 ± 1) nm and R_{maj} = (42 ± 6) nm (ABnOHRAc only).[17] Since no differences are observed with SANS between case A and B of the dye stacking we can conclude that the nanoassembly shape rather depends on the dyes used, in particular the predominant dye, than on the dye stacking characteristics. By varying the dye mixing ratio it is possible to control the shape and dimensions of the nanoparticles.

In conclusion, we have demonstrated that dye mixtures can be used to tune electrostatic self-assembly on the molecular and nanoscale level. A mixture of two different dyes together with an oppositely charged dendrimer results in the formation of stable and well-defined ternary dye-dendrimer nanoparticles, the structure of which depends on the dyes and on the mixing ratio. For Ar27-ABnOHRAc-dendrimer assemblies, a new structure is found: for large amounts of Ar27 ellipsoidal nanoparticles form, which are different from the structures built by Ar27-dendrimer (core-shell spheres) or by ABnOHRAc-dendrimer (flexible cylinders with elliptical cross-section) assemblies. On the molecular level, heterostacking can arise in addition to the well-known homostacking. It can occur between the homostacks or the heterointeraction can split the homostacks resulting in new heterostacks formed by the different dye molecules. Overall, we have demonstrated the possibility of using electrostatic self-assembly to induce dye heterostacking. Self-assembly of

two ionic dyes with a macroion represents a key to tune stacking and nanoparticle size and shape. This opens the route to a facile combination of functionalities in conjunction with a targeted structure design. Such a toolbox principle can yeld desired properties and possibly novel complex functionalities with a value in solar energy conversion and in photocatalysis.

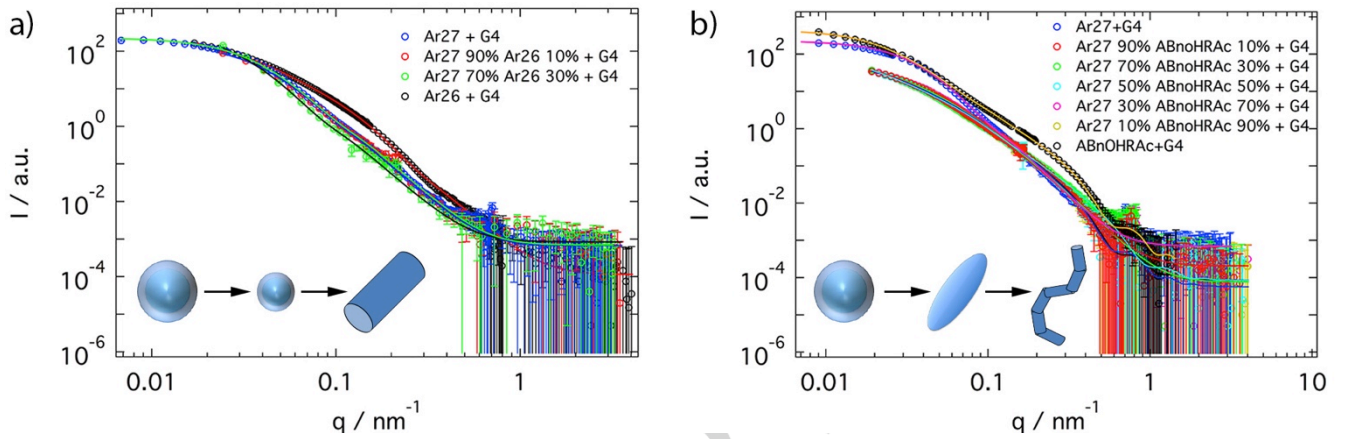

Figure 3. SANS results for ternary mixed-dye-dendrimer samples: a) Ar27-Ar26-dendrimer at different dye mixing ratios and b) Ar27-ABnOHRAc-dendrimer at different dye mixing ratios.

Acknowledgements

Financial support of the German Science Foundation (DFG) and the Interdisciplinary Center for Molecular Materials (ICMM, Universität Erlangen-Nürnberg) is gratefully acknowledged. This work benefitted from SasView software, originally developed by the DANSE project under NSF award DMR-0520547. We acknowledge the support of Institut Laue-Langevin.

Keywords: Dendrimers • Self-assembly • Nanomaterials • Supramolecular chem. • Dyes

[1] a) H. Ringsdorf, B. Schlarb, J. Venzmer, *Angew. Chem., Int. Ed. Engl.* **1988**, *27*, 113. b) J. F. G. A. Jansen, E. M. M. de Brabander-van den Berg, E. Meijer, *Science* **1994**, *266*, 1226-1229. c) D. E. Discher, A. Eisenberg, *Science* **2002**, *297*, 967. d) C. Schmuck, M. Schwegmann, *J. Am. Chem. Soc.* **2005**, 127, 3373. e) P. Jonkheijm, P. van der Schoot, A. P. H. J. Schenning, E. W. Meijer, *Science* **2006**, *313*, 80. f) J. R. Capadona, O. Van Den Berg, L. A. Capadona, M. Schroeter, S. J. Rowan, D. J. Tyler, C. Weder, *Nature Nanotechnology* **2007**, *2*, 765–769 g) F. M. Bayer, K. Hiltrop, K. Huber, *Langmuir* **2010**, *26*, 13815-13822. h) S. Srivastava, A. Santos, K. Critchley, K.-S. Kim, P. Podsiadlo, K. Sun, J. Lee, C. Xu, G. D. Lilly, S. C. Glotzer, N. A. Kotov, *Science* **2010**, *327*, 1355. i) I. Boehm, K. Isenbuegel, H. Ritter, R. Branscheid, U. Kolb, *Angew. Chem. Int. Ed.* **2011**, *50*, 7407-7409. j) Y.-C. Yeh, R. Tang, R. Mout, Y. Jeong, V. M. Rotello, *Angew. Chem. Int. Ed.* **2014**, *53*, 5137-5141.

[2] a) R. P. Sijbesma, F. H. Beijer, L. Brunsveld, B. J. B. Folmer, J. H. K. Hirschberg, R. F. M. Lange, J. K. L. Lowe, E. W. Meijer, *Science* **1997**, *278*, 1601-1604. b) J. B. Beck, S. J. Rowan, *J, Am. Chem. Soc.* **2003**, *125*, 13922-13923. c) G. Gröger, W. Meyer-Zaika, C. Böttcher, F. Gröhn, C. Ruthard, C. Schmuck, *J. Am. Chem. Soc.* **2011**, *133*, 8961-8971. d) M. Vybornyi, A. V. Rudnev, S. M. Langenegger, T. Wandlowski, G. Calzaferri, R. Haener, *Angew. Chem. Int. Ed.* **2013**, *52*, 11488-11493

[3] a) D. E. Discher, A. Eisenberg, *Science* **2002**, *297*, 967–973. b) M. Antonietti, S. Förster, *Adv. Mater.* **2003**, *15*, 1323–1333. c) R. J. White, K. Tauer, M. Antonietti, M.-M. Titirici, *J. Am. Chem. Soc.* **2010**, *132*, 17360–17363. d) Y. Guo, Y. Zhao, M. Han, J. Zhao, C. Hao, X. Wang, X. Wang, *Soft Matter* **2013**, *9*, 10306-10313.

[4] a) J. R. Sánchez-Valencia, J. Toudert, L. González-García, A. R. González-Elipe, A. Barranco, *Chem. Commun.* **2010**, *46*, 4372–4374. b) J. R. Sánchez-Valencia, F. J. Aparicio, J. P. Espinós, R. R. Gonzalez-Felipe, A. Barranco, *Phys. Chem. Chem. Phys.* **2011**, *13*, 7071–7082.

[5] a) F. Gröhn, K. Klein, S. Brand, *Chem.—Eur. J.* **2008**, *14*, 6866–6869. b) I. Willerich, F. Gröhn, *Chem.—Eur. J.* **2008**, *14*, 9112–9116. c) Y. Li, U. H. Yildiz, K. Müllen, F. Gröhn, *Biomacromolecules* **2009**, *10*, 530–540. d) C. Ruthard, M. Maskos, U. Kolb, F. Gröhn, *Macromolecules* **2009**, *42*, 830–840. e) F. Gröhn, *Soft Matter* **2010**, *6*, 4296-4302.

[6] a) I. Willerich, T. Schindler, H. Ritter, F. Gröhn, *Soft Matter* **2011**, *7*, 5444–5450. b) I. Willerich, F. Gröhn, *Macromolecules* **2011**, *44*, 4452. c) D. Moldenhauer, F. Gröhn, *J. Polym. Sci. Part. B: Polym. Phys.* **2013**, *51*, 802-816.

[7] a) I. Willerich, H. Ritter, F. Gröhn, *J. Phys. Chem. B* **2009**, *113*, 3339–3354. b) I. Willerich, Y. Li, F. Gröhn, *J. Phys. Chem. B* **2010**, *114*, 15466–15476.

[8] a) I. Willerich, T. Schindler, H. Ritter, F. Gröhn, *J. Phys. Chem. B* **2011**, *115*, 9710–9719. b) I. Willerich, F. Gröhn, *J. Am. Chem. Soc.* **2011**, *133*, 20341-20356.

[9] a) V. V. Shelkovnikov, R. V. Markov, A. I. Plekhanov, A. E. Simanchuk, Z. M. Ivanova, *High Energy Chem.* **2002**, *36*, 260–264.

b) F. Würthner, S. Yao, T. Debaerdemaeker, R. Wortmann, *J. Am. Chem. Soc.* **2002**, *124*, 9431–9447.

[10] a) M. V. Martínez-Díaz, G. de la Torre, T. Torres, *Chem. Commun.* **2010**, *46*, 7090–7108. b) S. Yagai, K. Iwai, M. Yamauchi, T. Karatsu, A. Kitamura, S. Uemura, M. Morimoto, H. Wang, F. Würthner, *Angew. Chem. Int. Ed.* **2014**, *53*, 2602–2606.

[11] a) E. G. McRae, *Aust. J. Chem.* **1961**, *14*, 229. b) E. G. McRae, *Aust. J. Chem.* **1961**, *14*, 344. c) E. G. McRae, *Aust. J. Chem.* **1961**, *14*, 354.d) M. Kasha, H. R. Rawls, A. El-Bayoumi *Pure Appl. Chem.* **1965**, *11*, 371. d) B. Neumann, K. Huber, P. Pollmann, *Phys. Chem. Chem. Phys.* **2000**, *2*, 3687-3695.

[12] a) H. Kashida, H. Asanuma, M. Komiyama, *Angew. Chem.* **2004** *116*, 6684-6687. b) C. B. Winiger, S. M. Langenegger, G. Calzaferri, R. Häner, *Angew. Chem. Int. Ed.* **2015**, *54*, 3643–3647.

[13] a) R. Michels, T. Sinemus, J. Hoffmann, B. Brutschy, K. Huber, *J. Phys. Chem. B* **2013**, *117*, 8611−8619.

[14] a) A. R. Monahan, D. F. J. Blossey, *Phys Chem.* **1970**, *74*, 4014. b) The twist angles measured in ref. 7a have been recalculated according to the equation reported in ref. 15a.

[15] a) G. Mariani, D. Moldenhauer, R. Schweins, F. Gröhn, *J. Am. Chem. Soc.* **2016**, *138*, 1280-1293.

[16] a) The samples have been prepared at a concentration of $3.5 \cdot 10^{-5}$ mol/kg. At this concentration the samples with the mixture of Ar26 and Ar27 are not stable for long time when Ar26 is more than 30 %, hence these samples have not been measured with SANS.

[17] a) In addition, the Kuhn length l_k increases as the ABnOHRAc amount increases from l_k = (100 ± 10) nm to l_k = (140 ± 10) nm.

Entry for the Table of Contents

COMMUNICATION

Different kinds of dye-heterostacks can form upon electrostatic self-assembly of mixtures of two different multivalent azo dyes with dendrimer macroions. Dye mixing can be used to tune the shape of the ternary organic nano-assemblies.

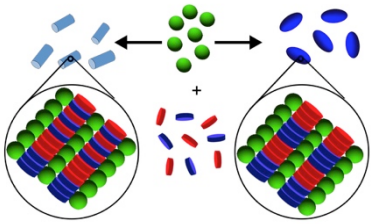

*G. Mariani, A. Kutz, R. Schweins, F. Gröhn**

Page No. – Page No.

Inducing hetero-aggregation of different azo dyes through electrostatic self-assembly.

SUPPORTING INFORMATION

Chemicals

Poly(amidoamine) (PAMAM) dendrimer of 4th generation was obtained from Dendritech, Midland, MI, USA and Sigma-Aldrich, Germany. The azo dyes Acid Red 26 (Ar26, C.I. 16150) and Acid Red 27 (Ar27, C.I. 16185) were obtained from Acros, Belgium. Disodium 4-((3-(hydroxymethyl)phenyl)diazenyl)-3-hydroxynaphthalene-2,7-disulfonate (ABnOHRAc) was synthesized by azo-coupling. The precursors for synthesis were 3-aminobenzyl alcohol (ABnOH, Merck KGaA, Germany), disodium 3-hydroxynaphthalene-2,7-disulfonate (R-Acid, RAc, Sigma-Aldrich, Germany). All azo dyes were then purified.

Characterization of the Azo Dyes

Yields were calculated on basis of carbon content from elemental analysis. NMR spectra showed that the product is salt-free except for <1 wt% sodium acetate and a small amount of ethanol <1 wt% which could not be removed despite extended drying under high vacuum. The purities given below are corrected for residual amounts of sodium acetate and ethanol, which were determined by NMR. Azo dyes are known to possess multiple molecules of crystal water. Thus, the pure dye contents are below 99%, which does not indicate impurities.

Ar26: ^{1}H NMR (D_2O, 300 MHz, 25 °C), δ [ppm]: 7.62 (s, 1H); 7.52 – 7.40 (m, 2H); 7.38 (s, 1H); 6.53 (d, J = 8.0 Hz, 1H); 5.95 (d, J = 8.1 Hz, 1H); 5.35 (s, 1H); 1.44 (d, J = 7.5 Hz, 6H). Anal. Calcd for $C_{18}H_{14}N_2Na_2O_7S_2$: C, 45.00; Found: C, 43.16; dye content: 96%.

Ar27: (D_2O, 300 MHz, 25 °C), δ [ppm]: 8.05 (d, J = 7.8 Hz, 1H); 8.01 – 7.93 (m, 2H); 7.87 (d, J = 8.4 Hz, 1H); 7.75 (d, J = 8.4 Hz, 1H); 7.68 – 7.50 (m, 2H); 7.16 (d, J

= 7.5 Hz, 1H); 7.11 – 6.91 (m, 2H). Anal. Calcd for $C_{20}H_{11}N_2Na_3O_{10}S_3$: C, 39.74; Found: C, 37.54; dye content: 94%.

ABnOHRAc: ^{1}H NMR (D_2O, 400 MHz, 20 °C), δ [ppm]: 7.95 (d, J = 8.8 Hz, 1H); 7.71 (dd, J = 8.6, 1.8 Hz, 1H); 7.64 (s, 1H); 7.40 (d, J = 1.2 Hz, 1H); 7.00 (t, J = 8.0 Hz, 1H); 6.92 (d, J = 7.6 Hz, 1H); 6.87 – 6.85 (m, 2H); 4.35 (s, 2H). Anal. Calcd for $C_{17}H_{12}N_2Na_2O_8S_2$: C, 42.33; Found: C, 40.02; dye content: 94%.

Sample Preparation

Stock solutions were prepared in D_2O at the pD where the dendrimer is fully deprotonated (10.5). pD-values were adjusted by adding NaOD or DCl standard solutions. The two dye stock solutions were added to an aqueous solution of dendrimers at the same pD. The two dye stock solutions were mixed to acheve the desired percentage. After mixing, the appropriate amount of DCl was added at once under turbulent mixing to adjust the sample pD to 3.5 inducing assembly formation.

Dynamic Light Scattering

Measurements were carried out on an ALV CGS 3 goniometer with ALV 5000 correlator (ALV Germany) equipped with a HeNe laser with a wavelength of λ = 632.8 nm and 20 mW output power. Measurements covered an angular range of $30° \leq \theta \leq 150°$. The instrument performs simultaneously static and dynamic light scattering measurements. In this study, to study nanoparticle dimensions as a function of pH the dynamic results have been used. Data analysis was carried out by converting the measured intensity autocorrelation function into the scattered electric field autocorrelation function using the Siegert relation. The electric field autocorrelation functions were further analyzed by regularized inverse LaPlace transformation using the program CONTIN by S. Provencher to obtain the distribution of relaxation times. From this, the apparent diffusion coefficient was calculated using the relation D_{app} =

$q^{-2} \cdot \tau^{-1}$. To determine the hydrodynamic radius R_H, the apparent diffusion coefficient D_{app} is extrapolated to zero scattering angle and then converted into R_H through the Stokes-Einstein relationship.

UV-Vis Spectroscopy. Absorption spectra were recorded on a JASCO V-630 spectrometer using plastic cuvettes with 1 cm path length at dye concentrations of $c \approx 2\ 10^{-5}$ mol L^{-1}. Once obtained in the case of pure dye and dendrimer G4, the experimental extinction coefficient has been fitted according to the relation:

$$\varepsilon_D = \varepsilon_J \exp\left[-4ln2\frac{(\nu - \nu_J)^2}{\Delta\upsilon_{1/2,J}^2}\right] + \sum_{i=0}^{1} \varepsilon_i \exp\left[-4\ ln2\ \frac{(\nu - \nu_i)^2}{\Delta\nu_{1/2,i}^2}\right]$$

Where ε_D is the extinction coefficient of the dimer. This separation can be done because the spectral separation between the H- and J- band is greater than the vibronic progression. Therefore the first term of the equation refers to the J-band with ε_J as extinction coefficient, ν_J as wavenumber and $\Delta\nu_{1/2,J}$ as half-width of the Gaussian. The second term represents the H-band extended to two vibronic transitions. The experimental absorbance (A_{meas}) obtained for the sample composed by two dyes have been fitted according to the equation:

$$A_{meas} = dye_1 \cdot A_{dye_1} + (1 - dye_1) \cdot A_{dye_2}$$

Where dye_1 is the percentage of the first dye in solution divided by 100, A_{dye1} and A_{dye2} the absorbance of the samples with respectively only the first dye and dendrimer G4 and the second dye and dendrimer G4.

Small Angle Neutron Scattering

Samples for SANS were prepared in D_2O with a dendrimer concentration of 0.5 g L^{-1} and 0.2 g L^{-1} for the samples not stable at the first concentration and transferred into quartz cells with 2 mm path length. SANS studies were performed on D11 at the Institut Laue-Langevin, Grenoble, France and on KWS2, at the Jülich Center for

neutron scattering at FRM II, Munich, Germany. On D11 two different λ have been used: 6 Å and 13 Å. The first has been used for 3 different sample-detector distances, 1.2 m, 8 m and 39 m, while the latter has been used only in case of big nanoparticles at 39 m. The wavelength spread ($\Delta\lambda/\lambda$) was 0.09. A total scattering vector range of: $0.007\ nm^{-1} < q < 5\ nm^{-1}$ was investigated. At KWS2, a wavelength of 4.55 Å was used with 3 sample-detector distances: 2 m, 8 m and 20 m. For some samples a different combination has been used: 2 m, 4 m and 20 m: the 8 m distance was replaced with 4m to obtain a very similar scattering vector with a higher neutron flux. In this case a total scattering vector of $0.035\ nm^{-1} < q < 5\ nm^{-1}$ was covered. Data were corrected for empty cell scattering, electronic background and detector uniformity and then converted to absolute scale using secondary standards. Then the scattering of the solvent and the incoherent background have been subtracted from the data. The scattering curve I(q) has been, firstly, analyzed by Guinier analysis, where possible, and by inverse Fourier transformation to obtain the pair distribution function P(r) through the relationship: $I(q) = 4\pi \int P(r) \sin(qr) / qr\ dr$. On the basis of the first results, structural modeling by standard fitting packages such as SASview has been used to obtain the particles shape and dimensions. For some samples the instrument resolution has been taken in account in the fitting process to check its influence on the obtained results.

4.5 Electrostatic Self-Assembly of Dendrimer Macro-Ions and Multivalent Dye Counterions: the Role of Solution Ionic Strength

Macromolecules

Article

pubs.acs.org/Macromolecules

Electrostatic Self-Assembly of Dendrimer Macroions and Multivalent Dye Counterions: The Role of Solution Ionic Strength

Giacomo Mariani,[†,‡] Ralf Schweins,[‡] and Franziska Gröhn*[,†]

[†]Department of Chemistry and Pharmacy and Interdisciplinary Center for Molecular Materials (ICMM), Friedrich-Alexander-Universität Erlangen-Nürnberg, Egerlandstraße 3, D-91058 Erlangen, Germany

[‡]Institut Laue-Langevin DS/LSS, 71 Avenue des Martyrs, F-38000 Grenoble, France

ABSTRACT: The fundamental understanding of the driving forces in electrostatic self-assembly is highly desirable for the design of novel systems and of more effective synthesis strategies. The focus of this study is the effects of the electrostatic interaction on supramolecular self-assembled nanoparticles formed by cationic dendrimers as model polyelectrolytes and oppositely charged di- and trivalent dyes, elucidated by changing the solution ionic strength. Increasing ionic strength results in the formation of larger nanoparticles, although the screened electrostatic interaction of the building blocks may be expected to result in the formation of smaller particles. Yukawa potential and DLVO theory have been used to understand this phenomenon. The screened electrostatic potential decreases the nanoparticle repulsion resulting in larger aggregates, which also causes an increase of the nanoparticle charge leading to stabilization. Contrarily, the ionic strength has no effects on the nanoparticle shape and on the dye stacking due to their $\pi-\pi$ interaction. This shows how the electrostatic interaction controls the dimensions of the nanoaggregates through the stabilization mechanism, while the secondary interactions, and in particular the $\pi-\pi$ interaction, encode the nanoparticle shape. Revealing these relationships is a key step in understanding the ionic association of building blocks under secondary interactions.

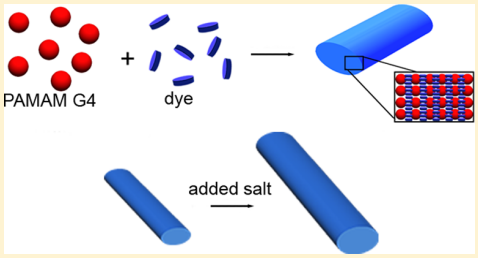

INTRODUCTION

The synthesis of nanoparticles with suitable properties for different applications is crucial in material science. Among the different synthesis strategies, self-assembly has special importance in the organization of soft matter.[1−15] Great potential lies in nature-inspired self-assembled systems such as carrier systems for drug delivery.[2,3,16−18] The key for this application is the possibility to form nontoxic nanoparticles with a size and shape tunable via external triggers such as pH or light. For example, it has been demonstrated that nanoparticle shape and size strongly influence the circulation lifetime once intravenously administered.[19−21] Among the other self-assembly strategies, electrostatic self-assembly is of special importance due to the wide range of different building blocks available and the striking number of different morphologies that can be formed.[8,22−29]

Theoretical and experimental studies have revealed that physicochemical parameters such pH and ionic strength are of crucial importance to control the nanoparticle structure and stability in electrostatically self-assembled systems. In the case of charged diblock copolymers, the morphology of the assemblies depends on the added salt or pH: spherical or cylindrical micelles and vesicles, or even more complex structures such as toroids, are formed.[30−37] Hence, fundamental understanding of the self-assembly has special importance for the design of novel systems and for the improvement of the modern synthesis strategies. In addition, self-assembly in aqueous solution is of special interest for medical application. For this reason, the driving forces and the basic principles of self-assembly have been investigated theoretically in the past years.[38−40] Recently, the combination of different noncovalent interactions has come into focus for a more versatile nanostructure design.[2,8,9] For example, we have introduced a new concept of electrostatic self-assembly leading to the formation of responsive supramolecular nanoparticles in aqueous solution with narrow size distribution and varying shape.[41−44] The process is based on a general combination of interactions rather than on specific binding motifs; in particular, macroions are interconnected through structural multivalent organic counterions that can mutually interact through secondary interactions such as $\pi-\pi$ stacking or geometric factors.[45,46] Using appropriate building blocks, supramolecular nanoparticles sensitive to light and pH have been formed. For instance, with a dye that isomerizes upon UV irradiation the control of the nanoassembly dimensions via irradiation has been achieved.[44,47−50] Particular potential lies in porphyrin−polyelectrolyte assemblies as novel functional photocatalytic nanosystems for light conversion.[51] Recently, we focused on the driving factors of the self-assembly since they are the key for making tailored nanoparticles with desired shape and dimensions. It has been shown that the delicate balance of different interactions plays a central role. Thermodynamics has

Received: March 22, 2016
Revised: October 14, 2016

DOI: 10.1021/acs.macromol.6b00565
Macromolecules XXXX, XXX, XXX−XXX

Scheme 1. Self-Assembly and Molecular Building Block Structures

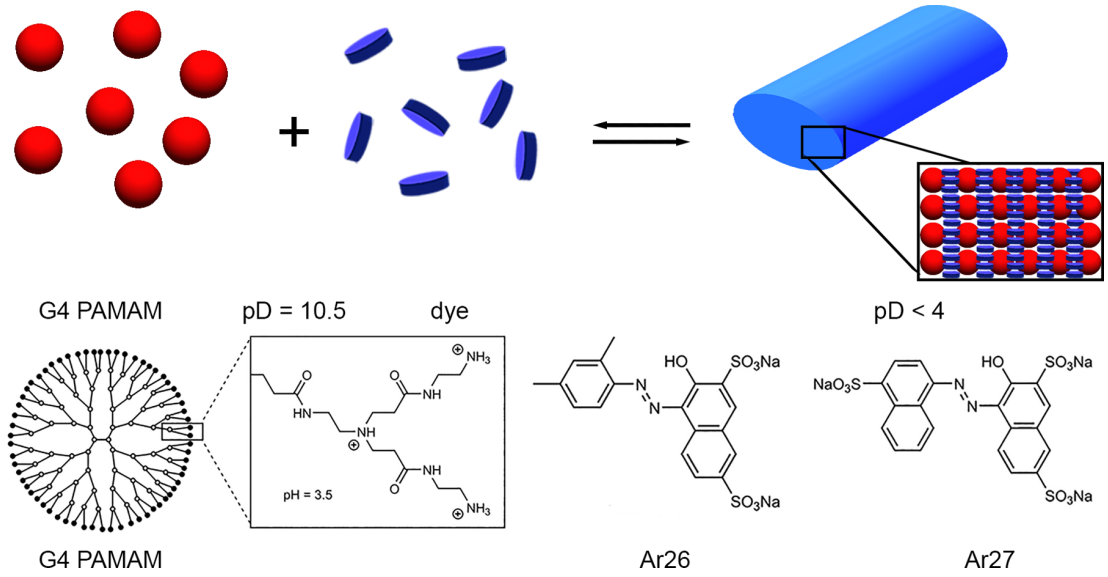

revealed a quantitative relationship of the size of the self-assembled nanoparticles and the free energy of dye−dendrimer association.[52−54] Yet, many questions remain unanswered with regard to what specifically controls the self-assembly within the balance of the interactions. For instance, to what extent the electrostatic interaction of the building blocks influences the nanoparticle morphology is still an open question.

In this study, we investigate the controlling factors in electrostatic self-assembly focusing on the ionic interactions of the building blocks. Knowing the behavior of the nano-assemblies at different salt concentration has crucial importance for applications in salty environments as e.g. in drug delivery. Thus, experiments modifying the ionic strength of the solution have been performed; this acts on the electrostatic interaction among the molecular building blocks via the screening of their charges.

We present the investigation of electrostatically self-assembled nanoparticles formed by polyamidoamine (PAMAM) dendrimers of generation 4 and oppositely charged azo dyes. Two dye species with different valency and molecular structure have been used: Ar26 (divalent) and Ar27 (trivalent). This permits to vary two crucial parameters in the self-assembly process: the strength of the electrostatic interaction of dye and dendrimer and of the mutual dye interaction. The molecular building blocks and the self-assembly process are depicted in Scheme 1. The effects of the ionic strength on the nanoparticle stabilization will be related to ζ-potential measurements. Dynamic light scattering (DLS) and small-angle neutron scattering (SANS) have been used to study the effects of the ionic strength on the nanoparticle structure. In addition, the dye−dye stacking has been investigated by UV−vis spectroscopy.

EXPERIMENTAL PART

Chemicals. Poly(amidoamine) (PAMAM) dendrimer of generation 4 was purchased from Dendritech (Midland, MI) and Sigma-Aldrich (Germany). The azo dyes Acid Red 26 (Ar26, C.I. 16150) and Acid Red 27 (Ar27, C.I. 16185) were obtained from Acros, Belgium. All azo dyes were purified according to the literature.[55]

Characterization of the Azo Dyes. Yields were calculated on the basis of carbon content from elemental analysis. NMR spectra showed that the product is salt-free except for <1 wt % sodium acetate and a small amount of ethanol <1 wt % which could not be removed despite extended drying under high vacuum. The purities given below are corrected for residual amounts of sodium acetate and ethanol, which were determined by NMR. Azo dyes are known to possess multiple molecules of crystal water. Thus, the pure dye contents are below 99%, which does not indicate impurities.

Ar26: ^{1}H NMR (D_2O, 300 MHz, 25 °C), d [ppm]: 7.62 (s, 1H); 7.52−7.40 (m, 2H); 7.38 (s, 1H); 6.53 (d, J = 8.0 Hz, 1H); 5.95 (d, J = 8.1 Hz, 1H); 5.35 (s, 1H); 1.44 (d, J = 7.5 Hz, 6H). Anal. Calcd for $C_{18}H_{14}N_2Na_2O_7S_2$: C, 45.00. Found: C, 43.16; dye content: 96%.

Ar27: (D_2O, 300 MHz, 25 °C), d [ppm]: 8.05 (d, J = 7.8 Hz, 1H); 8.01−7.93 (m, 2H); 7.87 (d, J = 8.4 Hz, 1H); 7.75 (d, J = 8.4 Hz, 1H); 7.68−7.50 (m, 2H); 7.16 (d, J = 7.5 Hz, 1H); 7.11−6.91 (m, 2H). Anal. Calcd for $C_{20}H_{11}N_2Na_3O_{10}S_3$: C, 39.74. Found: C, 37.54; dye content: 94%.

Sample Preparation. Stock solutions were prepared in D_2O at the desired pD (pH in D_2O) where the PAMAM dendrimer is fully deprotonated (pD = 11). pD values were adjusted by adding NaOD or DCl standard solutions. All pD values were counterchecked by a freshly calibrated pH electrode according to pD = pH + 0.44.[56] Dendrimer stock solution and salt solution at the same pD were added. Under mixing, the appropriate amount of DCl was added at once to adjust the pD inducing assembly formation. Final pD is 3.5 for all the samples. The salt concentration has been varied adding NaCl before the nanoparticle formation at pD = 11. The ionic strength I_s has been calculated taking into account all the added salt and the added DCl and NaOD according to the equation

$$I_S = \frac{1}{2}\sum_{i=1}^{n} c_i z_i^2 \qquad (1)$$

where c_i is the molar concentration of ion i, z_i is the charge number of the ion, and the sum is taken over all the ions in solution.

Dynamic and Static Light Scattering. Measurements were carried out on an ALV CGS 3 goniometer with ALV 5000 correlator (ALV Germany) equipped with a HeNe laser with a wavelength of λ = 632.8 nm and 20 mW output power. The samples have been prepared at a dendrimer concentration of 9.3×10^{-6} mol kg^{-1}. Measurements covered an angular range of $30° \leq \theta \leq 150°$. The measured intensity autocorrelation function has been converted into the scattered electric field autocorrelation function using the Siegert relation. The electric field autocorrelation functions were further analyzed by regularized

DOI: 10.1021/acs.macromol.6b00565
Macromolecules XXXX, XXX, XXX−XXX

inverse Laplace transformation using the program CONTIN by S. Provencher to obtain the distribution of relaxation times.[57,58] From this, the apparent diffusion coefficient was calculated using the relation $D_{app} = q^{-2}\tau^{-1}$. To determine the hydrodynamic radius R_H, the apparent diffusion coefficient D_{app} is extrapolated to zero scattering angle and then converted into R_H through the Stokes–Einstein relationship. Static light scattering (SLS) measurements have been performed with the same instrument to combine the results with the SANS curves to extend the q-range for the larger nanoparticles. Measured intensities have been corrected for scattering volume with a toluene standard, and the solvent intensity has been subtracted from the sample intensity prior to further analysis.

ζ-Potential. The ζ-potential measurements were carried out on a Zetasizer Nano ZS analyzer with integrated 4 mW HeNe laser, $\lambda = 633$ nm (Malvern Instruments Ltd., U.K.). Samples with dendrimer concentrations 5.5×10^{-7} mol kg^{-1} have been prepared. The electrophoretic mobility has been measured using laser Doppler anemometry technique after applying an electric field across the sample solution. Considering the ionic strength of the samples, the ζ-potential is calculated from the electrophoretic mobility:[59,60]

$$\mu_e = \frac{2\varepsilon\zeta F(\kappa a)}{3\eta} \tag{2}$$

where μ_ε is the electrophoretic mobility, ζ the ζ-potential, η the solvent viscosity, and $F(\kappa a)$ the Henry function with κ the inverse of the Debye screening length and a the radius of the nanoparticle. The Henry function has been calculated at each ionic strength, and it results $F(\kappa a) = 1.3$ at $I_S = 0.004$, $F(\kappa a) = 1.4$ at $I_S = 0.014$, and $F(\kappa a) = 1.5$ at higher ionic strengths for both the dyes. All measurements were carried out at room temperature using folded capillary cells (DTS 1060) in three replicate measurements.

Small-Angle Neutron Scattering. Samples for SANS were prepared at a dendrimer concentration of 3.5×10^{-5} mol kg^{-1} and transferred into quartz cells with 2 mm path length. This concentration is higher as compared to the one used for light scattering and ζ-potential samples (around 1×10^{-7} mol kg^{-1}); however, concentration has almost no effects on the nanoparticle dimensions. SANS studies were performed on D11 at the Institut Laue-Langevin, Grenoble, France. A wavelength of 6 Å has been used for three different sample–detector distances: 1.2, 8, and 39 m. The wavelength spread ($\Delta\lambda/\lambda$) was 0.09. A total scattering vector range of 0.009 nm^{-1} < q < 5 nm^{-1} was investigated. Data were corrected for empty cell scattering, electronic background and detector uniformity and then converted to absolute scale using secondary standards. Then, the scattering of the solvent and the incoherent background have been subtracted from the data. For larger particles, SLS and SANS data have been combined to cover a larger q-range.

Structural modeling has been used to obtain the particles shape and dimensions. The SANS intensity can be described as $I(q) = \phi V_{NP}(\Delta\rho_{SLD})^2 P(q)$, where ϕ is the volume fraction, V_{NP} the nanoparticle volume, $\Delta\rho_{SLD}$ the difference in scattering length density between the nanoparticle and the solvent, and $P(q)$ the nanoparticle form factor. It describes the nanoparticle shape. Different models have been applied testing the fit goodness calculating the χ^2 value, starting from simple solid spheres and cylinders, etc. Models tested in this study also include a core–shell sphere, for which the intensity becomes[61,62]

$$I(q) = \frac{\phi}{V_{NP}}\left[3V_c(\rho_c - \rho_s)\frac{\sin qr_c - qr_c\cos qr_c}{(qr_c)^3} + 3V_s(\rho_s - \rho_{solv})\frac{\sin qr_s - qr_s\cos qr_s}{(qr_s)^3}\right]^2 \tag{3}$$

where V_s is the volume of the outer shell, V_c the volume of the core, r_s the radius of the shell, r_c the radius of the core, ρ_s the scattering length density of the shell, ρ_c the scattering length density SLD of the core, and ρ_{solv} the scattering length density of the solvent. In the case of cylinders with elliptical cross section, the scattering intensity is[63]

$$I(q) = \frac{\phi}{V_{NP}}\int d\psi \int d\phi \int p(\theta, \phi, \psi)F^2(\mathbf{q}, \alpha, \psi)\sin\theta\, d\theta \tag{4}$$

with the functions $F(q,\alpha,\psi) = 2[(J_1(a)/a))((\sin b)/b)]$, $a = q\sin\alpha\sqrt{r_{major}{}^2\sin^2\psi + r_{minor}{}^2\cos^2\psi}$, $b = q\frac{L}{2}c\cos\alpha$, and J_1 is the first-order Bessel function.

The scattering length density of the nanoparticles has been measured at ionic strength $I_S = 0.004$ M, matching the scattering of the aggregates with the solvent scattering. For Ar26–G4 dendrimer at $I_S = 0.004$ M, the SLD is $\rho_{nanoparticle} = 1.82 \times 10^{-6}$ Å^{-2}. For Ar27–G4 dendrimer the core has $\rho_c = 3.5 \times 10^{-6}$ Å^{-2} and the shell $\rho_c = 2.6 \times 10^{-6}$ Å^{-2}. Based on the very similar composition of the aggregates at higher ionic strength, the same SLD has been used for all the experimental curves. For several cases the instrument resolution has been taken in account in the fitting process to check its influence on the obtained results. The polydispersity has been fixed to 0.3 (based on DLS and previous results). Comparison of results of fitting different models (as given in the Results section) in all cases lead to the choice of a best fit with $\chi^2 < 1.0$.

Starting parameters for the fit were varied to test for stability. The results at ionic strength $I_S = 0.004$ M have already been discussed in a previous study.[54] In that study, combining atomic force microscopy (AFM), light scattering, and SANS, it was found in agreement of scattering and imaging methods that Ar26 and G4 dendrimer results in a cylinder with elliptical cross section, while Ar27 and G4 forms core–shell spheres. As these samples are the starting samples for the variation of ionic strength herein, the main fits of the curves at higher ionic strength have been performed starting from the previously obtained parameters.

UV–Vis Spectroscopy. Absorption spectra were recorded on a JASCO V-630 spectrometer using quartz cuvettes with 1 cm path length at dye concentrations of $c \approx 2 \times 10^{-5}$ mol L^{-1}. The experimental extinction coefficient has been fitted according to the relation[64–67]

$$\varepsilon_D = \varepsilon_J \exp\left[-4\ln 2\frac{(\nu - \nu_J)^2}{\Delta\nu_{1/2,J}{}^2}\right] + \sum_{i=0}^{1}\varepsilon_i \exp\left[-4\ln 2\frac{(\nu - \nu_i)^2}{\Delta\nu_{1/2,i}{}^2}\right] \tag{5}$$

where ε_D is the extinction coefficient of the dimer. This separation can be done because the spectral separation between the H- and J-band is greater than the vibronic progression. Therefore, the first term of the equation refers to the J-band with ε_J as extinction coefficient, ν_J as wavenumber, and $\Delta\nu_{1/2,J}$ as half-width of the Gaussian. The second term represents the H-band extended to two vibronic transitions. The results can be used to calculate the twist angle between the stacked dye molecules according to the equation[68]

$$\beta = 2\arctan\sqrt{\frac{f_J}{f_H}} \tag{6}$$

where f_i is the oscillator strength for the ith band calculated by integration of the respective peak area.

RESULTS AND DISCUSSION

In this study, we investigate the effects of the solution ionic strength on nanoparticles formed by electrostatic self-assembly. The focus lies on understanding the effects that the solution environment has on the nanoassembly structure at molecular and supramolecular scale and on the electrostatic stabilization. To elucidate the effect of dye valency in this context, two different dyes have been studied in combination with G4 dendrimers: a divalent one (Ar26) and a trivalent one (Ar27). The ionic strength has been changed adding different amounts of NaCl: from c(NaCl) = 0.01 M to c(NaCl) = 0.05 M. These values correspond to solution ionic strengths of $I_S = 0.014$ and

DOI: 10.1021/acs.macromol.6b00565
Macromolecules XXXX, XXX, XXX–XXX

I_S = 0.054, respectively. This range has been chosen because at c(NaCl) = 0.06 M the samples are not stable and tends to precipitate.[45] The loading ratio is defined as the molar ratio of dye sulfonate groups to dendrimer primary amines l = $c(SO_3^-)/c(NH_2)$. Samples have been prepared at loading ratio fixed l = 1.8, since at this loading ratio stable nanoparticles are formed and only the nanoassemblies are present in solution.[54] Nanoparticle stability will be discussed in conjunction with ζ-potential measurements at different salt concentrations. The effects of the ionic strength on nanoparticle structure will be discussed based on DLS and SANS results. Finally, the effects induced by the ionic strength on the molecular level of the interactions will be analyzed by UV−vis spectroscopy.

Dynamic Light Scattering. To study the effects of ionic strength on the dimensions of the nanoparticles, DLS measurements have been performed. The electric field autocorrelation function $g^1(\tau)$ and the relaxation time distribution $A(\tau)$ for Ar26−dendrimer samples at different salt concentrations are given in Figure 1a. Well-defined

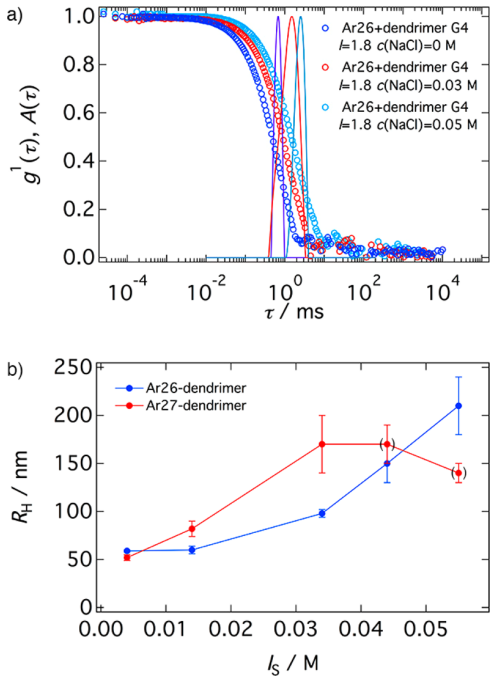

Figure 1. Dynamic light scattering data in dependence on added salt: (a) electric field autocorrelation function $g^1(t)$ and distribution of relaxation time $A(\tau)$; (b) hydrodynamic radius R_H as a function of ionic strength. Large nanoparticles are formed as the ionic strength increases.

nanoparticles are formed at each ionic strength. An expressed shift of the relaxation time to longer times is observed as the salt concentration increases. This shows an increase of the nanoparticle size as can be seen in Figure 1b where the corresponding hydrodynamic radii R_H for Ar26−dendrimer and Ar27−dendrimer are plotted as a function of salt concentration. In both cases, R_H increases as the ionic strength increases. In particular, for the Ar26−dendrimer samples, R_H continuously increases from R_H = 59 ± 1 nm to R_H = 210 ± 30 nm, while for Ar27−dendrimer it reaches a limit of 180 nm for I_S = 0.034 M and remains constant at higher salt concentrations. The Ar27−dendrimer samples at I_S = 0.044 M and I_S = 0.054 M precipitate during the measurements, and hence, R_H values represent only the soluble particles. Overall, the scenario is the same for the two systems, and valency plays a role only on the details, as for example the salt concentration at which the samples are not stable anymore. The size increase is in difference to what may be expected considering the thermodynamics of the self-assembly. In our previous studies, it has been shown that the free energy change of the dye−dendrimer interaction is composed by one electrostatic contribution and one that arises from the secondary interaction and that this determines the size of the assembled particles with large particles resulting from a large free energy exchange.[53] The addition of salt causes the screening of the electrostatic interaction between the building blocks reducing the free energy change. Hence, a decrease in size should be expected upon salt addition. The observed size increase can be explained considering that the added salt is affecting not only the dye−dendrimer electrostatic interaction but also the nanoparticle stabilization. Thereby, the electrostatic interaction of the nanoparticles has been analyzed in the framework of the DLVO theory (Derjaguin−Landau−Verwey−Overbeek).[69,70] This theory describes the forces between charged particles through a liquid medium. For two identical particles, the interaction is composed of attractive Hamaker interaction and screened electrostatic Yukawa repulsion. The latter is due to the formation of an ion cloud around charged molecules in solution. When two like-charged particles come close to each other, the electrostatic forces lead to repulsion contrasted by the attractive part of the potential. The addition of salt does not significantly affect the attractive force, while it screens the repulsion lowering the energy barrier against aggregation.[71] Here, this results in the formation of larger nanoparticles. In addition, the DLVO theory predicts the existence of a critical salt concentration at which interparticle repulsion is at its minimum and there is no more energy barrier against aggregation, resulting in nanoparticle precipitation.[71,72] In the case here, we observe nanoparticle precipitation at the critical concentration of c(NaCl) = 0.06 M for Ar26 and of c(NaCl) = 0.04 M for Ar27. Consequently, in the following, the samples have been prepared at c(NaCl) lower than the critical concentration. DLVO theory is known to fail in the description of highly charged systems[73,74] or at very low salt concentration.[72,75,76] This conditions are not reachable in the system herein since a certain amount of salt is required to reach pH = 3.5 and form the nanoparticles; hence, only ionic strengths $I_S \geq$ 0.004 M have been investigated.

The effects of the dendrimer concentration on the aggregation behavior have been studied by dynamic light scattering. Two samples have been investigated: one at the typical concentration of the SANS samples $c = 3.5 \times 10^{-5}$ mol kg^{-1} and one at the typical concentration of light scattering and ζ-potential experiments $c = 1.5 \times 10^{-7}$ mol kg^{-1}. The first results in a hydrodynamic radius R_H = 70 ± 2 nm and the second in R_H = 67 ± 3 nm (Figure 2). Hence, the dendrimer concentration has no significant effects on the nanoparticle dimensions.

ζ-Potential. The ζ-potential measurements have been performed to gain insight into the nature of the nanoparticle stabilization and to quantitatively understand the effects of the ionic strength. This technique measures the difference of electrostatic potential between the solvent and the layer of fluid attached to the dispersed nanoparticles, and therefore it permits to almost "directly" investigate the electrostatic interaction. In

DOI: 10.1021/acs.macromol.6b00565
Macromolecules XXXX, XXX, XXX−XXX

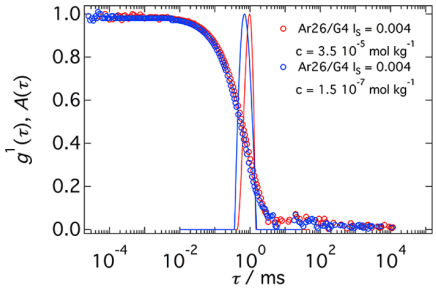

Figure 2. Dynamic light scattering data in dependence on dendrimer concentration: electric field autocorrelation function $g^1(\tau)$ and distribution of relaxation time $A(\tau)$.

addition, in the case of an electrostatically stabilized nanoassembly, the ζ-potential may be correlated to the nanoparticle stability.

Results for the two dye−dendrimer systems in dependence on ionic strength are reported in Figure 3. The two systems

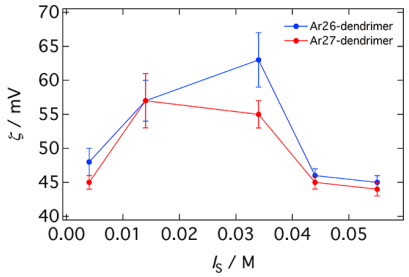

Figure 3. ζ-potential for different dye−dendrimer systems at l = 1.8.

show corresponding behavior: at first, the ζ-potential increases as the ionic strength increases, and then, at higher ionic strength it decreases. It is worth noting that the fact that the loading ratio is constant implies that the number of dye charges per dendrimer is the same for the two systems. Yet, the ionic strength at which the ζ-potential starts to decrease depends on the dye valency. In the case of Ar26 the change takes place at I_S = 0.034 M, while for Ar27 it occurs at I_S = 0.014 M.

To better understand the phenomenon, the ionic strength can be converted into the Debye screening length:

$$\kappa^{-1} = \sqrt{\frac{\varepsilon_r \varepsilon_0 k_B T}{2 N_A e^2 I_S}} \tag{7}$$

where ε_0 is the electric constant, ε_r is the dielectric constant, k_B the Boltzmann constant, T the absolute temperature, e the elementary charge, and N_A the Avogadro number. The Debye length represents how far the electrostatic effects persist or, in other words, the size of the counterion cloud. For the Ar26−dendrimer samples, the ζ-potential starts to decrease when the Debye screening length is 1.76 nm (corresponding to I_S = 0.034 M), while for the Ar27−dendrimer system, this happens already at 2.57 nm (corresponding to I_S = 0.014 M). This is related to the fact that Ar27−dendrimer assemblies precipitate at lower ionic strength (I_S = 0.044 M) as compared to Ar26−dendrimer (I_S = 0.064 M) and shows that the nanoparticles are less stable at higher ionic strength.

The ζ-potential behavior as a function of the ionic strength in the two systems can be understood considering it together with the light scattering results and the DLVO theory. Upon salt addition, two interconnected phenomena take place: the screening of the electrostatic repulsion as predicted by the DLVO theory and the increase in nanoparticle size as seen by DLS. The latter corresponds to an increase of the number of dendrimer molecules interconnected in the nanoassemblies and therefore to an increase of the nanoparticle charge. At this loading ratio, all the dyes are bound to the dendrimers.[44] Binding is slightly understoichiometric so that assemblies have a positive charge. Each dendrimer brings positive excess charge so that more interconnected dendrimers result in a higher positive charge of the supramolecular assemblies. For low salt concentration, this effect overcomes the electrostatic screening resulting in an increase of the ζ-potential. As the salt concentration increases, the screening dominates and therefore the ζ-potential decreases. The balance of the two phenomena depends on the dye valency: for Ar27 the ζ-potential starts to decrease (i.e., electrostatic screening overcoming charge increase) at lower salt concentration as compared to Ar26.

The ζ-potential results can be combined with DLS results, and R_H can be used to estimate the effective charge Q_{eff} and the effective surface charge density σ_{eff} of the nanoparticles according to[50,77]

$$Q_{eff} = 4\pi\varepsilon\zeta R_{eff} \approx 4\pi\varepsilon\zeta R_H \tag{8}$$

$$\sigma_{eff} = \frac{Q_{eff}}{4\pi R_{eff}^2} = \frac{\varepsilon\zeta}{R_{eff}} \approx \frac{\varepsilon\zeta}{R_H} \tag{9}$$

The results are given in Figure 4. For Ar26, the effective charge Q_{eff} (Figure 4a) increases continuously as the salt concentration

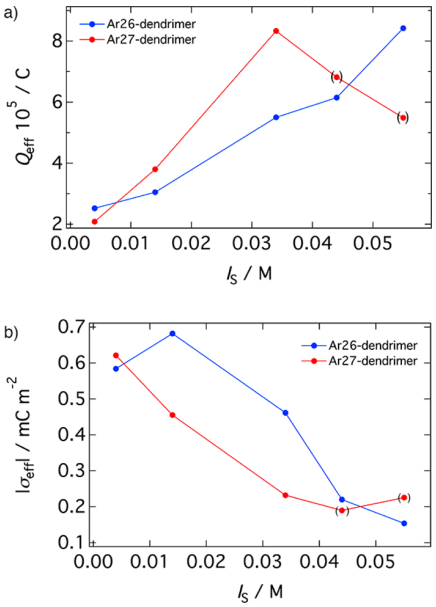

Figure 4. (a) Effective charge as a function of the solution ionic strength. (b) Effective surface charge density as a function of the ionic strength for Ar26−dendrimer and A27−dendrimer assemblies.

increases, while the effective surface charge density σ_{eff} (Figure 4b) decreases to σ_{eff} = 0.2 mC m^{-2} at c(NaCl) = 0.05 M. The same behavior is found for Ar27. The results are in good agreement with the proposed model. In particular, Q_{eff} perfectly shows the constant increase in nanoparticle charge due to the increase in size. In the case of Ar27 the effective charge Q_{eff} increases faster than for Ar26. In contrast, σ_{eff} decreases with

DOI: 10.1021/acs.macromol.6b00565
Macromolecules XXXX, XXX, XXX−XXX

Scheme 2. Representation of the Nanoparticle Dimensions, the Debye Screening Length (Black Circles and Black Lines), the Distance between the Nanoparticles (Black Lines), and the Yukawa Screening Length (Distance at Which the Screened Potential Reaches $u_{el}(r)$ = 0.01 V) (Red Circle and Red Lines) at Different Ionic Strengths for the Two Dye−Dendrimer Systems

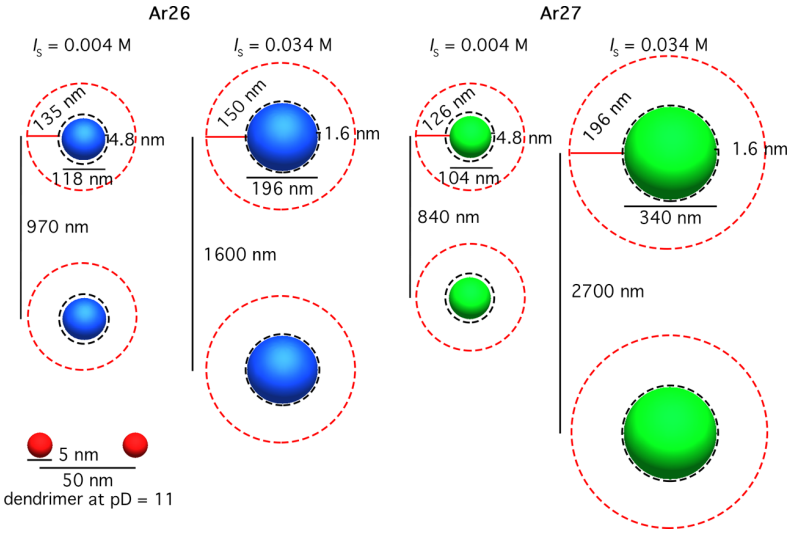

the ionic strength due to the increased screening, not fully compensated by the increase in nanoparticle charge.

The nanoparticle stabilization can be further understood considering the interparticle distance d_N. This can be calculated based on the hydrodynamic radius R_H of the nanoassemblies knowing the volume of one dendrimer molecule, the number of dendrimers in solution, and thus the aggregation number. The latter varies between 7600 dendrimers per particle at I_S = 0.004 M and 150 000 dendrimers per particle at I_S = 0.055 M in the case of Ar26 and G4. The resulting interparticle distances d_N are represented in Scheme 2. As expected, the interparticle distance d_N shows a significant increase when the nanoparticles are formed (from d_N = 50 nm to d_N = 970 nm after nanoparticle formation in the case of Ar26). For the two systems, the interparticle distance increases as the solution ionic strength increases. Comparing Ar26 and Ar27, d_N is the same at low ionic strength, while the Ar27 interparticle distance is almost twice as large as the one for Ar26 at I_S = 0.034 M. Interestingly, the interparticle distance is always significantly larger than the Debye screening length. With this, it is possible to calculate the screened electrostatic potential between the two nanoparticles according to the equation[69]

$$u_{el}(r) = \frac{Q_{eff}^{\ 2}}{\varepsilon} \frac{e^{-\kappa(r-2R_H)}}{r(1+\kappa R_H)^2} \quad \text{for } r > R_H \tag{10}$$

For Ar26, the resulting potentials are depicted in Figure 5. To evaluate the effects of the screened Coulomb interaction, the distance at which the potential reaches the values of u_{el} = 0.01 V is also indicated for each ionic strength. For I_S = 0.004 M this distance is 135 nm. As the ionic strength increases to I_S = 0.0014 M, the electrostatic potential becomes more short-ranged and it becomes 0.01 V at 100 nm. As the ionic strength further increases, the potential becomes more long-ranged: 0.01 V is reached at 150 nm for I_S = 0.034 M and at 236 nm for I_S = 0.054 M. The decrease and subsequent increase of the Yukawa potential range with the ionic strength takes place because the screened electrostatic potential depends on the nanoparticle effective charge. At low ionic strenght the size and the effective

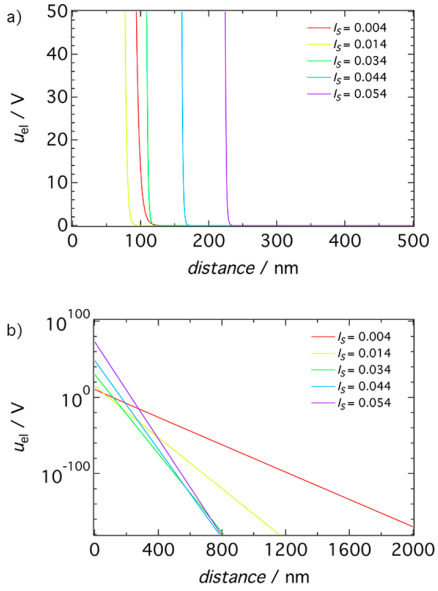

Figure 5. Screened electrostatic potential for Ar26 and G4 at different solution ionic strengths.

charge almost do not vary while the Debye length decreases resulting in a more short-ranged potential. At high ionic stength the size of the nanoparticles and thereby the effective charge increases, resulting in a longer-ranged potential. It is worth noting that the length at which the electrostatic potential is "completely" screened is always significantly smaller than the interparticle distance d_N.

Hence, we have demonstrated how increasing the ionic strength of the solution increases the ζ-potential for low salt concentration and decreases it at high salt concentration. This behavior can be described applying the DLVO theory and in particular considering two interconnected phenomena: the electrostatic screening of the nanoparticle charge and the increase of the nanoparticle charge due to the increasing size.

DOI: 10.1021/acs.macromol.6b00565
Macromolecules XXXX, XXX, XXX−XXX

The effective charge Q_{eff} increases as the ionic strength increases, while the effective surface charge density σ_{eff} decreases. Despite the overall process being the same for the two dyes, valency has a crucial role on the balance of screening and charge increase. For the divalent dye Ar26 the screening overcomes the charge increase at I_S = 0.034 M, while for Ar27 the turning point is at I_S = 0.014 M.

Small-Angle Neutron Scattering and Static Light Scattering. To understand whether and how the ionic strength acts on the nanoparticle structure and in particular on the shape, SLS and SANS measurements have been performed. Figure 6a shows the results for Ar26−dendrimer

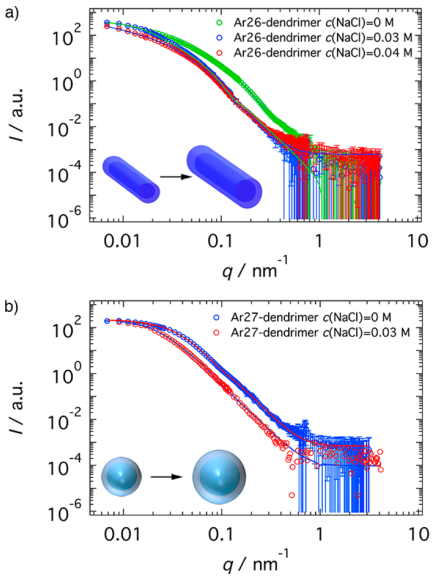

Figure 6. SLS-SANS: (a) Ar26−dendrimer with l = 1.8 at different salt concentrations and (b) Ar27−dendrimer with l = 1.8 at different salt concentrations; lines represent the best fits.

assemblies. At first, considering the case where no added salt is present in solution, the low q signal of the SANS curve clearly indicates the presence of large nanoscale aggregates in solution. From the leveling off of the $I(q_{min})$, a total dimension around at least 300 nm for the nanoparticles can be estimated. To characterize the nanoassemblies, the experimental curve has been fitted using structural models. Results are given in Figure 6. The experimental curves at higher ionic strength I_S first have been fitted with the same model used to describe the scattering of the I_S = 0.004 M samples. Different models have been tested in particular for the system forming elongated nanoparticles (Ar26/G4). For example, the form factor of ellipsoids has been tried for Ar26/G4 at ionic strength I_S = 0.034 M; however, the agreement with the experimental data (χ^2 = 4.0) is not as good as for the cylinder with elliptical cross-section form factor (χ^2 = 0.9, Figure 7a). To extend the investigated q range, the SANS data have been combined with static light scattering measurements. Despite the difference in concentration, the light scattering data perfectly extend the SANS curve permitting to measure the length of the cylindrical aggregate.

In the case of Ar26 and no added salt, SANS reveals cylinders with elliptical cross section. The cylinder length is l = 300 ± 10 nm, the major axis r_{maj} = 44 ± 4 nm, and the minor one r_{min} = 11 ± 1 nm. When salt is added, the SANS curve characteristics clearly shift to lower q-values: this indicates a change to larger

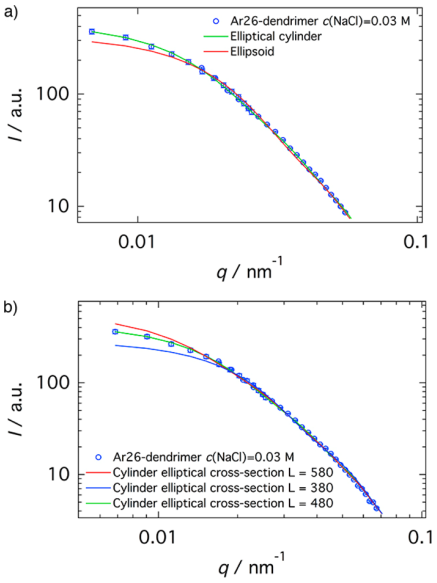

Figure 7. SLS-SANS: comparison of fits. (a) Ar26−dendrimer with l = 1.8 at c(NaCl) = 0.03 M; it is evident that the best fit is obtained for the cylinder with elliptical cross-section model. Fit goodness: χ^2 (elliptical cylinder) = 0.9 and χ^2 (ellipsoid) = 4.2. (b) Ar26−dendrimer with l = 1.8 at c(NaCl) = 0.03 M; lines represent the best fits obtained with different lengths (χ^2(480) = 0.7, χ^2(580) = 2.0, and χ^2(380) = 3.6).

nanoparticle dimensions. This finding is in accordance with the dynamic light scattering results. When the ionic strength is I_S = 0.034 M, Ar26 and dendrimer aggregate again in cylinders with elliptical cross section. The length increases to l = 480 ± 20 nm, and the axes almost double: the major axis becomes r_{maj} = 94 ± 4 nm and the minor one r_{min} = 24 ± 1 nm. (Figure 7b shows an enlargement of the low q-part displaying the length determination through the structural fit.) Interestingly, the aspect ratio remains unchanged at approximately 4. When the ionic strength increases to I_S = 0.044 M, the nanoparticle shape again remains unchanged and the aspect ratio increases: the length increases to l = 550 ± 50 nm, while the cross section remains constant. Hence, SLS-SANS confirms the increase in size upon increasing the ionic strength, as already observed with DLS. In addition, it shows that the ionic strength has no effects on the general nanoparticle shape for Ar26−dendrimer assemblies. A similar behavior has been observed for the assemblies formed by Ar27 (Figure 6b). When no added salt is present in solution, the system aggregates forming core−shell spheres with a total radius R_{tot} = 44 ± 3 nm and a core radius R_{core} = 13 ± 1 nm. As the salt concentration increases, the SLS-SANS curves shift toward lower q-values as for Ar26. However, in the case of Ar27, at I_S = 0.034 M the system again forms core−shell spheres with a total radius of R_{tot} = 60 ± 3 nm and an inner core of R_{core} = 30 ± 1 nm. It is worth noting that the increase takes place only in the inner core, while the shell radius remains constant around 30 nm. For Ar27, samples are not stable at ionic strength higher than I_S = 0.034 M. It is therefore clear that the ionic strength has no effect on the overall nanoparticle shape, independent of the dye valency. As observed with light scattering, the nanoassemblies become larger as the ionic strength increases. The ionic strength at which precipitation occurs strongly depends on the dye valency: divalent dyes form stable nanoparticle up to higher

DOI: 10.1021/acs.macromol.6b00565
Macromolecules XXXX, XXX, XXX−XXX

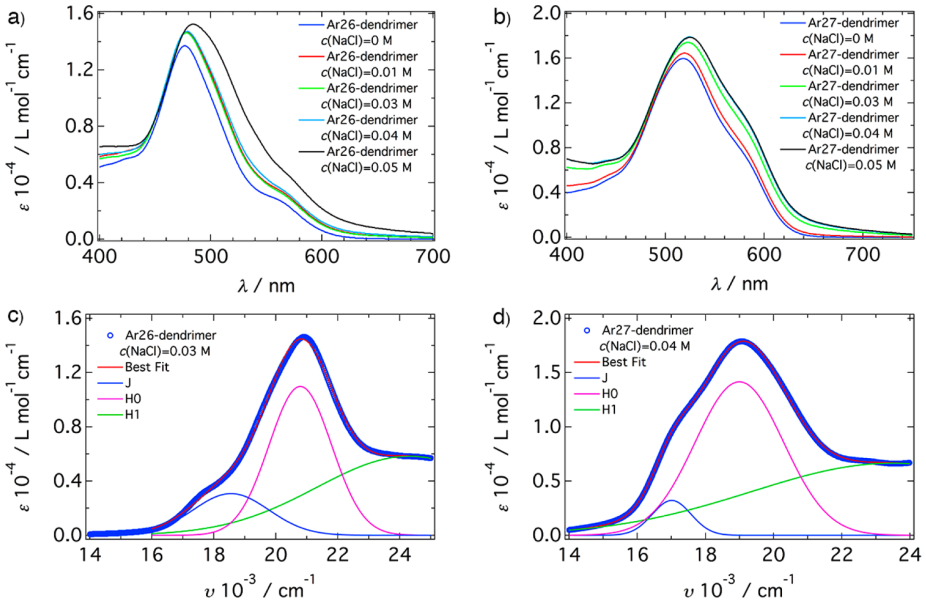

Figure 8. UV−vis spectra at different salt concentrations for (a) Ar26−dendrimer and (b) Ar27−dendrimer. Exciton theory applied to Ar26−dendrimer at (c) c(NaCl) = 0.03 and (d) to Ar27−dendrimer at c(NaCl) = 0.04.

salt concentrations as compared to trivalent ones. This can be due to a difference in the interparticle interaction strength in the two dye−dendrimer systems.

UV−Vis Spectroscopy. UV−vis spectroscopy has been used to directly investigate the effects of salt on the molecular scale of the association. The resulting spectra are given in Figure 8. When dendrimers and dyes form nanoassemblies due to ionic interactions, a change in the UV−vis spectra is observed. This is caused by the mutual interaction of the dye molecules induced by their spatial proximity.[43,45,78,79] The dye molecules can mutually interact forming π-stacked structures resulting in the splitting of the first excited state of the monomer.[80] This phenomenon is described by exciton theory, which can be used to characterize the geometry of the dye stacking.[64−67] In particular, it provides an important geometric parameter: the twist angle between the stacked dye molecules β.[68] This parameter is of key importance to understand how the dye molecules arrange when the nanoparticles are formed and how the salt concentration acts on the dye arrangement. UV−vis spectra are given in Figure 8a,b. Ar26 and Ar27 combined with dendrimers have similar solvatochromism: the peaks shift to higher wavelengths as the ionic strength increases. This is the well-known bathochromic shift induced by the increasing solvent ionic strength due to a difference in dipole moment between the ground and excited state of the dye molecule.[81−84] In particular, a bathochromic increase upon solvent polarity is observed for weakly polar molecules with low polarity in the ground state and increased polarity in the excited state.[85]

In Figure 8c,d, examples of fits obtained applying the exciton theory are given. The resulting twist angles at different salt concentrations for the two systems are reported in Figure 9. For Ar26−dendrimer assemblies the twist angle remains constant around β = 57° lying between β = 55 ± 1° and β = 60 ± 1°. A similar behavior is observed for Ar27−dendrimer assemblies, for which the twist angle is constant around β = 35° (between β = 31 ± 1° and β = 38 ± 1°). Therefore, the solvent ionic strength modifies the UV−vis spectra inducing a bathochromic shift, but this does not affect the dye−dye

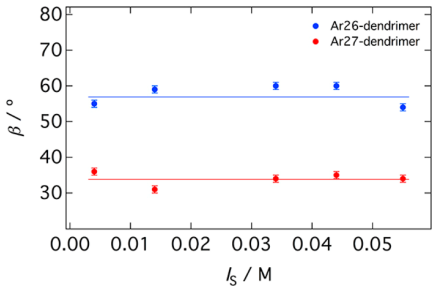

Figure 9. Twist angle β of dyes stacking within dye−dendrimer assemblies at different salt concentrations.

interaction. In both cases, the twist angle, i.e., the dye arrangement in the nanoparticle, remains constant as the ionic strength increases. These molecular scale association results are directly related to the SANS nanoscale results: as the ionic strength increases, the nanoparticle shape remains constant while their dimension increases, and this is accompanied by an unchanged dye stacking.

General Discussion. To clarify the results, the thermodynamics of the self-assembly must be considered. In particular, the free energy change in the process can be written as[53]

$$\Delta G_{\text{dye-den}} = \Delta G_{\text{electr}} + \Delta G_{\text{sec}} \quad (11)$$

The first term describes the electrostatic interaction and therefore depends on the ionic strength, while the second term summarizes the secondary interactions, which here are the dye−dye interactions. Hence, it is not electrostatic and can be independent of the ionic strength as confirmed by the UV−vis measurements. It can be concluded that the electrostatic interaction controls the nanoparticle size, while the secondary interaction, and specifically the π−π interaction, controls the nanoparticle shape. This is in good agreement with our recent results where it has been shown that the shape of nanoparticles composed by G4 dendrimers and different azo dyes at pH = 3.5

DOI: 10.1021/acs.macromol.6b00565
Macromolecules XXXX, XXX, XXX−XXX

and l = 1.8 is controlled only by the strength of the $\pi-\pi$ interaction.[54]

At this point, a qualitative analysis of the first term is of interest: as the ionic strength increases, the electrostatic part of the dye−dendrimer interaction should decrease resulting in a smaller ΔG_{electr}. Previous results at constant ionic strength for similar systems revealed that the aggregation number and thus the nanoparticle size are strongly related to the ΔG_{electr} and in particular that a lower ΔG_{electr} results in smaller nanoparticles. Consequently, a decrease in size with increasing ionic strength might be expected. Yet, larger nanoparticles are formed. This is because the increased ionic strength does not only affect the dye−dendrimer interaction and nanoparticle formation but also the inter-nanoparticle interaction and their stabilization. The screening effect in the second process causes the observed increase in particle size.

CONCLUSIONS

The effects of solvent ionic strength on electrostatically self-assembled nanoparticles made of cationic dendrimers and oppositely charged azo dyes were elucidated. The nanoparticle size increases as the ionic strength increases; this is in difference to the expected decrease in size due to the lowering of the electrostatic interaction of the building blocks. DLVO theory has been used to describe nanoparticle stabilization and the size trend as the ionic strength increases. The screened electrostatic potential causes the decrease of the nanoparticle repulsion, resulting in larger assemblies. This causes the increase of the nanoparticle charge and hence nanoparticle stabilization. The interplay of the two interconnected phenomena regulates the nanoparticle size and hence can be used to tune the nanoassembly size. In difference, the shape of the nanoparticles and the dye stacking do not depend on the ionic strength. This is understood considering the thermodynamics of the self-assembly: the free energy gain of the process can be divided into one electrostatic term arising from the dye−dendrimer interaction and one describing the $\pi-\pi$ interaction of the dye molecules. The second term is independent of the ionic strength. Hence, the electrostatic interaction controls the nanoparticle dimensions though the control of the stabilization process, while the $\pi-\pi$ interaction encodes the nanoparticle shape.

The understanding of the interplay of the different interactions in ionic association of molecules under secondary interactions has specific importance in material science. For example, it allows for the control of the nanoparticle dimension without inducing changes of their shape, which is of crucial importance for the applications of electrostatic self-assembly in different ionic strength environment for example in the field of gravimetric nanosensors. In drug delivery one can take advantage of a certain nanoparticle shape and size selectively realized in one type of cells with a certain pH such as tumor cells. Additionally, the ionic strength can be used to form targeted nanoparticles simply combining cationic dendrimers and oppositely charged azo dyes at the added salt concentration of choice.

AUTHOR INFORMATION

Corresponding Author

*E-mail franziska.groehn@fau.de.

Funding

This work was funded by German Science Foundation (DFG), the Interdisciplinary Center for Molecular Materials (ICMM), and Institut Laue-Langevin (ILL).

Notes

The authors declare no competing financial interest.

ACKNOWLEDGMENTS

This work benefitted from SasView software, originally developed by the DANSE project under NSF award DMR-0520547. The Institut Laue-Langevin (ILL), France, and the Laboratoire Leon Brillouin (LLB), France, are gratefully acknowledged for the beam time. The support of the Partnership for Soft Condensed Matter (PSCM) is gratefully acknowledged.

REFERENCES

(1) Ringsdorf, H.; Schlarb, B.; Venzmer, J. Molecular architecture and function of polymeric oriented systems: models for the study of organization, surface recognition, and dynamics of biomembranes. *Angew. Chem., Int. Ed. Engl.* **1988**, *27*, 113.

(2) Zhou, S.; Burger, C.; Chu, B.; Sawamura, M.; Nagahama, N.; Toganoh, M.; Hackler, U. E.; Isobe, H.; Nakamura, E. Spherical bilayer vesicles of fullerene-based surfactants in water: a laser light scattering study. *Science* **2001**, *291*, 1944.

(3) Discher, D. E.; Eisenberg, A. . Polymer vesicles. *Science* **2002**, *297*, 967.

(4) Schmuck, C.; Schwegmann, M. A molecular flytrap for the selective binding of citrate and other tricarboxylates in water. *J. Am. Chem. Soc.* **2005**, *127*, 3373.

(5) Jonkheijm, P.; van der Schoot, P.; Schenning, A. P. H. J.; Meijer, E. W. Probing the solvent-assisted nucleation pathway in chemical self-assembly. *Science* **2006**, *313*, 80.

(6) Capadona, J. R.; Van Den Berg, O.; Capadona, L. A.; Schroeter, M.; Rowan, S. J.; Tyler, D. J.; Weder, C. A versatile approach for the processing of polymer nanocomposites with self-assembled nanofibre templates. *Nat. Nanotechnol.* **2007**, *2*, 765−769.

(7) Nikolic, M. S.; Olsson, C.; Salcher, A.; Kornowski, A.; Rank, A.; Schubert, R.; Frömsdorf, A.; Weller, H.; Förster, S. Micelle and vesicle formation of amphiphilic nanoparticles. *Angew. Chem., Int. Ed.* **2009**, *48*, 2752.

(8) Xu, Y.; Bolisetty, S.; Ballauff, M.; Müller, A. H. E. Switching the Morphologies of Cylindrical Polycation Brushes by Ionic and Supramolecular Inclusion Complexes. *J. Am. Chem. Soc.* **2009**, *131*, 1640−1641.

(9) Yan, M.; Fresnais, J.; Berret, J.-F. Growth mechanism of nanostructured superparamagnetic rods obtained by electrostatic co-assembly. *Soft Matter* **2010**, *6*, 1997−2005.

(10) Bayer, F. M.; Hiltrop, K.; Huber, K. Hydrogen-Bond-Induced Heteroassembly in Binary Colloidal Systems. *Langmuir* **2010**, *26*, 13815−13822.

(11) Srivastava, S.; Santos, A.; Critchley, K.; Kim, K.-S.; Podsiadlo, P.; Sun, K.; Lee, J.; Xu, C.; Lilly, G. D.; Glotzer, S. C.; Kotov, N. A. Light-controlled self-assembly of semiconductor nanoparticles into twisted ribbons. *Science* **2010**, *327*, 1355.

(12) Stuart, M. A. C.; Huck, W. T. S.; Genzer, J.; Muller, M.; Ober, C.; Stamm, M.; Sukhorukov, G. B.; Szleifer, I.; Tsukruk, V. V.; Urban, M.; Winnik, F.; Zauscher, S.; Luzinov, I.; Minko, S. Emerging applications of stimuli-responsive polymer materials. *Nat. Mater.* **2010**, *9*, 101−113.

(13) Cao, B.-R.; Xu, H.; Mao, C.-B. Controlled Self-Assembly of Rodlike Bacterial Pili Particles into Ordered Lattices. *Angew. Chem., Int. Ed.* **2011**, *50*, 6264−6268.

(14) Boehm, I.; Isenbuegel, K.; Ritter, H.; Branscheid, R.; Kolb, U. Fluorescent Nanowires Self-Assembled through Host-Guest Interactions in Modified Calcein. *Angew. Chem., Int. Ed.* **2011**, *50*, 7407−7409.

DOI: 10.1021/acs.macromol.6b00565
Macromolecules XXXX, XXX, XXX−XXX

(15) Yeh, Y.-C.; Tang, R.; Mout, R.; Jeong, Y.; Rotello, V. M. Fabrication of Multiresponsive Bioactive Nanocapsules through Orthogonal Self-Assembly. *Angew. Chem., Int. Ed.* **2014**, *53*, 5137−5141.
(16) White, R. J.; Tauer, K.; Antonietti, M.; Titirici, M.-M. Functional Hollow Carbon Nanospheres by Latex Templating. *J. Am. Chem. Soc.* **2010**, *132*, 17360−17363.
(17) Chang, M.; Yang, C.-S.; Huang, D.-M. Aptamer-Conjugated DNA Icosahedral Nanoparticles As a Carrier of Doxorubicin for Cancer Therapy. *ACS Nano* **2011**, *5*, 6156−6163.
(18) Guo, Y.; Zhao, Y.; Han, M.; Zhao, J.; Hao, C.; Wang, X.; Wang, X. A codendrimer of PAMAM decorated with oligoethylene glycol dendrons: synthesis, self-assembly, and application as a drug carrier. *Soft Matter* **2013**, *9*, 10306−10313.
(19) Geng, Y.; Dalhaimer, P.; Cai, S.; Tsai, R.; Tewari, M.; Minko, T.; Discher, D. E. Shape effects of filaments versus spherical particles in flow and drug delivery. *Nat. Nanotechnol.* **2007**, *2*, 249−255.
(20) Petros, R. A.; DeSimone, J. M. Strategies in the design of nanoparticles for therapeutic applications. *Nat. Rev. Drug Discovery* **2010**, *9*, 615−627.
(21) Popovic, Z.; Liu, W.; Chauhan, V. P.; Lee, J.; Wong, C.; Greytak, A. B.; Insin, N.; Nocera, D. G.; Fukumura, D.; Jain, R. K.; Bawendi, M. G. A nanoparticle size series for in vivo fluorescence imaging. *Angew. Chem.* **2010**, *122*, 8831−8834.
(22) Antonietti, M.; Maskos, M. Fine-Tuning of Phase Structures and Thermoplasticity of Polyelectrolyte-Surfactant Complexes: Copolymers of Ionic Monomers with *N*-Alkylacrylamides. *Macromolecules* **1996**, *29*, 4199−4205.
(23) Hoogeveen, N. G.; Cohen Stuart, M. A.; Fleer, G. J. Formation and Stability of Multilayers of Polyelectrolytes. *Langmuir* **1996**, *12*, 3675−3681.
(24) Ober, C. K.; Wegner, G. Polyelectrolyte-Surfactant Complexes in the Solid State: Facile building blocks for self-organizing materials. *Adv. Mater.* **1997**, *9*, 17−31.
(25) Decher, G. Fuzzy Nanoassemblies: Toward Layered Polymeric Multicomposites. *Science* **1997**, *277*, 1232−1237.
(26) Thünemann, A. F.; Beyermann, J. Immobilization of Retinoic Acid by Polyamino Acids: Lamellar-Structured Nanoparticles. *Macromolecules* **2000**, *33*, 6878−6885.
(27) Bertrand, P.; Jonas, A.; Laschewsky, A.; Legras, R. Ultrathin polymer coatings by complexation of polyelectrolytes at interfaces: suitable materials, structure and properties. *Macromol. Rapid Commun.* **2000**, *21*, 319−348.
(28) Faul, C. F. J.; Antonietti, M. Ionic Self-Assembly: Facile Synthesis of Supramolecular Materials. *Adv. Mater.* **2003**, *15*, 673−683.
(29) Berret, J.-F. Stoichiometry of Electrostatic Complexes Determined by Light Scattering. *Macromolecules* **2007**, *40*, 4260−4266.
(30) Zhang, L.; Yu, K.; Eisenberg, A. Ion-induced morphological changes in "crew-cut" aggregates of amphiphilic block copolymers. *Science* **1996**, *272*, 1777−1779.
(31) Shen, H.; Zhang, L.; Eisenberg, A. Multiple pH-Induced Morphological Changes in Aggregates of Polystyrene-*block*-poly(4-vinylpyridine) in DMF/H_2O Mixtures. *J. Am. Chem. Soc.* **1999**, *121*, 2728−2740.
(32) Guenoun, P.; Delsanti, M.; Gazeau, D.; Mays, J. W.; Cook, D. C.; Tirrell, M.; Auvray, L. Structural properties of charged diblock copolymer solutions. *Eur. Phys. J. B* **1998**, *1*, 77−86.
(33) Förster, S.; Hermsdorf, N.; Leube, W.; Schnablegger, H.; Regenbrecht, M.; Akari, S.; Lindner, P.; Böttcher, C. Fusion of Charged Block Copolymer Micelles into Toroid Networks. *J. Phys. Chem. B* **1999**, *103*, 6657−6668.
(34) Harada, A.; Kataoka, K. On−Off Control of Enzymatic Activity Synchronizing with Reversible Formation of Supramolecular Assembly from Enzyme and Charged Block Copolymers. *J. Am. Chem. Soc.* **1999**, *121*, 9241−9242.
(35) Kötz, J.; Kosmella, S.; Beitz, T. Self-assembled polyelectrolyte systems. *Prog. Polym. Sci.* **2001**, *26*, 1199−1232.
(36) Cohen Stuart, M. A.; Hofs, B.; Voets, I. K.; de Keizer, A. Assembly of polyelectrolyte-containing block copolymers in aqueous media. *Curr. Opin. Colloid Interface Sci.* **2005**, *10*, 30−36.
(37) Jansson, J.; Schillén, K.; Nilsson, M.; Söderman, O.; Fritz, G.; Bergmann, A.; Glatter, O. Small-Angle X-ray Scattering, Light Scattering, and NMR Study of PEO−PPO−PEO Triblock Copolymer/Cationic Surfactant Complexes in Aqueous Solution. *J. Phys. Chem. B* **2005**, *109*, 7073−7083.
(38) Douglas, J. F.; Dudowicz, J.; Freed, K. F. Crowding Induced Self-Assembly and Enthalpy-Entropy Compensation. *Phys. Rev. Lett.* **2009**, *103*, 135701.
(39) Kivenson, A.; Hagan, M. F. Mechanisms of Capsid Assembly around a Polymer. *Biophys. J.* **2010**, *99* (2), 619−628.
(40) Mahalik, J. P.; Muthukumar, M. Langevin dynamics simulation of polymer-assisted virus-like assembly. *J. Chem. Phys.* **2012**, *136*, 135101.
(41) Gröhn, F.; Klein, K.; Brand, S. Facile Route to Supramolecular Structures: Self-Assembly of Dendrimers and Naphthalene Dicarboxylic Acids. *Chem. - Eur. J.* **2008**, *14*, 6866−6869.
(42) Willerich, I.; Gröhn, F. Switchable Nanoassemblies from Macroions and Multivalent Dye Counterions. *Chem. - Eur. J.* **2008**, *14*, 9112−9116.
(43) Ruthard, C.; Maskos, M.; Kolb, U.; Gröhn, F. Finite-size networks from cylindrical polyelectrolyte brushes and porphyrins. *Macromolecules* **2009**, *42*, 830−840.
(44) Gröhn, F. Soft matter nanoparticles with various shapes and functionalities can form through electrostatic self-assembly. *Soft Matter* **2010**, *6*, 4296−4302.
(45) Willerich, I.; Ritter, H.; Gröhn, F. Structure and Thermodynamics of Ionic Dendrimer− Dye Assemblies. *J. Phys. Chem. B* **2009**, *113*, 3339−3354.
(46) Willerich, I.; Li, Y.; Gröhn, F. Influencing Particle Size and Stability of Ionic Dendrimer− Dye Assemblies. *J. Phys. Chem. B* **2010**, *114*, 15466−15476.
(47) Willerich, I.; Schindler, T.; Ritter, H.; Gröhn, F. Controlling the size of electrostatically self-assembled nanoparticles with cyclodextrin as external trigger. *Soft Matter* **2011**, *7*, 5444−5450.
(48) Willerich, I.; Gröhn, F. Thermodynamics of Photoresponsive Polyelectrolyte−Dye Assemblies with Irradiation Wavelength Triggered Particle Size. *Macromolecules* **2011**, *44*, 4452−4461.
(49) Ruthard, C.; Schmidt, M.; Gröhn, F. Porphyrin-Polymer Networks, Worms, and Nanorods: pH-triggerable Hierarchical Self-assembly. *Macromol. Rapid Commun.* **2011**, *32*, 706−711.
(50) Moldenhauer, D.; Gröhn, F. Nanoassemblies with light-responsive size and density from linear flexible polyelectrolytes. *J. Polym. Sci., Part B: Polym. Phys.* **2013**, *51*, 802−816.
(51) Frühbeißer, S.; Gröhn, F. *J. Am. Chem. Soc.* **2012**, *134*, 14267−14270.
(52) Willerich, I.; Schindler, T.; Ritter, H.; Gröhn, F. Effect of polyelectrolyte architecture and size on macroion−dye assemblies. *J. Phys. Chem. B* **2011**, *115*, 9710−9719.
(53) Willerich, I.; Gröhn, F. Molecular structure encodes nanoscale assemblies: understanding driving forces in electrostatic self-assembly. *J. Am. Chem. Soc.* **2011**, *133*, 20341−20356.
(54) Mariani, G.; Moldenhauer, D.; Schweins, R.; Gröhn, F. Elucidating Electrostatic Self-Assembly: Molecular Parameters as Key to Thermodynamics and Nanoparticle Shape. *J. Am. Chem. Soc.* **2016**, *138*, 1280−1293.
(55) Robinson, C.; Mills, H. A. T. The Colloid Chemistry of Dyes: The Aqueous Solutions of Benzopurpurine 4B and Its Isomer Prepared from m-Tolidine. Part I. *Proc. R. Soc. London, Ser. A* **1931**, *131*, 576−595.
(56) Krężel, A.; Bal, W. A formula for correlating pK_a values determined in D_2O and H_2O. *J. Inorg. Biochem.* **2004**, *98*, 161−166.
(57) Provencher, S. W. A constrained regularization method for inverting data represented by linear algebraic or integral equations. *Comput. Phys. Commun.* **1982**, *27*, 213−227.

DOI: 10.1021/acs.macromol.6b00565
Macromolecules XXXX, XXX, XXX−XXX

(58) Provencher, S. W. CONTIN: a general purpose constrained regularization program for inverting noisy linear algebraic and integral equations. *Comput. Phys. Commun.* **1982**, *27*, 229−242.
(59) Hunter, R. J. *Zeta Potential in Colloid Science*; Academic Press: New York, 1981.
(60) Swan, J. W.; Furst, E. M. A Simpler Expression for Henry's Function Describing the Electrophoretic Mobility of Spherical Colloids. *J. Colloid Interface Sci.* **2012**, *388*, 92−94.
(61) Guinier, A.; Fournet, G. *Small-Angle Scattering of X-Rays*; John Wiley and Sons: New York, 1955.
(62) Porod, G. *Small Angle X-ray Scattering*; Glatter, O., Kratky, O., Eds.; Academic Press: New York, 1982; Chapter 2, pp 17−52.
(63) Feigin, L. A.; Svergun, D. I. *Structure Analysis by Small-Angle X-Ray and Neutron Scattering*; Plenum: New York, 1987.
(64) McRae, E. G. Molecular Vibrations in the Exciton Theory for Molecular Aggregates. I. General Theory. *Aust. J. Chem.* **1961**, *14*, 329.
(65) McRae, E. G. Molecular Vibrations in the Exciton Theory for Molecular Aggregates. II. Dimeric Systems. *Aust. J. Chem.* **1961**, *14*, 344.
(66) McRae, E. G. Molecular Vibrations in the Exciton Theory for Molecular Aggregates. III. Polymeric Systems. *Aust. J. Chem.* **1961**, *14*, 354.
(67) Kasha, M.; Rawls, H. R.; Ashraf El-Bayoumi, M. The exciton model in molecular spectroscopy. *Pure Appl. Chem.* **1965**, *11*, 371.
(68) Monahan, A. R.; Blossey, D. F. Aggregation of arylazonaphthols. I. Dimerization of Bonadur Red in aqueous and methanolic systems. *J. Phys. Chem.* **1970**, *74*, 4014.
(69) Verwey, E. J. W.; Overbeek, J. T. G. *Theory of the Stability of Lyophobic Colloids*; Elsevier Publishing Company, Inc.: Amsterdam, 1948.
(70) Schmitz, K. S. *Macroions in Solution and Colloidal Suspension*; VCH Publishers: New York, 1993.
(71) Israelachvili, J. N. *Intermolecular and Surface Forces*; Academic Press: San Diego, CA, 2011.
(72) Everett, D. H. *Basic Principles of Colloid Science*; Royal Society of Chemistry: London, UK, 1988.
(73) Messina, R.; Holm, C.; Kremer, K. Strong Attraction between Charged Spheres due to Metastable Ionized States. *Phys. Rev. Lett.* **2000**, *85*, 872−875.
(74) Zhang, S.; Douglas, J. F.; Ermi, B. D.; Amis, E. J. Influence of counterion valency on the scattering properties of highly charged polyelectrolyte solutions. *J. Chem. Phys.* **2001**, *114*, 3299−3313.
(75) Förster, S.; Schmidt, M.; Antonietti, M. Static and dynamic light scattering by aqueous polyelectrolyte solutions: effect of molecular weight, charge density and added salt. *Polymer* **1990**, *31*, 781.
(76) Gröhn, F.; Antonietti, M. Intermolecular Structure of Spherical Polyelectrolyte Microgels in Salt-Free Solution. 1. Quantification of the Attraction between Equally Charged Polyelectrolytes. *Macromolecules* **2000**, *33*, 5938−5949.
(77) Evans, D. F.; Wennerström, H. *The Colloidal Domain*, 2nd ed.; Wiley-VCH: New York,1999.
(78) Jansen, J. F. G. A.; de Brabander-van den Berg, E. M. M.; Meijer, E. Encapsulation of guest molecules into a dendritic box. *Science* **1994**, *266*, 1226−1229.
(79) Richter-Egger, D. L.; Landry, J. C.; Tesfai, A.; Tucker, S. A. Charge Transfer Kinetics and Solvatochromism of 1-(9-Anthryl)-3-(4-dimethylaniline) Propane in 1,4-Dioxane: Nonideal Quadrupolar Charge Distribution and the Origin of the Dioxane Anomaly. *J. Phys. Chem. A* **2001**, *105*, 6826−6833.
(80) Neumann, B.; Huber, K.; Pollmann, P. A comparative experimental study of the aggregation of Acid Red 266 in aqueous solution by use of ^{19}F-NMR, UV/Vis spectroscopy and static light scattering. *Phys. Chem. Chem. Phys.* **2000**, *2*, 3687−3695.
(81) Botrel, A.; Le Beuze, A.; Jacques, P.; Strub, H. Solvatochromism of a typical merocyanine dye. A theoretical investigation through the CNDO/SCI method including solvation. *J. Chem. Soc., Faraday Trans. 2* **1984**, *80*, 1235−1252.
(82) Brunschwig, B. S.; Ehrenson, S.; Sutin, N. Solvent reorganization in optical and thermal electron-transfer processes: solvatochromism and intramolecular electron-transfer barriers in spheroidal molecules. *J. Phys. Chem.* **1987**, *91*, 4714−4723.
(83) Buncel, E.; Rajagopal, S. Solvatochromic studies of novel azo merocyanine dyes. The.pi.*azo scale of solvent polarity. *J. Org. Chem.* **1989**, *54*, 798−809.
(84) Buncel, E.; Rajagopal, S. Solvatochromism and solvent polarity scales. *Acc. Chem. Res.* **1990**, *23*, 226−231.
(85) Keum, S.-R.; Hur, M.-S.; Kazmaier, P. M.; Buncel, E. Thermo- and photochromic dyes: indolino-benzospiropyrans. Part 1. UV-VIS spectroscopic studies of 1,3,3-spiro(2*H*-1-benzopyran-2,2′-indolines) and the open-chain merocyanine forms; solvatochromism and medium effects on spiro ring formation. *Can. J. Chem.* **1991**, *69*, 1940−1947.

DOI: 10.1021/acs.macromol.6b00565
Macromolecules XXXX, XXX, XXX−XXX

4.6 Photoresponsive Nanoparticle Shape: From Micro-Meter-Long Nanocylinders to Compact Particles in Electrostatic Self-Assembly

Photoresponsive nanoparticle shape: From micrometer-long nanocylinders to compact particles in electrostatic self-assembly

G. Mariani,[a,b] D. Moldenhauer,[a] R. Schweins[b] and F. Gröhn[a]

[a]Department of Chemistry and Pharmacy and Interdisciplinary Center for Molecular Materials (ICMM), Friedrich-Alexander-Universität Erlangen-Nürnberg, Egerlandstraße 3, D-91058 Erlangen, Germany

[b]Institut Laue-Langevin DS/LSS, 71 Avenue des Martyrs, F-38000 Grenoble, France

In this study, we describe a light-triggered shape change of supramolecular nanostructures. Well-defined nano-objects form by electrostatically self-assembly of linear polyelectrolytes and oppositely charged dyes in aqueous solution; for example, 1 µm-long supramolecular flexible cylinders with a well-defined cross-section of 10 nm. Upon UV-irradiation, the shape of the nanoparticles changes into ellipsoids of 400 nm by 40 nm. The effects of building block chemistry and ratio are discussed, showing that the nano-object shape is encoded by the molecular dye structure. Photo-switchable nanoparticle properties bear great potential for medicine and nanotechnology

In this study, we report on how the shape of ionic supramolecular nano-objects in solution can be switched by light: a tremendous shape change, for example from flexible microfibers with nanoscale diameter to compact ellipsoidal particles, occurs in a system consisting of linear cationic polyelectrolytes and a multivalent anionic isomerizable dye. Self-organizing building blocks into supramolecular structures has become of high interest due to the potential for designing a variety of architectures and functions.[1-7] In particular, the possibility to prepare structures that can respond to external triggers is of great relevance. Here, light is especially promising as an effective and tunable non-invasive stimulus.[8-10] In the field of nanosensors, exceptional potential lies in systems where the nanoparticle shape can be controlled since, for example, the optical properties can be triggered,[11] and living cells are sensitive to nanoparticle shape.[12-14]
Ionic nanoparticles with light-tunable *size* recently have been created by electrostatic self-assembly.[15-17] Multivalent organic dyes serve as counterions interconnecting macroions such as ionic dendrimers under secondary for-ces like mutual p-p interaction.[18-21] The concept is based on a general combination of interactions rather than on specific binding motifs.[7,22] Nanoparticles with light-tunable size have been formed with the charged photo-isomerizable dye Acid Yellow 38 in combination with an oppositely charged dendrimer.[15,16] This is opposed to the photoswitchable supramolecular dye-hydrogel composites that respond to light with global contraction or expansion due to a change in hydrophobicity or to azobenzene-bearing polyetheramine particles that change their size and shape due to differences in packing of the *cis*- and *trans*-isomers.[23,24] While the effect of light on the nanoparticle *size* has been recently established, the question of whether light can be used to trigger the nanoassembly *shape* has remained a challenge so far. Shape responsivity is highly desirable for nanotechnology and pharmacy, especially when realized in aqueous solution. Simple linear polyelectrolytes would be highly suitable building blocks as they are readily available. Linear polyelectrolytes have been used to form assemblies according to this concept of electrostatic self-assembly, up to now only with spherosymmetric shape though.[25]
Herein, for the first time, a shape transition upon irradiation is found for electrostatically self-assembled nanoparticles. Moreover, defined and tunable nanoparticle shapes are shown to emerge from linear flexible polyelectrolytes and ionic dyes in solution. Self-assembly and molecular building blocks are sketched in Scheme 1.

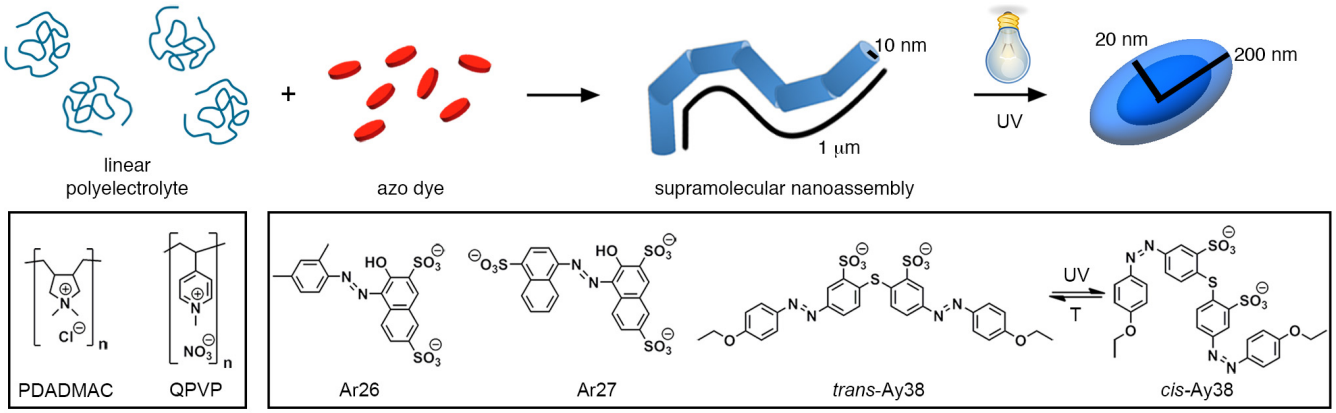

Scheme 1. Representation of the self-assembly process and of the azo dyes and linear polyelectrolytes.

Linear polyelectrolytes have been used in combination with three azo dyes differing in valency and light responsiveness. First, nanoparticle formation of poly(diallyldimethyl-ammonium chloride) (PDADMAC) combined with the divalent Acid Red 26 (Ar26) and with the trivalent Acid Red 27 (Ar27) is investigated by light scattering and small-angle neutron scattering (SANS). The results are given in Figure 1. The charge ratio I_c is the molar ratio of dye sulfonate groups to the quaternary ammonium groups of the polyelectrolyte: $I_c = c(RSO_3^-)/c(NR_4^+)$. Values below unity correspond to an excess of cationic macroion charges. The system forms nanoparticles with a narrow size distribution. Ar26 and PDADMAC yield assemblies with a hydrodynamic radius of R_H = (260 ± 20) nm; that is, multiple polymer molecules (R_H = (14 ± 0.5) nm) become interconnected by dye molecules into well-defined supramolecular particles (Figure 1a). SANS reveals the nanoparticle shape (Figure 1b). Ar26 and PDADMAC form core-shell ellipsoids with a major axis R_{maj} = (130 ± 10) nm and minor axis R_{min} = (15 ± 1) nm. The inner core has a major axis of r_{maj} = (90 ± 10) nm and minor axis of r_{min} = (10 ± 2) nm (red sketch). In contrast, Ar27 forms core-shell cylinders with length L = (700 ± 50) nm, inner radius R_c = (6 ± 1) nm and total radius R_t = (16 ± 1) nm (blue sketch). Samples with different I_c show that the loading ratio has no effect on nanoparticle shape. Hence, the association of linear polyelectrolytes with multivalent ionic dyes results in well-defined nanoparticles,

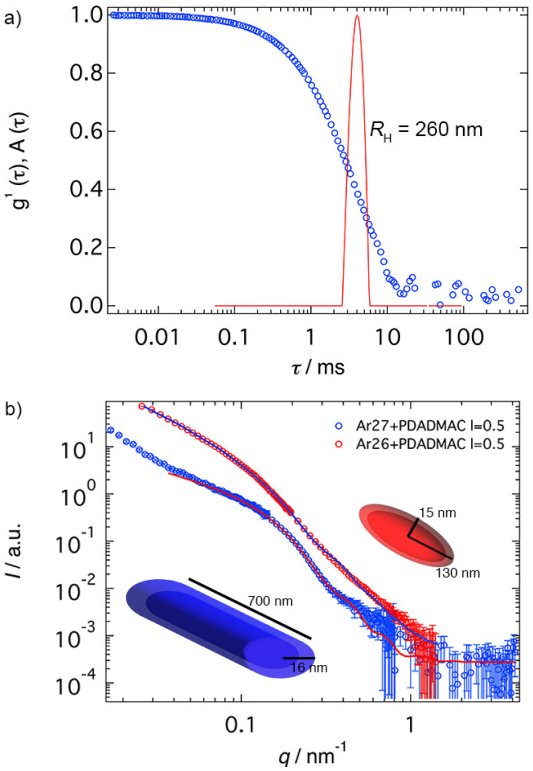

Figure 1. Scattering analysis of dye-linear polyelectrolyte assemblies: a) Dynamic light scattering of Ar26-PDADMAC at I_c = 0.5, electric field autocorrelation function $g^1(\tau)$ and distribution of relaxation time $A(\tau)$: well-defined particles result; b) SANS for Ar26-PDADMAC and Ar27-PDADMAC at I_c = 0.5: different dyes cause different supramolecular nanoparticle shapes.‡

the shape of which is encoded in the molecular counterion structure. On the molecular scale, binding of dyes to polyelectrolytes due to electrostatic interaction induces spatial proximity in the dye molecules, which then can mutually interact, forming π-stacks.[26-28] This can be elucidated by UV-Vis spectroscopy: p-stacking results in the splitting of the first excited state of the monomer.[20,29-33] The spectra of the dyes and dye-polyelectrolyte assemblies are given in Figure 2. The charge ratio is varied to investigate its role on the self-assembly.

For Ar26 and PDADMAC, when 1.0 < I_c < 0.7, the left shoulder in the spectra (representing J-stacks) decreases, while the central peak remains almost constant.[§] For a charge ratio I_c < 0.7, the spectra overall remain almost unchanged. Hence, adding more polyelectrolyte decreases the amount of J-stacks. For both dyes, the spectrum obtained for I_c = 1.0 differs from the other ones. At this charge ratio, nanoparticles are stable only for a limited time, as can also be observed by eye. This is consistent with an electrostatic stabilization of the particles that requires excess charge. To confirm this, the ζ-potential has been studied. Ar26-PDADMAC shows a higher positive ζ-potential (47 ± 1) mV in comparison to Ar27-PDADMAC (43 ± 1) mV. The positive value of the ζ-potential demonstrates that the nanoparticles are stabilized by an excess of polyelectrolyte charges. Moreover, the divalent dyes result in slightly higher-charged nanoparticles.

Fitting the UV spectra, the twist angles β of the stacked dye molecules lie between 40° and 55° (see SI for details). These values strongly depend on the dye's molecular structure: for Ar26-PDADMAC, the twist angle remains at β = 45° as the charge ratio changes, while for Ar27-PDADMAC, the angle decreases with decreasing charge ratio from β = 51° at I_c = 0.7 to b = 41° at I_c = 0.5. Hence, dyes with different molecular structures stack with different twist angles. Therefore, we have demonstrated that the linear polyelectrolyte PDADMAC and anionic dyes form well-defined nanoparticles; in particular, the nanoassembly shape is encoded by the dye's molecular structure.

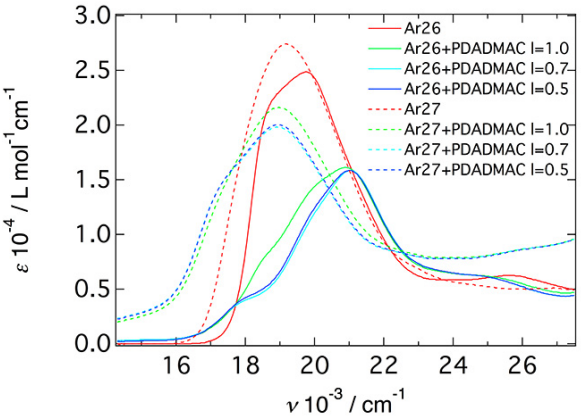

Figure 2. UV-Vis analysis of dye-linear polyelectrolyte assemblies at different charge ratio: a) Ar26-PDADMAC as solid lines and b) Ar27-PDADMAC as dashed lines.

Given that the shape crucially depends on the molecular structure of the dye counterion, it is highly promising to investigate whether light-switchable structures can be formed with a light-responsive dye as a connecting counterion. The dye Ay38 trans-cis isomerizes upon irradiation with UV light. SANS before and after irradiation is shown in Figure 3. It reveals a shape transition: before irradiation, Ay38-PDADMAC forms flexible cylinders with elliptical cross-sections; after irradiation, the system exhibits core-shell ellipsoids. The flexible cylinder is longer than 1 µm, and the cross-section has a major axis R_{maj} = (14 ± 1) nm and a minor axis R_{min} = (5 ± 2) nm. The ellipsoid formed upon irradiation has a major axis R_{maj} = (200 ± 20) nm and a minor axis R_{min} = (20 ± 1) nm; the inner core has r_{maj} = (60 ± 5) nm and r_{min} = (10 ± 1) nm.[§§] To our knowledge, this is the first time that shape changes induced by light have been observed for electrostatically self-assembled nanoparticles. Assemblies that can convert light energy into "mechanical" energy are extremely promising for applications including medicine and nanotechnology. In addition, the particles are based on commonly available linear polyelectrolytes in combination with commercial azo dyes. To check the generality of the concept and gain more understanding, an aromatic polyelectrolyte is investigated: Poly(*N*-methyl-4-vinylpyridinium nitrate) (QPVP) with a molecular weight similar to that of PDADMAC. For Ar26 and QPVP, light scattering again shows well-defined nanoparticles that are slightly smaller than the ones formed with PDADMAC (data see SI). The hydrodynamic radius of the PVP-Ar26 assembles is R_H = (210 ± 20) nm as compared to R_H = (260 ± 20) nm for Ar26-PDADMAC. SANS confirms that different dye molecular structures yield different shapes (Figure 4). Ar26-QPVP forms core-shell ellipsoids with major axis R_{maj} = (120 ± 10) nm and minor axis R_{min} = (15 ± 1) nm with the inner core's axes r_{maj} = (30 ± 2) nm and r_{min} = (5 ± 1) nm. In difference, Ar27-QPVP forms core-shell cylinders like Ar27-PDADMAC. The length is L = (370 ± 10) nm and the total radius is R_t = (25 ± 2) nm with an inner radius of R_c = (10 ± 1) nm. Finally, the light-responsive Ay38 is used as a counterion for QPVP (data see SI). Interestingly, in this case, irradiation does not induce a shape transition, and the nanoparticle size remains almost unchanged. This may be due to the additional π-interaction that can occur between the aromatic rings of the polymer and the dye, likely preventing shape changes. To identify possible differences in dye stacking, UV-Vis spectroscopy has been performed (spectra see SI). A decrease of J-stacks is again observed for a charge ratio I_c < 1.0, similar to the samples with PDADMAC. The effect is more expressed for QPVP. The twist angle is higher for QPVP than for PDADMAC, indicating that dye stacking also strongly depends on the linear polyelectrolyte (41° for Ar26-PDADMAC and 52° for Ar26-QPVP at I_c = 0.7).

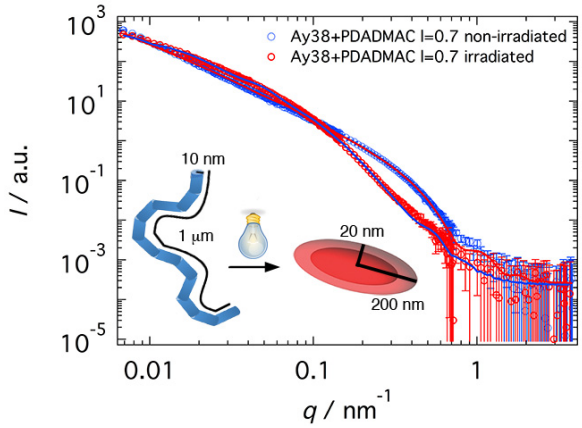

Figure 3. Light switchable nanoparticle shape: SANS for Ay38-PDADMAC assemblies before and after irradiation (I_c = 0.7). Light induces a shape transition from flexible cylinders with elliptical cross-section to core-shell ellipsoids.

Conclusions

Stable and well-defined nanoparticles with a strongly light-switchable structure form with an ionic azo dye and an oppositely charged polyelectrolyte through ionic and π-π interaction in aqueous solution. Versatile self-assembly is possible with a simple linear flexible polyelectrolyte. Crucially depending on the molecular dye structure, nano-object shapes range from core-shell ellipsoids over highly anisotropic cylinders to flexible fiber-like nanostructures with nano-diameter and micrometer length. The chemistry of the polyelectrolyte regulates the dye stacking and excess charge stabilizes the nanoparticles with a specific shape in solution. Nanoparticles consisting of Ay38 and PDADMAC exhibit a shape change from a µm-long flexible cylinder to compact core-shell ellipsoids upon UV-light-irradiation. Hence, light energy is converted into nanoscale shape changes. This new route for the conversion of light into mechanical energy is highly promising for applications in drug delivery, nanosensors and solar energy conversion.

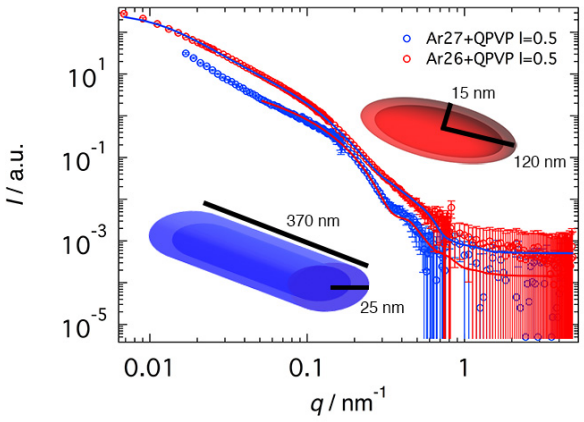

Figure 4. SANS results for A26-QPVP and Ar27-QPVP[8] at I_c = 0.5.

Acknowledgements

Financial support of the German Science Foundation (DFG) and the Interdisciplinary Center for Molecular Materials (ICMM, Universität Erlangen-Nürnberg) is gratefully acknowledged. This work benefitted from SasView software, originally developed by the DANSE project under NSF award DMR-0520547. We acknowledge the support of Institut Laue-Langevin.

Notes and references

‡ For Ar27 the SANS curve rises up at low q. This indicates that few larger assemblies are present in solution.
§ SANS measurements between $0.5 < l_c < 0.7$ show a constant nanoparticle shape.
§§ SANS measurements in accordance with DLS show that the nanoparticle size decreases upon irradiation

1 D. E. Discher, A. Eisenberg, *Science*, 2002, **297**, 967;
2 C. Schmuck, M. Schwegmann, *J. Am. Chem. Soc.*, 2005, **127**, 3373;
3 P. Jonkheijm, P. van der Schoot, A. P. H. J. Schenning, E. W. Meijer, *Science*, 2006, **313**, 80;
4 C. Koopmans, H. Ritter, *J. Am. Chem. Soc,.* 2007, **129**, 3502;
5 S. Srivastava, A. Santos, K. Critchley, K.-S. Kim, P. Podsiadlo, K. Sun, J. Lee, C. Xu, G. Lilly, S. C. Glotzer, N. A. Kotov, *Science*, 2010, **327**, 1355;
6 K. Zhang, A. Geissler, X. Chen, S. Rosenfeldt, Y. Yang, S. Förster, F. Müller-Plathe, *ACS Macro Lett.*, 2015, **4**, 214;
7 G. Mariani, D. Moldenhauer, R. Schweins, F. Gröhn, *J. Am. Chem. Soc.*, 2016, **138**, 1280;
8 T. Tazawa, S. Yagai, Y. Kikkawa, T. Karatsu, A. Kitamura, A. Ajayaghosh, *Chem. Commun.*, 2010, **46**, 1076;
9 P. K. Jha, V. Kuzovkov, B. A. Grzybowski, M. Olvera de la Cruz, *Soft Matter*, 2012, **8**, 227;
10 Z. Zhu, E. Senses, P. Akcora, S. A. Sukhishvili, *ACS Nano*, 2012, **6**, 3152–3162;
11 A. S. Al-Shereiqi, B. J. Boyd, K. Saito, K. *Chem. Commun.,* 2015, **51**, 5460;
12 B. D. Chithrani , A. A. Ghazani , W. C. W. Chan *Nano Lett.* 2006, **6**, 662;
13 W. Jiang, Y. S. Kim Betty, J. T. Rutka, C. W. Chan, *Nat Nano* 2008, **3**, 145;
14 X. Huang, X. Teng, D. Chen, F. Tang, J. He, *Biomaterials* 2010, **31**, 438;
15 I. Willerich, F. Gröhn, *Angew. Chem. Int. Ed.*, 2010, **49**, 8104;
16 I. Willerich, F. Gröhn, *Macromolecules*, 2011, **44**, 4452;
17 D. Moldenhauer, F. Gröhn, *J. Polym. Sci. Part. B: Polym. Phys.*, 2013, **51**, 802;
18 I. Willerich, F. Gröhn, *Chem. - Eur. J.*, 2008, **14**, 9112;
19 I. Willerich, H. Ritter, F. Gröhn, *J. Phys. Chem. B*, 2009, **113**, 3339;
20 F. Gröhn, *Soft Matter*, 2010, **6**, 4296;
21 I. Willerich, F. Gröhn, *J. Am. Chem. Soc.*, 2011, **133**, 20341;
22 I. Willerich, T. Schindler, H. Ritter, F. Gröhn, *J. Phys. Chem. B*, 2011, **115**, 9710.
23 T. Ikeda, J. Mamiya, Y. Yu, *Angew. Chem., Int. Ed*., 2007, **46**, 506;
24 B. Yu, X. Jiang, R. Wang, J. Yin, *Macromolecules*, 2010, **43**, 10457;
25 U. H. Yildiz, K. Koynov, F. Gröhn, *Macromol. Chem. Phys.*, 2009, **210**, 1678;
26 J. F. G. A. Jansen, E. M. M. de Brabander-van den Berg, E. Meijer, *Science*, 1994, **266**, 1226;
27 B. Neumann, K. Huber, P. Pollmann, *Phys. Chem. Chem. Phys.*, 2000, **2**, 3687;
28 D. L. Richter-Egger, J. C. Landry, A. Tesfai, S. A. Tucker, *J. Phys. Chem.*, *B* 2001, **105**, 6826;
29 E. G. McRae, *Aust. J. Chem.*, 1961, **14**, 329;
30 E. G. McRae, *Aust. J. Chem.*, 1961, **14**, 344;
31 E. G. McRae, *Aust. J. Chem.*, 1961, **14**, 354;
32 M. Kasha, H. R. Rawls, A. El-Bayoumi *Pure Appl. Chem.*, 1965, **11**, 371;
33 Monahan, A. R.; Blossey, D. F. *J. Phys Chem.*, 1970, **74**, 4014;

SUPPORTING INFORMATION

Chemicals

Poly(diallyldimethylammonium chloride) (20 wt % in water, M_w = 100,000–200,000 g mol^{-1}) and poly(4-vinylpyridine) ($M_W \approx$ 60000 g mol^{-1}) were purchased from Sigma Aldrich and used as received. For PDADMAC the average molecular mass was determined as M_w = 131,300 g mol^{-1} by light scattering and a hydrodynamic radius of R_h = 14 nm was determined. Acid Yellow 38 (Ay38, C.I. 25135, dye content about 40%) was obtained from MP Biomedicals, Santa Ana, CA. The azo dyes Acid Red 26 (Ar26, C.I. 16150) and Acid Red 27 (Ar27, C.I. 16185) were obtained from Acros, Geel, Belgium. The crude dyes were purified by precipitation of a boiling aqueous dye solution with saturated sodium acetate solution followed by repeated recrystallization from ethanol. Purity of the dyes (>98%) was checked by elemental analysis and ^{1}H NMR.

Synthesis of Poly(*N*-methyl-4-vinylpyridinium nitrate)

Poly(4-vinylpyridine) (5.0 g, 47.6 mmol) was dissolved in dry methanol (50 mL). Any suspension or undissolved material was removed by filtration. The clear solution was brought to reflux in a 100 mL three-neck flask equipped with a condenser and a dropping funnel. Afterwards methyl iodide (4.5 mL, 10.3 g, 72.0 mmol) was added dropwise to the reaction solution and refluxing was continued for 12 h. The precipitated product was collected, thoroughly washed with methanol and dried under vacuum at 40 °C. To remove the yellow-orange color (pyridinium iodide) a part of the product was redissolved in distilled water to 20% (w/v), 0.15 g of silver nitrate per mL of polymer solution was added to precipitate iodide ions (replacing them with nitrate) and the solution was centrifuged with a Sigma 2-16K centrifuge at 14,000 rpm for 20 min. Sodium chloride was then added to remove excess silver ions by precipitation and centrifugation. The solution was filtered with a 0.2 μm filter to remove any dust and lyophilization yielded a white powder of QP4VP. Degree of quaternization was estimated to 98.8% with ^{1}H NMR. ^{1}H NMR (D_2O, 300 MHz, d): 2.09 (s, 3H, CH, CH_2); 4.47 (s, 3H, CH_3); 7.60 (s, 2H, $ArH_{3/5}$); 8.55 (s, 2H, $ArH_{2/6}$).

Sample Preparation

The samples for light scattering were prepared in MilliQ ultrapure water (> 18.2 MΩ cm), while the samples for SANS were prepared in D_2O. With respect to the charge ratio, an amount of polyelectrolyte stock solution was diluted with water. Afterwards the appropriate amount of dye stock solution was added at once under turbulent stirring inducing assembly formation.

Sample Irradiation

Samples were irradiated in a Horiba Yvon Jobin Fluoromax spectrometer. The excitation slit was set to 380 ± 1 nm. Irradiation was carried out for 20 min. It was checked that longer irradiation times did not influence the results, that is, the photostationary state was reached.

Light Scattering

Measurements were carried out on an ALV CGS 3 goniometer with ALV 5000 correlator (ALV Germany) equipped with a HeNe laser with a wavelength of λ = 632.8 nm and 20 mW output power. Measurements covered an angular range of $30° \leq \theta \leq 150°$. The instrument performs simultaneously static and dynamic light scattering measurements. Data analysis was carried out by converting the measured intensity autocorrelation function into the scattered electric field autocorrelation function using the Siegert relation. The electric field autocorrelation functions $g^1(\tau)$ were further analyzed by regularized inverse Laplace transformation using the program CONTIN by S. Provencher to obtain the distribution of relaxation times $A(\tau)$. From this, the apparent diffusion coefficient D_{app} was calculated using the relation $D_{app} = q^{-2}\, t^{-1}$. To determine the hydrodynamic radius R_H, the apparent diffusion coefficient D_{app} is extrapolated to zero scattering angle and then converted into R_H through the Stokes-Einstein relationship. To extend the SANS spectrum at lower q, the static results have been used. This approach extends the curves in the q range between 6.8 10^{-4} and 2.5 10^{-3} nm^{-1}.

UV-Vis Spectroscopy.

Absorption spectra were recorded on a Shimadzu UV-1800 spectrometer using quartz cuvettes with 1 cm path length at dye concentrations of c = 2 10^{-5} mol L^{-1}. The experimental extinction coefficient has been fitted according to the relation:

$$\varepsilon_D = \varepsilon_J \exp\left[-4ln2\,\frac{(\nu-\nu_J)^2}{\Delta\nu^2_{1/2,J}}\right] + \sum_{i=0}^{1} \varepsilon_i \exp\left[-4\,ln2\,\frac{(\nu-\nu_i)^2}{\Delta\nu^2_{1/2,i}}\right]$$

Where ε_D is the extinction coefficient of the dimer. This approximation is valid since the spectral separation between the H- and J-band is greater than the vibronic progression. Therefore the first term of the equation refers to the J-band with ε_J as extinction coefficient, ν_J as wavenumber and $\Delta\nu_{1/2,J}$ as half-width of the Gaussian. The second term represents the H-band extended to two vibronic transitions. From the fits, the twisting angle β can be obtained:

$$\beta = 2\,arctan\sqrt{\frac{f_J}{f_H}}$$

With f_i is the oscillator strength for the i-th band calculated by integration of the respective peak area.

Small Angle Neutron Scattering

Samples for SANS at a polyelectrolyte concentration of 0.5 g L^{-1} and transferred into quartz cells with 2 mm path length. SANS studies were performed on D11 at the Institut Laue-Langevin, Grenoble, France and on KWS2, at the Jülich Center for neutron scattering at FRM II, Munich, Germany. On D11 λ = 6 Å was used for 3 different sample-detector distances, 1.2 m, 8 m and 39 m. The wavelength spread

($\Delta\lambda/\lambda$) was 0.09. A total scattering vector range of: 0.007 $nm^{-1} < q < 5\ nm^{-1}$ was investigated. At KWS2, a wavelength of 4.55 Å was used with 3 sample-detector distances: 2 m, 8 m and 20 m. For some samples a different combination has been used: 2 m, 4 m and 20 m: the 8 m distance was replaced with 4m to obtain a very similar scattering vector with a higher neutron flux. In this case a total scattering vector of $0.035\ nm^{-1} < q < 5\ nm^{-1}$ was covered. Data were corrected for empty cell scattering, electronic background and detector uniformity and then converted to absolute scale using secondary standards. Then the scattering of the solvent and the incoherent background have been subtracted from the data. The scattering curve I(q) has been, firstly, analyzed by Guinier analysis, where possible, and by inverse Fourier transformation to obtain the pair distribution function P(r) through the relationship: $I(q) = 4\pi \int P(r) \sin(qr) / qr\, dr$. On the basis of the first results, structural modeling by standard fitting packages such as SASview has been used to obtain the particles shape and dimensions. For some samples the instrument resolution has been taken in account in the fitting process to check its influence on the obtained results.

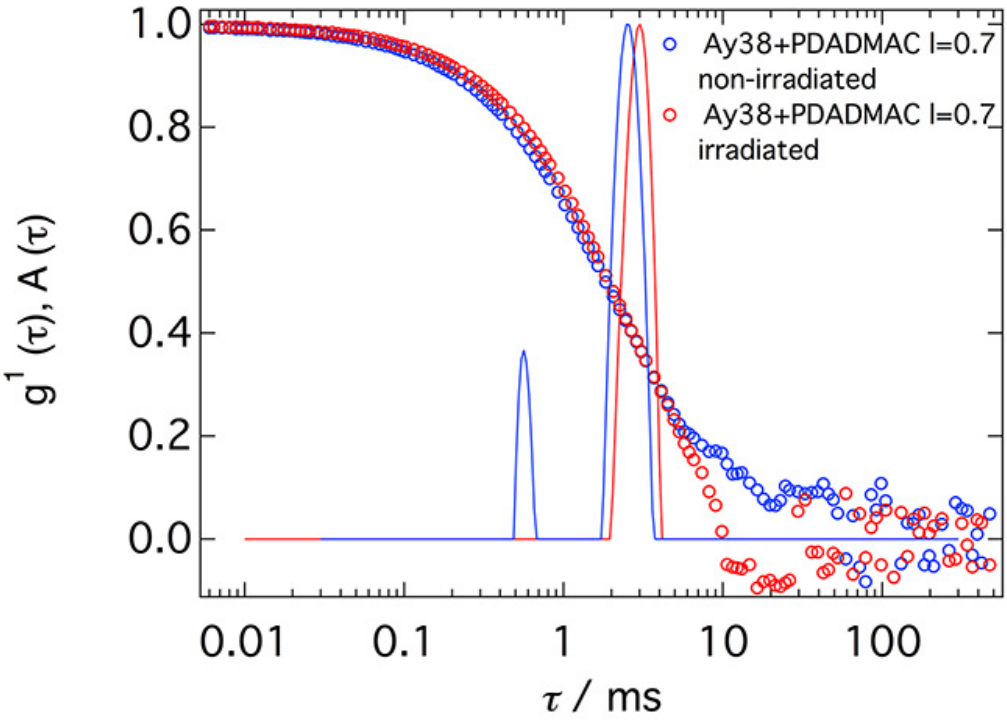

Figure S1 Dynamic light scattering analysis of PDADMAC and Ay38 at l_c = 0.7 before and after irradiation.

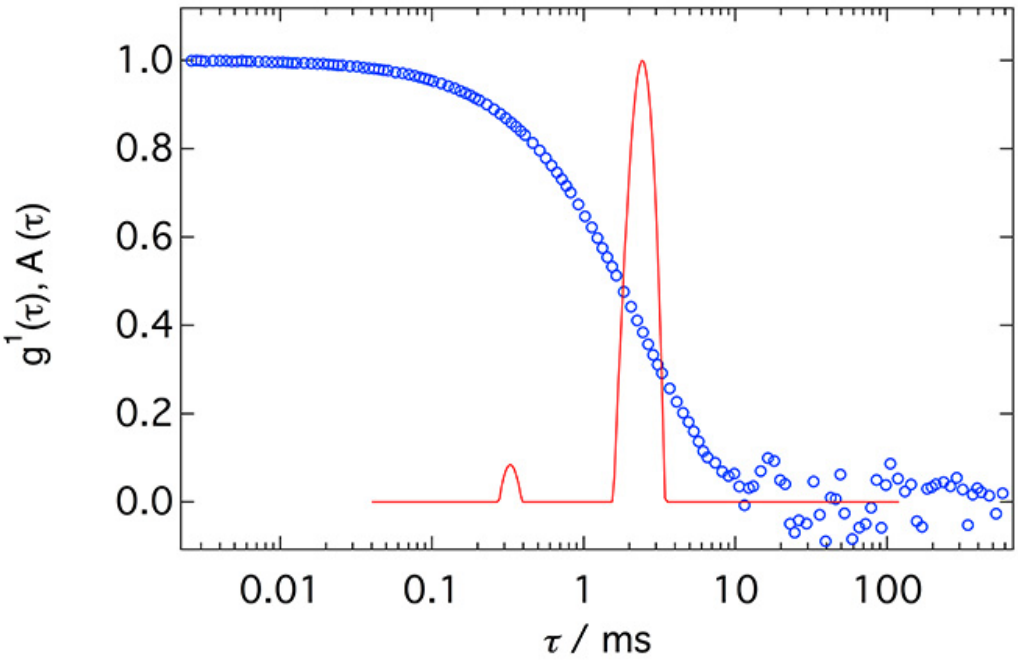

Figure S2 Dynamic light scattering analysis of QPVP and Ar26 at l_c = 0.4.

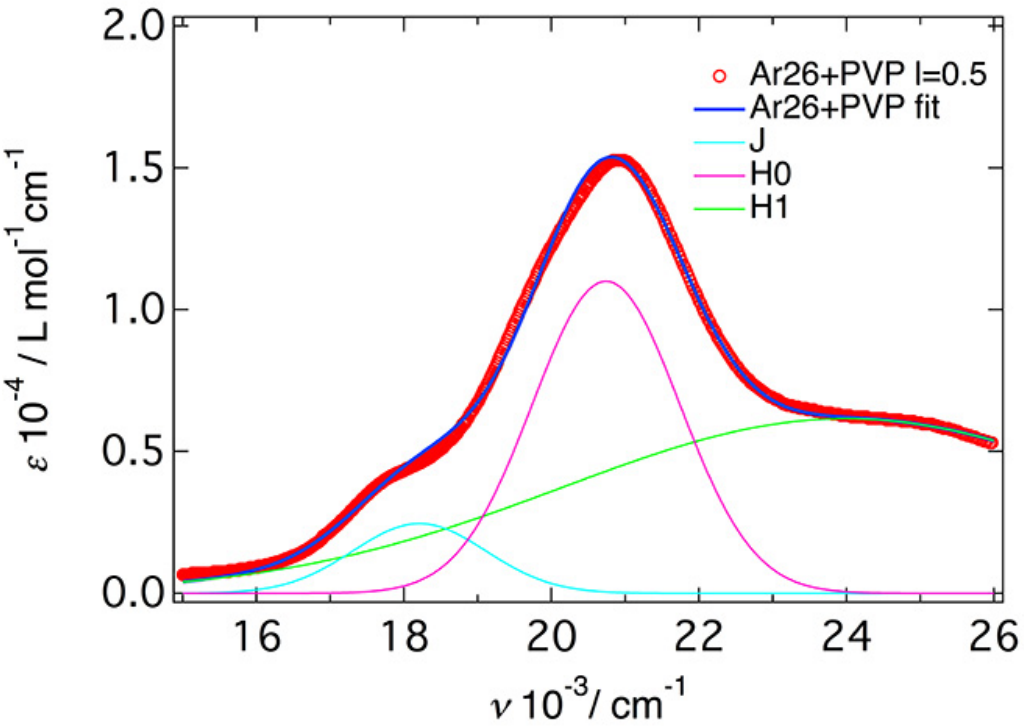

Figure S3 Exciton theory applied to Ar26 + QPVP, the three Gaussian used to describe the UV-Vis spectra are reported.

Table 1 Analysis of Mutual Dye Geometry According to Exciton Theory

Sample	charge ratio l_c	Twist angle β / °
Ar26 + PDADMAC	0.5	45 ± 1
	0.7	45 ± 1
Ar26 + QPVP	0.5	48 ± 1
	0.7	52 ± 1
Ar27 + PDADMAC	0.5	51 ± 1
	0.7	41 ± 1
Ar27 + QPVP	0.5	50 ± 1
	0.7	44 ± 1

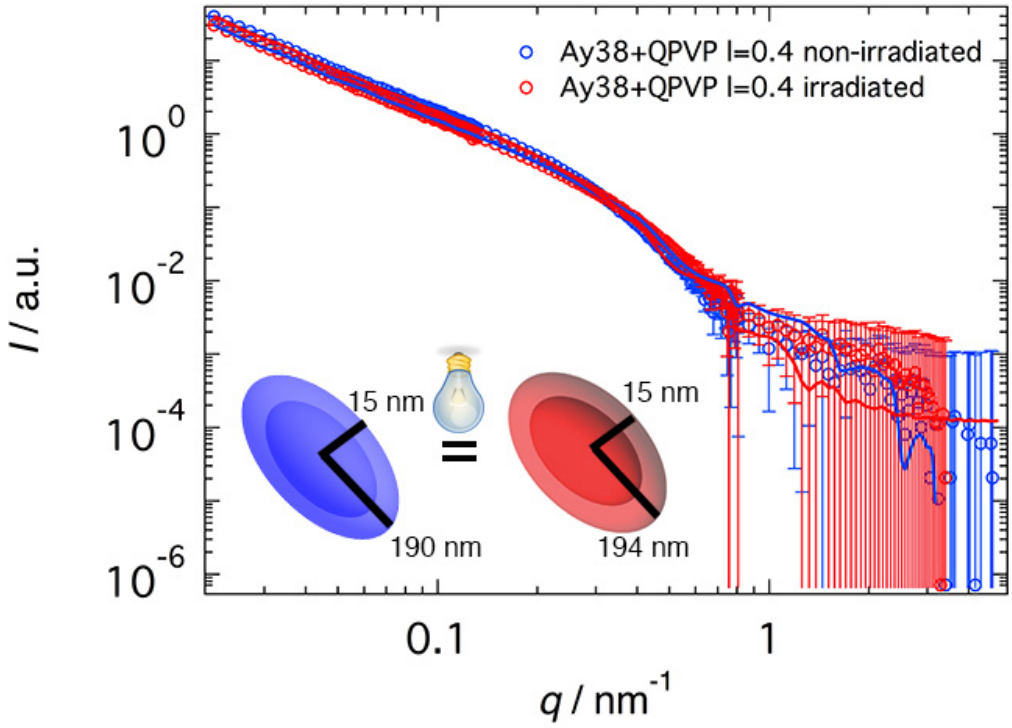

Figure S4 SANS results for Ay38-QPVP before and after irradiation at l_c = 0.4. No shape transition is observed upon irradiation.

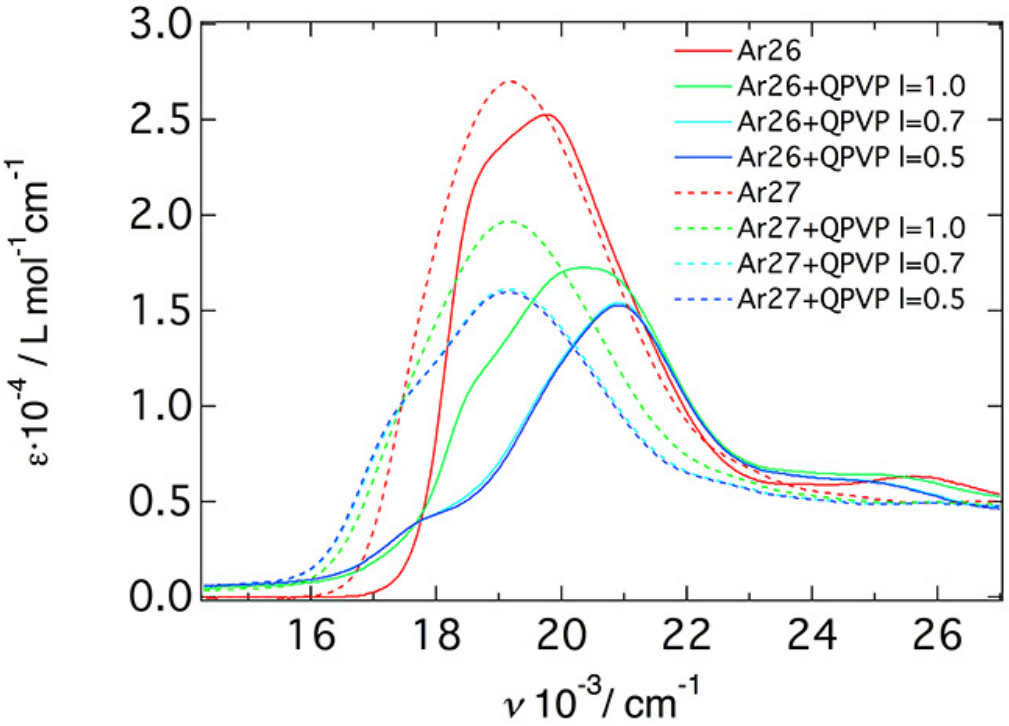

Figure S5 UV-Vis analysis of linear dye-polyelectrolyte systems: a) Ar26-QPVP samples at different charge ratios as solid lines and b) Ar27-QPVP samples as dashed lines at different charge ratios.

Chapter 5 Other Contributions

5.1 Porphyrin Diacid-Polyelectrolyte Assemblies: Effective Photocatalysts in Solution

polymers

MDPI

Article

Porphyrin Diacid-Polyelectrolyte Assemblies: Effective Photocatalysts in Solution

Sabine Frühbeißer [1], Giacomo Mariani [1,2] and Franziska Gröhn [1,*]

[1] Department of Chemistry and Pharmacy, Friedrich-Alexander University Erlangen-Nürnberg, Interdisciplinary Center for Molecular Materials (ICMM), Egerlandstraße 3, Erlangen 91058, Germany; sabine.fruehbeisser@fau.de (S.F.); giacomo.mariani@fau.de (G.M.)

[2] Institut Laue-Langevin DS/LSS, 71 Avenue des Martyrs, Grenoble F-38000, France

* Correspondence: franziska.groehn@fau.de; Tel.: +49-85-20731

Academic Editor: Christine Wandrey

Received: 19 March 2016; Accepted: 25 April 2016; Published: 4 May 2016

Abstract: Developing effective and versatile photocatalytic systems is of great potential in solar energy conversion. Here we investigate the formation of supramolecular catalysts by electrostatic self-assembly in aqueous solution: Combining positively charged porphyrins with negatively charged polyelectrolytes leads to nanoscale assemblies where, next to electrostatic interactions, π–π interactions also play an important role. Porphyrin diacid-polyelectrolyte assemblies exhibit a substantially enhanced catalytic activity for the light-driven oxidation of iodide. Aggregates with the hexavalent cationic porphyrin diacids show up to 22 times higher catalytic activity than the corresponding aggregates under neutral conditions. The catalytic activity can be increased by increasing the valency of the porphyrin and by choice of the loading ratio. The structural investigation of the supramolecular catalysts took place via atomic force microscopy and small angle neutron scattering. Hence, a new facile concept for the design of efficient and tunable self-assembled photocatalysts is presented.

Keywords: self-assembly; porphyrins; supramolecular catalyst; supramolecular structures; polyelectrolytes; photocatalysis

1. Introduction

Many functional structures in nature are based on non-covalent self-assembly principles. In the last years, self-assembly has emerged as a powerful method to create supramolecular structures of various sizes, shapes, architectures and functionalities [1–12]. Due to their size scale and versatile chemistry, polymers are very suitable building blocks to form a variety of stable assemblies in solution. In particular, polyelectrolytes have been successfully used for the formation of a variety of polyelectrolyte complexes, polyelectrolyte-surfactant complexes and in layer-by-layer deposition [13–24]. More recently, electrostatic self-assembly of multivalent organic counterions with oppositely charged polyelectrolytes has allowed formation of a broad range of nanoscale architectures in solution [25–33]. It is thus highly interesting to now exploit this concept of polyelectrolyte-organic counterion assembly to promote electrostatic self-assembly for the formation of functional nanoassemblies in solution.

Porphyrins and metalloporphyrins play a key role in several fundamental processes in life [34–40]. Extensive efforts have been undertaken to mimic efficient photoinduced electron-transfer processes which take place in photosynthesis and to create artificial systems. Among the variety of examined electron donors, porphyrins are very promising as they are the skeleton of chlorophyll and absorb intensively in the visible spectrum and exhibit high extinction coefficients [34,40–46]. Therefore, they have become very attractive for applications in various fields [47–53]. Water-soluble

porphyrins are of particular interest due to their application in biological or medical fields [54]. The aggregation behavior of porphyrins has been studied extensively, and they have been combined with many-faceted molecules in supramolecular chemistry [55–67]. Porphyrins are often used for hydrogen production and for hydrogen storage which is an important challenge for the automotive industry [68–76]. Moreover, porphyrins can form interesting structures which are advantageous for several applications. Hasobe *et al.* reported the formation of hexagonal hollow nanotubes consisting of zinc *meso*-tetra(4-pyridyl) porphyrin which show a high power conversion efficiency (PCE) when filled with C_{60} or C_{70} [77].

Under acidic conditions the number of charges of free-base porphyrins can be tuned from four to six, resulting in porphyrin diacids, which also show interesting photophysical properties: They exhibit long-lived triplet states and their Q-bands appear in the near-IR-region. Therefore, a large fraction of the solar spectrum can be collected and hence porphyrin diacids represent potentially good photosensitizers [78–81]. In comparison to free-base and metalloporphyrins, however, much less attention has been paid to porphyrin diacids.

We recently found that porphyrin-polyelectrolyte assemblies with a tetravalent porphyrin show a substantially higher catalytic activity than pure porphyrin under neutral conditions [67].

Herein, for the first time, we investigate the catalytic activity of porphyrin-polymer assemblies under strongly acidic conditions where the free-base porphyrins carry two additional charges in the inner ring and in total are six-fold positively charged. We compare free-base porphyrin with the Zn-TMPyP as a metalloporphyrin. The building blocks used in this study are illustrated in Scheme 1. As macroion component, either an anionic cylindrical poly(styrene sulfonate) brush molecule (PSS brush) with about 12 nm diameter and 100 nm length or the corresponding anionic linear polystyrene sulfonate is used. These polyelectrolytes are combined with cationic *meso*-tetrakis(4-*N*-methylpyridinium) porphyrin (TMPyP), *meso*-tetrakis(4-(trimethylammonium) phenyl)-porphyrin (TAPP) or tetravalent *meso*-tetrakis-(*N*-methyl-4-pyridyl)-porphyrin-Zn(II) tetrachloride. The chosen model reaction for the investigation of the catalytic activity is the light-induced oxidation of iodide in aerobic conditions. The study shows that efficient supramolecular catalysts for photooxidation can be formed by electrostatic self-assembly in aqueous solution, as indicated in Scheme 2.

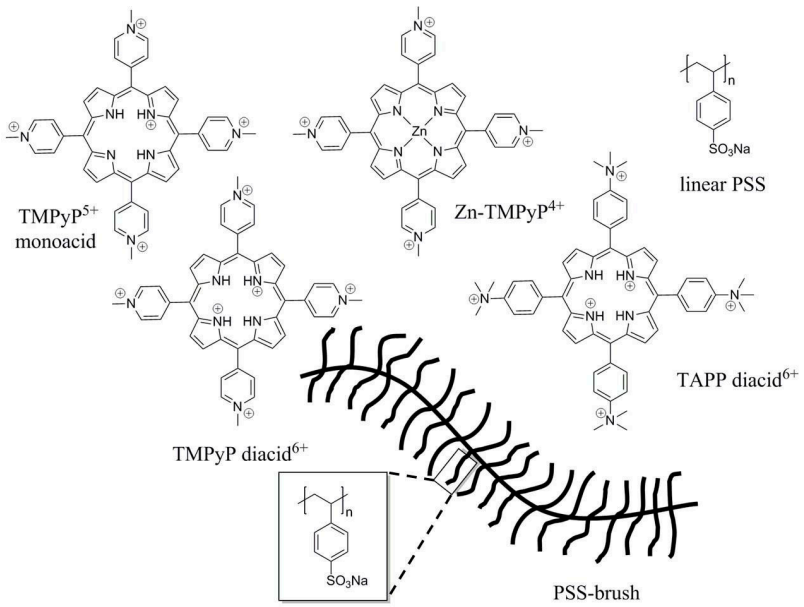

Scheme 1. Building blocks used in this study: Cylindrical polystyrene sulfonate brushes or linear polystyrene sulfonate are combined with cationic porphyrins to build nanoscale assemblies in acidic aqueous solution.

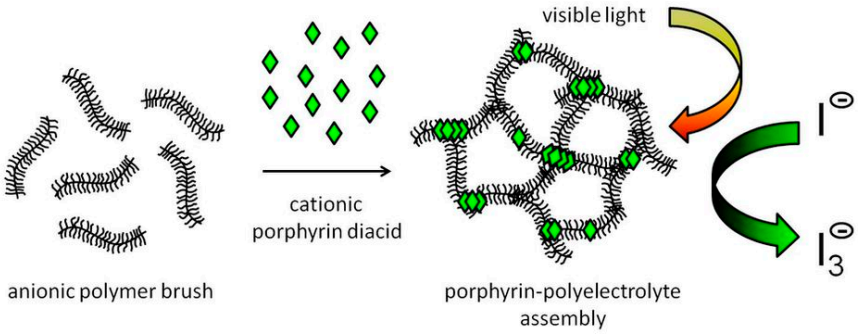

Scheme 2. Formation of a supramolecular polyelectrolyte-porphyrin photocatalyst by electrostatic self-assembly.

2. Materials and Methods

2.1. Chemicals

TAPP, TMPyP and potassium iodide were purchased from Sigma-Aldrich, Selmsdorf, Germany. Zn-TMPyP was purchased from TriPorTech, Selmsdorf, Germany. The cylindrical PSS brush was synthesized through polymerization of polystyrene macromonomers and subsequent sulfonation as described previously [82]. A polystyrene macromonomer was synthesized by anionic polymerization of styrene and subsequent end-functionalization by *p*-vinylbenzyl chloride. The macromonomer was characterized by MALDI-TOF giving M_w = 4450 g·mol^{-1} with M_w/M_n = 1.06 from size exclusion chromatography (SEC) analysis (defining the later side chain length of the polymer brush being $P_{w,side\ chain}$ = 43). Free radical homopolymerization of this macromonomer yielded a polystyrene brush with M_w = 2.13 × 10^6 g·mol^{-1} and M_w/M_n = 3.02 (SEC). To obtain lower polydispersities the polystyrene brush was fractionated by continuous polymer fractionation (CPF). A high molecular mass fraction with M_w = 4.12 × 10^6 g·mol^{-1} and M_w/M_n = 1.51 (weight average degree of polymerization of the total polymer $P_{w,total}$ = 39,000 and of the main chain $P_{w,main\ chain}$ = 900) was chosen. The polystyrene brush was then sulfonated with sulfuric acid/acetic anhydride in 1,2-dichloroethane at 50 °C. This results in a NaPSS brush with 100% sulfonation according to elemental analysis. Light-scattering analysis confirmed the polymeranalogous reaction to take place without degradation. Linear polystyrene was purchased from PSS standards with a molecular mass fraction with M_w = 666,000 g·mol^{-1} and a PDI < 1.2.

2.2. Sample Preparation

Samples were prepared by mixing aqueous solutions of the components and keeping them in darkness prior to further investigations. The irradiation was performed with a 300 W halogen lamp with a visible spectrum similar to daylight.

2.3. UV/Vis Spectroscopy

UV/Vis spectra were recorded using a SHIMADZU UV Spectrophotometer (UV-1800), Kyoto, Japan, with a slit width of 1 nm using quart cuvettes from Hellma with 1 and 10 cm path length. The spectral range covered 200 nm $\leqslant \lambda \leqslant$ 800 nm.

2.4. Atomic Force Microscopy

Measurements were performed with a SolverPro AFM (NT-MDT Co., Moscow, Russia) equipped with a 50 µm scanner, an optical zoom and a damping activated table. The tip in tapping mode was a HA-NC noncontact mode cantilever with a resonance frequency of 130–180 kHz and a spring constant of 4.5 nm^{-1} (±20%) (also NT-MDT). For sample preparation, a droplet of 20 µL of the sample was

added onto a freshly prepared mica surface and incubated for 5 min and dried in air. The TAPP-PSS brush sample l = 0.4 was spincoated at 3000 rpm.

2.5. Small Angle Neutron Scattering (SANS)

Measurements were performed at beamline KWS2 at the Jülich Centre for Neutron Science at the Heinz Maier-Leibnitz Zentrum (MLZ), Garching, Germany, and at the beamline D11 at Institut Laue Langevin (ILL), Grenoble, France. Data shown result from MLZ. Three configurations with neutron wavelengths λ = 4.55 Å and a sample-detector distance of d = 2 m, d = 8 m and d = 20 m were used. Data were corrected for empty cell scattering, electronic background, detector uniformity and analyzed after subtracting solvent scattering and incoherent background. Error bars lie within 1%–5% at low q and increase up to 15% at 0.9 $nm^{-1} \leqslant q$.

3. Results

An important parameter for the investigation of the assemblies is the loading ratio, which is the molar ratio of porphyrin charges to polyelectrolyte charges:

$$l_{\text{charge}} = \frac{c(\text{–NR}_3^+, \text{Porphyrin})}{c(\text{–SO}_3^-, \text{Polyelectrolyte})} \quad (1)$$

The structural investigation of the catalytically active aggregates takes place via atomic force microscopy (AFM) and small angle neutron scattering (SANS).

Under strong acidic conditions (pH < 2) the two inner nitrogen bases of a metal-free porphyrin ring become protonated leading to a hexavalent species in the case of cationic tetraphenylporphyrins accompanied by a strong colour change from red to green [83]. The valency increase from four to six is accompanied by an increase in symmetry from D_{2H} to D_{4H}. Therefore, the planarity of the macrocycle of TMPyP and TAPP disappears and the metal-free porphyrins have the same symmetry as for example Zn-TMPyP. In the case of TMPyP, both, a pentavalent and a hexavalent porphyrin, can be received depending on pH. For the TMPyP monoacid pH 1.7 is sufficient whereas the diaicd is generated by dissolving the porphyrin directly in 1 M hydrochloric acid, *i.e.*, at pH = 0. Going from the tetravalent free-base porphyrin to the pentavalent TMPyP monoacid leads to a decrease of symmetry from D_{2H} to C_{2V}. This one additional charge has a tremendous effect on the catalytic activity as will be discussed in the following.

3.1. Atomic Force Microscopy (AFM)

In the AFM images shown in Figure 1, a loading ratio l = 0.4 was chosen for comparison, as this turned out to be the ratio with the highest catalytic activity under neutral conditions [31]. Structural differences are evident for the aggregates formed by the different porphyrin species with PSS brush. Figure 1a,b displays network-like structures formed by TAPP diacid and PSS brush, which were already found under neutral conditions [26,30]. Under acidic conditions these networks exhibit smaller dimensions in length (up to 645 nm) and even smaller dimensions in height (4 to 5.5 nm) as compared to former studies under neutral conditions that showed TAPP-PSS brush assemblies several μm in length and up to 15 nm in height [26].

To investigate the influence of each additional charge in the case of TMPyP systematically, the structure of TMPyP-PSS brush samples under neutral conditions was investigated (Figure 1g,h). Under neutral conditions, TMPyP-PSS brush forms well-defined, network-like structures which are 21 nm in height and exhibit also slightly larger meshes. In contrast, TMPyP monoacid (Figure 1e,f) forms rather undefined networks with several μm size which are up to 64 nm high. Hence, one additional charge causes a transition from well-defined network-like structures to rather undefined networks. Increasing the number of charges further so that the TMPyP diacid (Figure 1c,d) is present, again well-defined network-like structures result. They exhibit a height of 32 nm. Considering the

PSS brush structures in the obtained aggregates more closely, one can see that the diameter of the PSS brush is up to twice as large in TMPyP diacid-PSS brush aggregates (Figure 1d) than under neutral conditions (Figure 1h). For the TAPP-PSS brush, one can see that there is nearly no difference in PSS brush width in the two considered pH regions. Furthermore, Figure 1i,j displays network-like structures for Zn-TMPyP and PSS brush under neutral conditions which are 17 nm in height and several hundreds of nm in size and which are therefore very similar to structures formed with TAPP and TMPyP under equivalent conditions (Figure 1g,h).

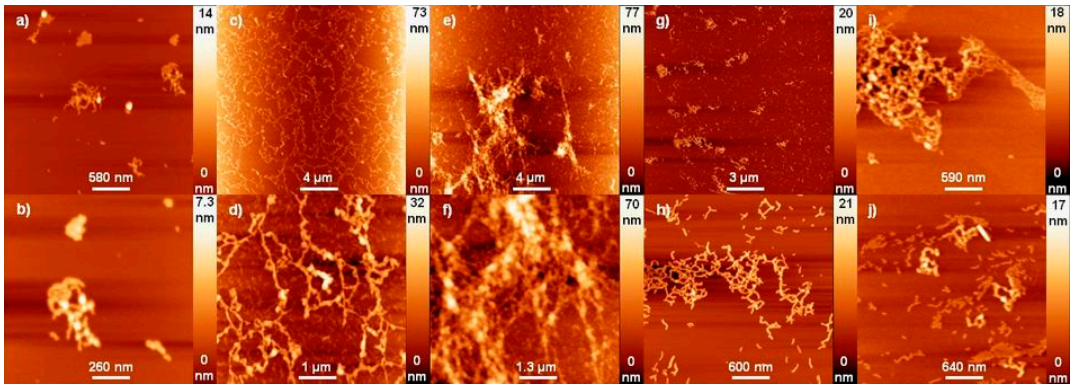

Figure 1. Atomic force microscopy (AFM) of porphyrin/PSS brush samples deposited onto a mica surface: (**a**,**b**) TAPP diacid-PSS brush sample with l = 0.4; (**c**,**d**) TMPyP diacid-PSS brush sample with l = 0.4; (**e**,**f**) TMPyP monoacid-PSS brush sample with l = 0.4; (**g**,**h**) TMPyP-PSS brush l = 0.5 in neutral solution; (**i**,**j**) Zn-TMPyP-PSS brush l = 0.4 in neutral solution.

Several reasons could be responsible for the formation of well-defined or rather undefined structures with the different TMPyP species. The even or odd number of charges may be one reason for this because the PSS brush molecules can distribute less regularly with only one charge in the porphyrin ring. Increasing the number of charges from five to six, networks with TMPyP diacid (Figure 1d) (32 nm) are half as high as those with TMPyP monoacid (64 nm) and much more defined. Structural differences between TMPyP monoacid and TMPyP diacid can derive from their different symmetry (C_{2V} D_{4H}). In addition, differences of the porphyrins TMPyP and TAPP can originate from the different ionic strengths. pK_a values for TAPP diacid and for TMPyP diacid are 3.6 and 1.4, respectively, indicating that TMPyP is the most acidic and the ionic strength is much larger in the TMPyP diacid sample than in the TAPP diacid sample. Usually, high ionic strength leads to a decrease in porphyrin-porphyrin charge repulsion due to screening and therefore the π-systems of two porphyrin macrocycles are more prone to interact intermolecularly. One might expect that the networks of TMPyP diacid-PSS brush exhibit tighter meshes due to the higher ionic charge, but it is in fact the opposite. The reason for this is not directly evident. High ionic strength was also investigated for TAPP diacid-PSS brush by dissolving both also directly in 1 M hydrochloric acid. The sample precipitates immediately and investigation with AFM was not possible. At higher ionic strength, screening of the electrostatic forces takes place leading to a stronger aggregation tendency. The structural investigation by AFM showed that TAPP diacid in combination with PSS brush also forms network-like structures similar to those under neutral conditions. In contrast, TMPyP diacid assembles into "huge" broader meshed networks and TMPyP monoacid makes larger undefined structures with PSS brush.

3.2. Structural Investigation by Small Angle Neutron Scattering (SANS)

To gain further insight into the structure and the shape of the aggregates in solution, small angle neutron scattering (SANS) measurements for each system were performed at polyelectrolyte concentrations of c (PSS brush) = 1 g· L^{-1}, except for the TMPyP diacid sample where the concentration was c (PSS brush) = 0.05 g· L^{-1}. Data are reported in Figure 2a. Scattering curves (Figure 2a) give

evidence of the cylindrical shape of the PSS brush as the slope in a log/log representation for the intermediate q-range is -1.09, according to the scaling of the form factor P(q) with q^{-1} for long rods. From the first point or from the point where a plateau can be seen, the minimum length or approximate length of the cylinder is found via $l = 2\pi/q_{\min}$ which is approximately 250 nm. To gain more information, the curves have been analyzed by Guinier analysis (Figure 2b). The linearity of a cross-section Guinier plot confirms the cylinder shape. From the slope, the cross-section radius of gyration R_{Gc}, can be obtained, which for the PSS brush is R_{Gc} = 4.8 nm. Assuming a homogeneous structure, this R_{Gc} can be converted into a cross-section radius and consequently into a diameter, which is 13.8 nm, in good agreement with former studies [26,30]. To see how the porphyrin influences the PSS brush in the aggregates, samples with the same loading ratio l were investigated for each porphyrin.

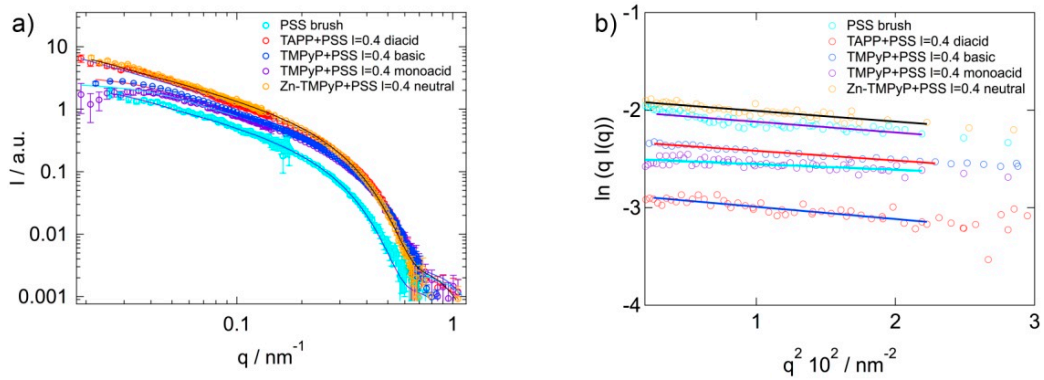

Figure 2. Small angle neutron scattering of PSS brush and different porphyrins: (**a**) scattering curves I(q); (**b**) cross-section Guinier plot. Straight lines reflect the corresponding fit.

In each case, cylindrical nanoassemblies were found. Table 1 shows the cylinder lengths, R_{Gc} and radii. On the basis of this first analysis, the experimental curves have been fitted according to structural models to obtain the particle shape and dimensions. Results are given in Figure 2a (solid lines) and Table 1. It can be seen that all the determined radii are smaller than the one of the PSS brush alone, while lying all in the same range. TMPyP diacid-PSS brush differs, as with 12 nm the radius is nearly twice as large as that of the PSS brush. The result fits well with the observations during sample preparation as precipitation occurs immediately for polyelectrolyte concentrations of c (PSS brush) = 1 g· L^{-1}, which is why a distinct smaller concentration has to be used.

Table 1. Cylinder lengths, cross-section radii and radii from SANS data.

Sample	R_{GC} [1] (nm)	Diameter [1] (nm)	Model	Length (nm)	Radius (nm)
PSSbrush neutral	4.8	13.8	Cylinder	140 ± 10	5.9 ± 0.1
TMpyP + PSSbrush	4	11.4	Cylinder	100 ± 10	5.1 ± 0.1
TMPyPmonoacid + PSSbrush l = 0.4	4.0	11.4	Cylinder	93 ± 3	4.8 ± 0.1
TMPyP diacid + PSS brush l = 0.4	–	–	Cylinder	2,700 *	12 ± 0.1
Zn-TMPyP + PSS brush l = 0.4	4.6	13	Cylinder	200 *	5.8 ± 0.1
TAPP diacid + PSSbrush l = 0.4	4.3	12.3	Cylinder	100 *	5.2 ± 0.1

[1] Determined via Guinier approximation and modeling; * Length taken from AFM.

Hence, SANS results showed that cylindrical aggregates are formed, which is consistent with AFM where individual strands of the networks exhibit a cylindrical shape. The lengths of these cylinders range from 93 to 2700 nm. Differences in length are also evident from the AFM images: for the TMPyP diacid-PSS brush sample, large network-like structures were found, the single-strand dimensions of which are given in comparison are the longest and widest. The largest radius for the cylinders formed by TMPyP diacid and PSS brush is in good agreement to the corresponding AFM.

An exception is the TMPyP monoacid, where structures found in AFM are quite undefined. All the diameters are smaller than that of TMPyP diacid and also the determined lengths are all distinctly smaller. Hence, overall SANS and AFM results are in very good agreement.

The observation that, with the exception of TMPyP daicid, the radii are all smaller than those of PSS brush in a broader view agrees very well with observations from former studies, where SANS measurements under neutral conditions with and without salt were performed [62,66]. It was observed that PSS brush had the largest radius followed by TAPP-PSS brush and TMPyP-PSS brush. Thus the shrinkage herein can derive from the larger number of charges of the porphyrin, which causes the porphyrin to enter more into the inside of the PSS brush, as the PSS brush has more power to bind it due to the additional two charges and therefore smaller diameters result. Former studies pointed out that side-chain interconnections seem to be responsible for the smaller diameters of the porphyrin-PSS brush assemblies under neutral conditions, [30] which also is the case for TAPP diacid and TMPyP monoacid. The behavior of TMPyP diacid, in contrast, appears to be different and is not understood yet.

3.3. Spectroscopic Investigation

The difference in valency becomes evident spectrochemically as can be seen in Figure 3. Here, samples with and without polyelectrolyte under neutral and acidic conditions are investigated for the three different porphyrins. Figure 3a–c exhibit the complete spectrum, whereas Figure 3d–f focus on the enlarged Q-bands. Under neutral conditions, the Soret band of pure TAPP (Figure 3a) is red-shifted for TAPP-PSS brush aggregates with l = 0.4, indicating the formation of J-aggregates and a head-to-tail interaction of the transition dipole moments. Changing the pH from neutral to acidic, the TAPP Soret band undergoes a bathochromic shift indicating the formation of J-aggregates. This bathochromic shift with 9 nm under neutral conditions is slightly larger than under acidic conditions with 6 nm indicating larger interactions between the TAPP and the PSS brush or the formation of larger J-aggregates under neutral conditions. This pH change is, as already mentioned, accompanied by an increase of symmetry, which again is accompanied by a reduction of the number of Q-bands from four to two. The presence of PSS brush leads to a small further red-shift of the TAPP diacid Soret band (Figure 3b). The Q-bands undergo no spectral shift upon combination with the polyelectrolyte under neutral conditions, while this is different under acidic conditions. Here, a slight bathochromic shift of the Q-bands in the presence of PSS brush can be seen. Spectral data from Figure 3 are summarized in Table 2. In the case of TMPyP (Figure 3c), no band shifts of the Soret band from the neutral TMPyP to TMPyP monoacid can be observed. The presence of PSS brush in neutral conditions leads to a small change of the Soret band characteristics but not to a band shift. For the TMPyP diacid, a clear bathochromic shift of the Soret band can be observed indicating the formation of J-aggregates and a head-to-tail interaction of the transition dipole moments as for TAPP diacid, which in the presence of PSS brush is slightly more expressed. For TMPyP monoacid, the presence of PSS brush leads to a red-shift of the Soret band and for the illustrated charge ratio to a band splitting, indicating that more than one dominant species exists. In addition, in the Q-region, some spectral shifts occur (Figure 3d). For the neutral TMPyP samples, a slight red-shift of the Q-bands with polyelectrolyte addition can be seen. This is also the case for the TMPyP diacid. For Zn-TMPyP (Figure 3e) less spectral changes are expected, because the metal center prevents the increase of charge and also symmetry changes are not expected. Thus, only for pure Zn-TMPyP Soret band can a slight blue shift by changing the milieu from neutral to acidic be observed, thereby indicating the formation of H-aggregates and a face-to-face interaction. However, the corresponding Q-bands show shifts (Figure 3f).

For the pure Zn-TMPyP in solution, the first Q-band rises at 519 nm, the second at 563 nm and, additionally, a weak shoulder at higher wavelengths is present. In the presence of the PSS brush under acidic conditions, four Q-bands can be seen, which are almost at the same wavelengths as TMPyP under neutral conditions, indicating that Zn-TMPyP becomes demetallated under such acidic conditions.

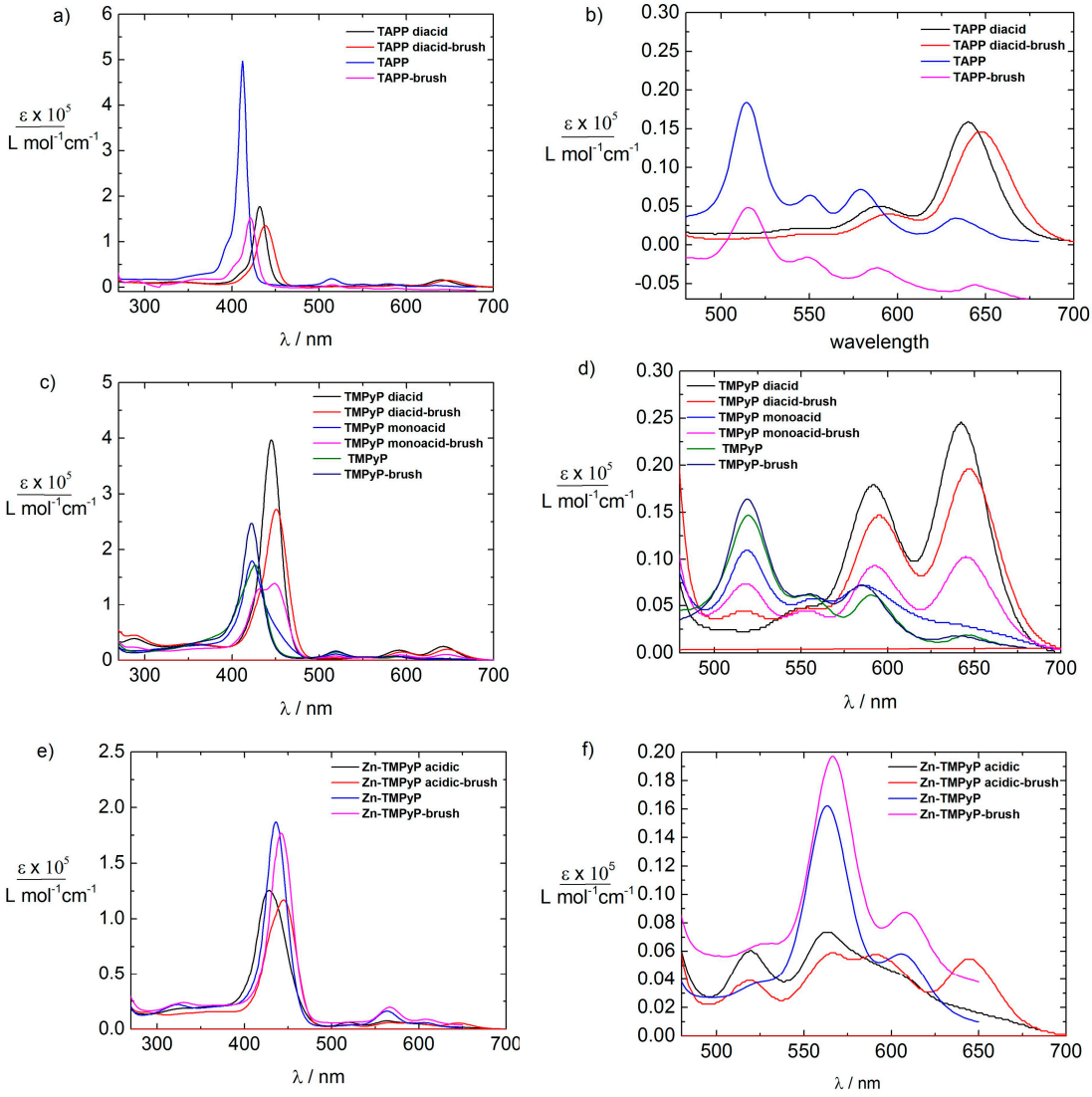

Figure 3. Spectral changes of porphyrin-PSS brush aggregates upon changing the pH from neutral to highly acidic: (**a**) TAPP-sample with PSS brush $l = 0.4$; (**b**) Zoom of the Q bands of (**a**); (**c**) TMPyP-sample with PSS brush $l = 0.1$ for the diacid and monoacid, $l = 0.4$ under neutral conditions; (**d**) Zoom of the Q bands of (**c**); and (**e**) Zn-TMPyP-sample with PSS brush $l = 0.4$; (**f**) Zoom of the Q bands of (**e**).

Table 2. Spectroscopic data for porphyrin-PSS brush assemblies in different media.

System	Soret-Band (nm)	Qy(1,0) (nm)	Qy(0,0) (nm)	Qx(1,0) (nm)	Qx(0,0) (nm)
TAPP diacid	432	589	640	–	–
TAPP diacid $l = 0.4$	438	594	647	–	–
TAPP	412	514	549	579	634
TAPP $l = 0.4$	421	516	549	588	644
TMPyP diacid	445	591	642	–	–
TMPyp diacid $l = 0.1$	450	595	647	–	–
TMPyp monoacid	423	518	558	586	
TMPyP monoacid $l = 0.4$	430/447	518	554	592	644
TMPyp	422	519	555	584	640
TMPyP $l = 0.4$	424	520	555	591	646
Zn-TMPyP acidic	428	519	563	–	–
Zn-TMPyP acidic $l = 0.4$	445	518	566/591/645	–	–
Zn-TMPyP	436	562	606	–	–
Zn-TMPyP $l = 0.4$	442	566	608	–	–

The spectroscopic investigation therefore showed that the structure formation of porphyrin and polyelectrolyte always leads to a red-shift indicating the formation of J-aggregates. For the TMPyP monoacid, additionally a band splitting can be observed indicating the presence of more than one species, which fits very well to the rather undefined structures in AFM.

3.4. Catalysis

Recently we found that at pH = 7 porphyrin-polyelectrolyte assemblies catalyze the light-induced oxidation of iodide in aqueous solution more effectively than the unassociated porphyrin [67]. Here, we performed a study of the catalysis of different porphyrins under strongly acidic conditions. The free-base porphyrins are two-fold protonated, resulting in two additional charges, *i.e.*, hexavalent porphyrins. Due to the fact that electrostatic interactions between the positively charged porphyrins and the negatively charged polyelectrolytes are responsible for structure formation and the structure formation itself under neutral conditions has caused a higher catalytic performance, two additional charges are expected to have a substantial influence on the catalytic activity. Therefore, porphyrin diacid-polyelectrolyte assemblies are promising for catalysis especially under strong acidic conditions where a variety of systems cannot be used. For the main part of the catalysis study, three different porphyrins, TAPP, TMPyP and Zn-TMPyP, are each combined with a cylindrical PSS brush and the catalytic activity of these aggregates was compared with the one of porphyrin only in acidic solution. In addition, measurements were also done with linear PSS to identify the role of the polyelectrolyte architecture.

The chosen model reaction is the light-induced oxidation of iodide into triiodide, because I^-/I_3^- is used, for example, in solar cell applications. The generation of triiodide can be monitored through two characteristic absorption bands at 287 and 353 nm in the UV/Vis spectrum. The development of the triiodide absorption as a function of time for the different systems is plotted in Figure 4. Triiodide concentrations are summarized in Table 3. The system of TAPP diacid and PSS brush is exemplarily chosen and the influence of the loading ratio l on the catalytic activity was investigated over a large l regime $0.01 \leqslant l \leqslant 2$. As can be seen from Figure 4a, the catalytic activity of TAPP diacid-PSS brush assemblies increases successively with an increasing amount of polyelectrolyte: that is, the concentration of triiodide increases from $l = 2$ successive up to $l = 0.03$ where the highest catalytic activity can be observed. Further increase of polyelectrolyte leads to a smaller catalytic activity, which shows that $l = 0.03$ is the optimum loading ratio which is necessary for an improvement of the catalytic activity. At $l = 0.01$, the amount of TAPP is too small to allow for building sufficient aggregates. Between $0.3 \leqslant l \leqslant 0.6$, no differences can be seen. Similar observations can be made for the TMPyP monoacid-PSS brush system, where the considered regime was $0.1 \leqslant l \leqslant 0.5$. As can be seen in Figure 4b, a distinct difference in the catalytic activity with and without polyelectrolyte can be observed. The highest catalytic activity was found for $l = 0.1$. For the Zn-TMPyP-PSS brush system, the results of which are illustrated in Figure 4c, samples with $0.1 \leqslant l \leqslant 0.8$ were investigated. Similar to the results for the TMPyP monoacid-PSS brush system, a distinct increase in catalytic activity through the polyelectrolyte can be seen.

Table 3. Generated concentrations of triiodide (mol/L).

Porphyrin species	With PE	Without PE	Activity increase with PE
TMPyP diacid	4.2×10^4	4.2×10^4	unchanged
TAPP diacid	1.5×10^4	5.9×10^5	2.5×
Zn-TMPyP	8.7×10^5	6.1×10^5	1.3×
TMPyP monoacid	7.8×10^5	2.3×10^5	3.4×

Hence, the activity increases with increasing amount of polyelectrolyte so that for $l = 0.1$ the highest amount of triiodide was found. For the TMPyP diacid-PSS brush system, the observations are different as can be seen in Figure 4d. The pure TMPyP diacid solution is the catalytically most

active one of the investigated porphyrin only solutions. With polyelectrolyte, the catalytic activity is the same as without polyelectrolyte. Among the considered loading ratios, l = 0.1 shows the highest catalytic activity, but the activity does not continuously increase with increasing amount of polyelectrolyte. Among the considered systems, TMPyP diacid-PSS brush assemblies with c (I_3^-) = 4.2 × 10^{-4} mol· L^{-1} generate the highest concentration of triiodide followed by TAPP diacid with c (I_3^-) = 1.5 × 10^4 mol· L^{-1}, Zn-TMPyP with c (I_3^-) = 8.7 × 10^{-5} mol· L^{-1} and TMPyP monoacid with c (I_3^-) = 7.8 × 10^{-5} mol· L^{-1}, as can be seen in Table 3.

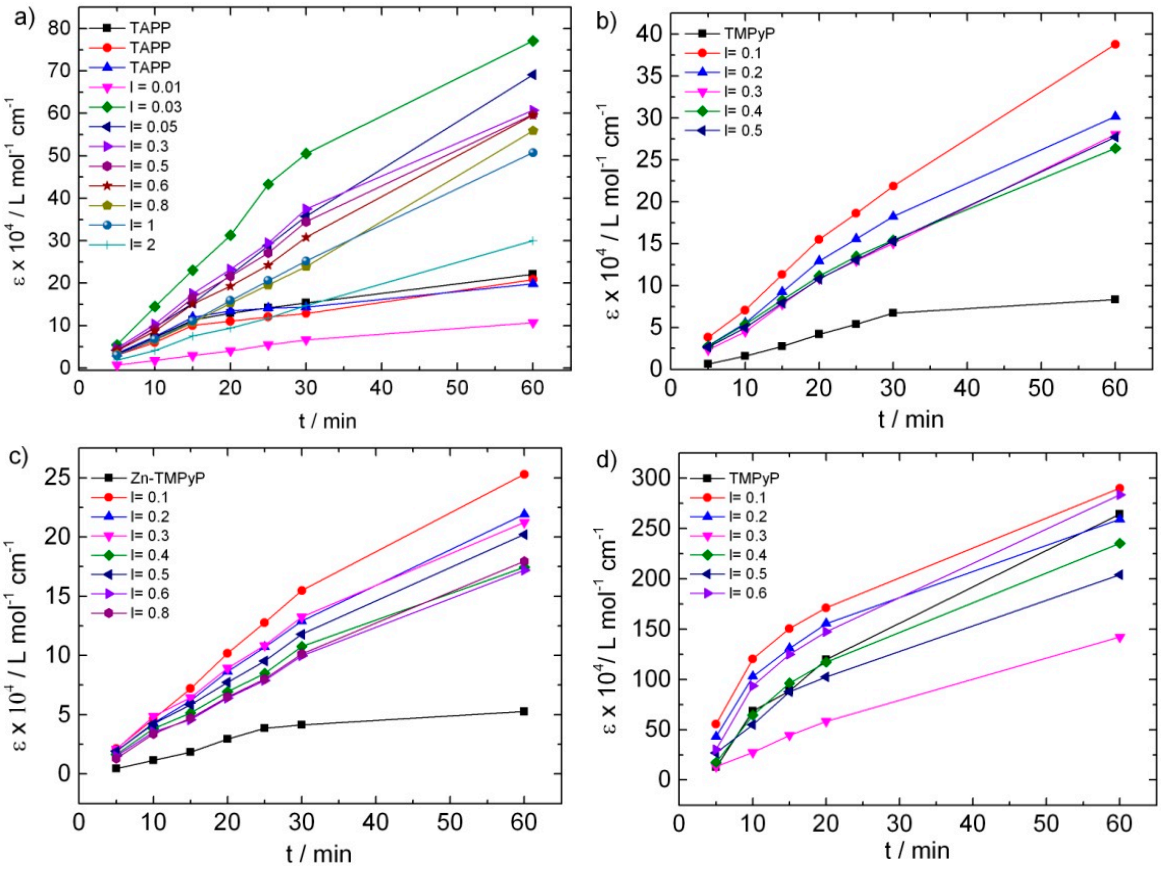

Figure 4. Kinetics of tri-iodide formation: extinction coefficient ε at λ = 353 nm *versus* irradiation time for samples in acidic iodide solution: (**a**) TAPP diacid-PSS brush; (**b**) TMPyP monoacid-PSS brush; (**c**) Zn-TMPyP-PSS brush; (**d**) TMPyP diacid-PSS brush.

These observations are also evident from the corresponding turnover numbers (TON) and the turnover frequency (TOF), which are summarized in Table 4. TON describes the amount of triiodide which can be generated with the chosen porphyrin concentration. TOF is the turnover per time. The catalytic activity of TMPyP diacid-PSS brush assemblies is evident with a TON of 109 and a TOF of 1.82, which are higher than those of pure TMPyP diacid and essentially larger than those of the other systems. Thus, the catalytic activity of TAPP diacid, TMPyP monoacid and Zn-TMPyP can be obviously enhanced with regard to triiodide generation in the presence of polyelectrolyte.

From the results it can be seen that one additional charge in the case of TMPyP enhances the catalytic activity tremendously. The effect of the porphyrin diacids is much more significant than with the porphyrin under neutral pH conditions [31]. Under acidic conditions, the triiodide generation is up to 13.6 times larger than in the pH 7 case in the TAPP diacid-PSS brush and up to 4.1 times larger in the case of TMPyP monoacid-PSS brush, and finally up to 22.1 times larger in the case of TMPyP diacid-PSS brush.

Table 4. Corresponding TON/TOF of investigated porphyrin-polyelectrolyte assemblies.

Porphyrin species	TON		TOF/min^{-1}	
	With PE	Without PE	With PE	Without PE
TMPyP diacid	109	104	1.82	1.73
TAPP diacid	20	6	0.66	0.1
TAPPneutral	2	–	0.03	–
Zn-TMPyP	8	47	0.14	0.8
TMPyP monoacid	10	3	0.14	0.04
TMPyP neutral	4	2	0.06	0.04

To identify if a certain polyelectrolyte architecture is necessary to increase the catalytic activity, measurements with linear PSS as polyelectrolyte at one chosen loading ratio l = 0.4 were performed. As shown in Figure 5, also with the linear polyelectrolyte, the catalytic activity becomes enhanced whereas in the case of TMPyP diacid, the catalytic activity without linear PSS is slightly higher than that with linear PSS. The concentrations of generated triioide are slightly higher for the TMPyP diacid with linear PSS as with the PSS brush, while the other porphyrins lie in the same range as with PSS brush, as given in Table 5. This is in contrast to neutral conditions. From Figure 5 and Table 5, it is evident that most triiodide is generated with the TMPyP diacid system, which is consistent with the results of the PSS brush. For selected samples, the influence of long-time irradiation on the catalytic performance of porphyrin diacid-PSS brush aggregates was investigated. Samples were irradiated up to five hours. A more extended irradiation interval was not possible for the TMPyP diacid samples due to absorption limits reached at the chosen concentration. Again, the extinction coefficients are plotted versus the irradiation time in Figure 6. It becomes evident that the further increase of the catalytic activity due to the four-hour longer irradiation is not that significant for the majority of the porphyrin-polyelectrolyte samples. Only for the TMPyP diacid system can a clear enhancement of the catalytic activity be observed. Consistent with the results for one-hour irradiation, the highest concentration of generated triiodide is found for TMPyP diacid-PSS brush aggregates, as summarized in Table 5. Yet, still no increase of the iodide concentration due to the polyelectrolyte can be seen. The activity of both samples is nearly the same as after one-hour irradiation. For the remaining three porphyrin-PSS brush systems, a clear increase of the catalytic activity caused by the polyelectrolyte is evident. Again, the observations can be underlined with the corresponding TON and TOF, which are summarized in Table 6. The maximum increase with a 7.5-times higher concentration of generated triiodide was found for TAPP diacid-PSS brush.

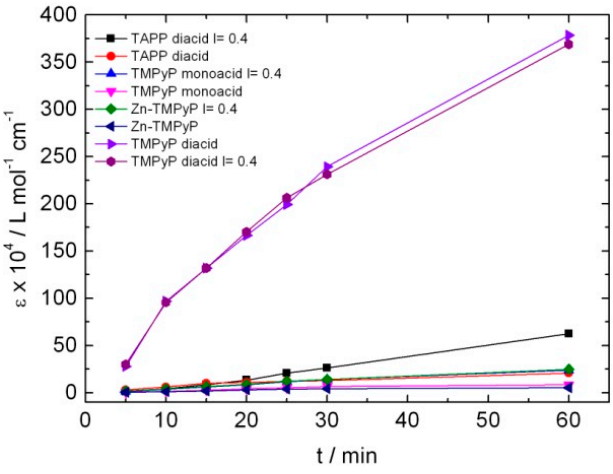

Figure 5. Kinetics of triiodide formation: extinction coefficient ε at λ = 353 nm *versus* irradiation time for porphyrin-linear PSS in acidic aqueous iodide solution.

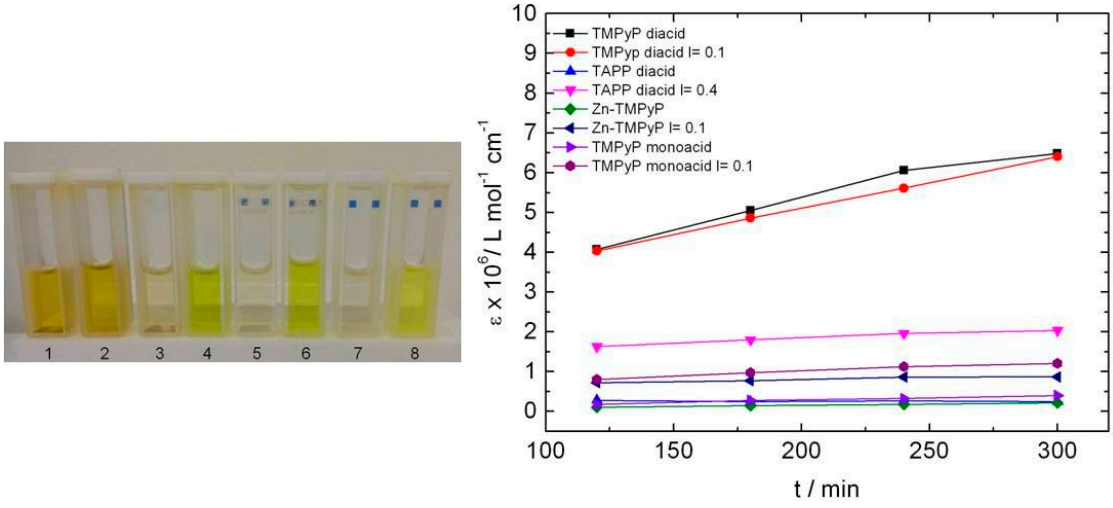

Figure 6. (**Left**) Image of samples after 2 h of irradiation with visible light. The increased catalytic activity can be seen by eye. Samples with polyelectrolyte (2, 4, 6, 8) are intensively yellow-colored. 1, 2: TMPyP diacid; 3, 4: TAPP diacid; 5, 6: Zn-TMPyP; 7, 8: TMPyP monoacid; (**Right**) kinetics of triiodide formation: extinction coefficient ε at λ = 353 nm *versus* irradiation time (5 h) for different porphyrin-PSS brush assemblies in acidic aqueous iodide solution.

Table 5. Generated concentrations of triiodide (mol/L) after 5 h of irradiation.

Porphyrin species	With PE	Without PE	Increased activity with PE
TMPyP diacid	9.42×10^4	1.00×10^3	slightly less catalytically active
TAPP diacid	5.26×10^4	7.01×10^5	7.5×
Zn-TMPyP	2.59×10^4	7.73×10^5	3.6×
TMPyP monoacid	2.01×10^4	7.35×10^5	2.7×

Table 6. TON/TOF for the long-term studies of porphyrin-polyelectrolyte assemblies.

Porphyrin species	TON		TOF/min^{-1}	
	With PE	Without PE	With PE	Without PE
TMPyP diacid	243	246	0.81	0.82
TAPP diacid	78	10	0.25	0.03
Zn-TMPyP	33	9	0.11	0.03
TMPyP monoacid	46	16	0.15	0.05

The increase of the catalytic activity can additionally be seen from the color of the investigated samples in Figure 6. Samples with porphyrin and polyelectrolyte evidently are more intensively yellow-colored.

The reusability of the porphyrin diacid-PSS brush-assemblies was also investigated. For this, a sample of TAPP diaicd-PSS brush and a TAPP diacid solution, which were already irradiated and used as catalyst, were irradiated on the next day again. The measurements showed that TAPP diacid-PSS brush assemblies are still catalytically active.

4. Discussion

Possible origins for the difference in catalytic activity are different lifetimes of the excited triplet states, the symmetry of the porphyrins as well as the electronic structure of the porphyrins. As shown in Scheme 3, the generation of triiodide from iodide occurs via irradiation of the porphyrin as a photosensitizer and its excited triplet state. Thereby, $^1O_2$ is generated which oxidizes iodide into

triiodide. Table 7 summarizes the excited triplet state lifetimes for the porphyrins used. From this, it may be assumed that Zn-TMPyP should exhibit the highest catalytic activity under neutral conditions due to the largest lifetime and that TAPP should be more catalytically active than TMPyP, both under neutral and acidic conditions.

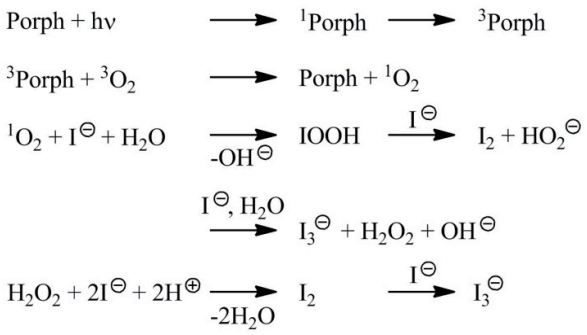

Scheme 3. Reaction scheme of the investigated model reaction.

Table 7. Lifetimes of the excited triplet states of the different porphyrins under different conditions.

Porphyrin	pH	$\Phi_{Triplet}$	t_T
TMPyP	7	0.92 [64]	0.17 ms [84]
TAPP	7	0.8 [65]	0.54 ms [85]
Zn-TMPyP	7	0.9 [64]	2 ms [84]
TMPyP diacid	acidic	–	90 µs [76]
TAPP diacid	acidic	–	268 µs [76]
Zn-TMPyP	acidic	–	–

Results above show the opposite. Therefore, effects other than the lifetimes of the excited triplet states evidently are more significant for the difference in catalytic activity. Generally, molecular symmetry can also play a role for the different catalytic behavior, but TMPyP and TAPP exhibit the same symmetry under neutral and acidic conditions, so that the molecular symmetry also turns out not to be the reason for the difference in catalytic activity.

A likely cause contributing to the enhancement of the catalytic activity is the prevention of uncontrolled aggregation, as previously observed under neutral conditions. Therefore, for porphyrin diacid-PSS brush systems, the change of the Soret band during irradiation was considered in detail (Figure 7). The behavior is quite complex. With polyelectrolyte, the intensity of the Soret band increases with increasing irradiation time until its disappearance after 60 min of irradiation. Without polyelectrolyte, one can first see a decrease of the Soret band and afterwards an increase and disappearance of the Soret band already after 20 min of irradiation. This observation indicates that TMPyP diacid-PSS brush assemblies are destroyed with increasing irradiation time, and more free TMPyP diacid becomes present in the solution. Different observations can be made in the case of TAPP diacid. With polyelectrolyte, only a slight decrease of the Soret band can be observed, whereas without polyelectrolyte, the Soret band decreases, indicating undefined aggregation, which is prevented by the PSS brush in the assembly system. The same result can be seen for TMPyP monoacid and Zn-TMPyP. This observation of the Soret band behavior fits well with the long-term photocatalytic activity results. There, the amount of generated triiodide for the TMPyP diacid sample and for the TMPyP diacid-PSS brush sample in relation to the short-term experiment did not increase tremendously. With the results from Figure 7 it becomes evident that this is because TMPyP diacid-PSS brush assemblies are not stable enough under the investigated conditions, so that after one-hour irradiation, aggregates no longer exist and therefore the catalytic activity of the samples with and without polyelectrolyte is the same. In the case of TAPP diacid, the aggregates are more stable and are still present after one-hour irradiation and therefore a distinctly larger increase of the triiodide concentration can be observed in the long-term

studies. In summary, the prevention of aggregation through the polyelectrolyte is likely the reason for the enhanced catalytic activity of TAPP diacid, while for TMPyP diacid, this appears not to be the case.

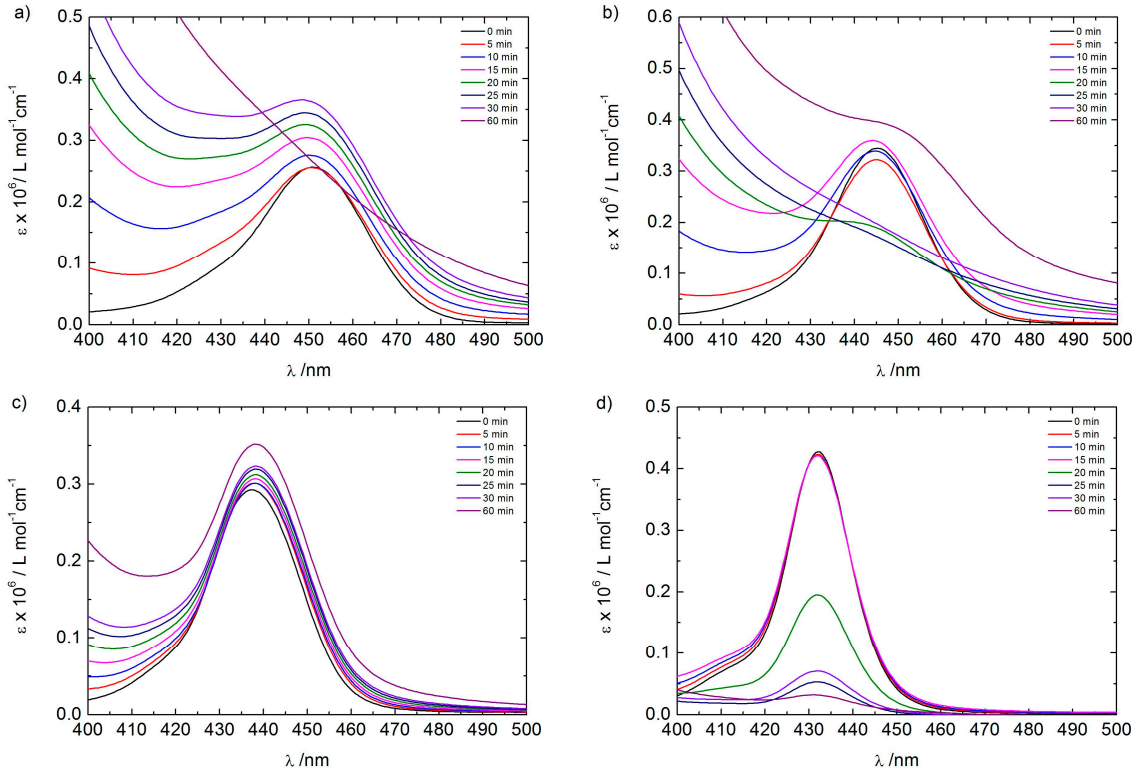

Figure 7. Change of the porphyrin Soret band during irradiation; (**a**) TMPyP diacid + PSS brush, l = 0.1; (**b**) TMPyP diacid; (**c**) TAPP diacid + PSS brush, l = 0.4; (**d**) TAPP diacid.

Differences between the TMPyP and TAPP system can derive from their electronic structures. Wang investigated the interactions of porphyrin-borate complexes and he also applied density functional theory [86]. For TMPyP, he observed a redshift of the Soret band when complexed with borate resulting from the reduced energy levels of the TMPyP in complexes. The methylpyridinium groups with their four positive charges exhibit an electron-withdrawing character and have both an inductive and a mesomeric effect. The inductive effect appears to have no influence on the energy of the π-orbitals. It proceeds via the σ-bonds of the substituents towards the porphyrin σ-system. On the contrary, the mesomeric effect reflects proceeds via the porphyrin π-system. For resonance interaction, the substituents need to rotate towards a coplanar configuration. Therefore, the dihedral angles between the methylpyridinium groups and the pyrrole rings for the TMPyP monomer were considered: all are 67.30° and become smaller when TMPyP is complexed. This means that TMPyP exhibits a higher planarity and becomes flattened in porphyrin-borate complexes [86]. TAPP, conversely, has localized charges on the substituents, which cannot be delocalized onto the porphyrin π-system so effectively. Cho investigated the electronic perturbation of *meso*-substituted free-base porphyrins [87]. P-aminophenyl acts as an electron-donating group and additionally participates in the extension of the π-conjugation of the HOMO of the porphyrin unit. *P*-aminophenyl-sibstituted porphyrins should have characteristic properties resulting from the unique MO interactions of the porphyrin and the *p*-aminophenyl substituents. It was concluded that the *p*-aminophenyl substituent can efficiently perturb the π-electronic system of the porphyrin unit. Due to the fact that the dihedral angle is important for efficient interunit interactions, Cho also investigated the dihedral angle, revealing an angle between the porphyrin and *p*-aminophenyl, pentafluorophenyl or phenyl substituents that is approximately 70°. The *p*-aminophenyl substituent should be the energetically and geometrically most

effective unit for interunit interactions with the porphyrin. The LUMOs of free-base porphyrins are localized on the porphyrin unit; however, electron delocalization through *p*-aminophenyl substituents has its origin in an intramolecular charge transfer character in the excited states. P-aminophenyl substituents with non-orthogonal geometry lead to efficient electron delocalization. This is supported by a large electron density on the *p*-aminophenyl substituent in the HOMO [87]. Thus, these are significant differences in the electronic structure of TMPyP and TAPP that can contribute to a different behavior in photocatalysis. With this understanding, the concept presented may be extended towards versatile and tunable photocatalytic structures that can be designed by electrostatic self-assembly, in particular with regard to solar energy conversion.

5. Conclusions

We have shown that electrostatic self-assembly of highly charged porphrins with polyelectrolytes in aqueous solution can yield a variety of nanostructures with significantly improved properties for photocatalysis. The study revealed an enhancement of the photocatalytic activity of different porphyrin diacids through assembly with the poly(styrene sulfonate) (PSS) brush. The diacids of *meso*-tetrakis(4-(trimethylammonium) phenyl)-porphyrin (TAPP) and *meso*-tetrakis(4-*N*-methylpyridinium) porphyrin (TMPyP) have been investigated as well as TMPyP monoacid and Zn-TMPyP. The results showed in the case of TMPyP that the more charges the porphyrin exhibits, the higher the generated amount of triiodide. TMPyP diacid-PSS brush assemblies generate up to 22 times more triiodide than TMPyP-PSS brush assemblies under neutral conditions and otherwise same conditions. The amount of polyelectrolyte also influences the catalytic activity of porphyrin-PSS brush assemblies: A maximum of catalytic activity enhancement was found for $l = 0.03$. Atomic force microscopy (AFM) revealed that porphyrin diacids assemble with PSS brush into larger networks with different density of meshes, which can be due to symmetry changes and a difference in ionic strength, while small angle neutron scattering (SANS) confirmed the cylindrical shape of the network moieties. The difference in catalytic activity was related to difference in electronic structure of the porphyrin and porphyrin-porphyrin interaction, while lifetimes and molecular geometry turned out to not be directly connected with the catalytic activity. Hence, electrostatic self-assembly of polyelectrolytes with multivalent functional counterions leads to functional nanostructures with tunable structure and activity. The advantage of the concept presented is a simple toolbox principle based on ionic interactions, which opens the route to a wide variety of tunable self-assembled catalysts formed with polyelectrolytes.

Acknowledgments: Financial support of Deutsche Forschungsgemeinschaft (DFG), the Interdisciplinary Center for Molecular Materials (ICMM, University Erlangen-Nürnberg) and Solar Technologies go Hybrid (Soltech) is gratefully acknowledged. The study is based upon experiments performed at D11 at ILL, Grenoble, France, and at the KWS 2 instrument operated by Jülich Centre for Neutron Science at the Heinz Maier-Leibnitz Zentrum (MLZ), Garching, Germany. The authors also gratefully acknowledge the financial support provided by Institut Laue Langevin and by JCS to perform the neutron scattering measurements at ILL and at MLZ, and thank Zhenyu Di (JCNS, Munich, Germany) for help with SANS experiments in Munich.

Author Contributions: Sabine Frühbeißer performed AFM, UV/Vis and all catalytic measurements. Giacomo Mariani contributed the SANS measurements and their data analysis. This study is part of the PhD thesis of Sabine Frühbeißer performed under supervision of Franziska Gröhn.

Conflicts of Interest: The authors declare no conflict of interest.

References

1. Zhang, J.; Xiao, F.; Xiao, G.; Liu, B. Assembly of a CdS quantum dot-TiO_2 nanobelt heterostructure for photocatalytic application: Towards an efficient visible light photocatalyst via facile surface charge tuning. *New J. Chem.* **2015**, *39*, 279–286. [CrossRef]
2. Lin, Z.-Q.; Sun, P.-J.; Tay, Y.-Y.; Liang, J.; Liu, Y.; Shi, N.-E.; Xie, L.-H.; Yi, M.-D.; Qian, Y.; Fan, Q.-L.; *et al.* Kinetically controlled assembly of a spirocyclic aromatic hydrocarbon into polyhedral micro/nanocrystals. *ACS Nano* **2012**, *6*, 5309–5319. [CrossRef] [PubMed]

3. Yang, B.; Xiao, J.; Wong, J.I.; Guo, J.; Wu, Y.; Ong, L.; Lao, L.L.; Boey, F.; Zhang, H.; Yang, H.Y.; *et al.* Shape-controlled micro/nanostructures of 9,10-diphenylanthracene (DPA) and their application in light-emitting devices. *J. Phys. Chem. C* **2011**, *115*, 7924–7927. [CrossRef]
4. Takacs, C.T.; Sun, Y.; Welch, G.C.; Perez, L.A.; Liu, X.; Wen, W.; Bazan, G.C.; Heeger, A.J. Solar cell efficiency, self-assembly, and dipole-dipole interactions of isomorphic narrow-band-gap molecules. *J. Am. Chem. Soc.* **2012**, *134*, 16597–16606. [CrossRef] [PubMed]
5. Xiao, J.; Yin, Z.; Wu, Y.; Guo, J.; Cheng, Y.; Li, H.; Huang, Y.; Zhang, Q.; Ma, J.; Boey, F.; *et al.* Chemical reaction between Ag Nanoparticles and TCNQ microparticles in aqueous solution. *Small* **2011**, *7*, 1242–1246. [CrossRef] [PubMed]
6. Busseron, E.; Ruff, Y.; Moulin, E.; Giuseppone, N. Supramolecular self-assemblies as functional nanomaterials. *Nanoscale* **2013**, *5*, 7098–7140. [CrossRef] [PubMed]
7. Förster, S.; Plantenberg, T. Funktionale Strukturhierarchien aus selbstorganisierenden polymeren. *Angew. Chem.* **2002**, *114*, 712–739. [CrossRef]
8. Philp, D.; Stoddart, J.F. Self-assembly in natural and unnatural systems. *Angew. Chem.* **1996**, *108*, 1242–1286. [CrossRef]
9. Schneider, H.J. Bindungsmechanismen in supramolekularen Komplexen. *Angew. Chem.* **2009**, *121*, 3982–4036. [CrossRef]
10. Ikkala, O.; Brinke, B. Functional materials based on self-assembly of polymeric supramolecules. *Science* **2002**, *295*, 2407–2409. [CrossRef] [PubMed]
11. Whitesides, G.M.; Grzybowski, B. Self-assembly at all scales. *Science* **2002**, *295*, 2418–2421. [CrossRef] [PubMed]
12. Marsden, H. R.; Kros, A. Self-assembly of coiled coils in synthetic biology: Inspiration and progress. *Angew. Chem. Int. Ed.* **2010**, *49*, 2988–3005. [CrossRef] [PubMed]
13. Decher, G. Fuzzy nanoassemblies: Toward layered polymeric multicomposites. *Science* **1997**, *277*, 1232–1237.
14. Donath, E.; Sukhorukov, G.B.; Caruso, F.; Davis, S.A.; Möhwald, H. Novel hollow polymer shells by colloid-templated assembly of polyelectrolytes. *Angew. Chem. Int. Ed.* **1998**, *37*, 2202. [CrossRef]
15. Bertrand, P.; Jones, A.; Laschewsky, A.; Legras, R. Ultrathin polymer coatings by complexation of polyelectrolytes at interfaces: Suitable materials, structure and properties. *Macromol. Rapid Commun.* **2000**, *21*, 319. [CrossRef]
16. Glinel, K.; Dejugnat, C.; Prevot, M.; Schöler, B.; Schönhoff, M.; von Klitzing, R. Responsive polyelectrolyte multilayers. *Colloids Surf. A* **2007**, *303*, 3. [CrossRef]
17. Antonietti, M.; Conrad, J.; Thünemann, A. Polyelectrolyte-surfactant complexes: A New type of solid, mesomorphous material. *Macromolecules* **1994**, *27*, 6007. [CrossRef]
18. Rädler, J.O.; Koltover, I.; Salditt, T.; Safinya, C.R. Structure of DNA-cationic liposome complexes: DNA intercalation in multilamellar membranes in distinct interhelical packing regimes. *Science* **1997**, *275*, 810. [CrossRef] [PubMed]
19. Faul, C.F. J.; Antonietti, M. Ionic self-assembly: Facile synthesis of supramolecular materials. *Adv. Mater.* **2003**, *15*, 673. [CrossRef]
20. Zakrevskyy, Y.; Stumpe, J.; Smarsly, B.; Faul, C.F. Photoinduction of optical anisotropy in an azobenzene-contining ionic self-assembly liquid-crystalline material. *J. Phys. Rev. E* **2007**, *75*, 031703. [CrossRef] [PubMed]
21. Thünemann, F.; Müller, M.; Dautzenberg, H.; Joanny, H.F.O.; Löwen, H. Polyelectrolyte complexes. *Adv. Polym. Sci.* **2004**, *166*, 113.
22. Cooper, C.L.; Dubin, P.L.; Kayitmazer, A.B.; Turksen, S. Polyelectrolyte-protein complexes. *Curr. Opin. Colloid Interface. Sci.* **2005**, *10*, 52. [CrossRef]
23. Müller, M.; Kessler, B.; Richter, S. Preparation of monomodal polyelectrolyte complex nanoparticles of PDADMAC/poly(maleic acid-*alt*-α-methylstyrene) by consecutive centrifugation. *Langmuir* **2005**, *21*, 7044. [CrossRef] [PubMed]
24. Böhme, U.; Scheler, U. Hydrodynamic size and charge of polyelectrolyte complexes. *J. Phys. Chem. B* **2007**, *111*, 8348. [CrossRef] [PubMed]
25. Gröhn, F.; Klein, K.; Brand, S. Facile route to supramolecular structures: Self-assembly of dendrimers and naphthalene dicarboxylic acids. *Chem. Eur. J.* **2008**, *14*, 6866–6889. [CrossRef] [PubMed]

26. Ruthardt, C.; Maskos, M.; Kolb, U.; Gröhn, F. Finite-size networks from cylindrical polyelectrolyte brushes and porphyrins. *Macromolecules* **2009**, *42*, 830–840. [CrossRef]
27. Willerich, I.; Gröhn, F. Photoswitchable nanoassemblies by electrostatic self-assembly. *Angew. Chem. Int. Ed.* **2010**, *44*, 8104. [CrossRef] [PubMed]
28. Gröhn, F.; Klein, K.; Koynov, K. A novel type of vesicles based on ionic and π-π interactions. *Macromol. Rapid Commun.* **2010**, *31*, 75. [CrossRef] [PubMed]
29. Willerich, I.; Gröhn, F. Molecular structure encodes nanoscale assemblies: Understanding driving forces in electrostatic self-assembly. *J. Am. Chem. Soc.* **2011**, *133*, 20341–20356. [CrossRef] [PubMed]
30. Ruthardt, C.; Maskos, M.; Kolb, U.; Gröhn, F. Polystyrene sulfonate-porphyrin assemblies: Influence of polyelectrolyte and porphyrin structure. *J. Phys. Chem. B* **2011**, *115*, 5716–5729. [CrossRef] [PubMed]
31. Frühbeißer, S.; Gröhn, F. Catalytic activity of macroion-porphyrin nanoassemblies. *J. Am. Chem. Soc.* **2012**, *134*, 14267–14270. [CrossRef] [PubMed]
32. Düring, J.; Hölzer, A.; Kolb, U.; Branscheid, R.; Gröhn, F. Supramolecular organic-inorganic hybrid assemblies with tunable particle size: Interplay of three noncovalent interactions. *Angew. Chem. Int. Ed.* **2013**, *52*, 8742–8745. [CrossRef] [PubMed]
33. Moldenhauer, D.; Gröhn, F. Nanoassemblies with light-responsive size and density from linear flexible polyelectrolytes. *J. Polym. Sci. B* **2013**, *51*, 802–816. [CrossRef]
34. Hasobe, T.; Fukuzumi, S. Nanostructured assembly of porphyrin clusters for light energy conversion. *J. Mater. Chem.* **2003**, *13*, 2515–2520. [CrossRef]
35. Merchat, M.; Bertolini, G.; Giacomini, P. Meso-substituted cationic porphyrins as efficient photosensitizers of Gram-positive and Gram-negative bacteria. *J. Photochem. Photobiol. B* **1996**, *32*, 153–157. [CrossRef]
36. Milanesio, M.E.; Alvarez, M.G.; Bertolotti, S.G. Photophysical characterization and photodynamic activity of metallo 5-(4- (trimethylammonium)phenyl)-10,15,20-tris(2,4,6-trimethoxyphenyl)porphyrin in homogeneous and biomimetic media. *Photochem. Photobiol. Sci.* **2008**, *7*, 963–972. [CrossRef] [PubMed]
37. Quiroga, E.D.; Alvarez, M.G.; Durantini, E.N. Susceptibility of Candida albicans to photodynamic action of 5,10,15,20-tetra(4-*N*-methylpyridyl)porphyrin in different media. *FEMS Immunol. Med. Microbiol.* **2010**, *60*, 123–131. [CrossRef] [PubMed]
38. Ethirajan, M.; Chen, Y.; Joshi, P. The role of porphyrin chemistry in tumor imaging and photodynamic therapy. *Chem. Soc. Rev.* **2011**, *40*, 340–362. [CrossRef] [PubMed]
39. Afonso, S.G.; Salamanca, R.; Batlle, A.M. The photodynamic and non-photodynamic actions of porphyrins. *Braz. J. Med. Biol. Res.* **1999**, *32*, 255–266. [CrossRef] [PubMed]
40. Dougherty, T.J.; Gomer, C.J.; Henderson, B.W. Photodynamic therapy. *J. Nat.Cancer Inst.* **1998**, *90*, 889–905. [CrossRef] [PubMed]
41. Kalyanasundaram, K.; Neumann-Spalart, M. Photophysical and redox properties of water-soluble porphyrins in aqueous media. *J. Phys. Chem.* **1982**, *86*, 5163–5169. [CrossRef]
42. Kubat, P.; Mosinger, J. Photophysical properties of metal complexes of meso-tetrakis (4-sulphonatophenyl) porphyrin. *J. Photochem. Photobiol. A* **1996**, *96*, 93–97. [CrossRef]
43. Kee, H.L.; Bhaumik, J.; Diers, J.R.; Mroz, P.; Hamblin, M.R. Photophysical characterization of imidazolium-substituted Pd(II), In(III), and Zn(II) porphyrins as photosensitizers for PDT. *J. Photochem. Photobiol. A* **2008**, *200*, 346–355. [CrossRef] [PubMed]
44. Owens, J.W.; Smith, R.; Robinson, R.; Robins, M. Photophysical properties of porphyrins, phthalocyanines, and benzochlorins. *Inorg. Chim. Acta* **1998**, *279*, 226–231. [CrossRef]
45. Prochazkova, K.; Zelinger, Z.; Lang, K.; Kubat, P. meso-Tetratolylporphyrins substituted by pyridinium groups: Aggregation, photophysical properties and complexation with DNA. *J. Phys. Org. Chem.* **2004**, *17*, 890–897. [CrossRef]
46. Ricchelli, F. Photophysical properties of porphyrins in biological membranes. *J. Photochem. Photobiol. B* **1995**, *29*, 109–118. [CrossRef]
47. Sun, W.-J.; Li, J.; Mele, G.; Zhang, Z.-Q.; Zhang, F.-X. Enhanced photocatalytic degradation of rhodamine B by surface modification of ZnO with copper (II) porphyrin under both UV–Vis and visible light irradiation. *J. Mol. Catal. A* **2013**, *233*, 84–91. [CrossRef]
48. Ishihara, S.; Labuta, J.; Van Rossom, W.; Ishikawa, D.; Minami, K.; Hill, J.P.; Ariga, K. Porphyrin-based sensor nanoarchitectonics in diverse physical detection modes. *Phys. Chem. Chem. Phys.* **2014**, *16*, 9713. [CrossRef] [PubMed]

49. Nakazono, T.; Parent, A.R.; Sakai, K. Cobalt porphyrins as homogeneous catalysts for water oxidation. *Chem. Commun.* **2013**, *49*, 6325–6327. [CrossRef] [PubMed]
50. Windle, C.D.; Campian, M.V.; Duhme-Klair, A.-K.; Gibson, E.A.; Perutz, R.N.; Schneider, J. CO_2 photoreduction with long-wavelength light: Dyads and monomers of zinc porphyrin and rhenium bipyridine. *Chem. Commun.* **2012**, *48*, 8189–8191. [CrossRef] [PubMed]
51. Urbani, M.; Grätzel, M.; Nazeeruddin, M.K.; Torres, T. Meso-substituted porphyrins for dye-sensitized solar cells. *Chem. Rev.* **2014**, *114*, 12330–12396. [CrossRef] [PubMed]
52. Xu, L.; Liu, L.; Liu, F.; Li, W.; Chen, R.; Gao, Y.; Zhang, W. Photodynamic therapy of oligoethylene glycol dendronized reduction-sensitive porphyrins. *J. Mater. Chem. B* **2015**, *3*, 3062–3071. [CrossRef]
53. Labuta, J.; Hill, J.P.; Ishihara, S.; Hanykova, L.; Ariga, K. Chiral sensing by nonchiral tetrapyrroles. *Acc. Chem. Res.* **2015**, *48*, 521–529. [CrossRef] [PubMed]
54. Xu, Y.; Zhao, L.; Bai, H.; Hong, W.; Li, C.; Shi, G. Chemically converted graphene induced molecular flattening of 5,10,15,20-tetrakis(1-methyl-4-pyridino)porphyrin and its application for optical detection of cadmium(II) ions. *J. Am. Chem. Soc.* **2009**, *131*, 13490–13497. [CrossRef] [PubMed]
55. Kano, K.; Minamizono, H.; Kitae, T.; Negi, S. Self-aggregation of cationic porphyrins in water. Can π–π stacking interaction overcome electrostatic repulsive force? *J. Phys. Chem. A* **1997**, *101*, 6118–6124. [CrossRef]
56. Iosif, A. Aggregation of tetrakis(4-methylpyridy1)porphyrin and tetrakis(4-sulphonatopheny1)porphyrin in water. *J. Prakt. Chem.* **1997**, *339*, 420–425. [CrossRef]
57. Pasternack, R.F. Aggregation properties of water-soluble porphyrins. *Ann. N. Y. Acad. Sci.* **1973**, *206*, 614–630. [CrossRef] [PubMed]
58. Lauceri, R.; de Napoli, M.; Mammana, A.; Nardis, S. Hierarchical self-assembly of water-soluble porphyrins. *Synth. Met.* **2004**, *147*, 49–55. [CrossRef]
59. Kano, K.; Takei, M.; Hashimoto, S. Cationic porphyrins in water. ^{1}H NMR and fluorescence studies on dimer and molecular complex formation. *J. Phys. Chem.* **1990**, *94*, 2181–2187. [CrossRef]
60. Pasternack, R.F.; Huber, P.R.; Boyd, P. On the aggregation of meso-substituted water-soluble porphyrins. *J. Am. Chem. Soc.* **1972**, *94*, 4511–4517. [CrossRef] [PubMed]
61. De Luca, G.; Romeo, A.; Villari, V.; Micali, N.; Foltran, I.; Foresti, E.; Lesci, I.G.; Roveri, N.; Zuccheri, T.; Monsu' Scolaro, L. Self-organizing functional materials via ionic self assembly: Porphyrins hand J-aggregates on synthetic chrysotile nanotubes. *J. Am. Chem. Soc.* **2009**, *131*, 6920–6921. [CrossRef] [PubMed]
62. Elemans, J.A.A.W.; van Hameren, R.; Nolte, R.J. M.; Rowan, A.E. Molecular materials by self-assembly of porphyrins, phthalocyanines, and perylenes. *Adv. Mater.* **2006**, *18*, 1251–1266. [CrossRef]
63. Tu, S.; Kim, S.H.; Joseph, J.; Modarelli, D.A.; Parquette, J.R. Self-assembly of a donor-acceptor nanotube. A strategy to create bicontinuous arrays. *J. Am. Chem. Soc.* **2011**, *133*, 19125–19130. [CrossRef] [PubMed]
64. Vilaplana, R.A.; Gonzalez-Vilcheza, F.; Pasternack, R.F. Formation of supramolecules in solution. interaction between transition-metal complexes and water-soluble porphyrins. *J. Chem. Soc. Dalton Trans.* **1991**, 1831–1834. [CrossRef]
65. Taggart, J.C.; Welch, E.Z.; Mulqueen, M.F.; Dioguardi, V.B.; Cauer, A.G.; Kokona, B.; Fairman, R. Testing the role of charge and structure on the stability of peptide−porphyrin complexes. *Biomacromolecules* **2014**, *15*, 4544–4550. [CrossRef] [PubMed]
66. Shema-Mizrachi, M.; Pavan, G.M.; Levin, E.; Danani, A.; Lemcoff, N.G. Catalytic chameleon dendrimers. *J. Am. Chem. Soc.* **2011**, *133*, 14359–14367. [CrossRef] [PubMed]
67. Asha Jhonsi, M.; Renganathan, R. Investigations on the photoinduced interaction of water-soluble thioglycolic acid (TGA) capped CdTe quantum dots with certain porphyrins. *J. Colloid Interface Sci.* **2010**, *344*, 596–602. [CrossRef] [PubMed]
68. Amaoa, Y.; Tomonoua, Y.; Okura, I. Highly efficient photochemical hydrogen production system using zinc porphyrin and hydrogenase in CTAB micellar system. *Sol. Energy Mater. Sol. Cells* **2003**, *79*, 103–111. [CrossRef]
69. Kellett, R.M.; Spiro, T.G. Cobalt (I) porphyrin catalysis of hydrogen production from water. *Inorg. Chem.* **1985**, *24*, 2373–2377. [CrossRef]
70. Kalyanasundaram, K.; Grätzel, M. Light induced redox reactions of water soluble porphyrins, sensitization of hydrogen generation from water by zincporphyrin derivatives. *Helv. Chim. Acta* **1980**, *63*, 478–485. [CrossRef]

71. Tian, Y.; Martin, K.E.; Shelnutt, J.Y.-T.; Evans, L.; Busani, T.; Miller, J.E.; Medforth, C.J.; Shelnutt, J.A. Morphological families of self-assembled porphyrin structures and their photosensitization of hydrogen generation. *Chem. Commun.* **2011**, *47*, 6069–6071. [CrossRef] [PubMed]
72. Li, X.; Wang, M.; Zhang, S.; Pan, J.; Na, Y.; Liu, J.; Akermark, B.; Sun, L. Noncovalent assembly of metalloporphyrin and an iron hydrogenase active-site model: Photo-induced electron transfer and hydrogen generation. *J. Phys. Chem. B* **2008**, *112*, 8198–8202. [CrossRef] [PubMed]
73. Udal'tsov, A.V. Initial steps of photosynthetic water splitting by associates of porphyrin. *J. Photochem. Photobiol. A* **2000**, *130*, 21–33. [CrossRef]
74. Esswein, A.J.; Nocera, D.G. Hydrogen production by molecular photocatalysis. *Chem. Rev.* **2007**, *107*, 4022–4047. [CrossRef] [PubMed]
75. Darwent, J.R.; Douglas, P.; Harriman, A.; Porter, G.; Richoux, M.-C. Metal phthalocyanines as photosensitizers for reduction of water to hydrogen. *Coord. Chem. Rev.* **1982**, *44*, 83–126. [CrossRef]
76. Harriman, A.; Richoux, M.-C. Photoproduction of hydrogen from reductive quenching of a water-soluble zinc porphyrin. *J. Photochem.* **1981**, *15*, 336–339. [CrossRef]
77. Sandanayaka, A.S.D.; Murakami, T.; Hasobe, T. Preparation and photophysical and photoelectrochemical properties of supramolecular porphyrin nanorods structurally controlled by encapsulated-fullerene derivatives. *J. Phys. Chem. C* **2009**, *113*, 18369–18378. [CrossRef]
78. Harriman, A.; Richoux, M.-C. Luminescence of poprhyrins and metalloporphyrins VIII: Luminescence and hydrogen photogeneration from porphyrin conjugate diacids. *J. Photochem.* **1984**, *27*, 205–214. [CrossRef]
79. Fleischer, E.B. The structure of porphyrins and metalloporhyrins. *Acc. Chem. Res.* **1970**, *3*, 105–112. [CrossRef]
80. Kruk, M.M.; Starukhin, A.S.; Maes, W. Influence of macrocycle protonation on the photophysical properties of porphyrins. *Macroheterocycles* **2011**, *4*, 69–79. [CrossRef]
81. Stone, A.; Fleischer, E.B. The molecular and crystal structure of porphyrin diacids. *J. Am. Chem. Soc.* **1968**, *90*, 2735–2748. [CrossRef]
82. Dziezok, P.; Sheiko, S.S.; Fischer, K.; Schmidt, M.; Möller, M. Cylindrical molecular brushes. *Angew. Chem. Int. Ed. Engl.* **1997**, *36*, 2812–2815. [CrossRef]
83. Note: This green colour leads to problems for the common structural investigation with dynamic light scattering due to absorption of the light of the whole visible spectrum. Consequently dynamic light scattering cannot be used.
84. Kalyanasundaram, K. Photochemistry of water-soluble porphyrins: Comparative study of isomeric tetrapyridyl- and tetrakis(*N*-methylpyridiniumyl)porphyrins. *Inorg. Chem.* **1984**, *23*, 2453–2459. [CrossRef]
85. Kalyanasundaram, K. Photochemistry and sensitized evolution of hydrogen from water using water-soluble cationic porphyrins. *J. Chem. Soc. Faraday Trans. 2* **1983**, *79*, 1365–1374. [CrossRef]
86. Wang, L.-F.; Meng, X.-W.; Tang, F.-Q. Density functional theory study of electronic absorption spectra and intermolecular interactions of porphyrin–borate complexes. *J. Mol. Struct.: THEOCHEM* **2010**, *956*, 26–32. [CrossRef]
87. Cho, S.; Lee, J.; Han, H.S.; Lee, H.K.; Jeon, S. Characteristic electronic perturbation by asymmetric arrangements of *p*-aminophenyl substituents in free-base porphyrins. *J. Phys. Chem. A* **2014**, *118*, 4995–5001. [CrossRef] [PubMed]

5.2 Ionic Dye-Surfactant Nanoassemblies: Interplay of Electrostatics, Hydrophobic Effect, and π-π Stacking

Colloid Polym Sci (2016) 294:591–606
DOI 10.1007/s00396-015-3814-2

ORIGINAL CONTRIBUTION

Ionic dye–surfactant nanoassemblies: interplay of electrostatics, hydrophobic effect, and π–π stacking

Anne Kutz[1] · **Giacomo Mariani**[1,2] · **Franziska Gröhn**[1]

Received: 29 May 2015 / Revised: 29 November 2015 / Accepted: 2 December 2015 / Published online: 30 December 2015

Abstract The interplay of several non-covalent interaction forces is used as key to supramolecular structures. Combining cationic alkyltrimethylammonium bromide surfactants and the divalent anionic azo dye Acid Red 26 (Ar26) as small building blocks in aqueous solution, electrostatic interactions of the oppositely charged building blocks in combination with hydrophobic effect and π–π interactions play a major role in aggregate formation. Static and dynamic light scattering and small-angle neutron scattering (SANS) revealed different sizes of aggregates in the range of 2 nm≤R_H≤420 nm depending on surfactant length, concentration and of dye to surfactant loading ratio. A strong relationship of assembly size with surfactant concentration has been found, where initial surfactant monomers and micelles influence the aggregate formation differently. The stability of dye–surfactant aggregates which also shows a dependency on surfactant tail length has been related to ζ-potential measurements. Small-angle neutron scattering elucidated that dye–surfactant aggregates possess cylindrical shapes with different aspect ratios. UV/Vis spectroscopy gave information on the dye–dye π–π stacking geometry and extent, while the thermodynamic parameters for micellization and dye–surfactant binding ΔH, ΔG, and ΔS as well as stoichiometry and binding constant obtained by isothermal titration calorimetry revealed insight into the interplay of interactions.

✉ Franziska Gröhn
franziska.groehn@fau.de

[1] Department of Chemistry and Pharmacy, Interdisciplinary Center for Molecular Materials (ICMM), Friedrich-Alexander University Erlangen-Nürnberg, Egerlandstr. 3, 91058 Erlangen, Germany

[2] Institut Laue-Langevin, DS/LSS, 71 Avenue des Martyrs, 38000 Grenoble, France

Keywords Electrostatic self-assembly · Micelle · Surfactant · Azo dye · Dye–surfactant interaction · Dye–dye interaction · Light scattering · Small-angle neutron scattering

Introduction

The aggregation behavior of surfactants has been of research interest for a long time. Starting from studying the hydrophobic effect and micelle formation probing different properties such as surface tension or conductivity, influences of ionic strength and surfactant nature on micelle shape have come into focus [1–3]. Current research opens new application fields for surfactants, ranging from surfactant micelles in surface science [4–8], over the synthesis of gold or ZnS nanoparticles [9–11], to polyelectrolyte–surfactant assembly [12–23]. Currently, a large interest in the formation of versatile self-assembled nanostructures is due to their great potential for nanotechnology, material science, and electronic devices [24–29]. Therefore, it is highly desirable to develop concepts that open facile ways to create more complex supramolecular structures in aqueous solution based on simple amphiphiles. In recent years, surfactants have more and more been used to form supramolecular structures based on multiple non-covalent interactions like hydrophobic effect and electrostatic interactions and taking advantage of the variety of chemical structures that are available [30–39]. An interesting example is polyelectrolyte–surfactant complexes with a core–shell cylindrical morphology consisting of a fluorosurfactant and an anionic polyelectrolyte described by Štěpánek et al. [37, 40]. This group has widely studied polyelectrolyte–surfactant association, showing the formation of highly ordered nanoparticles or to water-insoluble complexes depending on the composition [41–43]. With applications in view, Gradzielski et al. created pH-responsive chitosan–surfactant complexes for

selective binding/release processes of pollutants [44, 45]. Recently, the formation of 1D nanofibers and nanohelixes from anionic azo dyes and cationic surfactants was described [46]. A supramolecular gel was formed out of surfactant-encapsulated polyoxometalate clusters using different ammonium surfactants [36]. Faul et al. built nanostructured complexes from surfactant and polyoxometalates with tunable photophysical properties promising for nanotechnology [47, 48].

In the field of supramolecular chemistry, electrostatic self-assembly is a promising method yielding nanoobjects through association of polyelectrolytes and/or small ionic building blocks [49–56]. The structure formation does not rely on specifically synthesized binding motifs but on a combination of non-covalent interactions, like electrostatic interactions with hydrogen bonding, π–π interaction, or geometric effects. The interplay of several kinds of long-range and short-range interaction forces is the key to the formation of well-defined structures with various architectures ranging from spheres over networks to hollow spheres and long cylinders, in this case, without involving surfactants or hydrophobic effect [53]. On one hand, a large variety of structures and functionalities in terms of assemblies in solution has been realized through the combination of electrostatics and π–π interaction [49, 50, 53]. On the other hand, versatile solid materials have been built from ionic surfactants and dyes, for example, by Faul et al. [29–33]. Only few studies on ionic dye–surfactant assemblies in solution exist [31, 57–63]. For future applications, it is now most crucial to fundamentally understand the interplay of the non-covalent interactions to lead to the possibility of a targeted creation of self-assembled surfactant–dye nanostructures in solution.

The present study targets the self-assembly of ionic dye molecules and oppositely charged surfactants into supramolecular assemblies in solution. In difference to classical surfactant systems, multivalent ionic dye molecules serve as counterions that can also undergo mutual π–π interaction. Hence, the interplay of hydrophobic effect, electrostatic interaction, and π–π interaction directs the structure formation. This makes the self-assembly both more complex and more versatile. A systematic study with variation of building blocks and formation conditions and a thorough characterization of structures and interactions is performed to allow gaining fundamental insight into the multiinteraction self-assembly. Specifically, self-assembled structures from combining the anionic divalent azo dye Ar26 with cationic alkyltrimethylammonium bromide surfactants of various chain lengths in aqueous solution have been investigated. Light scattering, UV/Vis spectroscopy, ζ-potential measurements, small-angle neutron scattering, and isothermal titration calorimetry are used to study the association, and assembly formation is considered at different initial surfactant concentrations: below, at, and above the critical micelle concentration for all surfactants. Focus is to elucidate the formation of the dye–surfactant structures and to establish the route to a promising type of self-assembled nanostructures in solution, resulting from a delicate interplay of non-covalent interactions.

Experimental section

Chemicals Cetyltrimethylammonium bromide (C_{16}TAB) was obtained from Merck Chemicals, tetradecylammonium bromide (C_{14}TAB) from Sigma-Aldrich, and dodecylammonium bromide (C_{12}TAB) from VWR (analytical grade >98 %). All surfactants were used without further purification. The azo dye Ar26 was purified by recrystallization to yield a dye content of >96 %. To prepare samples and stock solutions, deionized water was filtered twice through hydrophilic membrane filters with a pore size of 0.22 μm. To prepare small-angle neutron scattering samples, D_2O with a water content <0.1 % was used, which was purchased from Deutero GmbH.

Sample preparation Stock solutions of Ar26 were prepared by dissolving an appropriate amount of dye in neutral deionized and filtered water. Stock solutions of C_{16}TAB, C_{14}TAB, and C_{12}TAB were prepared accordingly. Light scattering samples were prepared by mixing aqueous stock solutions of the compounds: Deionized and filtered water was placed into light scattering cuvette, surfactant stock solution, and then, the dye stock solution was added. For small-angle neutron scattering, stock solutions of Ar26 and the surfactants were prepared in D_2O. To prepare SANS samples, surfactant stock solution were added to D_2O before adding an appropriate amount of Ar26 stock solution to yield a surfactant concentration of 0.5 g L^{-1}.

Light scattering Light scattering measurements were carried out on an ALV CGS 3 goniometer with ALV 5000 correlator (ALV Langen, Germany) equipped with a HeNe laser with a wavelength of λ=632.8 nm and 20 mW output power. Measurements covered an angular range of $30° \leq \theta \leq 150°$. Data analysis was carried out by converting the measured intensity autocorrelation function into the scattered electric field autocorrelation function using the Siegert relation. The electric field autocorrelation functions were further analyzed by inverse Laplace transformation using the program CONTIN by S. Provencher to yield the distribution of relaxation times [64]. From this, the apparent diffusion coefficient was calculated, and by extrapolation to zero, scattering vector square of the diffusion coefficient was obtained. Via Stokes–Einstein relationship, the diffusion coefficient was converted into the hydrodynamic radius.

UV/Vis spectroscopy Absorption spectra were recorded using a SHIMADZU UV Spectrophotometer (UV-1800) with a slit width of 1 nm using quartz cuvettes from Hellma/

Müllheim with 1 and 10 cm path length. The spectral range covered 200 nm≤λ≤800 nm.

Small-angle neutron scattering SANS measurements were performed at beamline KWS2 at the Jülich Centre for Neutron Science at the Heinz Maier-Leibnitz Zentrum (MLZ), Munich, Germany, Garching, Germany and at beamline D11 at the Institute Laue Langevin (ILL), Grenoble, France. At KWS2, three configurations with neutron wavelength λ=4.55 Å and sample-detector distances of d=2 m, d=8 m, and d=20 m were used. At D11, three configurations with a wavelength of λ=6 Å and sample-detector distances of d=1.2 m, d=8 m, and d=39 m were used. Data were corrected for empty cell scattering, electronic background, and detector uniformity and analyzed after subtracting solvent scattering and incoherent background. The scattering data were further analyzed and transformed into the pair distance distribution function *P(r)* using the general indirect Fourier transform program (GIFT) by O. Glatter, including smoothing of the primary data, desmearing, and transformation into real space [65, 66].

On the basis of the first results, structural modeling by standard fitting packages such as SASview has been used to obtain the particle shape and dimensions. The SANS intensity can be described as $I(q)= \phi\ V_{NP}\ (\Delta\rho_{SLD})^2\ P^2(q)$, where ϕ is the volume fraction, V_{NP} the nanoparticle volume, $\Delta\rho_{SLD}$ the difference in scattering length density between the nanoparticle and the solvent, and *P(q)* the nanoparticle form factor describing the nanoparticle shape. For example, for a sphere with radius r, the form factor $P(q)$ is

$$P(q) = 3\frac{\sin qr - qr\cos qr}{(qr)^3}$$

For a cylinder with length L and radius r, *P(q)* is

$$P(q) = \int_0^1 \frac{4J_1\left(qr\sqrt{1-x^2}\right)\sin\frac{qLx}{2}}{q^2 r\sqrt{1-x^2}Lx}\ dx$$

where J_1 is the first-order Bessel function.

ζ-Potential ζ-Potential measurements were carried out on Zetasizer Nano ZS from Malvern Instruments. For each measurement, five runs were performed. The Hückel formula was used to calculate the ζ-potential from the electrophoretic mobility.

Isothermal titration calorimetry ITC measurements were carried out with a VP-ITC microcalorimeter from MicroCal Inc. (Northampton, MA). Experiments were performed at 25 °C. For surfactant–dye experiments, 30–50 injections of 4–5 μl were used with a spacing time of 300 s. For micellization experiments, 50 injections of 2 μl were used with a spacing time of 350 s. Data analysis was done using a one-site model as implemented in MicroCal ITC data analysis software for Origin 7.

Results and discussion

Dye–surfactant self-assembled aggregates were prepared using the anionic azo dye Ar26 and oppositely charged alkyltrimethylammonium bromide surfactants C_nTAB of different chain length (n=12, 14, 16) as depicted in Scheme 1. Experiments were performed using concentrations below the critical micelle concentration cmc (c<cmc), close to the cmc (c≈cmc), and above the cmc (c>cmc) to study the influence of the presence of surfactant monomers versus micelles on the surfactant–dye aggregate formation. The cmc values for the surfactants with different chain length are $c(C_{12}TAB)= 1.534\times10^{-2}$ mol L^{-1}, $c(C_{14}TAB)=3.943\times10^{-3}$ mol L^{-1}, and $c(C_{16}TAB)=9.642\times10^{-4}$ mol L^{-1} [4, 67, 68]. To discuss data, the loading ratio l defined as the ratio of the molar concentration of sulfonate groups of the counterion Ar26 to the molar concentration of quaternary ammonium groups of the surfactant is

$$l = \frac{c\left(SO_3^-,\ Ar26\right)}{c\left(N^+,\ surfactant\right)}$$

For all surfactants, aggregate formation with the oppositely charged dye takes place over a wide range of loading ratios l leading to different structures depending on loading ratio and concentration as light scattering results and spectral changes

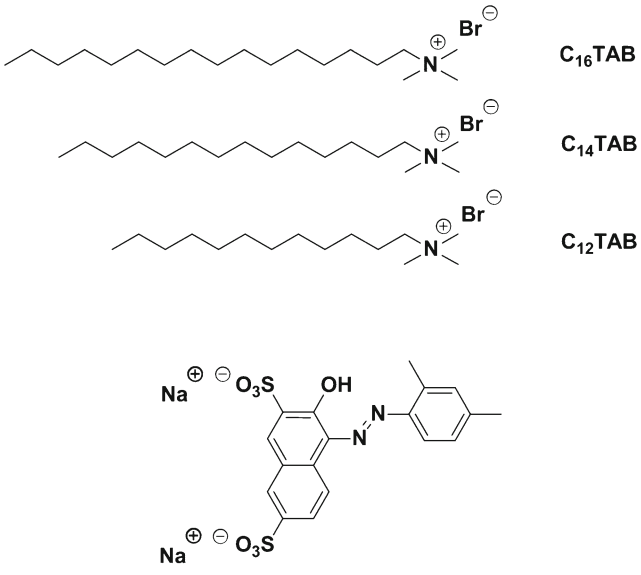

Scheme 1 Chemical structures of alkyltrimethylammonium surfactants C_nTAB (n=12, 14, 16) and azo dye Ar26 used as building blocks in this study

Table 1 Stability and dynamic light scattering results for C_{12}TAB-Ar26, C_{14}TAB-Ar26, and C_{16}TAB-Ar26 at different concentrations

Surfactant	$c(C_nTAB)$	Stable range	R_H range	R_H for l=0.5
C_{12}TAB	$c(C_{12}TAB)<cmc$	$l<1.5$, $1.5<l$	74–420 nm	390 nm
	$c(C_{12}TAB)\approx cmc$	$l<0.9$	2.6–21 nm	11 nm
	$c(C_{12}TAB)>cmc$	–	–	–
C_{14}TAB	$c(C_{14}TAB)<cmc$	$l<1.0$, $1.0<l$	Peak 1 12–20 nm	Peak 1 10 nm
			Peak 2 53–109 nm	Peak 2 76 nm
	$c(C_{14}TAB)\approx cmc$	$l<1.0$	Peak 1 3.7–14 nm	Peak 1 8 nm
			Peak 2 28–168 nm	Peak 2 59 nm
	$c(C_{14}TAB)>cmc$	$l<0.7$	4.7–16 nm	9 nm
C_{16}TAB	$c(C_{16}TAB)<cmc$	$l<1.0$, $1.0<l$	Peak 1 7–23 nm	Peak 1 20.5 nm
			Peak 2 48–113 nm	Peak 2 113 nm
	$c(C_{16}TAB)\approx cmc$	$l<0.9$	Peak 1 3.2–10 nm	Peak 1 10 nm
			Peak 2 41–61 nm	Peak 2 61 nm
	$c(C_{16}TAB)>cmc$	$l<0.9$	32–74 nm	74 nm

l loading ratio

indicate. Table 1 gives an overview of results determined by dynamic light scattering (DLS).

Association of dye and surfactant for $c(C_nTAB)<cmc$

C_{12}TAB-Ar26 aggregates A concentration of $c(C_{12}TAB)=5.0\times10^{-4}$ mol L^{-1} was chosen to prepare loading ratios $0.03\leq l\leq2.0$ with low Ar26 concentrations, so that initially the dye is molecularly dissolved and π–π stacking of dye monomers is induced by surfactant molecules. Figure 1a shows DLS results after mixing aqueous solution of the components for a sample with a loading ratio l=0.5. The electric field autocorrelation function $g^1(\tau)$ and the distribution of relaxation times $A(\tau)$ for the C_{12}TAB-Ar26 assembly sample reveal a hydrodynamic radius of R_H=390 nm with a narrow size distribution width of σ=0.15. A second peak is observed for l=0.03 and l=2.0, while other loading ratios show only one peak in the distribution of relaxation times $A(\tau)$, i.e., for C_{12}TAB-Ar26, the formation of one or two sizes of aggregates depends on the loading ratio.

Figure 1b depicts the hydrodynamic radii R_H in dependence on the loading ratio l. Samples at all loading ratios show a narrow size distribution. Aggregates in a size range of 74 nm$\leq R_H\leq$420 nm form, but precipitation occurs soon after preparation. A stability limit, which corresponds to the loading ratio at which precipitation occurs immediately after preparation, was found at l=1.5. The instability of these aggregates likely results from the short hydrophobic tail, as will be discussed in the following.

C_{14}TAB-Ar26 aggregates Samples with C_{14}TAB-Ar26 with a surfactant concentration below the cmc of $c(C_{14}TAB)=4.6\times10^{-4}$ mol L^{-1} and loading ratios $0.2\leq l\leq2.0$ were prepared. In this case, coexisting aggregates of two different sizes were formed over the complete loading ratio range: one in a size range of 12 nm$\leq R_H\leq$20 nm and larger aggregates with hydrodynamic radii 53 nm$\leq R_H\leq$109 nm.[1] Smaller sized aggregates likely correspond to smaller preformed building blocks made of dye and surfactant which stack to form the larger structures. These dye–surfactant aggregates show higher stability in comparison to C_{12}TAB-Ar26 assemblies and are stable for at least several hours.

C_{16}TAB-Ar26 aggregates C_{16}TAB-Ar26 aggregates were prepared at $c(C_{16}TAB)=4.2\times10^{-4}$ mol L^{-1} to yield loading ratios between $0.3\leq l\leq2.5$, all being stable. DLS revealed coexistence of two assembly sizes as shown in Fig. 1c for l=0.9 and l=2.5. Similar to C_{14}TAB-Ar26, larger sized aggregates likely are composed of preformed smaller aggregates, which leads to the coexistence of smaller and larger structures. Figure 1d depicts hydrodynamic radii R_H in dependence on loading ratio l. The hydrodynamic radii of the smaller aggregates cover a size range of 7 nm$\leq R_H\leq$23 nm, whereas a range of 48 nm$\leq R_H\leq$113 nm in dependence on l is found for the larger aggregates.[2] Inversion of the mixing order of the stock solutions results in the same size distribution, implying that equilibrium structures rather than kinetically trapped structures are formed. Considering the ratio of the radius of gyration R_G as obtained from static light scattering and the hydrodynamic radius R_H, a ratio R_G/R_H for C_{16}TAB-Ar26 aggregates of $1.3\leq R_G/R_H\leq1.7$ results. This indicates elongated aggregates, as can further be proven by SANS (see below).

Evidently, the long hydrophobic tail of C_{16}TAB surfactants causes a higher stability of the aggregates, likely because a long alkyl chain better counterparts the increasing size of the headgroups during interaction with Ar26. Only at l=1.0, dye–

[1] The weight of peak was found to be 15 % for the first peak and 85 % for the second peak.

[2] The weight of peak was found to be 16 % for the first peak and 84 % for the second peak.

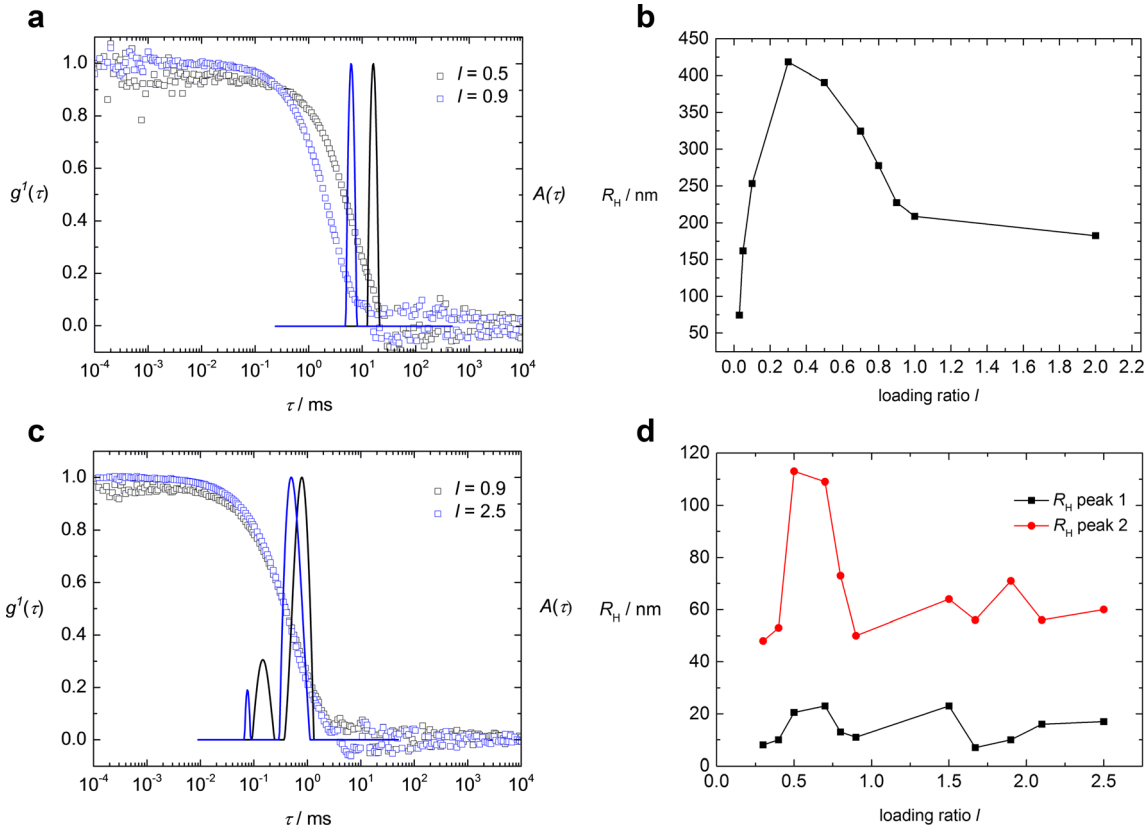

Fig. 1 **a** Electric field autocorrelation function $g^1(\tau)$ and distribution of relaxation times $A(\tau)$ for C_{12}TAB-Ar26 aggregates at $c(C_{12}TAB)=5.0\times10^{-4}$ mol L^{-1} with loading ratio $l=0.5$ and $l=0.9$ at a scattering angle $\theta=90°$; **b** hydrodynamic radii R_H versus l for C_{12}TAB-Ar26 aggregates at $c(C_{12}TAB)=5.0\times10^{-4}$ mol L^{-1}; **c** electric field autocorrelation function $g^1(\tau)$ and distribution of relaxation times $A(\tau)$ for C_{16}TAB-Ar26 aggregates at $c(C_{16}TAB)=4.2\times10^{-4}$ mol L^{-1} with $l=0.9$ and $l=2.5$ at $\theta=90°$; and **d** hydrodynamic radii R_H versus loading ratio l for C_{16}TAB-Ar26 aggregates at $c(C_{16}TAB)=4.2\times10^{-4}$ mol L^{-1}

surfactant aggregates precipitate. Assemblies below charge stoichiometry remain stable in solution for at least 3 weeks, whereas aggregates of higher loading ratio are stable for several days.

Association of dye and surfactant for $c(C_nTAB)\approx$cmc

As the cmc describes the starting point of micellization, experiments using surfactant concentrations at or slightly above the cmc were performed to study the influence of coexisting surfactant monomers and micelles on the dye–surfactant association.

C_{12}TAB-Ar26 aggregates C_{12}TAB-Ar26 aggregates were prepared at surfactant concentrations 1.33×10^{-2} mol $L^{-1}\leq c(C_{12}TAB)\leq2.1\times10^{-2}$ mol L^{-1}, which is a concentration range from slightly below to slightly above the cmc. Light scattering measurements of samples with loading ratios $0.2\leq l\leq0.9$ revealed hydrodynamic radii of 2.6 nm$\leq R_H\leq$21 nm. The stability limit for C_{12}TAB-Ar26 samples at the cmc was determined to be at a loading ratio $l=0.9$, above which precipitation occurs immediately. Hence, at concentrations slightly above the cmc, where micellization starts, electrostatic interactions between negatively charged Ar26 and positively charged surfactant monomers and micelles lead to the formation of small dye–surfactant assemblies in comparison to samples prepared at concentrations below the cmc.

C_{14}TAB-Ar26 aggregates Figure 2a depicts the electric field autocorrelation function $g^1(\tau)$ and the distribution of relaxation times $A(\tau)$ for a sample with $l=0.9$ at $c(C_{14}TAB)=3.82\times10^{-3}$ mol L^{-1} close to the cmc. The distribution of relaxation times $A(\tau)$ shows two peaks for all loading ratios. Thus, in contrast to what is found for C_{12}TAB-Ar26 (above) and C_{16}TAB-Ar26 (below), likely the C_{14}TAB-Ar26 association gives rise to aggregates of two different sizes. The hydrodynamic radii in total cover a size range of 3.7 nm$\leq R_H\leq$14 nm for the smaller aggregates and 28 nm$\leq R_H\leq$168 nm for the larger aggregates.[3]

The smaller aggregates likely represent C_{14}TAB micelles or C_{14}TAB micelles loaded with Ar26. The larger size of the second peak indicates the formation of aggregates consisting of several micelles connected by Ar26 ions. Due to the fact

[3] The weight of peak was found to be 65 % for the first peak and 35 % for the second peak.

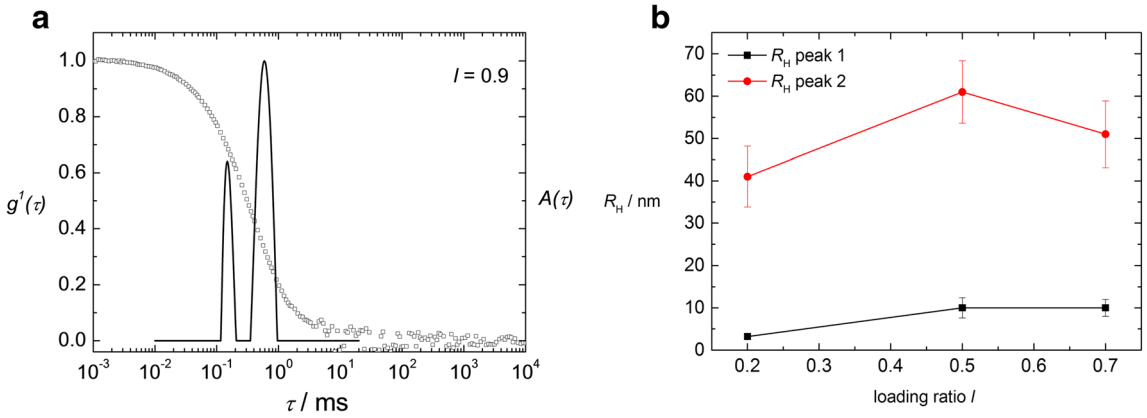

Fig. 2 **a** Electric field autocorrelation function $g^1(\tau)$ and distribution of relaxation times $A(\tau)$ for C_{14}TAB-Ar26 aggregates with $c(C_{14}TAB)=3.82\times10^{-3}$ mol L^{-1} with $I=0.9$ at $\theta=90°$ and **b** hydrodynamic radii R_H versus loading ratio I for C_{16}TAB-Ar26 aggregates at $c(C_{16}TAB)=1.9\times10^{-3}$ mol L^{-1}

that micelle formation just starts at the cmc, initially there are only a few micelles and a great amount of free surfactant monomers. It is hence likely that a larger structure results from aggregates of surfactant monomers electrostatically bound to Ar26 ions. Forming larger aggregates from dye and surfactant thus is due to an interplay of electrostatic interactions, induced hydrophobic effect, and π–π interactions.

C_{16}TAB-Ar26 aggregates Aggregates formed at a surfactant concentration slightly above the cmc ($c(C_{16}TAB)=1.9\times10^{-3}$ mol L^{-1}) with loading ratios $0.2\leq I\leq0.9$ were studied. Stable assemblies could only be prepared in this range, and the stability limit is $I=0.9$; above this limit, samples precipitate. Analysis of the samples with light scattering revealed two sizes of aggregates as the distribution of relaxation times $A(\tau)$ shows two peaks, similar to the C_{14}TAB-Ar26 case. Smaller assemblies exhibit hydrodynamic radii R_H of 3.2 nm$\leq R_H\leq$ 10 nm whereas larger aggregates are found to be in a size range of 41 nm$\leq R_H\leq$61 nm, as Fig. 2b displays. Those size ranges probably correspond to the formation of surfactant monomer–dye aggregates and surfactant micelles loaded with Ar26 ions.

Association of dye and surfactant for $c(C_nTAB)$>cmc

While the previous section focused on surfactant–dye aggregates formed from surfactant monomers, the following part deals with surfactant concentrations above the cmc where self-assembled aggregates will majorly form from pre-existing surfactant micelles.

C_{12}TAB-Ar26 aggregates Experiments with C_{12}TAB-Ar26 at surfactant concentrations above the cmc required high Ar26 concentrations to create appropriate loading ratios of $0.2\leq I\leq2.0$ and resulted in unstable aggregates that precipitated immediately.

C_{14}TAB-Ar26 aggregates C_{14}TAB-Ar26 samples were prepared at $c(C_{14}TAB)=2.0\times10^{-2}$ mol L^{-1} with loading ratios of $0.2\leq I\leq0.7$, above which precipitation occurs immediately. Figure 3 presents electric field autocorrelation functions $g^1(\tau)$ and distribution of relaxation times $A(\tau)$ for $I=0.5$ and $I=0.7$. As $I=0.7$ determines the stability limit, this loading ratio resulted to be unstable and precipitated soon.

The size range of C_{14}TAB-Ar26 aggregates is 4.7 nm$\leq R_H\leq$16 nm, where the hydrodynamic radius increases with increasing I. As the sample with $I=0.7$ was not very time stable and precipitated after 1 day, it is likely that the structure of these aggregates corresponds to single micelles loaded with dye ions acting as counterions, which in the transition range can further interconnect micellar aggregates with time.

C_{16}TAB-Ar26 aggregates A surfactant concentration of $c(C_{16}TAB)=4.8\times10^{-3}$ mol L^{-1} was chosen to prepare C_{16}TAB-Ar26 samples with loading ratios $0.2\leq I\leq0.9$ from pre-existing micelles. In this case, the stability limit above which precipitation occurs was found to be at $I=0.9$. Analysis of the aggregates by light scattering revealed occurrence of a main aggregate size in a range of 32 nm$\leq R_H\leq$39 nm. Only aggregates with $I=0.4$ are larger with $R_H=74$ nm. In contrast to C_{14}TAB-Ar26, the C_{16}TAB-Ar26 aggregates formed do not correspond to single micelles loaded with dye ions as the known size of spherical C_{16}TAB micelles is about 5 to 6 nm in diameter, and thus also, the smaller observed size here matches a structure of surfactant micelles connected by dye ions [1, 69–72].

Overall, for all investigated structures, samples prepared at surfactant concentrations slightly above the cmc mostly showed formation of aggregates of two different sizes. The broad size range may be understood by the fact that single micelles loaded with Ar26 ions, Ar26-interconnected micelles as well as surfactant monomers connected to Ar26 ions can occur through the interplay of the different interactions. Light scattering revealed hydrodynamic radii of 2.6 nm$\leq R_H\leq$21 nm

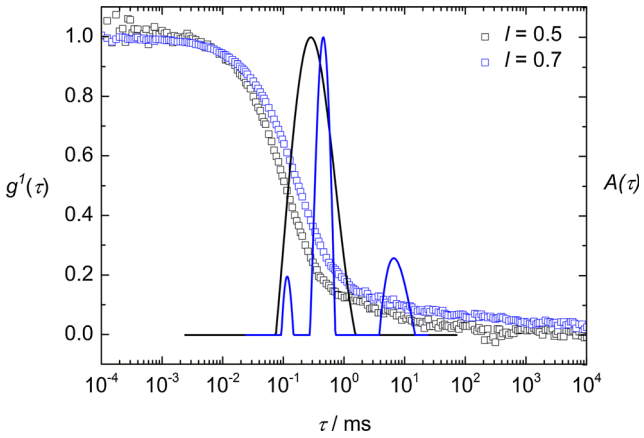

Fig. 3 Electric field autocorrelation function $g^1(\tau)$ and distribution of relaxation times $A(\tau)$ for C_{14}TAB-Ar26 aggregates at $c(C_{14}TAB)=2.0\times10^{-2}$ mol L^{-1} with $l=0.5$ and $l=0.7$ at $\theta=90°$

for C_{12}TAB-Ar26 aggregates. Higher values and multiple peaks were observed for C_{14}TAB-Ar26 aggregates in a size range of 3.7 nm$\leq R_H \leq$14 nm and 28 nm$\leq R_H \leq$168 nm. For C_{16}TAB-Ar26 aggregates, sizes of 3.2 nm$\leq R_H \leq$10 nm as well as 41 nm$\leq R_H \leq$51 nm in dependence on l were found. From these different size ranges, it can be concluded that a probable assembly structure could correspond to single micelles loaded with Ar26 ions or a connection of several micelles through Ar26 ions. Lowering the surfactant concentration below the cmc leads to interaction solely between cationic surfactant monomers and Ar26 ions and formation of aggregates in a size range 74 nm$\leq R_H \leq$420 nm for C_{12}TAB-Ar26 aggregates. In case of C_{14}TAB-Ar26 samples, two aggregate sizes with 12 nm$\leq R_H \leq$20 nm and 53 nm$\leq R_H \leq$109 nm were found. Similarly, C_{16}TAB-Ar26 aggregates showed sizes of 7 nm$\leq R_H \leq$23 nm and 48 nm$\leq R_H \leq$192 nm. At concentrations exceeding the cmc, dye–surfactant aggregates are formed from dye ions and pre-existing micelles. Here, only C_{14}TAB-Ar26 and C_{16}TAB-Ar26 aggregates were studied leading to size ranges of 4.7 nm$\leq R_H \leq$16 nm and 32 nm$\leq R_H \leq$74 nm, respectively. To understand this relatively complex behavior, further insight into dye–dye interaction, assembly charge, and structure is needed.

UV/Vis spectroscopy: analysis of π–π stacking

As light scattering showed the formation of dye–surfactant assemblies and revealed their size, UV/Vis spectroscopy was then performed to gain insight into inter-dye interactions accompanying aggregate formation. The pure Ar26 dye solution spectra in Fig. 4a exhibit a maximum absorption at λ_{max}= 505 nm. With increasing dye concentration, the spectral shape changes and bandsplitting into H- and J-band occurs. These changes in spectral shape and effects like hypsochromicity are an indication for interacting dye molecules. Ar26 shows self-aggregation upon increasing dye concentration as discussed previously [49, 50]. The corresponding blue-shifted maxima indicate formation of face-to-face aggregates, which is also called H-aggregation. The formation of a shoulder at higher wavelengths corresponds to a red-shifted J-band due to formation of J-aggregates of the dye. J-aggregates occur for red-shifted maxima and are described as head-to-tail aggregates in exciton theory. A possible model for the arrangement is a columnar stack with a helical twist [49, 50, 53]. Thus, changes in the pure Ar26 solution spectrum are due to π–π stacking of Ar26 monomers and formation of dimers or multimers.

To detect whether spectral changes are similar for all surfactants with different tail length also aggregate formation between C_{16}TAB monomers and Ar26 ions is monitored by UV/Vis spectroscopy for loading ratios varying 0.12$\leq l \leq$1.95. Figure 4c shows a hypsochromic shift of the main band absorption maximum and definite band splitting at lower loading ratios, again indicating aggregate formation through interplay of electrostatic, hydrophobic, and π–π interactions.

The absorbance of C_{12}TAB-Ar26 aggregates at surfactant concentrations below the cmc of the surfactant at different loading ratios 0.12$\leq l \leq$1.8 is presented in Fig. 4b. Evidently, the spectra change as a result of surfactant addition [57, 73]. The C_{12}TAB and the Ar26 concentration in the samples were kept low to avoid micellization and π–π stacking of the components prior to mixing. Starting from high loading ratios with dye excess, the absorbance decreases with continuous addition of C_{12}TAB. Spectral changes are a decrease of the dye monomer peak, a hypsochromic shift of the main band absorption maximum corresponding to the formation of H-aggregates and distinct band splitting. Those changes in absorption spectra indicate that aggregates are formed not only through electrostatic interactions but also with π–π interactions playing a major role. Lower loading ratios show band splitting and formation of a shoulder, corresponding to the J-band attributed to the formation of aggregates and dye π–π stacks. As the concentration of Ar26 is low, it can be concluded that the presence of C_{12}TAB is responsible for inducing π–π stacking between Ar26 monomers. The spectral changes cannot be caused by addition of salt or a change in the dielectric constant and are therefore due to electrostatic, hydrophobic, and π–π interaction between dye and surfactant [49, 50, 56]. Hence, this result is an evidence of the C_{12}TAB-Ar26 assembly formation being based on electrostatic and hydrophobic interactions and mutual π–π interaction of the dye ions. Similar observations were made for polyamidoamine (PAMAM) dendrimer-Ar26 aggregates showing spectral changes corresponding to band splitting and formation of H- and J-band due to inter-dye interactions [49, 50, 53]. Upon addition of PAMAM, dendrimer interactions between the polyelectrolyte and Ar26 occur leading to a hypsochromic shift of the main band absorption, which indicates a change in the aggregate type.

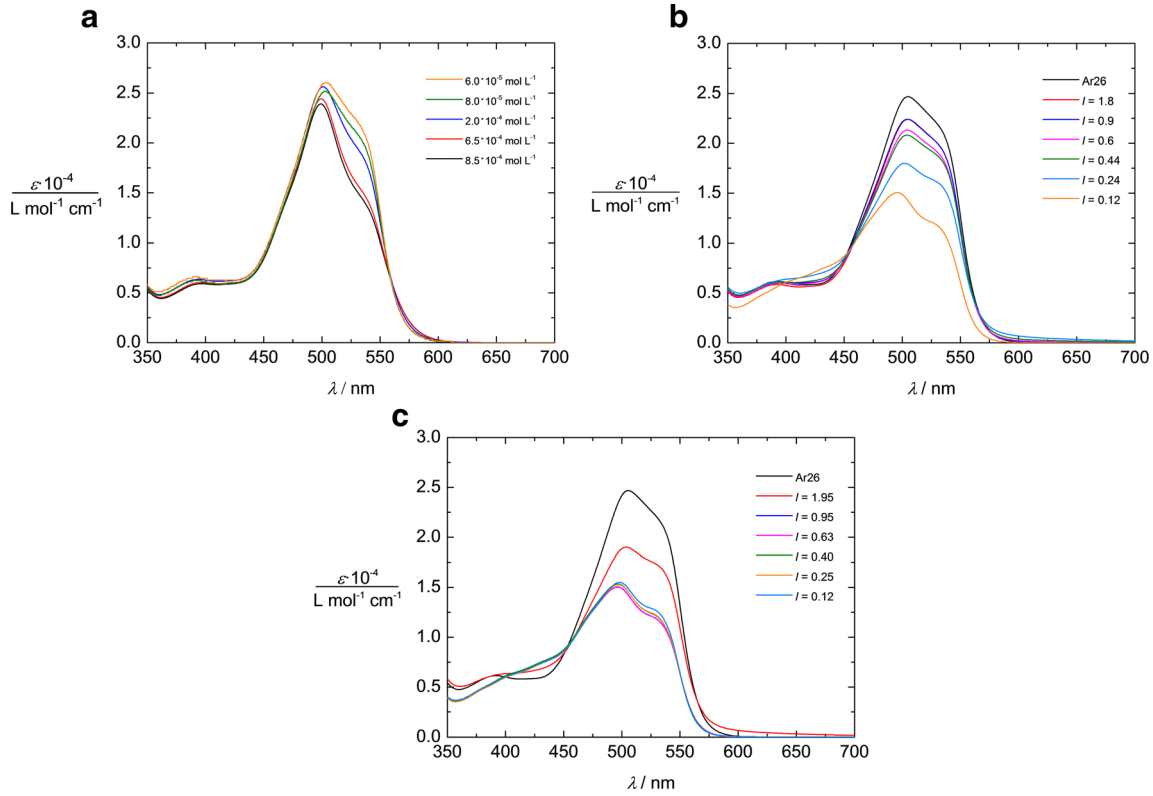

Fig. 4 **a** UV/Vis spectra of Ar26 in aqueous solution with varying concentration; **b** UV/Vis spectra of C_{12}TAB-Ar26 aggregates at surfactant concentration below the cmc for varying loading ratios at c(Ar26)=4.0×10^{-5} mol L^{-1}, note that l=0.9 and l=1.8 are nearly of same intensity and are not well distinguishable; and **c** UV/Vis spectra of C_{16}TAB-Ar26 aggregates at surfactant concentration below the cmc for varying loading ratios at c(Ar26)=3.8×10^{-5} mol L^{-1}

Similar to C_{12}TAB-Ar26 aggregates, spectroscopic measurements of C_{14}TAB-Ar26 aggregates at surfactant concentrations below the cmc revealed band splitting and formation of H- and J-band upon addition of C_{14}TAB, indicating aggregation of C_{14}TAB monomers with Ar26 ions as well as stacking of Ar26 monomers regarding lower loading ratios.

ζ-Potential: analysis of charge characteristics

ζ-Potential measurements were carried out for selected samples to determine the charge characteristics of the aggregates, as this is expected to contribute to the stabilization of the supramolecular assemblies in solution. An overview is shown in Table 2. As all prepared C_{12}TAB-Ar26 aggregates with concentrations of c(C_{12}TAB)=5.0×10^{-4} mol L^{-1} were unstable and precipitated soon after preparation, ζ-potential measurements were carried out only for a sample with dye excess, in this case l=2.0. Here, a value of ζ=−18.3 mV was determined, indicating the stabilization of the particles through negative charges. This is due to an excess of Ar26, which leads to negatively charged particles. Further, the relatively low value leads to the conclusion that the particles are not very well stabilized, which corresponds to a limited time stability due to limited repulsive forces between the charged particles. This assumption is proven as the sample with l=2.0 in fact precipitates soon after the performed measurement. In case of C_{14}TAB-Ar26 aggregates with l=0.5 at a concentration of c(C_{14}TAB)=4.6×10^{-4} mol L^{-1}, a ζ-potential of ζ=+47.2 mV was determined, leading to the conclusion that the particles with low loading ratios (l<1) are stabilized by positive charges in solution due to an excess of positively charged surfactant molecules. Because of the larger stability of the C_{16}TAB-Ar26 particles, samples with l<1 and l<1 were measured at a surfactant concentration of c(C_{16}TAB)=4.2×10^{-4} mol L^{-1}. Samples at l=0.5 with surfactant excess yield a ζ-potential of ζ=+63.9 mV, an expressed positive value in accordance with the observed particle stability. Samples with l=2.5, in contrast, exhibit a ζ-potential of ζ=−14.3 mV,

Table 2 ζ-Potentials for C_{12}TAB-Ar26, C_{14}TAB-Ar26, and C_{16}TAB-Ar26 assemblies

Surfactant	c(C_nTAB)/mol L^{-1}	Loading ratio l	ζ-Potential/mV
C_{12}TAB	5.0×10^{-4}	l=2.0	−18.3
C_{14}TAB	4.6×10^{-4}	l=0.5	+47.2
C_{16}TAB	4.2×10^{-4}	l=2.5	−14.3
C_{16}TAB	4.2×10^{-4}	l=0.5	+ 63.9

indicating a "stabilization" of aggregates by negative charges due to dye excess. Due to this relatively small value, the conclusion is drawn that particles at high loading ratios are unstable due to weak repulsive forces leading to flocculation, which is observed for this loading ratio soon after the measurement was performed.

Assembly structures

Regarding results from light scattering, UV/Vis spectroscopy, and ζ-potential measurements, conclusions about possible aggregate structures for the different concentration regimes can be drawn. For dye–surfactant aggregates obtained at surfactant concentrations slightly above the cmc, the combination of dye ions and surfactant molecules led to undefined aggregates of broad size ranges. From the calculated R_H, it was concluded that aggregates consist either of single surfactant micelles loaded with Ar26 ions as counterions or several surfactant micelles connected by Ar26 ions as linkers, which would lead to larger aggregates, as shown in Scheme 2. A probable third structure is surfactant monomers connected by Ar26 ions leading to cylindrical-shaped aggregates.

Another possible case could be that at high surfactant concentrations, incorporation of dye ions into the surfactant micelles occurs. But, as electrostatic interactions are one major contributing force leading to assembly formation, it is more likely that charged Ar26 ions act as counterions for the cationic surfactant headgroup due to attractive interactions and are not included into the micelle core. However, as the formed dye–surfactant aggregates at concentrations above and close to cmc are rather undefined, no further focus is put on the structure elucidation of dye–surfactant aggregates at concentrations above the cmc.

For samples below the surfactant cmc, conditions turned out to be more suitable for defined structure formation and hence to study and discuss the assembly formation in more detail. Due to low surfactant concentrations, no micelle formation was possible, so that aggregates form from surfactant monomers and dye ions. From UV/Vis spectroscopy and ζ-potential, it is clear that surfactant–dye aggregates at high dye–surfactant loading ratios are mainly influenced by electrostatic interactions as no expressed UV/Vis band splitting is observed. Hence, the combination of surfactant monomer and Ar26 ions will start with the formation of ion pairs and smaller aggregates. Regarding lower loading ratios, band splitting becomes more significant, leading to the conclusion that hydrophobic and π–π interactions are introduced. Upon addition of surfactant, hydrophobic effect of the hydrophobic tails of the surfactant monomers is increased and π–π stacking between dye monomers is initiated. This is schematically presented in Scheme 3. Based on results from static light scattering leading to R_G/R_H values > 1, the resulting dye–surfactant structure can possess elongated or cylindrical structure. This is in accordance with general considerations how dye and surfactant molecules will arrange in the aggregates due to interactions and structural as well as geometrical limitations. Because of differences in the length of the hydrophobic tail and resulting

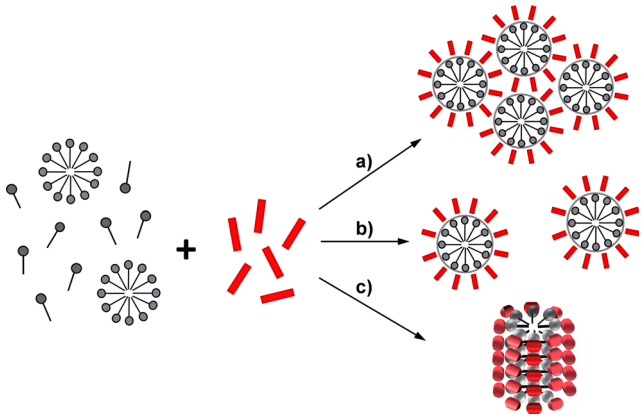

Scheme 2 Possible aggregate structures: **a** surfactant micelles connected by Ar26 ions as linkers, **b** formation of individual surfactant micelles with Ar26 acting as counterions near the micelle surface, and **c** cylindrical surfactant–dye aggregates from cylindrical surfactant micellization with condensed mutually π–π interacting Ar26 counterions

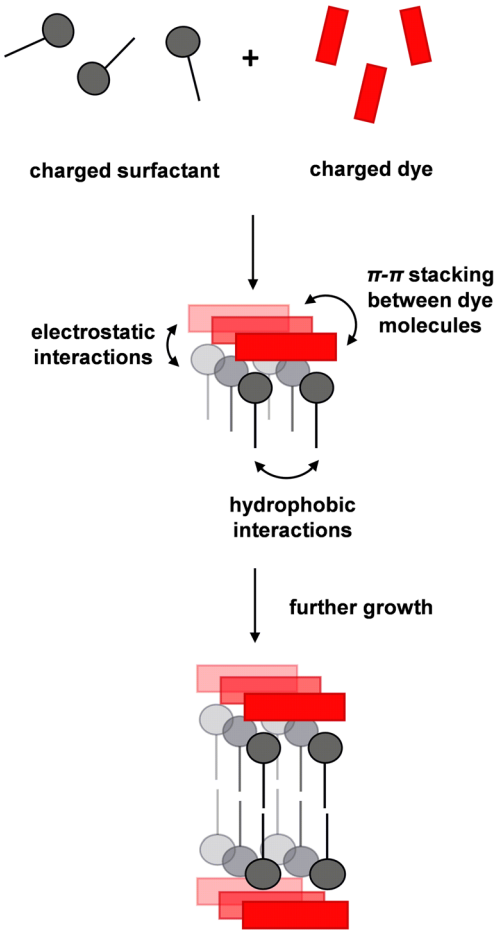

Scheme 3 Illustration of surfactant–dye aggregate formation: interplay of electrostatic interaction, hydrophobic effect, and π–π stacking

differences in the interplay of electrostatic and short-range attractive non-electrostatic interactions, the stability of the aggregates varies with surfactants. The instability of C_{12}TAB-Ar26 aggregates likely is a consequence of the interaction between anionic Ar26 and the cationic surfactant leading to an increasing size of the headgroup. With increasing headgroup size, the short hydrophobic tail cannot provide further stability of the assemblies resulting in precipitation of the aggregates. Going from 12 carbon atoms in C_{12}TAB to 14 carbon atoms in C_{14}TAB, the stability of the surfactant-Ar26 aggregates increases, as a slightly longer hydrophobic tail will more and more stabilize an increasing headgroup during interaction with Ar26 through a geometrical suitable longer alkyl chain. Therefore, aggregates consisting of surfactants with longer hydrophobic tails not only show stronger hydrophobic interactions but also higher stability.

A closer insight into the shape and structure of self-assembled aggregates is gained by SANS measurements. Overview on the here presented SANS results are given in Table 3.

First, SANS has been carried out for C_{16}TAB micelles in aqueous solution with high ionic strength but without added dye to test whether a change in micelle shape will result from high salt concentration. In general, a change in micelle shape from spherical to elongated can be achieved by adding high amounts of electrolytes. Figure 5 depicts the SANS curve and its analysis through the pair distance distribution function *P(r)* for a sample containing C_{16}TAB and KBr with $c(C_{16}TAB)$= 0.5 g L^{-1} and $c(KBr)=7.0\times10^{-4}$ mol L^{-1}. From the *P(r)* function, conclusions about the shape and the particle dimensions are drawn [74]. In this case, the depicted *P(r)* curve shows the typical shape of spherical particles. From the intercept of the curve with the *x*-axis, the diameter of the spherical micelles is obtained, revealing a value of 6.0 nm, as shown in the inset. Fitting of the SANS curve with a homogenous sphere model yields a micelle radius of 2.2 nm, which is slightly smaller than what was obtained using the *P(r)* analysis while confirming spherical micellar shape. Hence, it is proven that C_{16}TAB surfactants form spherical micelle structures in KBr containing aqueous solution at similar surfactant concentrations as used for SANS measurements of dye–surfactant assemblies.

With this, it is shown that electrolytes as KBr in a comparable concentration range do not change the spherical micelle shape to cylindrical. This is in accordance with studies showing that only very high surfactant and electrolyte concentration change the micelle shape from spherical to cylindrical [69–71]. The radius of the spherical C_{16}TAB micelles expected from the molecular dimensions is 2.5 nm, which is in agreement with reported values of 5 to 6 nm for the diameter of a homogenous spherical micelle [1, 69–72].

Further, SANS for selected C_{16}TAB-Ar26 aggregates at surfactant concentrations of $c(C_{16}TAB)$=0.5 g L^{-1} were performed. The SANS curve of C_{16}TAB-Ar26 aggregates with loading ratio l=0.7 is depicted in Fig. 6. It gives evidence of the cylindrical shape of the aggregates as the slope for the intermediate q range turns out to be −1.15. A Guinier plot for cylindrical objects (Fig. 6b) was then used to confirm the structure. It shows a linear behavior indicating cylindrical shape. Accordingly, other Guinier plots for spherical or disk-like aggregates did not show a linear behavior. From the slope of the cross-section Guinier plot, it is possible to calculate the cross-section radius of gyration $R_{G,c}$ as $R_{G,c}$=1.8 nm. Converting this $R_{G,c}$ into an approximate diameter of the cylindrical aggregates in assumption of a homogenous structure results in a diameter of d=5.1 nm. The dimensions for the cylindrical aggregates are therefore 440 nm in length and 5.1 nm in diameter as depicted in the inset of Fig. 6a. Applying a cylindrical model to fit the SANS curve depicted in Fig. 6a reveals a cylinder length of 440 nm and a radius of the structure of 2.3 nm. Hence, SANS data reveal cylindrical shape for the surfactant–dye associates at concentrations close

Table 3 SANS results including dimensions resulting from Guinier, *P(r)*, and model fit analysis

System	Surfactant concentration	Shape	Cross-section Guinier analysis	Dimension[a]
C_{16}TAB + KBr	0.5 g L^{-1}	Spherical	–	d=5.5 nm
C_{16}TAB-Ar26	0.5 g L^{-1}	Cylindrical	$R_{G,c}$=1.8 nm	r=2.3 nm
l=0.7			d=5.1 nm	L=440±3 nm
C_{16}TAB-Ar26	0.5 g L^{-1}	Cylindrical	$R_{G,c}$=1.8 nm	r=2.2 nm
l=0.5			d=5.1 nm	L=60±1 nm
C_{16}TAB-Ar26	0.2 g L^{-1}	Cylindrical	$R_{G,c}$=1.8 nm	r=2.3 nm
l=0.7			d=5.1 nm	L=400±20 nm
C_{14}TAB-Ar26	2 g L^{-1}	Cylindrical	$R_{G,c}$=1.7 nm	d=4.7 nm
l=0.7				L>153 nm
C_{14}TAB-Ar26	2 g L^{-1}	Cylindrical	$R_{G,c}$=2.0 nm	d=5.6 nm
l=0.5				L>233 nm

[a] Dimensions from *P(r)* and model fit analysis

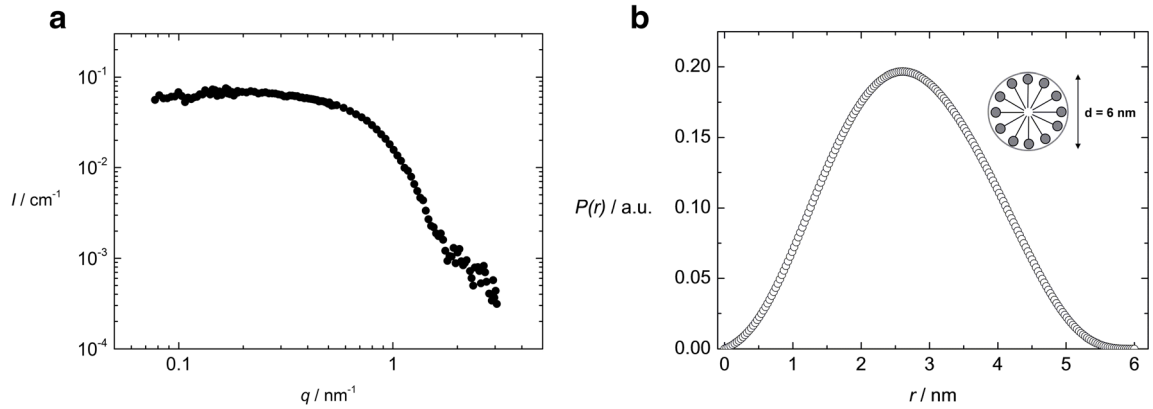

Fig. 5 **a** SANS curve for C_{16}TAB micelles in aqueous solution of high ionic strength with $c(C_{16}TAB)=0.5$ g L^{-1} and $c(KBr)=7.0\times10^{-4}$ mol L^{-1} and **b** *P(r)* analysis showing a spherical shape of micelles

to the cmc, which is in agreement with the $R_G/R_H>1$ from light scattering measurements.

Reported values for the fully stretched length of C_{16}TAB surfactant molecules are 2.2 to 2.45 nm, a value comparable to what we found as a radius [1, 72]. From this, it can be concluded that the calculated diameter of the cylindrical aggregates corresponds to two hydrophobically connected surfactant molecules, which are, in turn, connected to two Ar26 ions on the outside. Further, reported dimensions for cylindrical-shaped C_{16}TAB aggregates at high ionic strength are 2.3 nm in radius and up to 50 nm in length [68, 73], demonstrating smaller values than those obtained for C_{16}TAB-Ar26 aggregates from SANS data, which leads to the conclusion that the Ar26 dye not only acts as counterion but is part of the assembly formed.

In analogy, SANS data of C_{16}TAB-Ar26 aggregates with $l=0.5$ were analyzed as shown in Fig. 7. In this case, the slope of the log/log scattering curve is determined to be −1.16, again indicating formation of cylindrical structures. Here, a cylinder length can be approximately estimated as this curve levels off at smaller q. According to

$$L = \frac{2\pi}{q}$$

the length of the cylinder lies around 60 nm and is therefore smaller than what was found for $l=0.7$. From a Guinier plot, the cross-section radius of gyration $R_{G,c}$ is determined to be 1.8 nm, corresponding to an approximate diameter of a homogenous cylinder of 5.1 nm. The cylinder shape is confirmed by the model-free *P(r)* analysis, as depicted in Fig. 7c. The cylinder length from the *P(r)*, that is, the maximum dimension where *P(r)* decays to zero, is about 58 nm, while the diameter can be roughly estimated as 5 nm (inflection point). In addition, fitting the SANS curve with a cylindrical model shows good consistency with the data (fit also shown in Fig. 7a). Here, one obtains the length and the radius of the cylindrical aggregates with 60 and 2.2 nm, respectively.

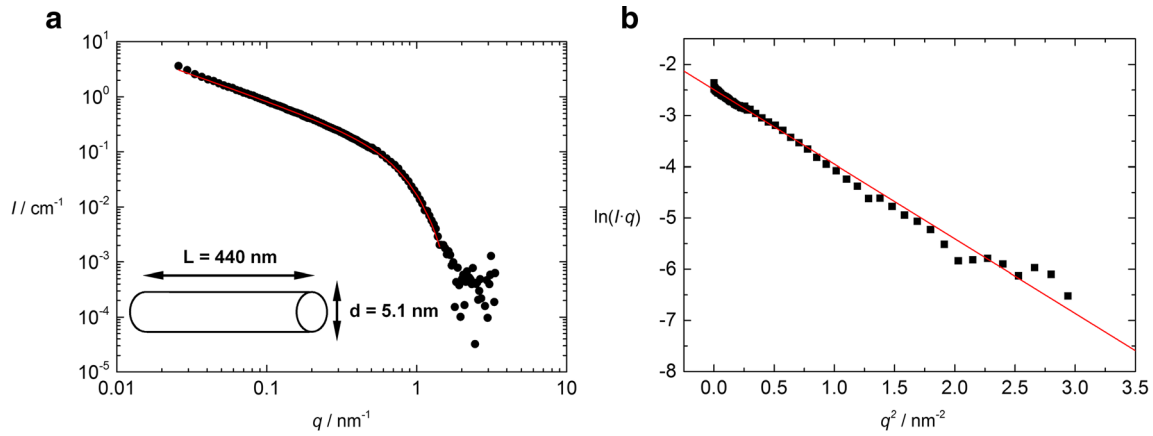

Fig. 6 **a** SANS curve for C_{16}TAB-Ar26 aggregates of $l=0.7$ at $c(C_{16}TAB)=0.5$ g L^{-1} fitted with a cylindrical model (*red*), *inset*: cylinder dimensions calculated from SANS data and **b** cross-section Guinier plot for C_{16}TAB-Ar26 aggregates of $l=0.7$ at $c(C_{16}TAB)=0.5$ g L^{-1} showing linear behavior

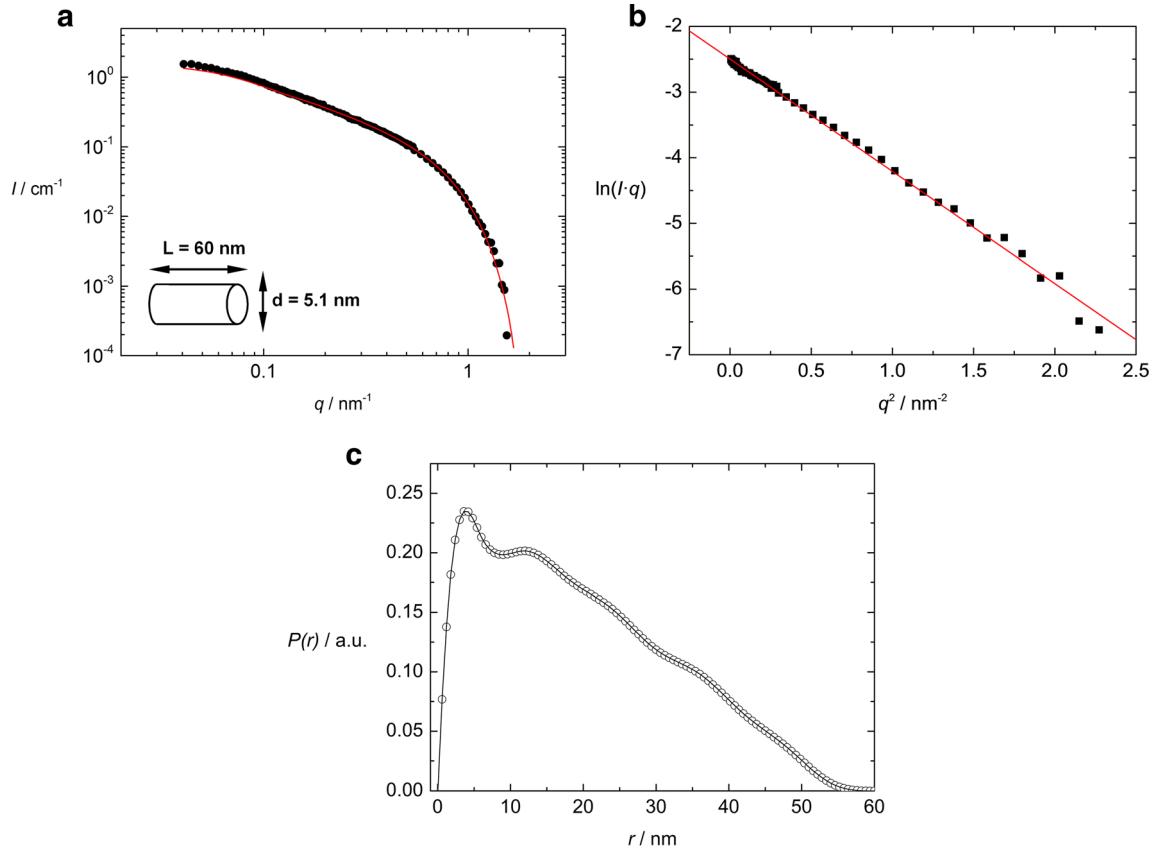

Fig. 7 **a** SANS curve for C_{16}TAB-Ar26 aggregates of l=0.5 at c(C_{16}TAB)=0.5 g L^{-1} fitted with a cylindrical model (*red*), *inset*: cylinder dimensions calculated from SANS data; **b** cross-section Guinier plot showing linear behavior; and **c** *P(r)* analysis proofing cylindrical shape

As the amount of Ar26 added to C_{16}TAB decreases with the loading ratio, it is likely that less Ar26 is bound in the aggregates leading to shorter cylinders as in the presence of a larger amount of dye. In C_{16}TAB-Ar26 aggregates at l=0.7 and l=0.5, two surfactants are hydrophobically connected and bound to one Ar26 ion, which leads to a diameter of about 5.1 nm. It may also be that the surfactants are not fully stretched and together with one Ar26 ion lead to a smaller diameter. This also is in accordance with the reported values of cylindrical-shaped C_{16}TAB aggregates at high ionic strength [75, 76]. Regarding SANS measurements of surfactant-Ar26 aggregates with the shorter surfactant C_{14}TAB, with l=0.7 and l=0.5 at concentrations slightly above the cmc, also cylindrical-shaped aggregates are found. The SANS curve reveals a slope of −1.14 and −1.22, respectively, indicating the cylindrical shape which is further proven by the linear behavior of the Guinier plot for elongated objects.[4]

Further, SANS measurements on C_{16}TAB-Ar26 aggregates at surfactant concentrations of c(C_{16}TAB)=0.2 g L^{-1} were performed to validate the cylindrical shape of dye–surfactant aggregates at surfactant concentrations below the cmc as suggested by static light scattering measurements. The SANS curve of C_{16}TAB-Ar26 aggregates of l=0.7 as depicted in Fig. 8a proves the cylindrical shape of the aggregates as its intermediate q range shows a slope of −1.1. A Guinier plot for elongated objects shows a linear behavior leading to a cross-section radius of gyration of $R_{G,c}$=1.8 nm. Calculating an approximate diameter of the cylindrical aggregates in assumption of a homogenous structure results in a diameter of d= 5.1 nm. Therefore, the final dimension of C_{16}TAB-Ar26 aggregates below cmc at l=0.7 are 400 nm in length and 5.1 nm in diameter as depicted in Fig. 8a. Regarding the dimensions of the aggregates, the diameter again corresponds to two hydrophobically connected surfactant monomers with Ar26 ions electrostatically connected to the headgroups of the surfactants. Again, modeling the SANS curve shown in Fig. 8a with a cylindrical model reveals a cylinder length of 400 nm and an aggregate radius of 2.3 nm.

Consequently, not only aggregates at surfactant concentrations slightly above the cmc show cylindrical shape but also the cylindrical shape is preserved when lowering the surfactant concentration and forming surfactant–dye aggregates from surfactant monomers. In

[4] For aggregates with l=0.7, dimensions of at least 153 nm in length and 4.7 nm in diameter were found whereas aggregates with l=0.5 were at least 233 nm in length and 5.6 nm in diameter.

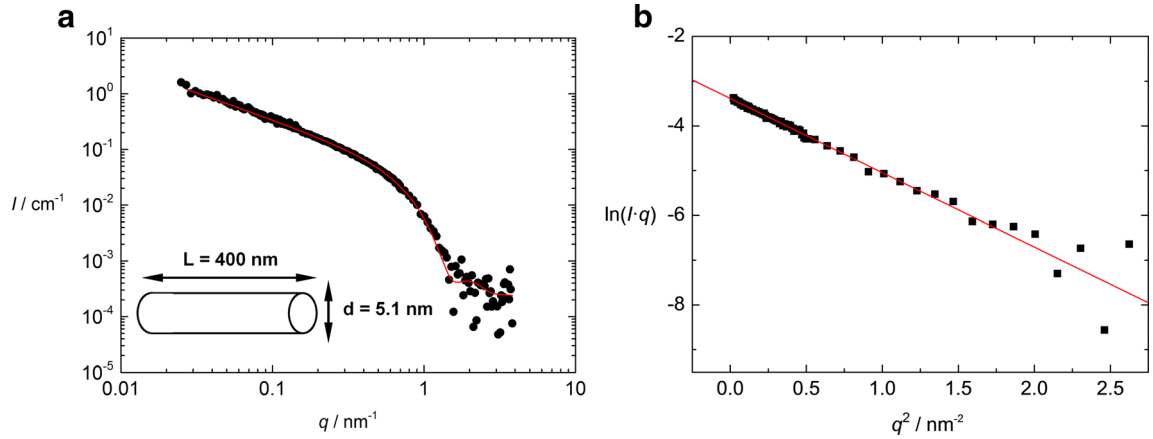

Fig. 8 **a** SANS curve for C_{16}TAB-Ar26 aggregates of l=0.7 at $c(C_{16}TAB)$=0.2 g L^{-1} fitted with a cylindrical model (*red*), *inset*: cylinder dimensions calculated from SANS data and **b** cross-section Guinier plot showing linear behavior

addition, cylindrical-shaped aggregates are formed independent of the length of the hydrophobic chain for C_{16}TAB-Ar26 aggregates as well as for dye–surfactant aggregates formed by C_{14}TAB.

Scheme 4 shows the cylindrical structures of the dye–surfactant assemblies as consistent with the SANS results. A cylindrical micelle arrangement of surfactant is caused by the hydrophobic effect, with the hydrophilic headgroups electrostatically connected to Ar26 ions pointing toward the bulk solution, where π–π stacking of the Ar26 ions then manifests the cylindrically shaped aggregate.

Thus, evidently, the cylindrical shape of dye–surfactant assemblies results from aggregate formation between Ar26 ions and C_{16}TAB monomers due to electrostatic interaction, hydrophobic effect, and π–π stacking. In addition, the dye/surfactant ratio can be used to tune the exact geometry of the cylindrical aggregates.

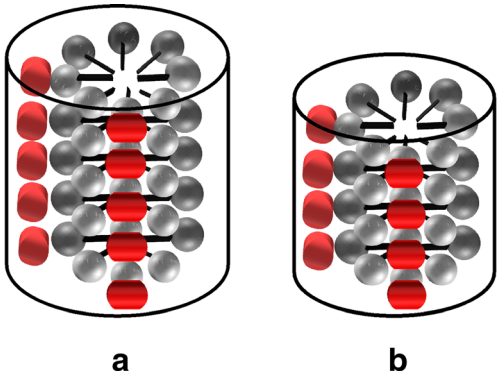

Scheme 4 Hydrophobically connected surfactants induce π–π stacking of Ar26 ions, leading to the formation of cylindrically shaped aggregates of different length: **a** at high dye/surfactant loading ratio and **b** at low dye–surfactant loading ratio

Isothermal titration calorimetry: analysis of thermodynamic parameters

Isothermal titration calorimetry (ITC) is a powerful tool to obtain thermodynamic parameters of a molecular binding process including information on intermolecular interactions and binding equilibria. Therefore, thermodynamic measurements of surfactant–dye aggregate formation using isothermal titration calorimetry were performed to gain quantitative insight into the interplay of electrostatic, hydrophobic, and π–π interaction energies contributing to the structure formation.

First, dilution experiments on C_{16}TAB micelles were performed to investigate the micellization and to determine the thermodynamic surfactant parameters which may contribute to the surfactant–dye aggregation. Micellization will strongly be influenced by surfactant structure as well as concentration and temperature, characteristic values known as critical micelle concentration and Krafft temperature. For micellization experiments of C_{16}TAB, the surfactant was diluted from a high concentration into water measuring the release or absorption of heat during dissociation of micelles [77, 78]. ITC data revealed an endothermic process; formation of C_{16}TAB micelles is therefore exothermic. The calculated thermodynamic parameter for the enthalpy of micellization is ΔH_{mic} = −8.0 kJ mol^{-1} and the cmc value of C_{16}TAB was determined to be $c(C_{16}TAB)=9.72\times10^{-4}$ mol L^{-1}. Regarding the mass-action model for ionic surfactants, which assumes dissociation equilibrium between micelles and monomer, the free energy of micellization is calculated to be ΔG_{mic}=−33.7 kJ mol^{-1} [79, 80]. With this, the change of entropy during micellization is determined to be ΔS_{mic}=+87.2 kJ^{-1} mol^{-1}, a positive value representing an entropically driven process [81, 82]. Further, the aggregate formation of Ar26 and C_nTAB surfactants of different chain length should be discussed [83]. Only C_{16}TAB-Ar26 and C_{14}TAB-Ar26 aggregate formations were studied as C_{12}TAB-Ar26 aggregates are unstable. Surfactant

Table 4 ITC titration results for surfactant–dye interaction

Surfactant	$\Delta H_{surfactant\text{-}dye}$/kJ (mol dye)$^{-1}$	N_{dye}/ (mol dye)$^{-1}$	$K_{surfactant\text{-}dye}$/L mol^{-1}	$\Delta G_{surfactant\text{-}dye}$/kJ (mol dye)$^{-1}$	$T\Delta S_{surfactant\text{-}dye}$/kJ (mol dye)$^{-1}$
C_{16}TAB (cell)	−22.0	0.38	3.2×10^6	−37.1	15
C_{16}TAB (syringe)	−20.0	0.32	3.6×10^6	−37.4	17
C_{14}TAB (cell)	−28.8	0.30	9.8×10^5	−34.2	5

concentrations were chosen to be below cmc to ensure aggregate formation only by surfactant monomers. In addition, the Ar26 concentration was kept below a value of c(Ar26)=2×10^{-4} mol L^{-1} to avoid formation of dye dimers and multimers prior to association with the surfactant. The binding process between surfactant and dye then takes place from monomers of dye and surfactant only. No experiments were performed above cmc as aggregates are unstable and result in precipitation in the measuring cell. Experiments were carried out by titrating a surfactant solution (in the cell) with Ar26 (in the syringe, "ligand") and vice versa, proving that the mixing order is not crucial for formation of aggregates and determination of thermodynamic parameters. Table 4 summarizes thermodynamic parameters determined by a one-site model for different titration experiments.

Figure 9 shows ITC data, revealing a dye binding stoichiometry of N_{dye}=0.38 (dye molecules per surfactant molecules) for C_{16}TAB-Ar26 aggregates. The determined stoichiometry value corresponds to a loading ratio of l=0.77 (dye charges per surfactant charges). Exothermic values for the association enthalpy $\Delta H_{surfactant\text{-}dye}$ indicate an enthalpically driven process determined by contributions of electrostatic interactions between charged dye and oppositely charged surfactant headgroup, possibly influenced by "dye dimers" by π–π stacking of Ar26. Main driving force for dye–surfactant aggregation is the enthalpy gain associated with structure formation, while entropic effects contribute to the driving force toward aggregation [34]. The free enthalpy gain of micellization is mostly due to only hydrophobic effects. Earlier studies on PAMAM dendrimer–dye aggregation demonstrated that $\Delta G_{dendr\text{-}dye}$ is composed of the contributions of electrostatic interactions between dendrimer and non-stacking sulfonate compounds as well as secondary dye–dye π–π interactions, implying that binding between dendrimer and dye is majorly based on those interactions [34, 37]. This approach is not possible for the surfactant–dye aggregates studied here due to a more complex interplay of more types of interactions including π–π and "hydrophobic interactions." The positive entropic contribution reflects the strong influence of the hydrophobic effect leading to aggregate formation and removal of alkyl chains from water similar to what is known for the micellization process. In comparison, for C_{14}TAB–dye association, a more exothermic $\Delta H_{surfactant\text{-}dye}$ is found. Considering the $T\Delta S_{surfactant\text{-}dye}$ for both systems, it turns out that the formation of C_{16}TAB-Ar26 aggregates is more entropically driven with a $T\Delta S_{surfactant\text{-}dye}$ value three times higher than for the C_{14}TAB-Ar26 systems. That means, in both cases, both entropy and enthalpy act in the same direction driving the association, with a shift toward the enthalpic contribution for the shorter surfactant tail. The entropy gain is more pronounced for C_{16}TAB-Ar26 due to a longer surfactant hydrophobic tail releasing more water molecules when forming aggregates. The entropy gain for C_{14}TAB-Ar26 also is less distinct as formation of a higher concentration of slightly smaller aggregates is accompanied by a larger amount of ordered water molecules around the surfactant headgroups. Despite the differences in $\Delta H_{surfactant\text{-}dye}$ and $T\Delta S_{surfactant\text{-}dye}$, the free energy gain $\Delta G_{surfactant\text{-}dye}$ is similar for the two systems. Comparing binding strengths $K_{surfactant\text{-}dye}$ more closely, a slightly stronger binding is exhibited by C_{16}TAB-Ar26, which is in agreement with the stability of the aggregates being higher than for the samples with shorter tail surfactants. Another difference in C_{14}TAB-Ar26 assembly is the somewhat smaller binding stoichiometry of N_{dye}=0.30 corresponding to a

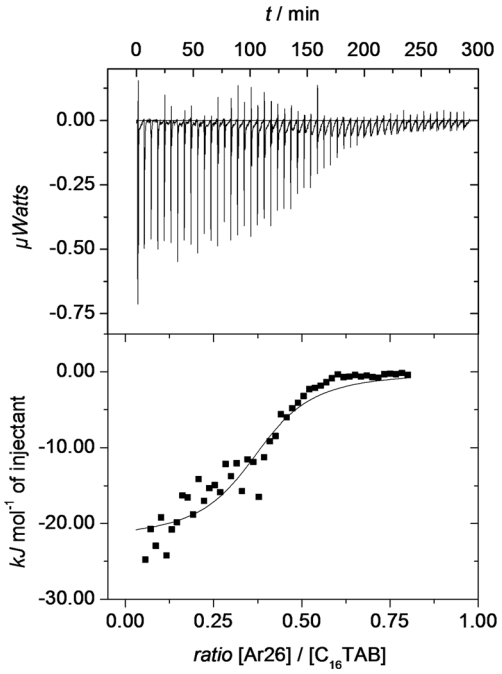

Fig. 9 ITC data for titrating C_{16}TAB solution with Ar26 solution at c(C_{16}TAB)<cmc including raw heat traces as well as the integrated heat per injection versus ratio between ligand and macromolecule

loading ratio of l=0.60, which is in accordance with the structural results indicating less Ar26 bound in a cylindrical C_{14}TAB-Ar26 aggregate.

Conclusion

Focus of this study was the investigation of self-assembled surfactant–dye structures that form by a combination of electrostatic interaction, hydrophobic effect, and π–π overlap. Alkyltrimethylammonium bromide surfactants with different tail chain lengths and the anionic dye Ar26 were applied as building blocks for self-assembly, leading to defined supramolecular structures over a wide concentration range. In particular, results revealed formation of well-defined cylindrical aggregates for surfactant concentrations below the cmc. The stability of the aggregates depends on surfactant length and the dye–surfactant loading ratio. Enhanced stability is achieved for surfactants with longer alkyl chains. Overall, surfactant tail length, loading ratio, and total concentration allow to tune the assembly size from R_H=2 nm to R_H= 420 nm. Thermodynamic measurements confirm the occurrence of an enthalpically driven binding process between dye molecules and surfactant monomers, mostly influenced by a combination of the aforementioned parameters and interactions. The presented results show that by combining the well-known fields of surfactant science and electrostatic self-assembly in solution, a further extension of the use of surfactants as building blocks for the formation of promising multicomponent nanoassemblies is achieved. As the aggregate formation is a result of more than one kind of interaction forces differing in directionality and strength, the delicate combination of those interactions resulted to be a key to well-defined and tunable supramolecular structures, where different shapes and functionalities can be created via a facile "toolbox principle." Potential applications of such nanoscale structures lie in the areas of drug delivery and medicine as well as in nanotechnology, sensors, and catalysis.

Acknowledgments This work is based upon experiments performed at D11 at Institit Laue Langevin, Grenoble France and at the KWS 2 instrument operated by JCNS at the Heinz Maier-Leibnitz Zentrum (MLZ), Garching, Germany. We thank Ralf Schweins (ILL) and Henrich Frielinghaus (MLZ) for help with SANS experiments.

Compliance with ethical standards

Funding This study was funded by the Interdisciplinary Center for Molecular Materials (ICMM, University Erlangen-Nürnberg). The authors gratefully acknowledge the financial support provided by Institit Laue Langevin, Grenoble France and by JCS to perform the neutron scattering measurements at ILL and at the Heinz Maier-Leibnitz Zentrum (MLZ), Garching, Germany.

Conflict of interest The authors declare that they have no conflict of interest.

References

1. Imae T, Kamiya R, Ikeda S (1985) J Colloid Interface Sci 108:215–225
2. Aswal VK (2003) J Phys Chem B 107:13323–13328
3. Diaz Garcia ME, Sanz-Medel A (1986) Talanta Int J Pure Appl Anal Chem 33:255–264
4. Ribeiro ACF, Lobo VMM, Valente AJM, Azevedo EFG, Miguel MG, Burrows HD (2004) Colloid Polym Sci 283:2777–283
5. Klitzing RV, Espert A, Asnacios A, Hellweg T, Colin A, Langevin D (1999) Colloids Surface A 149:131–140
6. Fitzgerald PA, Davey TW, Warr GG (2005) Langmuir 21:7121–7128
7. Seliverstova EV, Ibrayev NK, Kudaibergenov SE (2013) Russ J Phys Chem A 87:865–871
8. Seliverstova EV, Ibrayev NK, Kudaibergenov SE (2013) J Appl Polym Sci 129:289–295
9. Hu W, Ong WL, Ho GW (2010) Colloids Surf A 358:108–114
10. Kasture M, Sastry M, Prasad BLV (2010) Chem Phys Lett 484: 271–275
11. Gradzielski M, Kumar S, Mehta SK (2011) J Colloid Interface Sci 360:497–507
12. Gradzielski M, Wagner NJ, Schweins R, Prévost S, Heunemann P, Hoffmann I (2011) Langmuir 27:4386–4396
13. Sidhu J, Bloor DM, Couderc-Azouani S, Penfold J, Holzwarth JF, Wyn-Jones E (2004) Langmuir 20:9320–9328
14. Ganeva D, Faul CFJ, Götz C, Sanderson R (2003) Macromolecules 36:2862–2866
15. Ganeva D, Antonietti M, Faul CFJ, Sanderson R (2003) Langmuir 19:6561–6565
16. Wang Y, Kimura K, Dubin PL (2000) Macromolecules 33:3324–3331
17. Xia J, Zhang H, Rigsbee DR, Dubin PL, Shaikh T (1993) Macromolecules 26:2759–2766
18. Sudbeck EA, Dubin PL, Curran ME, Skelton I (1991) J Colloid Interface Sci 142:512–517
19. Dubin PL, Oteri R (1983) J Colloid Interface Sci 95:453–461
20. Antonietti M, Burger C, Effing J (1995) Adv Mater 7:751–753
21. Antonietti M, Conrad J, Thünemann A (1994) Macromolecules 27: 6007–6011
22. Thünemann AF, Lochhaas KH (1998) Langmuir 14:6220–6225
23. Hoffmann I, Farago B, Schweins R, Falus P, Sharp M, Gradzielski M (2013) EPL 104:28001
24. Antonietti M, Förster S (2003) Adv Mater 15:1323–1333
25. Wang Y, Han P, Xu H, Wang Z, Zhang X, Kabanov A (2009) Langmuir 26:709–715
26. Yan Q, Yuan J, Cai Z, Xin Y, Kang Y, Yin Y (2010) J Am Chem Soc 132:9268–9270
27. Ren Y, Baumgartner T (2012) Dalton Trans 41:7792–7800
28. Babu SS, Prasanthkumar S, Ajayaghosh A (2012) Angew Chem Int Ed 51:1766–1776
29. Faul CFJ (2014) Acc Chem Res 47:3428–3438
30. Faul CFJ, Antonietti M (2002) Chem Eur J 8:2764–2768
31. Priimagi A, Vapaavuori J, Rodriguez FJ, Faul CFJ, Heino MT, Ikkala O, Kauranen M, Kaivola M (2008) Chem Mater 20:6358–6363
32. Guan Y, Antonietti M, Faul CFJ (2002) Langmuir 18:5939–5945
33. Zakrevskyy Y, Stumpe J, Faul CFJ (2006) Adv Mater 18:2133–2136
34. Franke D, Egger CC, Smarsly B, Faul CFJ, Tiddy GJT (2005) Langmuir 21:2704–2712
35. Wang Y, Ma N, Wang Z, Zhang X (2007) Angew Chem Int Ed 46: 2823–2826
36. Wang Y, Li W, Wu L (2009) Langmuir 25:13194–13200

37. Štěpánek M, Škvarla J, Uchman M, Procházka K, Angelov B, Kováčik L, Garamus VM, Mantzaridis C, Pispas S (2012) Soft Matter 8:9412–9417
38. Minard-Basquin C, Weil T, Hohner A, Rädler JO, Müllen K (2003) J Am Chem Soc 125:5832–5838
39. Kaper H, Djerdj I, Gross S, Amenitsch H, Antonietti M, Smarsly BM (2015) Phys Chem Chem Phys 17:18138–18145
40. Škvarla J, Uchman M, Procházka K, Tošner Z, Garamusc VM, Pispas S, Štěpánek M (2014) Colloids Surf A 443:209–215
41. Uchman M, Gradzielski M, Angelov B, Tošner Z, Oh J, Chang T, Štěpánek M, Procházka K (2013) Macromolecules 46:2712–2181
42. Uchman M, Štěpánek M, Prévost S, Angelov B, Bednár J, Appavou M-S, Gradzielski M, Procházka K (2012) Macromolecules 45: 6471–6480
43. Hajduová J, Procházka K, Šlouf M, Angelov B, Mountrichas G, Pispas S, Stěpánek M (2012) Langmuir 29:5443–5449
44. Chiappisi L, Simon M, Gradzielski M (2015) ACS Appl Mater Interfaces 7:6139–6145
45. Chiappisi L, Gradzielski M (2015) Adv Colloids Interface Sci 220: 91–107
46. Huang J-B, Yan Y, Gao C, Peng Y, Cheng X-H (2013) Colloids Surf A 422:10–18
47. Zhang T, Liu S, Kurth DG, Faul CFJ (2009) Adv Funct Mater 19: 642–652
48. Zhang T, Spitz C, Antonietti M, Faul CFJ (2005) Chem Eur J 11: 1001–1009
49. Willerich I, Gröhn F (2008) Chem Eur J 14:9112–9116
50. Willerich I, Ritter H, Gröhn F (2009) J Phys Chem B 113:3339–3354
51. Willerich I, Li Y, Gröhn F (2010) J Phys Chem B 114:15466–15476
52. Willerich I, Schindler T, Gröhn F (2011) J Phys Chem B 115:9710–9719
53. Willerich I, Gröhn F (2011) J Am Chem Soc 133:20341–20356
54. Faul CFJ, Antonietti M (2003) Adv Mater 15:673–683
55. Willerich I, Gröhn F (2010) Angew Chem Int Ed 49:8104–8108
56. Gröhn F (2008) Macromol Chem Phys 209:2295–2301
57. Bielska M, Sobczyńska A, Prochaska K (2009) Dyes Pigments 80: 201–205
58. Karukstis KK, Savin DA, Koftus CT, D Angelo N (1998) J Colloid Interface Sci 203:157–163
59. Huang J-B, Yan Y, Gao C, Peng Y, Cheng X-H (2013) Colloids Surfaces A 422:10–18
60. Wang D, Long P, Dong R, Hao J (2012) Langmuir 28:14155–14163
61. Rudorf S, Rädler JO (2012) J Am Chem Soc 134:11652–11658
62. Hohner A, Bayer J, Rädler JO (2006) Eur Phys J E 21:41–48
63. Laiho A, Smarsly BM, Faul CFJ, Ikkala O (2008) Adv Funct Mater 18:1890–1897
64. Provencher SW (1982) Comput Phys Commun 27:229–242
65. Glatter O (1977) Acta Phys Austriaca 47:83–102
66. Glatter O (1977) J Appl Crystallogr 10:415–421
67. Greaves TL, Dummond C (2008) J Chem Soc Rev 37:1709–1726
68. Tadros TF (2005) Applied surfactants: principles and applications. VCH, Weinheim
69. Aswal VK (2003) Barc Newsl 237:37–42
70. Aswal VK, Goyal PS (2004) Praman – J Phys 63:65–72
71. Aswal VK, Goyal PS (2002) Chem Phys Lett 357:491–497
72. Naskar B, Dan A, Ghosh S, Aswal VK, Moulik PS (2012) J Mol Liq 170:1–10
73. Nasiruddin M, Sarwar A (2006) Fluid Phase Equilib 239:166–171
74. Iampietro DJ, Brasher LL, Kaler EW, Stradner A, Glatter O (1998) J Phys Chem B 102:3105–3113
75. Quirion F, Magid LJ (1986) J Phys Chem 90:5435–5441
76. Goyal PS, Srinivasa K, Dasannacharya BA, Kelkar VK (1991) Physica B 174:192–195
77. Ghai R, Falconer RJ, Collins BM (2012) J Mol Recognit 25:32–52
78. Chiad K, Stelzig SH, Gropeanu R, Weil T, Klapper M, Müllen K (2009) Macromolecules 42:7545–7552
79. Mosquera V, del Río JM, Attwood D, García M, Jones MN, Prieto G, Suarez MJ, Sarmiento F (1998) J Colloid Interface Sci 206:66–76
80. Lah J, Pohar C, Vesnaver G (2000) J Phys Chem B 104:2522–2526
81. Helgeson ME, Hodgdon TK, Kaler EW, Wagner NJ (2010) J Colloid Interface Sci 349:1–12
82. Bouchemal K, Agnely F, Koffi A, Djabourov M, Ponchel G (2010) J Mol Recognit 23:335–342
83. Courtois J, Berret J-F (2010) Langmuir 26:11750–11758

5.3 Functional Supramolecular Porphyrin-Dendrimer Assemblies for Light Harvesting and Photocatalysis

Submitted to Macromolecules

Functional Supramolecular Porphyrin-Dendrimer Assemblies for Light Harvesting and Photocatalysis

Anja Krieger,[†] Juan Pablo Fuenzalida Werner,[†] Giacomo Mariani,[†‡] Franziska Gröhn[†]

Department of Chemistry and Pharmacy and Interdisciplinary Center for Molecular Materials, Friedrich-Alexander-University Erlangen-Nürnberg, 91058 Erlangen, Germany

KEYWORDS

Dendrimers, Photocatalysis, Polyelectrolytes, Porphyrins, Self-Assembly

ABSTRACT

A new type of functional supramolecular assembly is formed by combining cationic porphyrin (TAPP) and the anionic generation 7.5 (G7.5) poly(amidoamine) (PAMAM) dendrimer in aqueous solution at basic pH. The interplay of non-covalent interactions is used as a key to control the formation of supramolecular structures and thereby to improve the photocatalytic activity of the porphyrin. The porphyrin-dendrimer assemblies show pH responsiveness. Their size, shape and internal structure are controlled by varying the loading ratio. Structures were analyzed by light scattering, small-angle neutron scattering, ζ-potential measurements, UV/Vis and fluorescence spectroscopy and atomic force microscopy. The assemblies show structures with high quantum yield which makes them suitable for light harvesting processes, for example,

in solar energy conversion. As a photocatalytic model reaction, the degradation of the anionic dye methyl orange is investigated, showing differing interactions with the assemblies based on their charge. A substantially enhanced photocatalytic activity was found.

INTRODUCTION

Self-assembly is a fascinating and effective method to design new materials.[1–4] The idea of using small molecules with different functionalities to form nanoparticles with desired properties is of high potential for catalysis and solar energy conversion.[5–10] The catalysts' efficiency can be enhanced by combining two or more building blocks with differnt properties.[11–13] The interplay of non-covalent interaction forces including electrostatic interaction, hydrogen bonds, van-der-Waals forces and geometric effects is a key to various well-defined self-assembled nanostructures.[14–19] Such soft materials for different applications can be formed by polymers which provide different functionalities,[20–23] leading to a variety of morphologies.[24,25] Another promising group of building blocks for self-assembly are porphyrins, which are well-known photosensitizers in nature where they are responsible for the light collection by chlorophyll in leafs. Currently, porphyrins are of high interest for solar energy conversion.[26–30] We have shown that cationic 5,10,15,20-tetrakis(4-trimethylammoniophenyl) porphyrin tetra(p-toluenesulfonate) (TAPP) and 5,10,15,20-tetrakis(1-methyl-4-pyridinio) porphyrin tetra(p-toluenesulfonate) (TMPyP) assemble with PSS-polyanions based on electrostatic interactions[31–34] and exhibit a higher photocatalytic activity for the oxidation of iodide to triiodide than the porphyrin only.[10] Porphyrins have also been incorporated into dendritic structures, where they were used as light absorbing molecule in the core or at the periphery of the dendrimers.[35–37]

Several influences like the pH of the solution, the porphyrin concentration and the ionic strength may promote self-aggregation of water-soluble porphyrins. It is well reported that the Soret signal of porphyrins can indicate self-aggregation due to its sensitivity to changes in the electronic structure.[38–40] Porphyrins can either build H-aggregates stacked in parallel as evident from a hypochromic shift or J-aggregates which show a bathochromic shift in the absorption spectra resulting from a decrease of the HOMO-LUMO gap.[41,42] TAPP does not self-aggregate due to its four positive charges leading to repulsion.[43] However, by adding oppositely charged polyelectrolytes or surfactants the repulsion of the permanent charges on the porphyrins can be overcome and porphyrins aggregate due to π-π interaction, the hydrophobic effect and the neutralization of the charges by electric interactions.[44–48] Several studies on self-assembled supramolecular dendrimer-porphyrin aggregates exist.[49–51] The self-stacking of porphyrins resulting in H- and J-aggregates, which also plays a role for the light harvesting properties, has been analysed for porphyrins in solution[52] as well as in solutions of assemblies with surfactants,[53,54] crown esters[55] and dendrimers.[56–58] H-aggregates quench the fluorescence by a rapid internal conversion to the lower energy level.[42,59–61] Previous studies focus on the aggregation behavior of porphyrins in the self-assembled aggregates only, while the nanostructure and the internal structure of the self-assembled aggregates has not been considered. Moreover, this study goes one step further and shows the advantage of such assemblies in photocatalysis.

Goal of this study is to fundamentally investigate the nanostructure of dendrimer-porphyrin assemblies, elucidate the tunability of their optical properties and study the use of these aggregates in photocatalysis. This may represent a step towards more versatile and potentially improved catalysts. The focus lies on TAPP-dendrimer assemblies with dendrimers of

generation 7.5, while TMPyP-G7.5 and TMPyP-G6.5 and TAPP-G6.5 have also been investigated. The building blocks are depicted in Scheme 1.

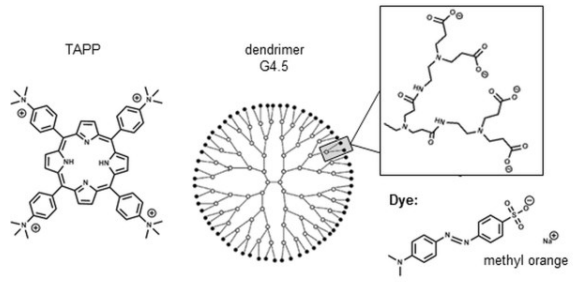

Scheme 1. Tools for the self-assembly: Chemical structure of building blocks for self-assembly: TAPP and PAMAM dendrimer generation G4.5 with ethylene diamine core; (G7.5 dendrimers were used in this study) and the dye methyl orange used for degradation in the photocatalytic model reaction.

EXPERIMENTAL SECTION

Chemicals. G7.5 dendrimer with ethylene diamine core was obtained from Dendritech as a solution of 5 wt.% in methanol. TAPP was purchased from Sigma-Aldrich with an analytical grade of 90%. Methylene blue and methyl orange were purified by recrystallization to yield a dye content of ≈ 100 %. To prepare samples and stock solutions, deionized water was used, which was filtered through two hydrophilic PTFE filters of a pore size of 0.2 µm.

Preparation of Porphyrin-Dendrimer-Aggregates. Stock solutions of TAPP were prepared by dissolving an appropriate amount of porphyrin in neutral deionized filtered water to yield an exact concentration. The porphyrin stock solutions were filtered by a 0.2 µm hydrophilic PTFE filter just before sample preparation. Stock solutions of G6.5 dendrimer and G7.5 dendrimer

were prepared by dissolving the dendrimer solution in deionized and filtered water and adjusting the solutions to pH 11 by adding 1 M NaOH. All samples were prepared by adding an appropriate amount of porphyrin to the water at pH 11. Then dendrimer stock solution was added drop by drop while stirring. For catalysis, dye stock solution was added. If necessary, the pH of the samples was adjusted afterwards by adding 1 M NaOH or 1 M HCl. For small-angle neutron scattering (SANS) and NMR spectroscopy, stock solutions of G7.5 and the TAPP were prepared in D_2O and the pH was adjusted with NaOD. Samples for photocatalysis were kept in darkness prior to further investigations. The irradiation was performed with a 300 W halogen lamp from esylux with a visible spectrum similar to daylight.

Light Scattering. Light scattering experiments were carried out on an ALV CGS 3 goniometer with ALV 5000 correlator (ALV Langen, Germany) equipped with a HeNe laser with a wavelength of $\lambda = 632.8$ nm and 20 mW output power. For dynamic light scattering an angular range of $30° \leq \theta \leq 150°$ is measured in 10° steps. In dynamic light scattering, the electric field autocorrelation $g^1(q, \tau)$ was calculated from the resulting intensity autocorrelation function $g^2(q, \tau)$ by the Siegert relation. After that $g^1(q, \tau)$ was analyzed by inverse LaPlace transformation using the program CONTIN by S. Provencher[62] to yield the distribution of relaxation times $A(\tau)$. Based on this the apparent diffusion coefficients D_{app} could be calculated. By plotting D_{app} against q^2 and subsequent extrapolation to zero the diffusion coefficient D was obtained. Via the Stokes-Einstein relationship the diffusion coefficient was converted into the hydrodynamic radius R_H. In static light scattering, the average sample, solvent (water) and standard (toluene) scattering intensity were recorded in dependence on the scattering angle. According to the Zimm equation, the radius of gyration R_G was determined by linear regression analysis.

UV/Vis Spectroscopy. UV/Vis spectra were recorded with a UV/Vis spectrometer UV 1800 from SHIMADZU. The slit width was 1 nm and quartz cuvettes from Hellma/Müllheim with 1 and 10 cm path length were used to investigate samples in a spectral range reached of 200 nm $\leq \lambda \leq$ 800 nm.

ζ-Potenial. The ξ-potentials of nanoparticles were measured at a Zetasizer Nano ZS from Malvern Instruments. For each measurement three runs of 60 s were performed. The Smoluchowski formula was used to determine the electrophoretic mobility and the ζ-potential.

Atomic Force Microscopy (AFM). A freshly cleaved mica substrate was functionalized by incubating a ~ 50 µl droplet of (3-aminopropyl)triethoxysilane (APTES) with c(APTES) = 0.05 vol%, rinsing the mica with water and drying it in air. APTES is then covalently bound to the mica surface yielding positively charged amino groups on the surface which are more favorable to bind negatively charged TAPP-G7.5 particles. AFM samples were prepared by spin-coating. 3 µl TAPP-dendrimer aqueous solution with c(TAPP) = $2.0 \cdot 10^{-5}$ mol l^{-1} were put on a mica plate and spin coated for 60 s by doing a speed ramp which contains steps from 0 rpm to 1400 rpm, 1400 rpm to 1600 rpm and 1600 rpm to 5000 rpm. AFM images were recorded in air with an AFM from NanoSurf (Boston, USA) in non-contact mode with a scan range 10 µm or 3 µm and 512 measuring points per line. The time/line result was adjusted to 0.5 s with a loop-gain of 11. The images were analysed with the software WSxM 4.0 Beta 7.0.[63]

Fluorescence Spectroscopy. Fluorescence spectroscopy was performed by using a Horiba Yvon Jobin fluorescence spectrometer with an excitation wavelength of λ = 405 nm and a slit width of 5 nm. The integration time was 0.1 s. The emission mode was set on 415 nm $\leq \lambda \leq$ 800 nm.

Small-Angle Neutron Scattering (SANS). SANS measurements were performed at beamline D11 at the Institut Laue-Langevin, Grenoble, France. Three configurations with neutron wavelength λ = 6 Å and sample-detector distances d of 1.2 m, 8 m and 39 m were used. The wavelength spread ($\Delta\lambda/\lambda$) was 0.09. A total scattering vector range of: 0.01 nm^{-1} < q < 5 nm^{-1} was investigated. The SANS intensity can be described as: $I(q) = \phi\, V_{NP}\, (\Delta\rho_{SLD})^2\, P(q)$, where V_{NP} is the nanoparticle volume, $\Delta\rho_{SLD}$ the difference in scattering length density between the nanoparticle and the solvent and P(q) the nanoparticle form factor. The latter parameter describes the nanoparticle shape. In the case here, the experimental intensity has been modeled as the sum of the contributions of two different nanoparticles: a sphere and an elliptical cylinder. For a sphere with radius *r*, the form factor P(q) is:[64,65]

$$P(q) = \left(3\frac{\sin qr - qr\cos qr}{(qr)^3}\right)^2 \quad (1)$$

While for the elliptical cylinder the intensity can be written as:[66]

$$I(q) = \frac{\phi}{V_{NP}} \int d\psi \int d\phi \int p(\theta,\phi,\psi) P(q,\alpha,\psi) \sin\theta\, d\theta \quad (2)$$

With the functions: $P(q,\alpha,\psi) = \left(2\,\frac{J_1(a)}{a}\frac{\sin b}{b}\right)^2$, $a = q \sin\alpha \sqrt{r_{major}^2 \sin^2\psi + r_{minor}^2 \cos^2\psi}$ and $b = q\frac{L}{2}\cos\alpha$. The polydispersity has been used as fixed parameter in the fit. Good agreement with the experimental results has been obtained using 0.2.

NMR: ^{1}H-NMR (300 MHz) was recorded on a Bruker Avance DPX 300 NMR spectrometer at ca. 25 °C. In ^{1}H NMR spectra, chemical shifts δ are referenced to the residual solvent peak 4.69 ppm in D_2O.

RESULTS AND DISCUSSION

TAPP-dendrimer self-assembled aggregates have been prepared by combining the cationic porphyrin and oppositely charged PAMAM dendrimer G7.5 with different loading ratios in aqueous solution. The loading ratio is defined as charge ratio of the fully charged molecules:

$$l = \frac{\text{c (porphyrin)} \cdot 4}{\text{c (dendrimer)} \cdot 1024}$$

with c the molar concentration. Titration experiments revealed deprotonation of all carboxylate groups of G7.5 at pH 11.With that, the dendrimer possesses 1024 negative charges and the loading ratio is equal to the charge ratio. Before the catalytic activity is investigated, the size, form and the inner structure of the TAPP-dendrimer soft-nanoparticles were analyzed.

Nanostructure Analysis

Exemplarily for the size and shape determination of the aggregates by light scattering an electric field autocorrelation function $g^1(\tau)$ and the distribution of relaxation times $A(\tau)$ are depicted in Figure 1 for TAPP-G7.5 dendrimer aggregates with $l = 0.05$ at pH 11.

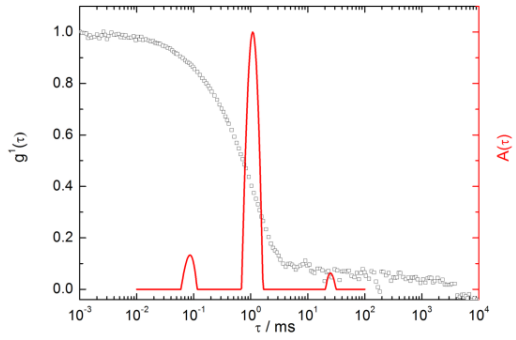

Figure 1. Dynamic light scattering of TAPP-G7.5 dendrimer aggregates at pH 11 with $I = 0.05$ at pH 11, c(TAPP) = $2.0 \cdot 10^{-5}$ mol l^{-1}: electric field autocorrelation function $g^1(\tau)$ and distribution of relaxation times $A(\tau)$ at scattering angle $\theta = 90°$; $R_H = 93$ nm with an average distribution width of $\sigma = 0.26$.

The autocorrelation function $g^1(\tau)$ gives a size of $R_H = 90$ nm for the main TAPP-G7.5 dendrimer particle species. The decay at larger τ is a feature of very few large particles ($R_H \approx 1000$ nm) and the decay at smaller τ can be attributed to a small amount of unbound dendrimer with $R_H = 5$ nm. The TAPP-dendrimer assemblies have a narrow size distribution and form defined aggregates. To understand the influence of the dendrimer amount on the self-assembly, it is elucidating to investigate aggregates with a constant dendrimer concentration c(G7.5) = $1.5 \cdot 10^{-6}$ mol l^{-1} and varying loading ratio. Light scattering results for TAPP-G7.5 dendrimer aggregates of constant dendrimer concentration determined by light scattering are given in Figure 2. Similar results are found upon inverting the order of the addition of the building blocks indicating a thermodynamically controlled process.[67]

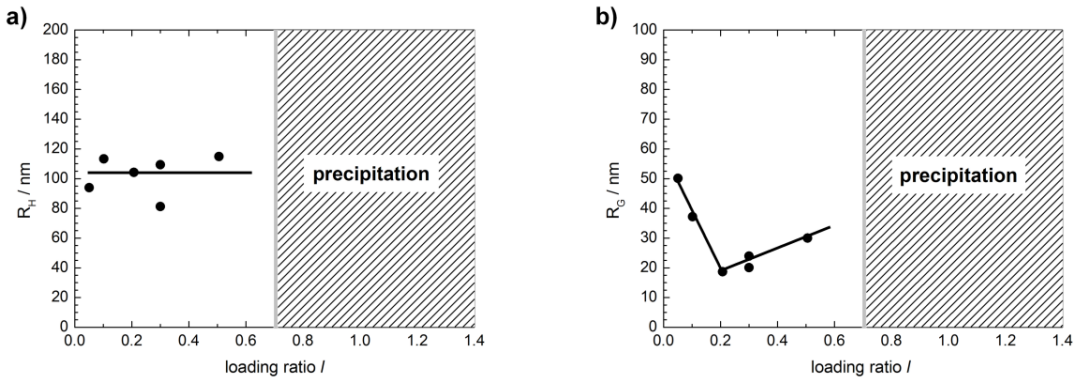

Figure 2. a) R_H and b) R_G of TAPP-G7.5 dendrimer aggregates at pH 11 depending on the loading ratio l , c(G7.5) = $1.5 \cdot 10^{-6}$ mol l^{-1}.

The size of the particles is constant for all $l < 0.7$ showing hydrodynamic radii of $R_H \approx 100$ nm. At $l \geq 0.7$ a very broad size distribution as well as precipitation of the samples is found. R_G/R_H, which is a parameter characteristic of the particles shape, varies between $0.18 \leq R_G/R_H \leq 0.53$ indicating a change in the structure of the aggregates. Hence, the particles are formed by dendrimer molecules becoming interconnected by porphyrins acting as linkers. At high loading ratios, there is a high TAPP concentration so all particles become linked and precipitate. Further, samples with a constant porphyrin concentration are analyzed since the catalytic activity of these samples can be well compared. Figure 3 depicts the behavior of R_H and R_G for TAPP-dendrimer aggregates depending on the loading ratio with a constant porphyrin concentration c(TAPP) = $2.0 \cdot 10^{-5}$ mol l^{-1}.

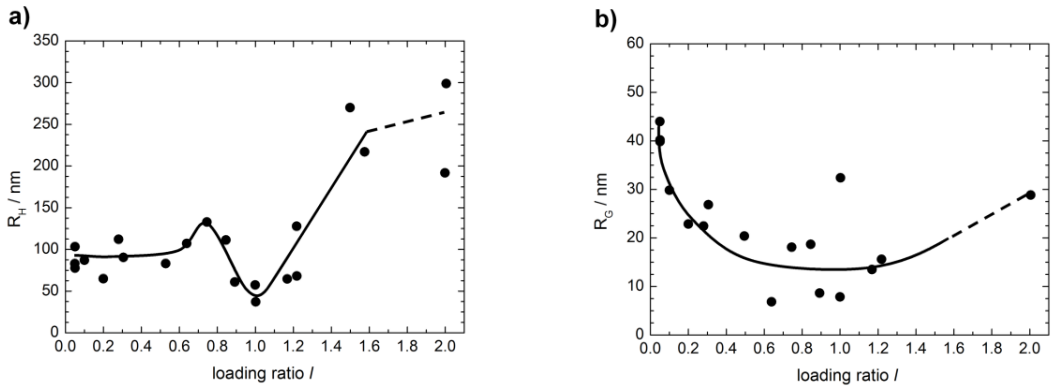

Figure 3. a) R_H and b) R_G of TAPP-G7.5 dendrimer aggregates at pH 11 depending on the loading ratio l with c(TAPP) = $2.0 \cdot 10^{-5}$ mol l^{-1}; scattered line are lines to guide the eye; $l = 0.05$ has a dendrimer concentration of c(G7.5) = $1.5 \cdot 10^{-6}$ mol l^{-1} that is equal to the TAPP-dendrimer aggregate of $l = 0.05$ with constant dendrimer concentration.

Both R_H and R_G show a minimum around $l \approx 1.0$, that is, is at charge compensation. The R_H decreases from $R_H = 300$ nm at $l = 2.0$ to $R_H = 50$ nm at $l = 1.0$, indicating more densely packed aggregates or smaller aggregation numbers. Varying the loading ratio between $0.05 \leq l \leq 0.8$ aggregates with hydrodynamic radii of 80 nm $\leq R_H \leq$ 140 nm are found, with a slight increase in size with increasing loading ratio. TAPP-G7.5 dendrimer aggregates with $l > 1$, where the positively charged TAPP is predominant, show a broader size distribution and larger values for R_H between 200 nm $\leq R_H \leq$ 300 nm. Similar results for the size of the TAPP-dendrimer aggregates are found upon inverting the order of the addition of the building blocks, again proving a thermodynamically controlled process.[67] The overall small values for R_G compared with the values of R_H lead to a noticeable small R_G/R_H ratios of $0.06 < R_G/R_H < 0.5$, which remains small even when one considers the different sizes of samples. The small R_G/R_H ratios

indicate a network-like microgel-structure with a denser core for TAPP-G7.5 dendrimer aggregates.[68–70] A few larger aggregates ($R_H > 1000$ nm) in TAPP-G7.5 dendrimer samples could not be removed with neither filtration nor centrifugation, which again indicates their network-like structure of low density. This may be in analogy to network-like aggregates found previously.[71,72]

The light scattering intensities of TAPP-G7.5 dendrimer aggregates, depicted in Figure 4, further indicate changes in size and soft nanoparticle number. Given the only slightly increasing R_H, the strong decrease in the scattering intensity between $0.05 \leq l \leq 0.6$ must correspond to a decreasing number of particles or a dramatic change in the particles' shape. With increasing l, the larger particle size leads to a higher scattering intensity. By normalizing the scattering intensity with the particle size assuming a simple $I \sim R_H^6$ relationship, a particle number density results. It becomes clear that the number of aggregates for $l > 0.5$ stays constant as the amount of free TAPP monomers in solution, whose presence is concluded from the following ζ-potential measurements, decreases with increasing the number of assemblies. For $l < 0.2$ the number of aggregates increases strongly.

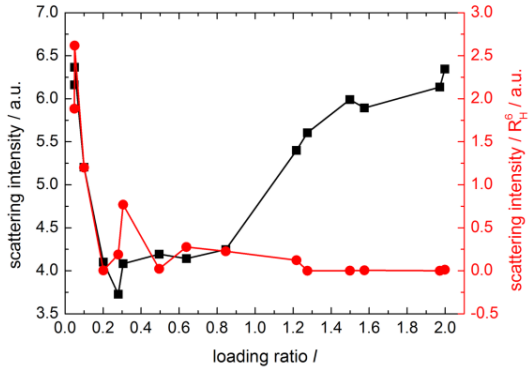

Figure 4. Extrapolated light scattering intensity and the R_H^6-normalized extrapolated light scattering intensity of TAPP-G7.5 dendrimer aggregates in aqueous solution with c(TAPP) = $2 \cdot 10^{-5}$ mol l^{-1} at pH 11.

For a further understanding of interactions and aggregation behavior in the TAPP-dendrimer photocatalyst system, ζ-potential measurements were performed. Figure 5 gives the measured ζ-potential values together with their standard deviations.

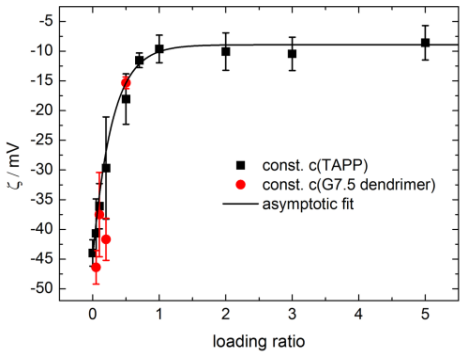

Figure 5. ζ-potential of TAPP-G7.5 dendrimer aggregates in aqueous solution with c(TAPP) = $2 \cdot 10^{-5}$ mol l^{-1} at pH 11 and TAPP-G7.5 dendrimer aggregates with c(G7.5 dendrimer) = $1.5 \cdot 10^{-6}$ mol l^{-1}.

All TAPP-G7.5 dendrimer aggregates show a negative ζ-potential indicating a dominant effect of the negatively charged dendrimer even in presence of an excess of positively charged TAPP. For high loading ratios it approaches ζ = -8.9 mV. The ζ-potential of the dendrimer only in solution is ζ= -44.0 ± 2.2 mV. For a more quantitative comparison of the different loading ratios it is useful to take the particles size into account. Particle charge Q_{eff} and effective surface charge density σ_{eff} are calculated:[73–75]

$$Q_{eff} = 4\pi \cdot \varepsilon_0 \varepsilon_{water} \cdot \zeta \cdot R_H \tag{3}$$

$$\sigma_{eff} = \frac{\varepsilon_0 \cdot \varepsilon_{water} \cdot \zeta}{R_H} \tag{4}$$

where ε_0 is the dielectric constant of water and ε_{water} is the electric permittivity of water.

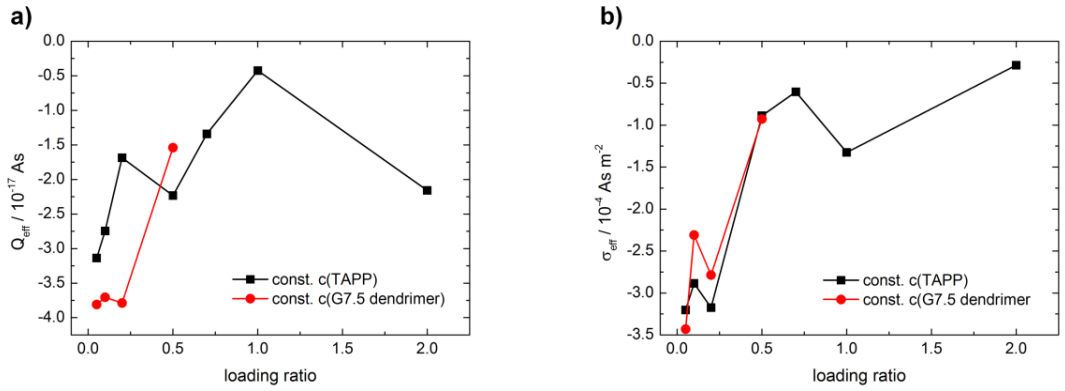

Figure 6: a) particle charge Q_{eff} and b) effective surface charge density σ_{eff} resulting from ζ-potential measurements; black squares: TAPP-G7.5 dendrimer aggregates in aqueous solution with c(TAPP) = $2 \cdot 10^{-5}$ mol l^{-1} at pH 11; and red circles: TAPP-G7.5 aggregates in aqueous solution with c(G7.5 dendrimer) = $1.5 \cdot 10^{-6}$ mol l^{-1} at pH 11.

Q_{eff} and σ_{eff} behave similarly to the ζ-potential, approaching a value around zero but do not become positive, as Figure 6 shows. For $l = 0.05$ the particles exhibit the most negative Q_{eff} and σ_{eff} due to the excess off G7.5 dendrimer. The surface of the aggregates with $l = 2.0$ is larger and the ζ-potential smaller due to an increasing amount of cationic porphyrin attaching, so that the effective surface charge density is quite small but still negative. Hence, the aggregates are still dominated by G7.5 dendrimer and form dendrimer-rich soft nanoparticles even at an excess of TAPP in solution. As a consequence, free TAPP molecules have to be present in solution. For $l > 2.0$, Q_{eff} and σ_{eff} cannot be calculated since an R_H cannot be determined by light scattering measurements due to a very broad size distribution. Samples with a constant dendrimer concentration show an equal behavior, indicating that the the loading ratio is the crucial controlling parameter.

AFM allows to image the TAPP-G7.5 aggregates on an APTES functionalized mica surface for $l = 0.05$ and $l = 1.6$, which is shown in Figure 7.

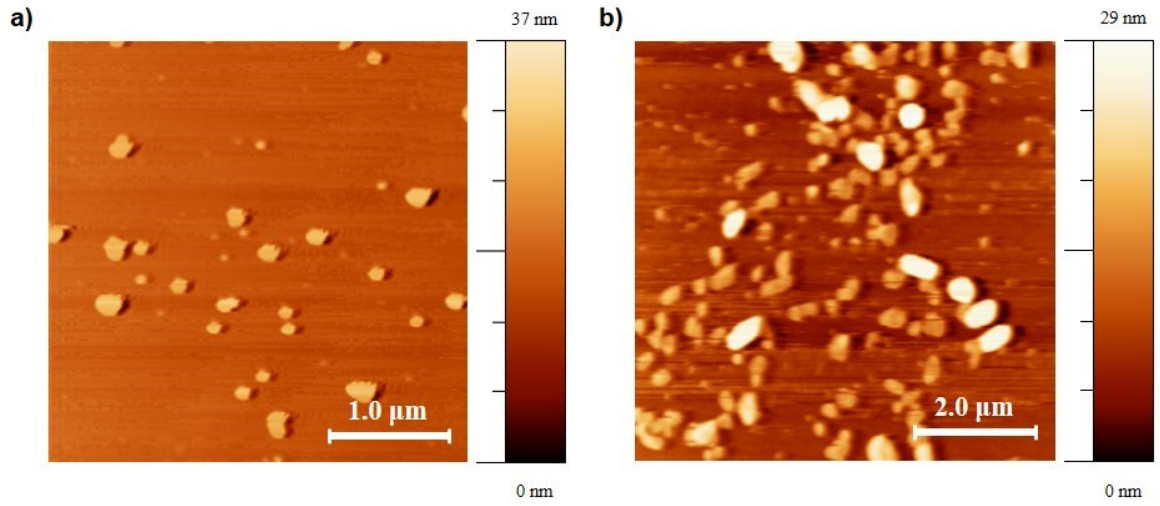

Figure 7. AFM images of spin-coated TAPP-G7.5 dendrimer aggregates at pH 11 (a) $l = 0.05$ and c(TAPP) = $2 \cdot 10^{-5}$ mol l^{-1} on an APTES (0.2 vol%) functionalized mica surface; (b) $l = 1.6$ and c(TAPP) = $1 \cdot 10^{-5}$ mol l^{-1} on an APTES (0.2 vol%) functionalized mica surface.

Figure 7a shows TAPP-G7.5 aggregates with $l = 0.05$ with a slightly elongated shape and a diameter of 150 nm ≤ d ≤ 250 nm. At l = 1.6 (Figure 7b) elongated particles of the same size in addition to particles of 300 nm ≤ d ≤ 500 nm arranged into larger structures of a size up to d = 800 nm. For both loading ratios, the volumes of the AFM structures are significantly smaller than the volume of the TAPP-G7.5 dendrimer particles in solution as found by light scattering since the network-structures substantially shrink upon drying during AFM sample preparation.

Further insight into the shape and structure directly in solution of self-assembled TAPP-G7.5 dendrimer assemblies with $l = 0.05$ is gained by SANS. The result is depicted in Figure 8a. The curve is composed of two different contributions: a first one around q = 0.3 nm^{-1} and a second one at lower q values (0.02 nm^{-1}). The experimental result has been fitted according to structural

models. The signal at q = 0.3 nm^{-1} corresponds to a size of (4.0 ± 0.2) nm and is due to the presence of free dendrimer G7.5 molecules not bound to the nano-assemblies. This is in good agreement with the light scattering results: a fraction of the dendrimer molecules does not aggregate and remains free in the bulk solution. The contribution at lower q values arises from the self-assembled nanoparticle formed by TAPP and G7.5 dendrimer. It corresponds to a cylinder with elliptical cross-section as shown in Figure 8b. The cross section has a semi-major axes a = (65 ± 6) nm and a semi-minor axes b = (22 ± 3) nm. The length of the cylinder can be calculated from the light scattering experiment and it results in l = 180 nm. The obtained value has been used as parameter in the fit of the SANS curve. The obtained value has been used as parameter in the fit of the SANS curve. This anisotropic shape of the assemblies is formed by a network of TAPP molecules and dendrimers, as depicted in Figure 8b.

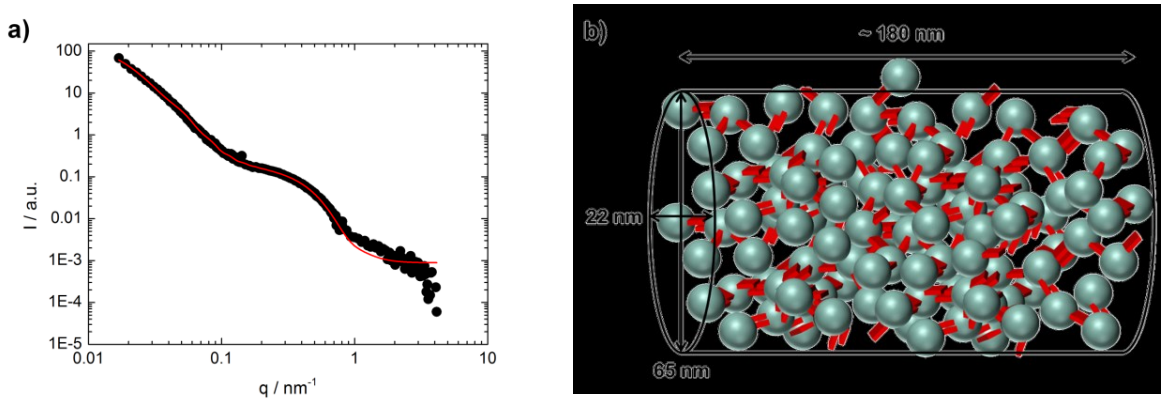

Figure 8. a) SANS curve (black) and cylinder fit (red) for TAPP-G7.5 dendrimer assemblies with l = 0.05, c(TAPP) = 1.7 ·10^{-4} mol l^{-1}; b) Schematic illustration of TAPP-G7.5 dendrimer assemblies with dimensions according to SANS measurement.

Internal Assembly Structure and Optical Properties

After analyzing the size as the overall shape of the TAPP-G.5 aggregates the internal structure and arrangement of the porphyrins were investigated to understand the photocatalytic behavior TAPP-G7.5 by UV/Vis spectroscopy and fluorescence spectroscopy. Here, the loading ratio of samples with TAPP and G7.5 dendrimer is varied between a high excess of TAPP and a high excess of dendrimer TAPP to determine the aggregation behavior, while the porphyrin concentration $c(TAPP) = 2.0 \cdot 10^{-5}$ mol l^{-1} is kept constant. UV/Vis spectra of TAPP-G7.5 dendrimer assemblies at pH 11, which were further used as photocatalysts for dye degradation, are shown in Figure 9.

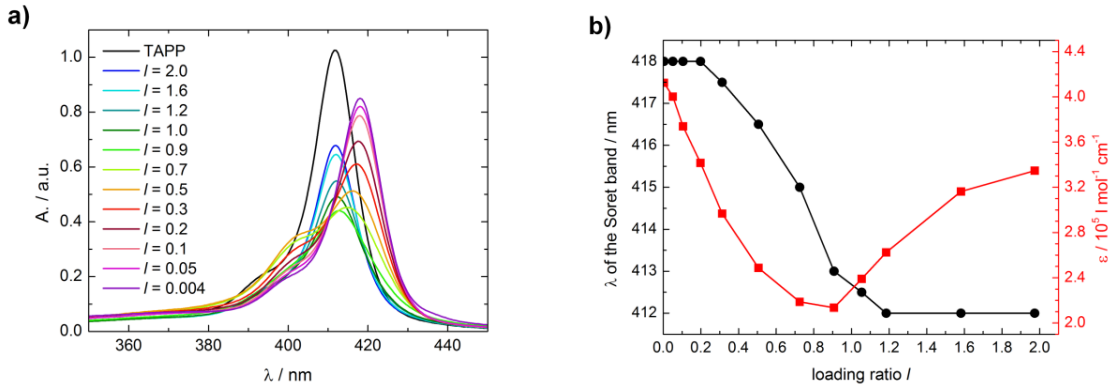

Figure 9. UV/Vis spectra of TAPP-G7.5 dendrimer aggregates depending on the loading ratio *l* with $c(TAPP) = 2.0 \cdot 10^{-5}$ mol l^{-1}: a) Soret bands and b) shift of the Soret band and changes in the extinction coefficient ε of the Soret band at pH 11.

Upon aggregation of porphyrins with G7.5 dendrimer the Soret band of TAPP shifts from λ = 412 nm for pure TAPP in solution to λ = 418 nm at $l \leq 0.2$. Other studies on porphyrins and PAMAM dendrimers also observed a bathochromic shift of the Soret band.[49,56–58,76] The shift

occurs over a wide range of loading ratios ($0.3 \leq l \leq 1.2$) due to interaction of the porphyrin with the dendrimer and the aggregation of TAPP in J-aggregates, which leads to a decrease in the energy difference between the orbitals. A minimum of the extinction coefficient is found at $l = 1.0$ indicating a transition point in the structure of TAPP G7.5 dendrimer. Around $l \approx 1.0$, which is also the loading ratio region in which smaller and denser TAPP-G7.5 soft nanoparticles can be found, the signal broadens and a shoulder at higher energy can be attributed the formation of H-aggregates. Moreover, the extinction coefficient ε is lowest ($\varepsilon = 2.1 \cdot 10^5\ \mathrm{l\ mol^{-1}\ cm^{-1}}$) for the main absorption band since the Soret band splits into two bands, indicating the co-formation of H-aggregates at higher energy and J-aggregates at lower energy. At $l \geq 1.2$, the environment of TAPP in the assemblies is comparable to the monomeric TAPP, that is, it binds monomerically or a substantial amount of monomeric TAPP exists. Therefore, in the networks less linking TAPP molecules are assembled to the dendrimers in comparison to $l < 1$, so that there is less interaction between the building blocks resulting in a few large dendrimer-rich soft nanoparticles. For higher amounts of dendrimer the binding equilibrium is shifted to the complex formation; TAPP molecules assemble to G7.5 dendrimer and form a larger amount of TAPP J-aggregates in the TAPP-dendrimer assemblies. Hence, this correlates with the larger number of TAPP-dendrimer soft nanoparticles. UV/Vis spectra of TMPyP-G6.5 dendrimer, TMPyP-G7.5 dendrimer and TAPP-G6.5 dendrimer aggregates, which are not shown here, show a similar behavior.

The aggregation of the porphyrins can be confirmed by ^{1}H - NMR since aromatic-aromatic interactions can be studied with this technique.[48,77–82] The broadening of the peaks and the decrease in intensity prove the aggregation in presence of G7.5 dendrimer. Due to the stacking of the porphyrin molecules within of the TAPP-G7.5 dendrimer aggregates the mobility of the

protons is reduced, so that the NMR signals broaden and the single peak doublets cannot be distinguished whereas the high concentration of TAPP (c(TAPP) = 4 · 10^4 mol l^{-1}) does not lead to self-association in D_2O as the ^1H – NMR spectrum in Figure 10 shows.[43] The downfield shift of TAPP-dendrimer assemblies at $l = 0.05$ results from the interaction of TAPP and G7.5 dendrimer but band broadening and low signal intensity do not allow a reliable analysis. However, the redshift observed in UV/Vis spectroscopy for $l = 0.05$ in combination with the NMR experiment leads to the conclusion that J-aggregates are formed.

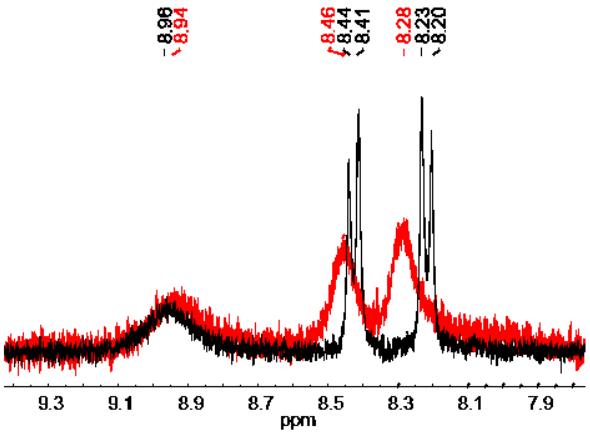

Figure 10. Comparison of porphyrin ^1H-NMR signals: black: TAPP; red: TAPP-dendrimer assemblies with $l = 0.05$; both c(TAPP) = 4 · 10^{-4} mol l^{-1}; the two duplets represent the protons in ortho- and para-position of the benzene ring and the broad downfield signal can be assigned to the eight β-pyrroles' protons of the porphyrin.

As aggregation is confirmed, the optical properties of the assemblies, which are in particular determined by the arrangement of TAPP within the aggregates, are investigated by fluorescence spectroscopy. All TAPP G7.5 dendrimer samples show a higher fluorescence than pure TAPP (Figure 11), which hardly fluoresces.

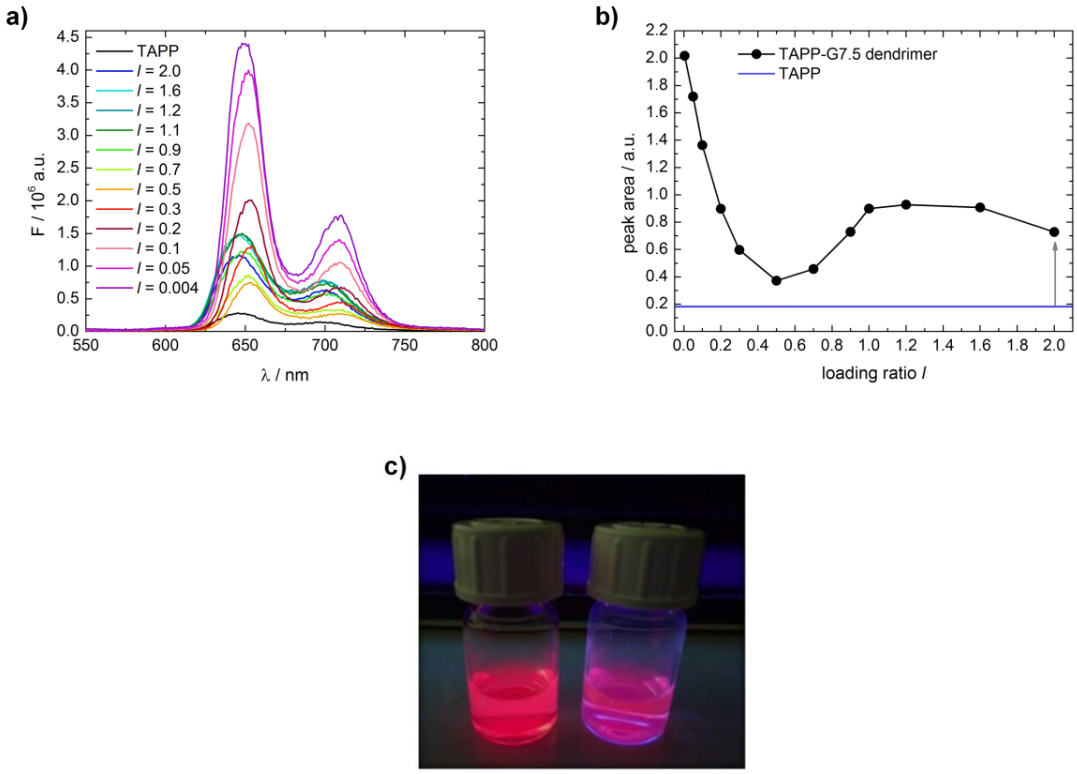

Figure 11. a) Fluorescence spectra of TAPP and TAPP-G7.5 dendrimer aggregates in aqueous solution with c(TAPP) = $2.0 \cdot 10^{-5}$ mol l^{-1} and varying loading ratio; $l \approx 0.004$ correspond to a 1:1 ratio of TAPP and G7.5 dendrimer; b) Area of the fluorescence peak at 574 nm $\leq \lambda \leq$ 800 nm depending on the loading ratio l; the blue line represents the fluorescence of TAPP; c) Left: TAPP-dendrimer assemblies with $l = 0.05$, right: TAPP-dendrimer assemblies with $l = 1.6$, both under exposure to UV-light.

All TAPP-G7.5 dendrimer samples show a higher fluorescence than pure TAPP, which hardly fluoresces. At a high concentration of G7.5 dendrimer the aggregates feature a very strong fluorescence in contrast to other previously investigated porphyrin-dendrimer assemblies where fluorescence is quenched with increasing amount of dendrimer.[49,59] According to literature,

porphyrin J-aggregates exhibit higher fluorescence than H-aggregates.[42,61] The fluorescence increases also due to the restriction of the porphyrins' motion in the assembly and a decrease in the number of the surrounding solvent molecules.[83–85] The large number of smaller TAPP-dendrimer aggregates, which is evident from DLS experiments, lead to a higher amount or larger J-aggregates, which yield the high fluorescence. In contrast to the TMPyP-G4.5 dendrimer aggregates analyzed by Costa et al., no evidence of electron transfer is found.[49] Here, aggregates with $1.0 \leq l \leq 2.0$ yield higher fluorescence than TAPP only due to the formation of network-like supramolecular structures with the dendrimer. In contrast, by adding more G7.5 and reaching a loading ratio of $0.5 \leq l \leq 1.0$ corresponding to the region where a blue shifted shoulder appears in the UV/Vis spectra, the fluorescence intensity decreases and is slightly Stokes-shifted. This is due to an increasing amount of porphyrin H-aggregates. The arrangement of porphyrins into H-aggregates results in a dipolar coupling which quenches the fluorescence to the lower energy level and a subsequent forbidden transition to the ground state occurs due to a rapid internal conversion. Upon splitting, the energy of the singlet excited state is higher than that of the triplet excited state; this leads to a relaxation of the excited electron in the excited singlet by rapid internal conversion or by intersystem crossing to the excited triplet state followed by internal conversion to the ground state, so that the aggregates do not fluoresce.[42,60] In contrast, J-aggregates have a smaller HOMO-LUMO gap leading to a higher quantum yield and a redshift not only in the UV/Vis spectra but also in the fluorescence spectra.[60] The high quantum yield of TAPP-G7.5 at $l = 0.05$ makes these assemblies promising photocatalysts for solar energy conversion, possibly with outstanding properties as light-harvesting systems. The high fluorescence may lead to a higher production of $^1O_2$ which can increase the catalytic activity.

Assembly Architecture and pH-switchability

Based on these results three different types of TAPP-G7.5 dendrimer aggregates occurring at $l = 0.05$, $l = 1.0$ and $l = 1.6$ can be distinguished, as illustrated in Scheme 2.

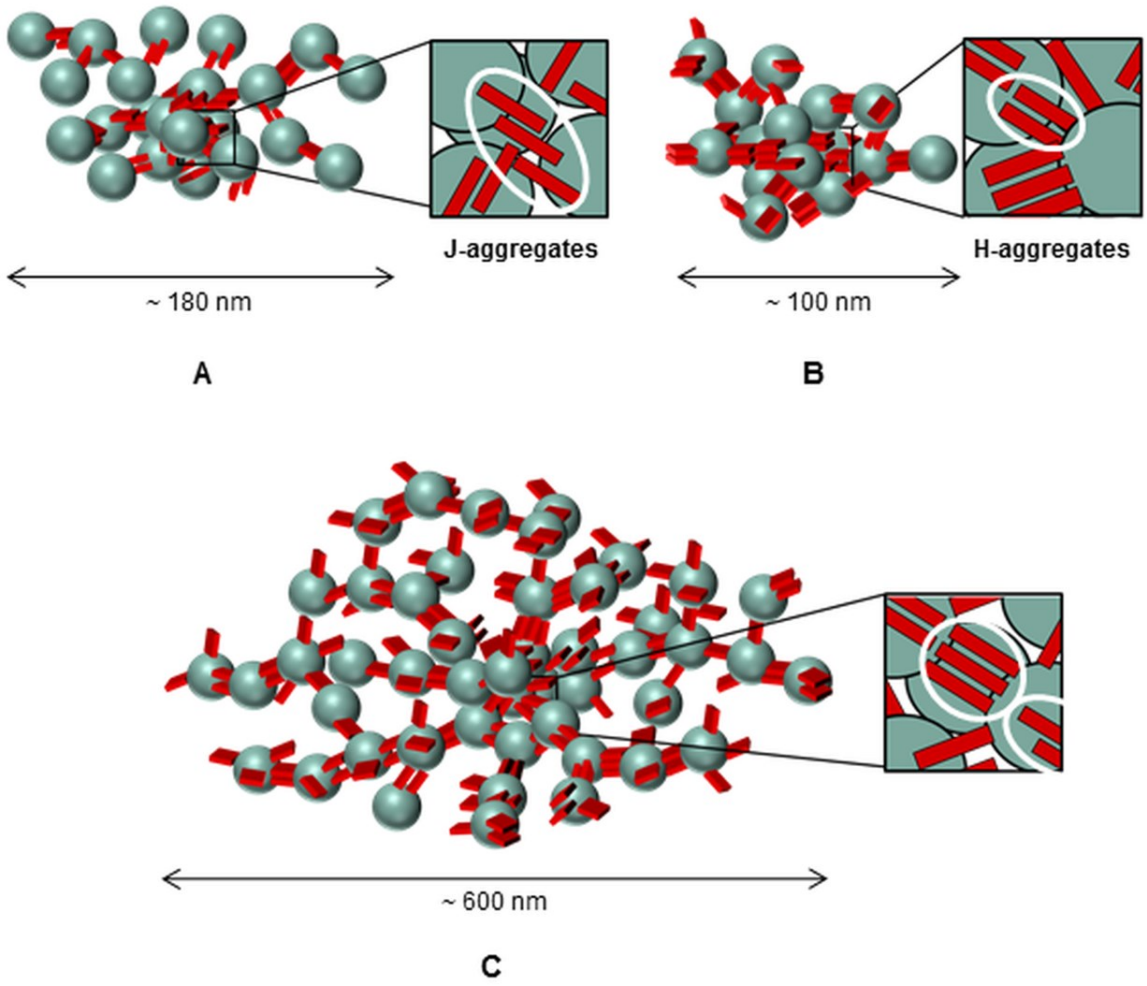

Scheme 2. Schematic illustration of a TAPP-G7.5 dendrimer aggregates with $l = 0.05$, $l = 1.0$ and $l = 1.6$; red: TAPP porphyrin molecules, blue: G7.5 dendrimers.

Aggregates with l = 0.05 (A) have a diameter of 180 nm according to the light scattering measurements. Their effective surface potential is highly negative due to the excess of G7.5. TAPP molecules are arranged in J-aggregates in the self-assembled particles which are responsible for the high fluorescence. Due to charge neutralization, the TAPP-dendrimer aggregates with l = 1.0 are contracted and have a smaller diameter of just 100 nm (B). Moreover, within of the TAPP-G7.5 dendrimer aggregates, the TAPP molecules form H-aggregates stacked in parallel. Although the overall amount of positive and negative charges in the system is equal, the aggregates possess a negative effective surface charge, which is less expressed than the one for l = 0.05. TAPP-dendrimer aggregates with l = 1.6 are assembled into larger supramolecular structures with a diameter of 400 nm to 600 nm in a network-like microgel structure with a dense core (C). The aggregates have small amounts of J-aggregates or less extended J-aggregates. Moreover, there are free TAPP molecules in solution. Although the positively charged TAPP is available in excess, the particles contain slightly more G7.5 molecules than TAPP, which leads to a small negative effective surface charge.

To elucidate whether electrostatic interactions are responsible for the redshift in absorption spectra and consequently for the aggregation of TAPP and dendrimer, the pH for a sample with l = 0.05 has been altered multiple times between pH 2 and pH 11. The results from UV/Vis spectroscopy are depicted in Figure 12.

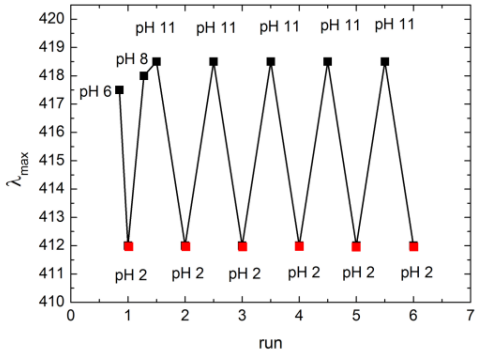

Figure 12. Behavior of TAPP-G7.5 dendrimer aggregates (c(TAPP) = $2.0 \cdot 10^{-5}$ mol l^{-1}, l = 0.05) upon pH-switching; changes of the Soret band with pH changing.

The pH responsive behavior of the aggregates is related to the varying number of charges available on the periphery of G7.5 dendrimer. Although it is expected from titration curves that the carboxylic groups of the dendrimer at pH 7 are still fully negatively charged, a small blue shift compared to pH 11 can be observed, indicating that not all 1024 negative charges are available for binding. At pH 4, all carboxylic groups and amino groups - except the amino groups in the core - are protonated, i.e. the carboxylate groups are no longer negatively charged and cationic TAPP does not assemble with the G7.5 dendrimer and no aggregates are formed. This proves that the electrostatic interactions between porphyrin and PAMAM dendrimer are essential for self-assembly and moreover, that the TAPP-G7.5 dendrimer aggregation is pH switchable. Scheme 3 depicts the formation of TAPP-G7.5 dendrimer aggregates at pH 11. Turning on and off the formation of nanoparticles by a simple pH switch can be useful for applications such as drug delivery.

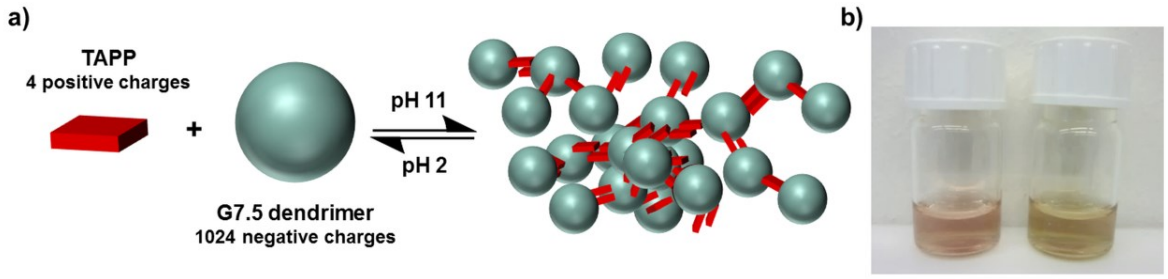

Scheme 3. a) Schematic illustration of TAPP-G7.5 dendrimer assembly formation; b) TAPP solution with c(TAPP) = $2.0 \cdot 10^{-5}$ mol l^{-1} before (left) and after (right) adding G7.5 showing changing color due to a shift of the Soret band.

Photocatalytic Activity

As supramolecular porphyrin-structures, and particularly the TAPP-dendrimer assemblies investigated here, show great potential for applications in the field of solar energy conversion, their photocatalytic activity is tested by using the degradation of the anionic dye methyl orang as a model reaction. Methyl orange is neither decomposed in aqueous solution using dendrimer only nor self-degraded upon visible light irradiation.

The dye degradation follows the reaction scheme:[10]

$$\text{TAPP} + h\nu \longrightarrow {}^1\text{TAPP} \longrightarrow {}^3\text{TAPP}$$

$${}^3\text{TAPP} + {}^3\text{O}_2 \longrightarrow {}^1\text{TAPP} + {}^1\text{O}_2$$

Scheme 4. Irradiated porphyrin generates singlet oxygen that can decompose dyes.

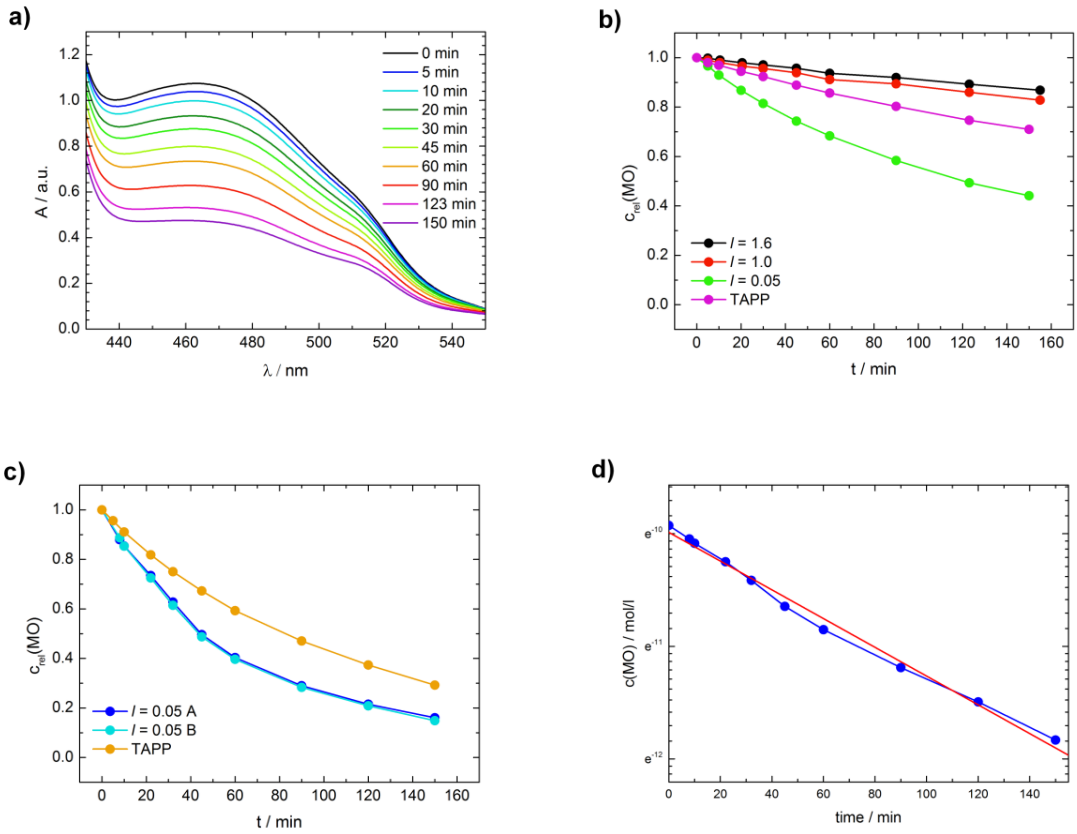

Figure 13. a) UV/Vis spectra of the photocatalytic degradation of methyl orange with TAPP-G7.5 dendrimer assemblies with $l = 0.05$ (c(methyl orange) = $4.0 \cdot 10^{-5}$ mol l^{-1}, c(TAPP) = $5.0 \cdot 10^{-6}$ mol l^{-1}); b) decrease of the methyl orange concentration measured at $\lambda = 464$ nm for TAPP-G7.5 dendrimer aggregates with different loading ratios and TAPP only upon irradiation with visible light; c) degradation of methyl orange with a higher catalyst concentration; for $l = 0.05$ at c(TAPP) = $2.0 \cdot 10^{-5}$ mol l^{-1}; different addition order of the building blocks in sample preparation for the sample a and b; sample A: TAPP, G7.5, methyl orange; sample B: G7.5, methyl orange, TAPP; d) degradation of methyl orange with higher catalyst concentration and $l = 0.05$ (c(TAPP) = $2.0 \cdot 10^{-5}$ mol l^{-1}); blue: data points, red: fit to first order reaction kinetics.

The degradation process of methyl orange occuring upon irradiation with visible light is monitored at λ = 464 nm, as shown in Figure 13 a) for TAPP-G7.5 dendrimer aggregates with $l = 0.05$. Upon dye addition, the Soret band of TAPP shifts from λ = 412 nm to λ = 413 nm, which indicates that the cationic porphyrin-dendrimer aggregate associates with the anionic methyl orange based on electrostatic interaction. Figure 13 b shows the photocatalytic activity of the porphyrin-dendrimer assemblies with different loading ratios. Assemblies with $l = 0.05$ have the highest photocactalytic actvitiy, where aggregates with $l = 1.0$ and $l = 1.6$ show a lower catalytic activity than TAPP only. TAPP-dendrimer aggregates with $l = 0.05$ revealed most expressed photocatalytic activity for methyl orange degradation likely due to larger surface of the higher number of aggregates, which has been revealed by DLS experiments, and due to the arrangement of TAPP molecules into J-aggregates within the self-assembled soft nanoparticles, leading to high fluorescence quantum yields. In contrast, aggregates with $l = 1.0$ and $l = 1.6$ exhibit decreased photocatalytic activity, which is even poorer than for TAPP only. Although both loading ratios feature a higher fluorescence than TAPP only, the porphyrin is stacked in H-aggregates which are decreasing the production of $^1O_2$.[86] The difference in catalytic activity of aggregates with $l = 1.0$ and aggregates with $l = 1.6$ can also be understood by taking the assembly size into account and the short $^1O_2$ life time, it is likely that the formed $^1O_2$ is quenched and cannot reach methyl orange molecules as easily as in pure TAPP within its diffusion length and the resulting catalytic activity is lower. Increasing the concentration of the photocatalyst improves the photocatalytic behavior. TAPP-dendrimer aggregates of higher concentration decompose 85% of methyl orange during 150 min, whereas at lower concentration only 56% dye is degraded. Further, the order of addition of the building blocks including methyl orange does not influence the photocatalytic activity as they do not influence the crucial structure. Therefore,

the interactions of dendrimer and TAPP determine the photocatalytic behavior. The UV/Vis analysis of the methyl orange degradation follows first order kinetics for all loading ratios of TAPP-dendrimer aggregates and TAPP in solution. Exemplarily the scenario for $l = 0.05$, which has a reaction rate of k = 0.78 1/s, is depicted in Figure 13c. Analysis of light scattering data of aggregates with $l = 0.05$ revealed an increasing particle size from $R_H = 120$ nm to $R_H = 250 - 350$ nm once the anionic dye methyl orange is added for photocatalytic measurements. This size increase can be attributed to π-π and electrostatic interactions of the cationic TAPP in the TAPP-dendrimer aggregates and the added anionic methyl orange molecules, causing further interconnection. After dye degradation, the size of the paricles decreased again to $R_H = 155$ nm, which is slightly larger than the size before the methyl orange addition as methyl orange is not decomposed completely. This proves that the TAPP-dendrimer soft nanoparticles stay intact after the catalytic reaction.

CONCLUSION

This study has shown that the method of electrostatic self-assembly can be effectively used to form well-defined functional porphyrin-dendrimer aggregates from cationic porphyrins and anionic dendrimers in solution at basic pH. TAPP-G7.5 dendrimer assemblies were investigated at different loading ratios, resulting in aggregates of different size and shape. All samples show negative ζ-potentials, which become less negative with an excess of porphyrin. Further, TAPP-dendrimer aggregate formation can be switched on and off by changing the pH as the main driving force for the self-assembly are electrostatic interactions, which are absent at lower pH due to protonation of the dendrimer. UV/Vis and NMR spectroscopy revealed the formation of porphyrin aggregates and the stacking of the porphyrins within the particles. Fluorescence

spectroscopy showed that the arrangement of TAPP in the particles changes with the loading ratio: for $l = 1.0$, TAPP is arranged in H-aggregates, whereas for $l = 0.05$, TAPP forms J-aggregates. These J-aggregates show high quantum yield and provide higher incident photon-to-photocurrent generation efficiency due to the stabilization of the excited state.

The photocatalytic behavior of these self-assembled porphyrin-dendrimer aggregates was tested using a photoinduced dye degradation as a model reaction. Upon visible light irradiation, porphyrins generate singlet oxygen which decomposes dyes. TAPP-dendrimer aggregates with $l = 0.05$ exhibit a 1.5-times higher catalytic activity for the degradation of the anionic dye methyl orange than the corresponding porphyrin only due to the arrangement in porphyrin-J-aggregates within the assemblies. The J-aggregates generate a higher amount of singlet oxygen compared to the H-aggregates formed in TAPP-G7.5 aggregates with $l = 1.0$ and $l = 1.6$. These properties make porphyrin-dendrimer aggregates with low loading ratio excellent light harvesting systems for solar energy conversion. Due to the increased fluorescence of the porphyrin in the aggregates together with the possibility to controlled the size and form of the porphyrin-dendrimer aggregates by the loading ratio, such systems can be used in photodynamic therapy and biological imaging.

AUTHOR INFORMATION

Corresponding Author

*E-mail: franziska.groehn@fau.de (F.G.).

Present Addresses

‡Matière et Systèmes Complexes (MSC) Laboratory, UMR CNRS 7057, University Paris Diderot-Paris 7, Sorbonne Paris Cité, Bâtiment Condorcet, 75205 Paris cedex 13, France

Notes

The authors declare no competing financial interest.

ACKNOWLEDGMENT

Financial support of Deutsche Forschungsgemeinschaft (DFG), the Interdisciplinary Center for Molecular Materials (ICMM, University Erlangen-Nürnberg), and Solar Technologies go Hybrid (SolTech) is gratefully acknowledged. We also thank the Cluster of Excellence Engineering of Advanced materials (EAM) of the Deutsche Forschungsgemeinschaft (DFG).

REFERCES

(1) Philp, D.; Stoddart, J. F. Self-Assembly in Natural and Unnatural Systems. *Angew. Chem. Int. Ed.* **1996**, *35*, 1154–1196.

(2) Heiligtag, F. J.; Niederberger, M. The fascinating world of nanoparticle research. *Mater. Today* **2013**, *16*, 262–271.

(3) Thorkelsson, K.; Bai, P.; Xu, T. Self-assembly and applications of anisotropic nanomaterials. *Nano Today* **2015**, *10*, 48–66.

(4) Ariga, K.; Hill, J. P.; Lee, M. V.; Vinu, A.; Charvet, R.; Acharya, S. Challenges and breakthroughs in recent research on self-assembly. *Sci. Technol. Adv. Mater.* **2008**, *9*, 14109.

(5) Dolbecq, A.; Mialane, P.; Keita, B.; Nadjo, L. Polyoxometalate-based materials for efficient solar and visible light harvesting: application to the photocatalytic degradation of azo dyes. *J. Mater. Chem.* **2012**, *22*, 24509.

(6) Xing, X.; Liu, R.; Yu, X.; Zhang, G.; Cao, H.; Yao, J.; Ren, B.; Jiang, Z.; Zhao, H. Self-assembly of CdS quantum dots with polyoxometalate encapsulated gold nanoparticles: enhanced photocatalytic activities. *J. Mater. Chem. A* **2013**, *1*, 1488–1494.

(7) Pearson, A.; Zheng, H.; Kalantar-Zadeh, K.; Bhargava, S. K.; Bansal, V. Decoration of TiO2 nanotubes with metal nanoparticles using polyoxometalate as a UV-switchable reducing agent for enhanced visible and solar light photocatalysis. *Langmuir* **2012**, *28*, 14470–14475.

(8) Biboum, R. N.; Njiki, C. P. Nanseu; Zhang, G.; Kortz, U.; Mialane, P.; Dolbecq, A.; Mbomekalle, I. M.; Nadjo, L.; Keita, B. High nuclearity Ni/Co polyoxometalates and colloidal TiO 2 assemblies as efficient multielectron photocatalysts under visible or sunlight irradiation. *J. Mater. Chem.* **2011**, *21*, 645–650.

(9) Prabhu, V. M.; Venkataraman, S.; Yang, Y. Y.; Hedrick, J. L. Equilibrium Self-Assembly, Structure, and Dynamics of Clusters of Star-Like Micelles. *ACS Macro Lett.* **2015**, *4*, 1128–1133.

(10) Frühbeißer, S.; Gröhn, F. Catalytic activity of macroion-porphyrin nanoassemblies. *J. Am. Chem. Soc.* **2012**, *134*, 14267–14270.

(11) Xiao, Z.; Zhou, Y.; Xin, X.; Zhang, Q.; Zhang, L.; Wang, R.; Sun, D. Iron(III) Porphyrin-Based Porous Material as Photocatalyst for Highly Efficient and Selective Degradation of Congo Red. *Macromol. Chem. Phys.* **2016**, *217*, 599–604.

(12) Jordan, P. C.; Patterson, D. P.; Saboda, K. N.; Edwards, E. J.; Miettinen, H. M.; Basu, G.; Thielges, M. C.; Douglas, T. Self-assembling biomolecular catalysts for hydrogen production. *Nature Chem* **2015**.

(13) Cao, W.; Huang, R.; Qi, W.; Su, R.; He, Z. Self-Assembly of Amphiphilic Janus Particles into Monolayer Capsules for Enhanced Enzyme Catalysis in Organic Media. *ACS Appl. Mater. Interfaces* **2015**, *7*, 465–473.

(14) Faul, C.; Antonietti, M. Ionic Self-Assembly: Facile Synthesis of Supramolecular Materials. *Adv. Mater.* **2003**, *15*, 673–683.

(15) Gröhn, F. Soft matter nanoparticles with various shapes and functionalities can form through electrostatic self-assembly. *Soft Matter* **2010**, *6*, 4296.

(16) Cook, T. R.; Zheng, Y.-R.; Stang, P. J. Metal-organic frameworks and self-assembled supramolecular coordination complexes: comparing and contrasting the design, synthesis, and functionality of metal-organic materials. *Chem. Rev.* **2013**, *113*, 734–777.

(17) Grzelczak, M.; Vermant, J.; Furst, E. M.; Liz-Marzán, L. M. Directed self-assembly of nanoparticles. *ACS nano* **2010**, *4*, 3591–3605.

(18) Lee, S. W.; Gallant, B. M.; Byon, H. R.; Hammond, P. T.; Shao-Horn, Y. Nanostructured carbon-based electrodes: bridging the gap between thin-film lithium-ion batteries and electrochemical capacitors. *Energy Environ. Sci.* **2011**, *4*, 1972.

(19) Düring, J.; Butz, B.; Spiecker, E.; Gröhn, F. Formation of CdS in Supramolecular Dendrimer–Dye Assemblies. *Macromolecules* **2015**, *48*, 8399–8411.

(20) Bates, F. S.; Hillmyer, M. A.; Lodge, T. P.; Bates, C. M.; Delaney, K. T.; Fredrickson, G. H. Multiblock polymers: panacea or Pandora's box? *Science (New York, N.Y.)* **2012**, *336*, 434–440.

(21) Kowalczuk, A.; Trzcinska, R.; Trzebicka, B.; Müller, A. H.; Dworak, A.; Tsvetanov, C. B. Loading of polymer nanocarriers. *Progress in Polymer Science* **2014**, *39*, 43–86.

(22) Walther, A.; Müller, A. H. E. Janus particles: synthesis, self-assembly, physical properties, and applications. *Chemical reviews* **2013**, *113*, 5194–5261.

(23) Robin, M. P.; Osborne, S. A. M.; Pikramenou, Z.; Raymond, J. E.; O'Reilly, R. K. Fluorescent Block Copolymer Micelles That Can Self-Report on Their Assembly and Small Molecule Encapsulation. *Macromolecules* **2016**, *49*, 653–662.

(24) Venkataraman, S.; Lee, A. L.; Maune, H. T.; Hedrick, J. L.; Prabhu, V. M.; Yang, Y. Y. Formation of Disk- and Stacked-Disk-like Self-Assembled Morphologies from Cholesterol-Functionalized Amphiphilic Polycarbonate Diblock Copolymers. *Macromolecules* **2013**, *46*, 4839–4846.

(25) Kamps, A. C.; Cativo, M. H. M.; Chen, X.-J.; Park, S.-J. Self-Assembly of DNA-Coupled Semiconducting Block Copolymers. *Macromolecules* **2014**, *47*, 3720–3726.

(26) Balaban, T. S. Tailoring porphyrins and chlorins for self-assembly in biomimetic artificial antenna systems. *Acc. Chem. Res.* **2005**, *38*, 612–623.

(27) Angaridis, P. A.; Lazarides, T.; Coutsolelos, A. C. Functionalized porphyrin derivatives for solar energy conversion. *Polyhedron* **2014**, *82*, 19–32.

(28) Cabau, L.; Vijay Kumar, C.; Moncho, A.; Clifford, J. N.; López, N.; Palomares, E. A single atom change "switches-on" the solar-to-energy conversion efficiency of Zn-porphyrin based dye sensitized solar cells to 10.5%. *Energy Environ. Sci.* **2015**.

(29) Hasobe, T. Porphyrin-Based Supramolecular Nanoarchitectures for Solar Energy Conversion. *J. Phys. Chem. Lett.* **2013**, *4*, 1771–1780.

(30) Walter, M. G.; Rudine, A. B.; Wamser, C. C. Porphyrins and phthalocyanines in solar photovoltaic cells. *J. Porphyrins Phthalocyanines* **2010**, *14*, 759–792.

(31) Ruthard, C.; Maskos, M.; Kolb, U.; Gröhn, F. Polystyrene sulfonate-porphyrin assemblies: influence of polyelectrolyte and porphyrin structure. *J. Phys. Chem. B* **2011**, *115*, 5716–5729.

(32) Ruthard, C.; Maskos, M.; Yildiz, H.; Gröhn, F. Association of a cylindrical polyelectrolyte brush with tetravalent counterions. *Macromol. Rapid Commun.* **2011**, *32*, 523–527.

(33) Ruthard, C.; Schmidt, M.; Gröhn, F. Porphyrin-polymer networks, worms, and nanorods: pH-triggerable hierarchical self-assembly. *Macromol. Rapid Commun.* **2011**, *32*, 706–711.

(34) Ruthard, C.; Maskos, M.; Kolb, U.; Gröhn, F. Finite-Size Networks from Cylindrical Polyelectrolyte Brushes and Porphyrins. *Macromolecules* **2009**, *42*, 830–840.

(35) Hasobe, T.; Kashiwagi, Y.; Absalom, M. A.; Sly, J.; Hosomizu, K.; Crossley, M. J.; Imahori, H.; Kamat, P. V.; Fukuzumi, S. Supramolecular Photovoltaic Cells Using Porphyrin Dendrimers and Fullerene. *Adv. Mater.* **2004**, *16*, 975–979.

(36) Kim, Y.; Mayer, M. F.; Zimmerman, S. C. A new route to organic nanotubes from porphyrin dendrimers. *Angew. Chem. Int. Ed. Engl.* **2003**, *42*, 1121–1126.

(37) Rajesh, C. S.; Capitosti, G. J.; Cramer, S. J.; Modarelli, D. A. Photoinduced Electron-Transfer within Free Base and Zinc Porphyrin Containing Poly(Amide) Dendrimers. *J. Phys. Chem. B* **2001**, *105*, 10175–10188.

(38) Helmich, F.; Lee, C. C.; Schenning, Albertus P H J; Meijer, E. W. Chiral memory via chiral amplification and selective depolymerization of porphyrin aggregates. *J. Am. Chem. Soc.* **2010**, *132*, 16753–16755.

(39) Pasternack, R. F.; Huber, P. R.; Boyd, P.; Engasser, G.; Francesconi, L.; Gibbs, E.; Fasella, P.; Cerio Venturo, G.; Hinds, L. d. Aggregation of meso-substituted water-soluble porphyrins. *J. Am. Chem. Soc.* **1972**, *94*, 4511–4517.

(40) Sakae, H.; Nagatani, H.; Morita, K.; Imura, H. Spectroelectrochemical characterization of dendrimer-porphyrin associates at polarized liquid|liquid interfaces. *Langmuir* **2014**, *30*, 937–945.

(41) Hollingsworth, J. V.; Richard, A. J.; Vicente, M Graça H; Russo, P. S. Characterization of the self-assembly of meso-tetra(4-sulfonatophenyl)porphyrin (H(2)TPPS(4-)) in aqueous solutions. *Biomacromolecules* **2012**, *13*, 60–72.

(42) Toncelli, C.; Pino-Pinto, J. P.; Sano, N.; Picchioni, F.; Broekhuis, A. A.; Nishide, H.; Moreno-Villoslada, I. Controlling the aggregation of 5,10,15,20-tetrakis-(4-sulfonatophenyl)-porphyrin by the use of polycations derived from polyketones bearing charged aromatic groups. *Dyes Pigments* **2013**, *98*, 51–63.

(43) Kano, K.; Takei, M.; Hashimoto, S. Cationic porphyrins in water: proton NMR and fluorescence studies on dimer and molecular complex formation. *J. Phys. Chem.* **1990**, *94*, 2181–2187.

(44) Mandal, S.; Nayak, S. K.; Mallampalli, S.; Patra, A. Surfactant-assisted porphyrin based hierarchical nano/micro assemblies and their efficient photocatalytic behavior. *ACS Appl. Mater. Interfaces* **2014**, *6*, 130–136.

(45) Kano, K.; Fukuda, K.; Wakami, H.; Nishiyabu, R.; Pasternack, R. F. Factors Influencing Self-Aggregation Tendencies of Cationic Porphyrins in Aqueous Solution. *J. Am. Chem. Soc.* **2000**, *122*, 7494–7502.

(46) Moreno-Bondi, M. C.; Orellana, G.; Turro, N. J.; Tomalia, D. A. Photoinduced electron-transfer reactions to probe the structure of starburst dendrimers. *Macromolecules* **1990**, *23*, 910–912.

(47) Moreno-Villoslada, I.; Fuenzalida, J. P.; Tripailaf, G.; Araya-Hermosilla, R.; Pizarro, Guadalupe del C; Marambio, O. G.; Nishide, H. Comparative study of the self-aggregation of rhodamine 6G in the presence of poly(sodium 4-styrenesulfonate), poly(N-phenylmaleimide-co-acrylic acid), poly(styrene-alt-maleic acid), and poly(sodium acrylate). *J. Phys. Chem. B* **2010**, *114*, 11983–11992.

(48) Moreno-Villoslada, I.; González, F.; Rivera, L.; Hess, S.; Rivas, B. L.; Shibue, T.; Nishide, H. Aromatic-aromatic interaction between 2,3,5-triphenyl-2H-tetrazolium chloride and poly(sodium 4-styrenesulfonate). *J. Phys. Chem. B* **2007**, *111*, 6146–6150.

(49) Paulo, P. M. R.; Costa, S. M. B. Interactions in noncovalent PAMAM/TMPyP systems studied by fluorescence spectroscopy. *J. Phys. Chem. B* **2005**, *109*, 13928–13940.

(50) Costa-Coquelard, C.; Sorgues, S.; Ruhlmann, L. Photocatalysis with polyoxometalates associated to porphyrins under visible light: an application of charge transfer in electrostatic complexes. *J. Phys. Chem. A* **2010**, *114*, 6394–6400.

(51) Zeng, F.; Zimmerman, S. C. Dendrimers in Supramolecular Chemistry: From Molecular Recognition to Self-Assembly. *Chem. Rev.* **1997**, *97*, 1681–1712.

(52) Kano, H.; Kobayashi, T. Time-resolved fluorescence and absorption spectroscopies of porphyrin J-aggregates. *J. Chem. Phys.* **2002**, *116*, 184–195.

(53) Maiti, N. C.; Mazumdar, S.; Periasamy, N. J- and H-Aggregates of Porphyrin-Surfactant Complexes: Time-Resolved Fluorescence and Other Spectroscopic Studies. *J. Phys. Chem. B* **1998**, *102*, 1528–1538.

(54) Barber, D. C.; Freitag-Beeston, R. A.; Whitten, D. G. Atropisomer-specific formation of premicellar porphyrin J-aggregates in aqueous surfactant solutions. *J. Phys. Chem.* **1991**, *95*, 4074–4086.

(55) Maiti, N. C.; Ravikanth, M.; Mazumdar, S.; Periasamy, N. Fluorescence Dynamics of Noncovalently Linked Porphyrin Dimers, and Aggregates. *J. Phys. Chem.* **1995**, *99*, 17192–17197.

(56) Kubát, P.; Lang, K.; Janda, P.; Anzenbacher, P. Interaction of porphyrins with a dendrimer template: self-aggregation controlled by pH. *Langmuir* **2005**, *21*, 9714–9720.

(57) Kubát, P.; Lang, K.; Zelinger, Z. Interaction of porphyrins with PAMAM dendrimers in aqueous solution. *J. Mol. Liq.* **2007**, *131-132*, 200–205.

(58) Paulo, P. M. R.; Gronheid, R.; De Schryver, F. C.; Costa, S. M. B. Porphyrin−Dendrimer Assemblies Studied by Electronic Absorption Spectra and Time-Resolved Fluorescence. *Macromolecules* **2003**, *36*, 9135–9144.

(59) Castriciano, M. A.; Romeo, A.; Angelini, N.; Micali, N.; Guccione, S.; Scolaro, L. M. Spectroscopic investigation and molecular modeling on porphyrin/PAMAM supramolecular adduct. *Photochem. Photobiol.* **2011**, *87*, 292–301.

(60) Ou, Z.-m.; Yao, H.; Kimura, K. Preparation and optical properties of organic nanoparticles of porphyrin without self-aggregation. *J. Photochem. Photobiol. A* **2007**, *189*, 7–14.

(61) Li, X.; Zhang, L.; Mu, J. Formation of new types of porphyrin H- and J-aggregates. *Colloids Surf., A* **2007**, *311*, 187–190.

(62) Provencher, S. W. CONTIN: A general purpose constrained regularization program for inverting noisy linear algebraic and integral equations. *Comput. Phys. Commun.* **1982**, *27*, 229–242.

(63) Horcas, I.; Fernández, R.; Gómez-Rodríguez, J. M.; Colchero, J.; Gómez-Herrero, J.; Baro, A. M. WSXM: a software for scanning probe microscopy and a tool for nanotechnology. *Rev. Sci. Instrum.* **2007**, *78*, 13705.

(64) Guinier, A.; Fournet, G. *Small angle scattering of X-rays*; J. Wiley & Sons: New York, 1955.

(65) Glatter, O.; Kratky, O. *Small angle x-ray scattering*; Academic Press: London, New York, 1982.

(66) Svergun, D. I.; Feĭgin, L. A.; Taylor, G. W. *Structure analysis by small-angle x-ray and neutron scattering*; Plenum Press: New York, 1987.

(67) Willerich, I.; Gröhn, F. Molecular structure encodes nanoscale assemblies: understanding driving forces in electrostatic self-assembly. *J. Am. Chem. Soc.* **2011**, *133*, 20341–20356.

(68) Burchard, W. *Static and dynamic light scattering from branched polymers and biopolymers*; Advances in polymer science 48; Springer-Verlag: Berlin, 1983.

(69) Hellweg, T. Responsive core-shell microgels. *J. Polym. Sci. Part B: Polym. Phys.* **2013**, *51*, 1073–1083.

(70) Wellert, S.; Hertle, Y.; Richter, M.; Medebach, M.; Magerl, D.; Wang, W.; Demé, B.; Radulescu, A.; Müller-Buschbaum, P.; Hellweg, T.; Klitzing, R. von. Inner structure of adsorbed ionic microgel particles. *Langmuir* **2014**, *30*, 7168–7176.

(71) Blochowicz, T. Polymer-induced transient networks in water-in-oil microemulsions studied by small-angle x-ray and dynamic light scattering. *Phys. Rev. E* **2007**, *76*, 41505.

(72) Yildiz, Ü. H.; Koynov, K.; Gröhn, F. Fluorescent Nanoparticles through Self-Assembly of Linear Ionenes and Pyrenetetrasulfonate. *Macromol. Chem. Phys.* **2009**, *210*, 1678–1690.

(73) Moldenhauer, D.; Gröhn, F. Nanoassemblies with light-responsive size and density from linear flexible polyelectrolytes. *J. Polym. Sci. B Polym. Phys.* **2013**, *51*, 802–816.

(74) Hiemenz, P. C.; Rajagopalan, R. *Principles of colloid and surface chemistry*, 3rd ed.; Marcel Dekker: New York, 1997.

(75) Evans, D. F.; Wennerström, H. *The colloidal domain: Where physics, chemistry, biology, and technology meet*, 2nd ed.; Advances in interfacial engineering series; Wiley-VCH: New York, 1999.

(76) Paulo, P. M. R.; Costa, S. M. B. Non-covalent dendrimer-porphyrin interactions: the intermediacy of H-aggregates?Dedicated to the memory of Nobel Laureate, Lord George Porter FRSC FRS OM. *Photochem. Photobiol. Sci.* **2003**, *2*, 597.

(77) Maiti, N. C.; Mazumdar, S.; Periasamy, N. J- and H-Aggregates of Porphyrin−Surfactant Complexes: Time-Resolved Fluorescence and Other Spectroscopic Studies. *J. Phys. Chem. B* **1998**, *102*, 1528–1538.

(78) Kano, K.; Minamizono, H.; Kitae, T.; Negi, S. Self-Aggregation of Cationic Porphyrins in Water. Can π−π Stacking Interaction Overcome Electrostatic Repulsive Force? *J. Phys. Chem. A* **1997**, *101*, 6118–6124.

(79) Gómez-Tardajos, M.; Pino-Pinto, J. P.; Díaz-Soto, C.; Flores, M. E.; Gallardo, A.; Elvira, C.; Reinecke, H.; Nishide, H.; Moreno-Villoslada, I. Confinement of 5,10,15,20-tetrakis-(4-sulfonatophenyl)-porphyrin in novel poly(vinylpyrrolidone)s modified with aromatic amines. *Dyes Pigments* **2013**, *99*, 759–770.

(80) Kabiri, M.; Bushnak, I.; McDermot, M. T.; Unsworth, L. D. Toward a Mechanistic Understanding of Ionic Self-Complementary Peptide Self-Assembly: Role of Water Molecules and Ions. *Biomacromolecules* **2013**, *14*, 3943–3950.

(81) Flores, M. E.; Sano, N.; Araya-Hermosilla, R.; Shibue, T.; Olea, A. F.; Nishide, H.; Moreno-Villoslada, I. Self-association of 5,10,15,20-tetrakis-(4-sulfonatophenyl)-porphyrin tuned by poly(decylviologen) and sulfobutylether-β-cyclodextrin. *Dyes Pigments* **2015**, *112*, 262–273.

(82) Moreno-Villoslada, I.; Murakami, T.; Nishide, H. Comment on \"J- and H-aggregates of 5,10,15,20-tetrakis-(4-sulfonatophenyl)-porphyrin and interconversion in PEG-b-P4VP micelles\". *Biomacromolecules* **2009**, *10*, 3341-2; discussion 3343-4.

(83) Liu, X.; Zeng, Y.; Liu, J.; Li, P.; Zhang, D.; Zhang, X.; Yu, T.; Chen, J.; Yang, G.; Li, Y. Highly Emissive Nanoparticles Based on AIE-Active Molecule and PAMAM Dendritic "Molecular Glue". *Langmuir* **2015**, *31*, 4386–4393.

(84) Rösch, U.; Yao, S.; Wortmann, R.; Würthner, F. Fluorescent H-Aggregates of Merocyanine Dyes. *Angew. Chem.* **2006**, *118*, 7184–7188.

(85) Baglan, M.; Ozturk, S.; Gür, B.; Meral, K.; Bozkaya, U.; Bozdemir, O. A.; Atılgan, S. Novel phenomena for aggregation induced emission enhancement. *RSC Adv.* **2013**, *3*, 15866.

(86) Tanielian, C.; Wolff, C.; Esch, M. Singlet Oxygen Production in Water. *J. Phys. Chem.* **1996**, *100*, 6555–6560.

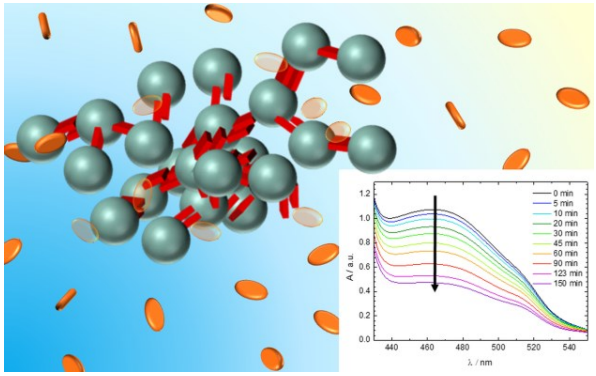

Chapter 6 Ongoing Collaborations

The structural characterization techniques used in this work have been applied successfully to different nanosystems. Ongoing studies not yet published are reported in this chapter.

6.1 Supramolecular Structures from a Switchable Zwitterion-Based Amphiphile

One of the side projects concerned the characterization of a new low molecular weight amphiphile with an ionic head and aromatic tail group. Recently, the group of Prof. C. Schmuck has developed a small zwitterion that is self-complementary and forms highly stable dimers in polar solvents. This molecule has been combined with a nonpolar tail group to form pH-switchable zwitterionic amphiphiles. In this system, the head group will mainly interact with neighbouring molecules via electrostatic interactions, while the tails can interact by a combination of mostly π-π and hydrophobic interactions. To gain insights into the assemblies size and shape directly in solution SANS was performed in parallel to light scattering measurements done by Anne Kutz. This technique accesses informations on both the overall assembly shape and its internal structures. The charge of the head is strongly pH dependent: for pH < 5 the overall charge of the head is positive, at pH $= 7$ the head charge is neutral overall but zwitterionic, finally at pH > 8 the overall charge of the head is negative. The effects of

the different protonation states on the nano-assembly shape have been investigated comparing samples at pH = 2.5, pH = 6.5 and pH = 9 in D2O. Results are reported in Figure 6.1. The data have been analysed with the Guinier approximation for elongated objects (Figure 6.2).

Figure 6.1: *SANS for the amphiphile at pH 2.5 (black), pH 6.5 (red) and pH 9 (green).*

Figure 6.2: *Guinier approximation for elongated objects for the amphiphile at pH 6.5 in D2O.*

Further, for all protonation states the SANS data were fitted according to the structural model for cylinders. All the fits show that the cylinder internal moieties are not hollow as in the case of vesicular aggregates, which is in agreement with AFM results. At pH = 9 the cross-section radius is $R = (20 \pm 2)$ nm and the length is $L = (270 \pm 10)$ nm, while in zwitterionic state at pH = 6.5 the radius is $R = (26 \pm 2)$ nm and length $L = (300 \pm 10)$ nm. For the cationic amphiphile at pH = 2.5 the radius is $R = (32 \pm 2)$ nm and the length is $L = (580 \pm 30)$ nm. Evidently, the nanoparticles become larger as the pH decreases: the cross-section radius increases from 20 nm at pH = 9 to 32 nm at pH = 2.5, while the length almost doubles. Due to the dependence of the radius on the pH, we conclude that the radial construction must be linked to the polarity or rather the interaction of the polar head group with the solvent. The largest assemblies were found under acidic conditions leading to the conclusion that the amphiphile is less polar at this protonation state. This causes the aggregation in radial and even in lateral direction to increase. In addition, a Guinier approach was used to study how the nanoassemblies are structured internally. For the assemblies in D2O at pH = 6.5, the Guinier analysis at smaller size scales showed the presence of cylinders with a cross-section radius of gyration of $R_{gc} = (8 \pm 2)$ nm. This suggests that the large fibres are composed of cylindrical subunits with smaller diameter. Since the diameter of the overall cylinders is 52 nm, three smaller cylinders at least are

required to form the larger cylinder. Given that the overall structure is cylindrical a trimeric packing of the smallest aggregates fits best (Figure 6.3). For the other protonation states we also studied the aggregates using the Guinier approach. In both cases, the nanoparticles are again composed of smaller cylinders with a cross-section radius of gyration of $R_{gc} = (9 \pm 1)$ nm. This indicates that the cylindrical aggregates at basic and acidic pH are composed of comparable cylindrical building blocks.

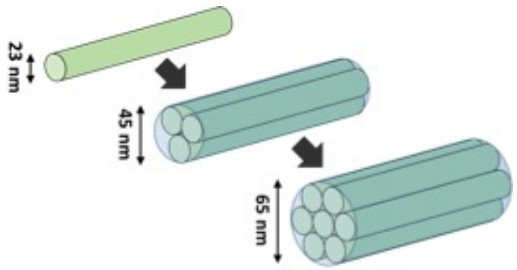

Figure 6.3: *Structural model based on SANS results to describe the assembly formation for pH 6.5 in D2O.*

Due to the dependence between size and pH we assume a lateral growth of the assemblies resulting from the hydrophobic effect or π-π interaction. To verify this hypothesis the effect of the solvent on the aggregates was studied. If the assumption is correct, we would expect a reduction of the lateral length and more or less a constant radial size with reducing solvent polarity. The effects of the solvent were analyzed using D2O, CD3OD and DMSO d6. The experimental results are reported in Figure 6.4. The scattering curves for the samples in D2O and CD3OD are almost identical, while the one in DMSO d6 differs. The intensity of the latter is significantly lower than the others. This can be due to a different contrast between the solvent and the nano-aggregates or a difference in dimensions. The molecules in D2O at pH 6.5 aggregate into cylindrical nanoparticles with $R_{gc} = (24 \pm 1)$ nm and $L_{Gui} = (300 \pm 10)$ nm, while in CD3OD formation of cylinders with $R_{gc} = (24 \pm 1)$ nm and length $L_{Gui} = (240 \pm 20)$ nm is observed.

Hence, the shape and radius of the fibres remain unchanged in the different solvents, but their length is significantly larger in D2O. This is in good agreement with the aggregation model suggested above. While the molecular dimensions of the building unit are the same in the different solvents, the hydrophobic effect is much more expressed in the aqueous solution. Thus, the larger length in D2O is consistent with the hypothesis that the tail hydrophobicity determines the cylinder length.

Figure 6.4: *SANS curves for the amphiphile assembly at pH 6.5 in D2O (black), DMSO-d6 (green) and CD3OD (red).*

6.2 Polyoxometalate-Dendrimer Assemblies for Catalysis

Another collaboration involved nanomaterials for photocatalysis. These materials are of great importance for the development of novel concepts for solar energy conversion. These systems are inspired by natural ones where solar energy is exploited in photosynthesis through catalysis by small species inside a larger non-covalent assembly. Hydrogen-bridged associates are often unstable in polar solutions or require the complex synthesis of specific architectures and binding motifs. Hence, the concept of electrostatic self-assembly to interconnect macroions and oppositely charged catalytically active species into supramolecular nanostructures is highly promising. The possibility to increase the catalytic activity of a representative Keggin-type tungsten oxide cluster in aqueous solution and modify its selectivity through self-assembly with a macroion has been proven. Moreover, the type of the underlying assembly represents a novel type of electrostatic self-assembly to form stable nanoscale structures in solution. This

system was mainly investigated by Anne Kutz; my contribution has been the structural characterisation of photocatalytically active self-assembled nanostructure in aqueous solution consisting of ionic polyoxometalate clusters and oppositely charged ionic dendrimers. SANS and light scattering measurements have revealed that finite nanoparticles form when POM is combined with dendrimers due to ionic interaction (Figure 6.5). The structure of the assemblies is a worm-like Gaussian coil with diameter of 6.2 nm. This thickness is consistent with the generation 4 dendrimers of 4.5 nm diameter with POM clusters of about 1.2 nm size attached and slightly penetrating the dendrimer on both sides. In addition, POM clusters must of course be located in-between dendrimers serving as ionic connectors.

Figure 6.5: *Static light scattering and SANS data of POM-dendrimer assemblies with l = 0.7 and c(dendrimer) = 0.5 g L-1; symbols: data points, black line at high q: flexible cylinder.*

Chapter 7 List of Publications

1. **Elucidating electrostatic self-assembly: molecular parameters as key to thermodynamics and nanoparticle shape**
   G. Mariani, D. Moldenhauer, R. Schweins, F. Gröhn, *J. Am. Chem. Sci.*, **2016**, *138*, 1280-1293;

2. **Structure tuning of electrostatically self-assembled nanoparticles through pH**
   G. Mariani, R. Schweins, F. Gröhn, *J. Phys. Chem. B*, **2016**, *120*, 1380-1389;

3. **Ionic dye-surfactant nanoassemblies: interplay of electrostatics, hydrophobic effect, and π-π stacking**
   A. Kutz, G. Mariani, F. Gröhn, *Colloid. Polym. Sci.*, **2016**, *294*, 591-606;

4. **Porphyrin diacid-polyelectrolyte assemblies: effective photocatalysts in solution**
   S. Frühbeißer, G. Mariani, F. Gröhn, *Polymers*, **2016**, *80*, 180;

5. **Electrostatic self-assembly of dendrimer macroions and multivalent dye counterions: the role of solution ionic strength**
   G. Mariani, R. Schweins, F. Gröhn, *Macromolecules, accepted*;

6. **Inducing hetero-aggregation of different azo dyes through electrostatic self-assembly**
   G. Mariani, A. Kutz, R. Schweins, F. Gröhn, *Submitted*;

7. **Functional supramolecular porphyrin-dendrimer assemblies for light harvesting and photocatalysis**
   A. Krieger, J. P. Fuenzalida Werner, G. Mariani, F. Gröhn, *Submitted*;

8. **Structure tuning of electrostatically self-assembled nanoparticles through pH: the role of charge ratio**
   G. Mariani, R. Schweins, F. Gröhn, *Submitted*;

9. **Photoresponsive nanoparticle shape: from micrometer-long nanocylinders to compact particles in electrostatic self-assembly**
   G. Mariani, D. Moldenhauer, R. Schweins, F. Gröhn, *In final preparation*;

10. **Structure-property relationship of a stimulus responsive aromatic amphiphile in colloidal solution**
    E. Zellermann, A. Kutz, G. Mariani, F. Gröhn, C. Schmuck, *In final preparation*;

11. **Self-assembled polyoxometalate-dendrimer structures for photocatalysis**
    A. Kutz, G. Mariani, R. Schweins, C. Streb, F. Gröhn, *In final preparation*;

Chapter 8 Conference Contributions

- *International conference on neutron scattering*, Edinburgh, July 2013. Poster: **Electrostatic self-assembly investigated by time-resolved SANS**.
- *Italian society for neutron scattering annual meeting* , Milan, September 2013. Talk: **Supramolecular dendrimer-dye self-assembly**.
- *International soft Matter conference 2013*, Rome, September 2013. Poster: **Electrostatic self-assembly investigated by time-resolved SANS**.
- *Institut Laue-Langevin annual science outing*, Villard de Lans, October 2013. Talk: **Supramolecular dendrimer-dye self-assembly**.
- *Macromolecular colloquium*, Freiburg, February 2015. Poster: **Encoding the shape of nano-assemblies through molecular building blocks: thermodynamics as key to a fundamental understanding of structure directing effects**.
- *Gordon research conference on neutron scattering*, Hong Kong, June 2015. Poster: **Unveiling the electrostatic self-assembly: thermodynamics as a key to fundamental understanding of structure-directing effects**.
- *Neutron scattering on nano-structured soft matter: synthetic- and bio-Materials*, Tutzing, October 2015. Talk: **Unveiling electrostatic self-assembly: thermodynamics as a key to fundamental understanding of structure-directing effects**.

Chapter 9 Curriculum Vitae

Personal data:

Giacomo Mariani

Birth Date and Place: 13/01/1986, Senigallia, Italy

Citizenship: Italian

Higher Education:

2011-2016	**PhD Studies in Chemistry** Interdisciplinary Center for Molecular Materials Department Chemistry and Pharmacy Friedrich-Alexander-Universität Erlangen-Nürnberg Supervisor: Prof. Dr. Franziska Gröhn Large Scale Structure Group Institut Laue-Langevin, Grenoble, France Supervisor: Dr. Ralf Schweins
2008-2011	MASTER in Physics of Matter University of Parma, Italy. Final mark: 110/110
2005-2008	BACHELOR in Physics University of Bologna, Italy. Final mark: 110/110

Education:

2001-2005	Maturità scientifica Liceo Scientifico E. Medi, Senigallia, Italy. Final mark: 100/100

Awards:

Jun. 2012	Best student lecturer, Bombannes Summer School
Apr. 2013	Best student lecturer, Annual ILL Student Clip Session

Bibliography

[1] G. Whitesides, J. Mathias, and C. Seto, "Molecular self-assembly and nanochemistry: a chemical strategy for the synthesis of nanostructures," *Science*, vol. 254, no. 5036, pp. 1312–1319, 1991.

[2] C. J. Pedersen, "Cyclic polyethers and their complexes with metal salts," *Journal of the American Chemical Society*, vol. 89, no. 26, pp. 7017–7036, 1967.

[3] J.-M. Lehn, "Supramolecular chemistry-scope and perspectives molecules, supermolecules, and molecular devices (nobel lecture)," *Angewandte Chemie International Edition in English*, vol. 27, no. 1, pp. 89–112, 1988.

[4] B. Dietrich, J. M. Lehn, and J. P. Sauvage, "Les cryptates," *Tetrahedron Letters*, vol. 10, no. 34, pp. 2889–2892, 1969.

[5] J. M. Lehn, "Cryptates: the chemistry of macropolycyclic inclusion complexes," *Accounts of Chemical Research*, vol. 11, no. 2, pp. 49–57, 1978.

[6] D. J. Cram and J. M. Cram, "Design of complexes between synthetic hosts and organic guests," *Accounts of Chemical Research*, vol. 11, no. 1, pp. 8–14, 1978.

[7] Y. Xia, "Editorial: Are we entering the nano era?," *Angewandte Chemie International Edition*, vol. 53, no. 46, pp. 12268–12271, 2014.

[8] B. Alberts, D. Bray, J. Lewis, M. Raff, K. Roberts, and J. D. Watson, *Molecular Biology of the Cell*. Garland, New York, 2002.

[9] G. M. Whitesides, "Self-assembling materials," *Sci. Am.*, vol. 273, no. 3, pp. 146–149, 1995.

[10] K. Kataoka, A. Harada, and Y. Nagasaki, "Block copolymer micelles for drug delivery: design, characterization and biological significance," *Advanced Drug Delivery Reviews*, vol. 47, no. 1, pp. 113 – 131, 2001.

[11] A. Rösler, G. W. Vandermeulen, and H.-A. Klok, "Advanced drug delivery devices via self-assembly of amphiphilic block copolymers," *Advanced Drug Delivery Reviews*, vol. 64, pp. 270 – 279, 2012.

[12] S. J. Maginn, "Crystal engineering: the design of organic solids," *Journal of Applied Crystal-*

lography, vol. 24, no. 3, p. 265, 1991.

[13] F. A. Evans and H. Wennerström, *The colloidal domain: where Physics, Chemistry, Biology and Technology meet*. VCH Publishers, New York, 1994.

[14] R. P. Sijbesma, F. H. Beijer, L. Brunsveld, B. J. B. Folmer, J. H. K. K. Hirschberg, R. F. M. Lange, J. K. L. Lowe, and E. W. Meijer, "Reversible polymers formed from self-complementary monomers using quadruple hydrogen bonding," *Science*, vol. 278, no. 5343, pp. 1601–1604, 1997.

[15] A. Kumar, N. L. Abbott, H. A. Biebuyck, E. Kim, and G. M. Whitesides, "Patterned self-assembled monolayers and meso-scale phenomena," *Accounts of Chemical Research*, vol. 28, no. 5, pp. 219–226, 1995.

[16] G. M. Whitesides and B. Grzybowski, "Self-assembly at all scales," *Science*, vol. 295, no. 5564, pp. 2418–2421, 2002.

[17] A. R. Monahan and D. F. Blossey, "Aggregation of arylazonaphthols. i. dimerization of bonadur red in aqueous and methanolic systems," *The Journal of Physical Chemistry*, vol. 74, no. 23, pp. 4014–4021, 1970.

[18] T. Zemb, M. Dubois, B. Demé, and T. Gulik-Krzywicki, "Self-assembly of flat nanodiscs in salt-free catanionic surfactant solutions," *Science*, vol. 283, no. 5403, pp. 816–819, 1999.

[19] F. Vögtle, *Supramolecular Chemistry*. Wiley, 1991.

[20] J. M. Lehn, *Supramolecular Chemistry; Concepts and Perspectives*. VHC, Weinheim, 1995.

[21] J. L. A. J. W. Steed, *Supramolecular Chemistry*. Wiley, Chichester, 2000.

[22] M. Gellert, M. N. Lipsett, and D. R. Davies, "Helix formation by guanylic acid," *Proceedings of the National Academy of Sciences of the United States of America*, vol. 48, pp. 2013–2018, 12 1962.

[23] J. T. Davis and G. P. Spada, "Supramolecular architectures generated by self-assembly of guanosine derivatives," *Chem. Soc. Rev.*, vol. 36, pp. 296–313, 2007.

[24] J. Chen and N. C. Seeman, "Synthesis from dna of a molecule with the connectivity of a cube," *Nature*, vol. 350, pp. 631–633, 04 1991.

[25] E. Winfree, F. Liu, L. A. Wenzler, and N. C. Seeman, "Design and self-assembly of two-dimensional dna crystals," *Nature*, vol. 394, no. 6693, pp. 539–544, 1998.

[26] H. Yan, S. H. Park, G. Finkelstein, J. H. Reif, and T. H. LaBean, "Dna-templated self-assembly of protein arrays and highly conductive nanowires," *Science*, vol. 301, no. 5641, pp. 1882–1884, 2003.

[27] P. W. K. Rothemund, A. Ekani-Nkodo, N. Papadakis, A. Kumar, D. K. Fygenson, and E. Winfree, "Design and characterization of programmable dna nanotubes," *Journal of the*

American Chemical Society, vol. 126, no. 50, pp. 16344–16352, 2004.

[28] P. Yin, R. F. Hariadi, S. Sahu, H. M. T. Choi, S. H. Park, T. H. LaBean, and J. H. Reif, "Programming dna tube circumferences," *Science*, vol. 321, no. 5890, pp. 824–826, 2008.

[29] R. P. Goodman, I. A. T. Schaap, C. F. Tardin, C. M. Erben, R. M. Berry, C. F. Schmidt, and A. J. Turberfield, "Rapid chiral assembly of rigid dna building blocks for molecular nanofabrication," *Science*, vol. 310, no. 5754, pp. 1661–1665, 2005.

[30] J. Chen and N. C. Seeman, "Synthesis from dna of a molecule with the connectivity of a cube," *Nature*, vol. 350, no. 6319, pp. 631–633, 1991.

[31] W. M. Shih, J. D. Quispe, and G. F. Joyce, "A 1.7-kilobase single-stranded dna that folds into a nanoscale octahedron," *Nature*, vol. 427, no. 6975, pp. 618–621, 2004.

[32] S. M. Douglas, H. Dietz, T. Liedl, B. Hogberg, F. Graf, and W. M. Shih, "Self-assembly of dna into nanoscale three-dimensional shapes," *Nature*, vol. 459, no. 7245, pp. 414–418, 2009.

[33] D. H. Williams and M. S. Westwell, "Aspects of weak interactions," *Chemical Society Reviews*, vol. 27, no. 1, pp. 57–64, 1998.

[34] G. M. Whitesides, E. E. Simanek, J. P. Mathias, C. T. Seto, D. Chin, M. Mammen, and D. M. Gordon, "Noncovalent synthesis: Using physical-organic chemistry to make aggregates," *Accounts of Chemical Research*, vol. 28, no. 1, pp. 37–44, 1995.

[35] J. C. MacDonald and G. M. Whitesides, "Solid-state structures of hydrogen-bonded tapes based on cyclic secondary diamides," *Chemical Reviews*, vol. 94, no. 8, pp. 2383–2420, 1994.

[36] S. C. Zimmerman and P. S. Corbin, *Heteroaromatic Modules for Self-Assembly Using Multiple Hydrogen Bonds*, pp. 63–94. Berlin, Heidelberg: Springer Berlin Heidelberg, 2000.

[37] F. H. Beijer, R. P. Sijbesma, J. A. J. M. Vekemans, E. W. Meijer, H. Kooijman, and A. L. Spek, "Hydrogen-bonded complexes of diaminopyridines and diaminotriazines: Opposite effect of acylation on complex stabilities," *The Journal of Organic Chemistry*, vol. 61, no. 18, pp. 6371–6380, 1996.

[38] C. Schmuck and W. Wienand, "Self-complementary quadruple hydrogen-bonding motifs as a functional principle: From dimeric supramolecules to supramolecular polymers," *Angewandte Chemie International Edition*, vol. 40, no. 23, pp. 4363–4369, 2001.

[39] U. Lüning and C. Kühl, "Heterodimers for molecular recognition by fourfold hydrogen bonds," *Tetrahedron Letters*, vol. 39, no. 32, pp. 5735–5738, 1998.

[40] B. J. B. Folmer, R. P. Sijbesma, H. Kooijman, A. L. Spek, and E. W. Meijer, "Cooperative dynamics in duplexes of stacked hydrogen-bonded moieties," *Journal of the American Chemical Society*, vol. 121, no. 39, pp. 9001–9007, 1999.

[41] N. Zimmerman, J. Moore, and S. Zimmerman, "Polymer chemistry comes full circle," *Chem-*

istry and industry, no. 15, pp. 604–610, 1998.

[42] A. Cifferi, *Supramolecular Polymers*. Marcel Dekker, New York, 2000.

[43] P. J. M. Stals, Y. Li, J. Burdyńska, R. Nicolaÿ, A. Nese, A. R. A. Palmans, E. W. Meijer, K. Matyjaszewski, and S. S. Sheiko, "How far can we push polymer architectures?," *Journal of the American Chemical Society*, vol. 135, no. 31, pp. 11421–11424, 2013.

[44] T. F. A. De Greef, M. M. J. Smulders, M. Wolffs, A. P. H. J. Schenning, R. P. Sijbesma, and E. W. Meijer, "Supramolecular polymerization," *Chemical Reviews*, vol. 109, no. 11, pp. 5687–5754, 2009.

[45] T. Aida, E. W. Meijer, and S. I. Stupp, "Functional supramolecular polymers," *Science*, vol. 335, no. 6070, pp. 813–817, 2012.

[46] R. Kramer, J. M. Lehn, and A. Marquis-Rigault, "Self-recognition in helicate self-assembly: spontaneous formation of helical metal complexes from mixtures of ligands and metal ions.," *Proceedings of the National Academy of Sciences of the United States of America*, vol. 90, no. 12, pp. 5394–5398, 1993.

[47] D. L. Caulder and K. N. Raymond, "Superamolecular self-recognition and self-assembly in gallium(iii) catecholamide triple helices," *Angewandte Chemie International Edition in English*, vol. 36, no. 13-14, pp. 1440–1442, 1997.

[48] M. Albrecht, M. Schneider, and H. Röttele, "Template-directed self-recognition of alkyl-bridged bis(catechol) ligands in the formation of helicate-type complexes," *Angewandte Chemie International Edition*, vol. 38, no. 4, pp. 557–559, 1999.

[49] J. Yu, W. Wei, E. Danner, R. K. Ashley, J. N. Israelachvili, and J. H. Waite, "Mussel protein adhesion depends on thiol-mediated redox modulation," *Nature chemical biology*, vol. 7, no. 9, pp. 588–590, 2011.

[50] N. Holten-Andersen, M. J. Harrington, H. Birkedal, B. P. Lee, P. B. Messersmith, K. Y. C. Lee, and J. H. Waite, "ph-induced metal-ligand cross-links inspired by mussel yield self-healing polymer networks with near-covalent elastic moduli," *Proceedings of the National Academy of Sciences*, vol. 108, pp. 2651–2655, 02 2011.

[51] S. W. Werneke, C. Swann, L. A. Farquharson, K. S. Hamilton, and A. M. Smith, "The role of metals in molluscan adhesive gels," *Journal of Experimental Biology*, vol. 210, no. 12, pp. 2137–2145, 2007.

[52] N. Holten-Andersen, A. Jaishankar, M. J. Harrington, D. E. Fullenkamp, G. DiMarco, L. He, G. H. McKinley, P. B. Messersmith, and K. Y. C. Lee, "Metal-coordination: using one of nature's tricks to control soft material mechanics," *Journal of Materials Chemistry B*, vol. 2, no. 17, pp. 2467–2472, 2014.

[53] R. J. Hunter, *Foundations of colloid science*. Oxford University Press, 2001.

[54] J. N. Israelachvili, *Intermolecular and surface forces*. London ; San Diego: Academic Press, 1991.

[55] K. A. Dill, "Dominant forces in protein folding," *Biochemistry*, vol. 29, pp. 7133–7155, 08 1990.

[56] D. F. Evans and B. W. Ninham, "Molecular forces in the self-organization of amphiphiles," *The Journal of Physical Chemistry*, vol. 90, no. 2, pp. 226–234, 1986.

[57] C. Tanford, *The Hydrophobic Effect: Formation of Micelles and Biological Membranes 2d Ed*. J. Wiley., 1980.

[58] J. N. Israelachvili, D. J. Mitchell, and B. W. Ninham, "Theory of self-assembly of hydrocarbon amphiphiles into micelles and bilayers," *J. Chem. Soc., Faraday Trans. 2*, vol. 72, pp. 1525–1568, 1976.

[59] S. T. Hyse, "Curvature and the global structure of interfaces in surfactant-water systems," *J. Phys. Colloques*, vol. 51, no. C7, pp. 209–228, 1990.

[60] M. Antonietti and S. Förster, "Vesicles and liposomes: A self-assembly principle beyond lipids," *Advanced Materials*, vol. 15, no. 16, pp. 1323–1333, 2003.

[61] M. Langer, J. Brandt, A. Lederer, A. S. Goldmann, F. H. Schacher, and C. Barner-Kowollik, "Amphiphilic block copolymers featuring a reversible hetero diels-alder linkage," *Polymer Chemistry*, vol. 5, no. 18, pp. 5330–5338, 2014.

[62] S. Förster and M. Antonietti, "Amphiphilic block copolymers in structure-controlled nanomaterial hybrids," *Advanced Materials*, vol. 10, no. 3, pp. 195–217, 1998.

[63] A. Taubert, A. Napoli, and W. Meier, "Self-assembly of reactive amphiphilic block copolymers as mimetics for biological membranes," *Current Opinion in Chemical Biology*, vol. 8, no. 6, pp. 598–603, 2004.

[64] A. Carlsen and S. Lecommandoux, "Self-assembly of polypeptide-dased block copolymer amphiphiles," *Curr. Opin. Colloid Interface Sci.*, vol. 14, pp. 329–339, 2009.

[65] Y.-C. Huang, M. Arham, and J.-S. Jan, "Alkyl chain grafted poly(l-lysine): self-assembly and biomedical application as carriers," *Soft Matter*, vol. 7, no. 8, pp. 3975–3983, 2011.

[66] S. Förster, N. Hermsdorf, C. Böttcher, and P. Lindner, "Structure of polyelectrolyte block copolymer micelles," *Macromolecules*, vol. 35, no. 10, pp. 4096–4105, 2002.

[67] E. G. Bellomo, M. D. Wyrsta, L. Pakstis, D. J. Pochan, and T. J. Deming, "Stimuli-responsive polypeptide vesicles by conformation-specific assembly," *Nat Mater*, vol. 3, no. 4, pp. 244–248, 2004.

[68] H. Kukula, H. Schlaad, M. Antonietti, and S. Förster, "The formation of polymer vesicles

or "peptosomes"by polybutadiene-block-poly(l-glutamate)s in dilute aqueous solution," *Journal of the American Chemical Society*, vol. 124, no. 8, pp. 1658–1663, 2002.

[69] J. Rodríguez-Hernández and S. Lecommandoux, "Reversible inside-out micellization of ph-responsive and water-soluble vesicles based on polypeptide diblock copolymers," *Journal of the American Chemical Society*, vol. 127, no. 7, pp. 2026–2027, 2005.

[70] K. Kita-Tokarczyk, J. Grumelard, T. Haefele, and W. Meier, "Block copolymer vesicles—using concepts from polymer chemistry to mimic biomembranes," *Polymer*, vol. 46, no. 11, pp. 3540–3563, 2005.

[71] R. P. Brinkhuis, F. P. J. T. Rutjes, and J. C. M. van Hest, "Polymeric vesicles in biomedical applications," *Polymer Chemistry*, vol. 2, no. 7, pp. 1449–1462, 2011.

[72] B.-Y. Chen, Y.-F. Huang, Y.-C. Huang, T.-C. Wen, and J.-S. Jan, "Alkyl chain-grafted poly(l-lysine) vesicles with tunable molecular assembly and membrane permeability," *ACS Macro Letters*, vol. 3, no. 3, pp. 220–223, 2014.

[73] J. Song, J. Zhou, and H. Duan, "Self-assembled plasmonic vesicles of sers-encoded amphiphilic gold nanoparticles for cancer cell targeting and traceable intracellular drug delivery," *Journal of the American Chemical Society*, vol. 134, no. 32, pp. 13458–13469, 2012.

[74] R. H. Utama, M. Drechsler, S. Förster, P. B. Zetterlund, and M. H. Stenzel, "Synthesis of ph-responsive nanocapsules via inverse miniemulsion periphery raft polymerization and post-polymerization reaction," *ACS Macro Letters*, vol. 3, no. 9, pp. 935–939, 2014.

[75] E. V. Anslyn and D. A. Dougherty, *Modern Physical Organic Chemistry*. University Science Books; Sausalito, CA,, 2005.

[76] E. A. Meyer, R. K. Castellano, and F. Diederich, "Interactions with aromatic rings in chemical and biological recognition," *Angewandte Chemie International Edition*, vol. 42, no. 11, pp. 1210–1250, 2003.

[77] D. J. Selkoe, "Cell biology of the amyloid beta-protein precursor and the mechanism of alzheimer's disease," *Annual Review of Cell Biology*, vol. 10, no. 1, pp. 373–403, 1994.

[78] R. Michels, T. Sinemus, J. Hoffmann, B. Brutschy, and K. Huber, "Co-aggregation of two anionic azo dyestuffs at a well-defined stoichiometry," *The Journal of Physical Chemistry B*, vol. 117, no. 28, pp. 8611–8619, 2013.

[79] C. G. Claessens and J. F. Stoddart, "Review commentary–interactions in self-assembly," *Journal of physical organic chemistry*, vol. 10, pp. 254–272, 1997.

[80] C. A. Hunter and J. K. Sanders, "The nature of. pi.-. pi. interactions," *Journal of the American Chemical Society*, vol. 112, no. 14, pp. 5525–5534, 1990.

[81] P. Chakrabarti and R. Bhattacharyya, "Geometry of nonbonded interactions involving pla-

nar groups in proteins," *Progress in biophysics and molecular biology*, vol. 95, no. 1, pp. 83–137, 2007.

[82] C. Hunter, "Aromatic interactions in proteins, dna and synthetic receptors," *Philosophical Transactions of the Royal Society of London A: Mathematical, Physical and Engineering Sciences*, vol. 345, no. 1674, pp. 77–85, 1993.

[83] G. B. McGaughey, M. Gagné, and A. K. Rappé, "π-stacking interactions alive and well in proteins," *Journal of Biological Chemistry*, vol. 273, no. 25, pp. 15458–15463, 1998.

[84] J. H. Williams, J. K. Cockcroft, and A. N. Fitch, "Structure of the lowest temperature phase of the solid benzene–hexafluorobenzene adduct," *Angewandte Chemie International Edition in English*, vol. 31, no. 12, pp. 1655–1657, 1992.

[85] S. A. Nepogodiev and J. F. Stoddart, "Cyclodextrin-based catenanes and rotaxanes," *Chemical reviews*, vol. 98, no. 5, pp. 1959–1976, 1998.

[86] J. C. Ma and D. A. Dougherty, "The cation-π interaction," *Chemical reviews*, vol. 97, no. 5, pp. 1303–1324, 1997.

[87] M. O. Sinnokrot and C. D. Sherrill, "High-accuracy quantum mechanical studies of π-π interactions in benzene dimers," *The Journal of Physical Chemistry A*, vol. 110, no. 37, pp. 10656–10668, 2006.

[88] D. M. Rogers, J. D. Hirst, E. P. Lee, and T. G. Wright, "Ab initio study of the toluene dimer," *Chemical physics letters*, vol. 427, no. 4, pp. 410–413, 2006.

[89] S. E. Wheeler, "Local nature of substituent effects in stacking interactions," *Journal of the American Chemical Society*, vol. 133, no. 26, pp. 10262–10274, 2011.

[90] M. J. Rashkin and M. L. Waters, "Unexpected substituent effects in offset π-π stacked interactions in water," *Journal of the American Chemical Society*, vol. 124, no. 9, pp. 1860–1861, 2002.

[91] C. Niu, L. Zhao, T. Fang, X. Deng, H. Ma, J. Zhang, N. Na, J. Han, and J. Ouyang, "Color- and morphology-controlled self-assembly of new electron-donor-substituted aggregation-induced emission compounds," *Langmuir*, vol. 30, no. 9, pp. 2351–2359, 2014.

[92] S. Kim, T. Y. Ohulchanskyy, H. E. Pudavar, R. K. Pandey, and P. N. Prasad, "Organically modified silica nanoparticles co-encapsulating photosensitizing drug and aggregation-enhanced two-photon absorbing fluorescent dye aggregates for two-photon photodynamic therapy," *Journal of the American Chemical Society*, vol. 129, no. 9, pp. 2669–2675, 2007.

[93] M. Baldo, M. Thompson, and S. Forrest, "High-efficiency fluorescent organic light-emitting devices using a phosphorescent sensitizer," *Nature*, vol. 403, no. 6771, pp. 750–753, 2000.

[94] C. Faul and M. Antonietti, "Ionic self-assembly: Facile synthesis of supramolecular materi-

als," *Advanced Materials*, vol. 15, no. 9, pp. 673–683, 2003.

[95] M. Antonietti, J. Conrad, and A. Thuenemann, "Polyelectrolyte-surfactant complexes: A new type of solid, mesomorphous material," *Macromolecules*, vol. 27, no. 21, pp. 6007–6011, 1994.

[96] J. O. Rädler, I. Koltover, T. Salditt, and C. R. Safinya, "Structure of dna-cationic liposome complexes: Dna intercalation in multilamellar membranes in distinct interhelical packing regimes," *Science*, vol. 275, no. 5301, pp. 810–814, 1997.

[97] A. F. Thünemann, J. Beyermann, C. von Ferber, and H. Löwen, "Immobilization of retinoic acid by polyamino acids: Lamellar-structured nanoparticles," *Langmuir*, vol. 16, no. 2, pp. 850–857, 2000.

[98] C. F. J. Faul and M. Antonietti, "Facile synthesis of optically functional, highly organized nanostructures: Dye–surfactant complexes," *Chemistry – A European Journal*, vol. 8, no. 12, pp. 2764–2768, 2002.

[99] Y. Zakrevskyy, J. Stumpe, and C. Faul, "A supramolecular approach to optically anisotropic materials: Photosensitive ionic self-assembly complexes," *Advanced Materials*, vol. 18, no. 16, pp. 2133–2136, 2006.

[100] E. Krämer, S. Förster, C. Göltner, and M. Antonietti, "Synthesis of nanoporous silica with new pore morphologies by templating the assemblies of ionic block copolymers," *Langmuir*, vol. 14, no. 8, pp. 2027–2031, 1998.

[101] P. Bertrand, A. Jonas, A. Laschewsky, and R. Legras, "Ultrathin polymer coatings by complexation of polyelectrolytes at interfaces: suitable materials, structure and properties," *Macromolecular Rapid Communications*, vol. 21, no. 7, pp. 319–348, 2000.

[102] K. Glinel, C. Déjugnat, M. Prevot, B. Schöler, M. Schönhoff, and R. v. Klitzing, "Responsive polyelectrolyte multilayers," *Colloids and Surfaces A: Physicochemical and Engineering Aspects*, vol. 303, no. 1–2, pp. 3–13, 2007.

[103] K. Zhang, Z. Hu, R. Xu, X.-F. Jiang, H.-L. Yip, F. Huang, and Y. Cao, "High-performance polymer solar cells with electrostatic layer-by-layer self-assembled conjugated polyelectrolytes as the cathode interlayer," *Advanced Materials*, vol. 27, no. 24, pp. 3607–3613, 2015.

[104] A. F. Thünemann, M. Müller, H. Dautzenberg, J.-F. Joanny, and H. Löwen, *Polyelectrolyte Complexes*, pp. 113–171. Berlin, Heidelberg: Springer Berlin Heidelberg, 2004.

[105] D. Störkle, S. Duschner, N. Heimann, M. Maskos, and M. Schmidt, "Complex formation of dna with oppositely charged polyelectrolytes of different chain topology: Cylindrical brushes and dendrimers," *Macromolecules*, vol. 40, no. 22, pp. 7998–8006, 2007.

[106] F. Gröhn and M. Antonietti, "Intermolecular structure of spherical polyelectrolyte micro-

gels in salt-free solution. 1. quantification of the attraction between equally charged polyelectrolytes," *Macromolecules*, vol. 33, no. 16, pp. 5938–5949, 2000.

[107] M. Antonietti, A. Briel, and F. Gröhn, "Spherical polyelectrolyte microgels in salt-free solution. 2. combined analysis of static structure and viscosity and quantitative testing of the mode‚àímode coupling approximation," *Macromolecules*, vol. 33, no. 16, pp. 5950–5953, 2000.

[108] S. Förster, M. Schmidt, and M. Antonietti, "Static and dynamic light scattering by aqueous polyelectrolyte solutions: effect of molecular weight, charge density and added salt," *Polymer*, vol. 31, no. 5, pp. 781–792, 1990.

[109] M. Sedlák and E. J. Amis, "Concentration and molecular weight regime diagram of salt‚Äêfree polyelectrolyte solutions as studied by light scattering," *The Journal of Chemical Physics*, vol. 96, no. 1, pp. 826–834, 1992.

[110] M. Antonietti, F. Gröhn, J. Hartmann, and L. Bronstein, "Nonclassical shapes of noble-metal colloids by synthesis in microgel nanoreactors," *Angewandte Chemie International Edition in English*, vol. 36, no. 19, pp. 2080–2083, 1997.

[111] J. S. Melinger, V. D. Kleiman, D. McMorrow, F. Gröhn, B. J. Bauer, and E. Amis, "Ultrafast dynamics of gold-based nanocomposite materials," *The Journal of Physical Chemistry A*, vol. 107, no. 18, pp. 3424–3431, 2003.

[112] E. J. W. Verwey and J. T. G. Overbeek, *Theory of the stability of lyophobic colloids*. Courier Corporation, 1999.

[113] K. S. Schmitz, *Macroions in Solution and Colloidal Suspension*. VCH Publishers: New York, 1993.

[114] H. Hamaker, "The london—van der waals attraction between spherical particles," *Physica*, vol. 4, no. 10, pp. 1058 – 1072, 1937.

[115] D. H. Everett, *Basic Principles of Colloid Science*. RSC Paperbacks, The Royal Society of Chemistry, 1988.

[116] R. Messina, C. Holm, and K. Kremer, "Strong attraction between charged spheres due to metastable ionized states," *Phys. Rev. Lett.*, vol. 85, pp. 872–875, 2000.

[117] Y. Zhang, J. F. Douglas, B. D. Ermi, and E. J. Amis, "Influence of counterion valency on the scattering properties of highly charged polyelectrolyte solutions," *The Journal of Chemical Physics*, vol. 114, no. 7, pp. 3299–3313, 2001.

[118] A. Kose, M. Ozaki, K. Takano, Y. Kobayashi, and S. Hachisu, "Direct observation of ordered latex suspension by metallurgical microscope," *Journal of Colloid and Interface Science*, vol. 44, no. 2, pp. 330–338, 1973.

[119] N. Ise, K. Ito, T. Okubo, S. Dosho, and I. Sogami, ""ordered" structure in dilute suspensions of highly charged polymer lattices as studied by microscopy. 2. the influence of ionic strength, dielectric constant, temperature, and viscosity," *Journal of the American Chemical Society*, vol. 107, no. 26, pp. 8074–8077, 1985.

[120] K. Ito, H. Okumura, H. Yoshida, Y. Ueno, and N. Ise, "Two-dimensional fourier analysis and quasielastic light-scattering measurements of colloid crystals," *Physical Review B*, vol. 38, no. 15, pp. 10852–10859, 1988.

[121] K. Ito, H. Yoshida, and N. Ise, "Void structure in colloidal dispersions," *Science*, vol. 263, no. 5143, pp. 66–68, 1994.

[122] I. Sogami and N. Ise, "On the electrostatic interaction in macroionic solutions," *The Journal of Chemical Physics*, vol. 81, no. 12, pp. 6320–6332, 1984.

[123] M. Tokuyama, "Theory of slow dynamics in highly charged colloidal suspensions," *Physical Review E*, vol. 58, no. 3, pp. R2729–R2732, 1998.

[124] M. Tokuyama, "Effective forces between macroions in highly charged colloidal suspensions," *Physical Review E*, vol. 59, no. 3, pp. R2550–R2553, 1999.

[125] S.-C. Lin, W. I. Lee, and J. M. Schurr, "Brownian motion of highly charged poly(l-lysine). effects of salt and polyion concentration," *Biopolymers*, vol. 17, no. 4, pp. 1041–1064, 1978.

[126] P. Mathiez, G. Weisbuch, and C. Mouttet, "Inelastic light-scattering study of polyadenilic acid," *Biopolymers*, vol. 18, no. 6, pp. 1465–1478, 1979.

[127] J. P. Wilcoxon and J. M. Schurr, "Electrophoretic light scattering studies of poly(l,Äêlysine) in the ordinary and extraordinary phase. effects of salt, molecular weight, and polyion concentration," *The Journal of Chemical Physics*, vol. 78, no. 6, pp. 3354–3364, 1983.

[128] K. S. Schmitz, M. Lu, and J. Gauntt, "Influence of ionic strength on the diffusion of polystyrene latex spheres, bovine serum albumin, and polynucleosomes," *The Journal of Chemical Physics*, vol. 78, no. 8, pp. 5059–5066, 1983.

[129] T. M. Bergstöm, L. Magnus, *Application of Theromdynamics to Biological and Material Science*. InTech, 2011.

[130] C. Seidel, "Physics of amphiphiles: Micelles, vesicles and microemulsions.," *Acta Polymerica*, vol. 37, no. 7, pp. 474–474, 1986.

[131] D. F. Evans and P. J. Wightman, "Micelle formation above 100 °c," *Journal of Colloid and Interface Science*, vol. 86, no. 2, pp. 515–524, 1982.

[132] D. F. Evans, M. Allen, B. W. Ninham, and A. Fouda, "Critical micelle concentrations for alkyltrimethylammonium bromides in water from 25 to 160 °c," *Journal of Solution Chemistry*, vol. 13, no. 2, pp. 87–101, 1984.

[133] H. Wennerström and B. Lindman, "Micelles. physical chemistry of surfactant association," *Physics Reports*, vol. 52, no. 1, pp. 1–86, 1979.

[134] D. J. Mitchell and B. W. Ninham, "Micelles, vesicles and microemulsions," *Journal of the Chemical Society, Faraday Transactions 2: Molecular and Chemical Physics*, vol. 77, no. 4, pp. 601–629, 1981.

[135] E. Guggenheim, *Mixtures: The Theory of the Equlibrium Properties of Some Simple Classes of Mixtures Solutions and Alloys*. The International series of monographs on physics, Clarendon Press, 1952.

[136] P. J. Flory, "Fifteenth spiers memorial lecture. thermodynamics of polymer solutions," *Discuss. Faraday Soc.*, vol. 49, pp. 7–29, 1970.

[137] K. Shinoda, "The formation of micelles," in *Colloidal Surfactants*, vol. 12 of *Physical Chemistry: A Series of Monographs*, pp. 1 – 96, Academic Press, 1963.

[138] B. Jönson, B. Lindman, K. Holmberg, and B. Kronberg, *Surfactants and Polymers in Aqueous Solution*. Wiley, 1998.

[139] A. Holtzer and M. F. Holtzer, "Use of the van't hoff relation in determination of the enthalpy of micelle formation," *The Journal of Physical Chemistry*, vol. 78, no. 14, pp. 1442–1443, 1974.

[140] L. Chiappisi, G. Lazzara, M. Gradzielski, and S. Milioto, "Quantitative description of temperature induced self-aggregation thermograms determined by differential scanning calorimetry," *Langmuir*, vol. 28, no. 51, pp. 17609–17616, 2012.

[141] X. Chi, A. J. Guerin, R. A. Haycock, C. A. Hunter, and L. D. Sarson, "The thermodynamics of self-assembly," *J. Chem. Soc., Chem. Commun.*, pp. 2563–2565, 1995.

[142] F. Würthner, "Bay-substituted perylene bisimides: Twisted fluorophores for supramolecular chemistry," *Pure and applied chemistry*, vol. 78, no. 12, pp. 2341–2349, 2006.

[143] I. Willerich, H. Ritter, and F. Gröhn, "Structure and thermodynamics of ionic dendrimer‚àídye assemblies," *The Journal of Physical Chemistry B*, vol. 113, no. 11, pp. 3339–3354, 2009.

[144] I. Willerich and F. Gröhn, "Molecular structure encodes nanoscale assemblies: Understanding driving forces in electrostatic self-assembly," *Journal of the American Chemical Society*, vol. 133, no. 50, pp. 20341–20356, 2011.

[145] V. J. Anderson and H. N. W. Lekkerkerker, "Insights into phase transition kinetics from colloid science," *Nature*, vol. 416, no. 6883, pp. 811–815, 2002.

[146] M. J. Solomon, "Directions for targeted self-assembly of anisotropic colloids from statistical thermodynamics," *Current Opinion in Colloid & Interface Science*, vol. 16, no. 2, pp. 158–167, 2011.

[147] S. C. Glotzer and M. J. Solomon, "Anisotropy of building blocks and their assembly into complex structures," *Nat Mater*, vol. 6, no. 7, pp. 557–562, 2007.

[148] P. Pfleiderer and T. Schilling, "Simple monoclinic crystal phase in suspensions of hard ellipsoids," *Physical Review E*, vol. 75, no. 2, pp. 020402–, 2007.

[149] M. Radu, P. Pfleiderer, and T. Schilling, "Solid-solid phase transition in hard ellipsoids," *The Journal of Chemical Physics*, vol. 131, no. 16, 2009.

[150] F. W. Starr, J. F. Douglas, and S. C. Glotzer, "Origin of particle clustering in a simulated polymer nanocomposite and its impact on rheology," *The Journal of Chemical Physics*, vol. 119, no. 3, pp. 1777–1788, 2003.

[151] J. M. Tavares, P. I. C. Teixeira, M. M. Telo da Gama, and F. Sciortino, "Equilibrium self-assembly of colloids with distinct interaction sites: Thermodynamics, percolation, and cluster distribution functions," *The Journal of Chemical Physics*, vol. 132, no. 23, 2010.

[152] J. Dudowicz, J. F. Douglas, and K. F. Freed, "Self-assembly by mutual association: Basic thermodynamic properties," *The Journal of Physical Chemistry B*, vol. 112, no. 50, pp. 16193–16204, 2008.

[153] S. Förster, M. Schmidt, and M. Antonietti, "Static and dynamic light scattering by aqueous polyelectrolyte solutions: effect of molecular weight, charge density and added salt," *Polymer*, vol. 31, no. 5, pp. 781–792, 1990.

[154] E. Amis and M. Sedlak *Macroion Characterization Chapter 26, ACS Symposium Series*, vol. 548, pp. 337–348, 1993.

[155] P.-G. d. De Gennes, P. Pincus, R. Velasco, and F. Brochard, "Remarks on polyelectrolyte conformation," *Journal de physique*, vol. 37, no. 12, pp. 1461–1473, 1976.

[156] Y. Ikeda, M. Beer, M. Schmidt, and K. Huber, "Ca2+ and cu2+ induced conformational changes of sodium polymethacrylate in dilute aqueous solution," *Macromolecules*, vol. 31, no. 3, pp. 728–733, 1998.

[157] G. Goerigk, K. Huber, and R. Schweins, "Probing the extent of the sr2+ ion condensation to anionic polyacrylate coils: a quantitative anomalous small-angle x-ray scattering study.," *The Journal of chemical physics*, vol. 127, no. 15, pp. 154908–154908, 2007.

[158] C. G. Sinn, R. Dimova, and M. Antonietti, "Isothermal titration calorimetry of the polyelectrolyte/water interaction and binding of ca2+: effects determining the quality of polymeric scale inhibitors," *Macromolecules*, vol. 37, no. 9, pp. 3444–3450, 2004.

[159] G. Decher, "Fuzzy nanoassemblies: toward layered polymeric multicomposites," *science*, vol. 277, no. 5330, pp. 1232–1237, 1997.

[160] G. B. Sukhorukov, E. Donath, H. Lichtenfeld, E. Knippel, M. Knippel, A. Budde, and

H. Möhwald, "Layer-by-layer self assembly of polyelectrolytes on colloidal particles," *Colloids and Surfaces A: Physicochemical and Engineering Aspects*, vol. 137, no. 1–3, pp. 253–266, 1998.

[161] I. Koltover, T. Salditt, J. O. Rädler, and C. R. Safinya, "An inverted hexagonal phase of cationic liposome-dna complexes related to dna release and delivery," *Science*, vol. 281, no. 5373, pp. 78–81, 1998.

[162] A. F. Thünemann and J. Beyermann, "Polyethylenimine complexes with retinoic acid: Structure, release profiles, and nanoparticles," *Macromolecules*, vol. 33, no. 18, pp. 6878–6885, 2000.

[163] C. K. Ober and G. Wegner, "Polyelectrolyte–surfactant complexes in the solid state: Facile building blocks for self-organizing materials," *Advanced Materials*, vol. 9, no. 1, pp. 17–31, 1997.

[164] C. D. Bain, P. M. Claesson, D. Langevin, R. Meszaros, T. Nylander, C. Stubenrauch, S. Titmuss, and R. von Klitzing, "Complexes of surfactants with oppositely charged polymers at surfaces and in bulk," *Advances in Colloid and Interface Science*, vol. 155, no. 1–2, pp. 32–49, 2010.

[165] D. Langevin, "Complexation of oppositely charged polyelectrolytes and surfactants in aqueous solutions. a review," *Advances in Colloid and Interface Science*, vol. 147–148, pp. 170–177, 2009.

[166] L. Chiappisi, I. Hoffmann, and M. Gradzielski, "Complexes of oppositely charged polyelectrolytes and surfactants - recent developments in the field of biologically derived polyelectrolytes," *Soft Matter*, vol. 9, pp. 3896–3909, 2013.

[167] T. E. Kaiser, H. Wang, V. Stepanenko, and F. Würthner, "Supramolecular construction of fluorescent j-aggregates based on hydrogen-bonded perylene dyes," *Angewandte Chemie International Edition*, vol. 46, no. 29, pp. 5541–5544, 2007.

[168] F. J. Hoeben, P. Jonkheijm, E. Meijer, and A. P. Schenning, "About supramolecular assemblies of π-conjugated systems," *Chemical Reviews*, vol. 105, no. 4, pp. 1491–1546, 2005.

[169] X. Zhang, S. Rehm, M. M. Safont-Sempere, and F. Würthner, "Vesicular perylene dye nanocapsules as supramolecular fluorescent ph sensor systems," *Nature chemistry*, vol. 1, no. 8, pp. 623–629, 2009.

[170] Z. Chen, A. Lohr, C. R. Saha-Möller, and F. Würthner, "Self-assembled π-stacks of functional dyes in solution: structural and thermodynamic features," *Chemical Society Reviews*, vol. 38, no. 2, pp. 564–584, 2009.

[171] J.-F. Gnichwitz, M. Wielopolski, K. Hartnagel, U. Hartnagel, D. M. Guldi, and A. Hirsch, "Cooperativity and tunable excited state deactivation: Modular self-assembly of depsipep-

tide dendrons on a hamilton receptor modified porphyrin platform," *Journal of the American Chemical Society*, vol. 130, no. 26, pp. 8491–8501, 2008.

[172] A. R. Monahan and D. F. Blossey, "Aggregation of arylazonaphthols. i. dimerization of bonadur red in aqueous and methanolic systems," *The Journal of Physical Chemistry*, vol. 74, no. 23, pp. 4014–4021, 1970.

[173] R. L. Reeves, M. S. Maggio, and S. A. Harkaway, "A critical spectrophotometric analysis of the dimerization of some ionic azo dyes in aqueous solution," *Journal of Physical Chemistry*, vol. 83, no. 18, pp. 2359–2368, 1979.

[174] B. Neumann, K. Huber, and P. Pollmann, "A comparative experimental study of the aggregation of acid red 266 in aqueous solution by use of 19f-nmr, uv/vis spectroscopy and static light scattering," *Phys. Chem. Chem. Phys.*, vol. 2, pp. 3687–3695, 2000.

[175] S. E. Inglés, A. Katzenstein, W. Schlenker, and K. Huber, "Time-resolved recording of ionic dyestuff aggregation by static light scattering," *Langmuir*, vol. 16, no. 7, pp. 3010–3018, 2000.

[176] Y. Guan, M. Antonietti, and C. F. Faul, "Ionic self-assembly of dye-surfactant complexes: influence of tail lengths and dye architecture on the phase morphology," *Langmuir*, vol. 18, no. 15, pp. 5939–5945, 2002.

[177] I. Willerich and F. Gröhn, "Switchable nanoassemblies from macroions and multivalent dye counterions," *Chemistry-A European Journal*, vol. 14, no. 30, pp. 9112–9116, 2008.

[178] G. Mariani, R. Schweins, and F. Gröhn, "Structure tuning of electrostatically self-assembled nanoparticles through ph," *The Journal of Physical Chemistry B*, vol. 120, no. 7, pp. 1380–1389, 2016.

[179] I. Willerich, Y. Li, and F. Gröhn, "Influencing particle size and stability of ionic dendrimer-dye assemblies," *The Journal of Physical Chemistry B*, vol. 114, no. 47, pp. 15466–15476, 2010.

[180] I. Willerich, T. Schindler, and F. Gröhn, "Effect of polyelectrolyte architecture and size on macroion–dye assemblies," *The Journal of Physical Chemistry B*, vol. 115, no. 32, pp. 9710–9719, 2011.

[181] D. Moldenhauer and F. Gröhn, "Nanoassemblies with light-responsive size and density from linear flexible polyelectrolytes," *Journal of Polymer Science Part B: Polymer Physics*, vol. 51, no. 10, pp. 802–816, 2013.

[182] J. Düring, A. Hölzer, U. Kolb, R. Branscheid, and F. Gröhn, "Supramolekulare organisch-anorganische hybridaggregate mit variabler partikelgröße: Zusammenspiel von drei nichtkovalenten wechselwirkungen," *Angewandte Chemie*, vol. 125, no. 33, pp. 8905–8908, 2013.

[183] A. Kutz, G. Mariani, and F. Gröhn, "Ionic dye–surfactant nanoassemblies: interplay of elec-

trostatics, hydrophobic effect, and π–π stacking," *Colloid and Polymer Science*, vol. 294, no. 3, pp. 591–606, 2015.

[184] A. Guinier and G. Fournet, *Small angle scattering of x-rays*. J. Wiley Sons, New York, 1995.

[185] O. Glatter and O. Kratky, *Small angle x-ray scattering*. Academic Press, London, 1982.

[186] M. Khajehpour and J. F. Kauffman, "Charge transfer kinetics and solvatochromism of 1-(9-anthryl)-3-(4-dimethylaniline) propane in 1,4-dioxane: Nonideal quadrupolar charge distribution and the origin of the dioxane anomaly," *The Journal of Physical Chemistry A*, vol. 105, pp. 10316–10321, 11 2001.

[187] E. McRae, "Molecular vibrations in the exciton theory for molecular aggregates. i. general theory," *Australian Journal of Chemistry*, vol. 14, no. 3, pp. 329–343, 1961.

[188] E. McRae, "Molecular vibrations in the exciton theory for molecular aggregates. ii. dimeric systems," *Australian Journal of Chemistry*, vol. 14, no. 3, pp. 344–353, 1961.

[189] E. McRae, "Molecular vibrations in the exciton theory for molecular aggregates. iii. polymeric systems," *Australian Journal of Chemistry*, vol. 14, no. 3, pp. 354–371, 1961.

[190] M. Kasha, H. Rawls, and M. Ashraf El-Bayoumi, "The exciton model in molecular spectroscopy," *Pure and Applied Chemistry*, vol. 11, no. 3-4, pp. 371–392, 1965.

[191] J. T. G. Overbeek *Kolloid Beith*, vol. 54, pp. 287–364, 1943.